NASA CR-165348

SSS-R-81-4798

ANALYSIS OF THE CHARGING OF THE SCATHA (P78-2) SATELLITE

P.R. Stannard, I. Katz, M.J. Mandell, J.J. Cassidy,
D.E. Parks, M. Rotenberg, P.G. Steen

SYSTEMS, SCIENCE AND SOFTWARE

(NASA-CR-165348) ANALYSIS OF THE CHARGING OF THE SCATHA (P78-2) SATELLITE Final Report, Mar. 1979 - Oct. 1980 (Systems Science and Software) 249 p HC A11/MF A01 CSCL 22B G3/15
N81-27169
Unclas
26828

Prepared for

NATIONAL AERONAUTICS AND SPACE ADMINISTRATION

NASA LEWIS RESEARCH CENTER

Contract NAS3-21762

NASA CR-165348

SSS-R-81-4798

ANALYSIS OF THE CHARGING OF THE SCATHA (P78-2) SATELLITE

P.R. Stannard, I. Katz, M.J. Mandell, J.J. Cassidy,
D.E. Parks, M. Rotenberg, P.G. Steen

SYSTEMS, SCIENCE AND SOFTWARE

Supported by

AIR FORCE GEOPHYSICS LABORATORY
HANSCOM AIR FORCE BASE, MA

Prepared for

NATIONAL AERONAUTICS AND SPACE ADMINISTRATION

NASA LEWIS RESEARCH CENTER

Contract NAS3-21762

1. Report No.
NASA CR-165348

2. Government Accession No.

3. Recipient's Catalog No.

4. Title and Subtitle
ANALYSIS OT THE CHARGING OF THE SCATHA
(P78-2) SATELLITE

5. Report Date
December 1980

6. Performing Organization Code

7. Author(s)
P. R. Stannard, I. Katz, M. J. Mandell, J. J. Cassidy,
D. E. Parks, M. Rotenberg, P. G. Steen

8. Performing Organization Report No.
SSS-R-81-4798

9. Performing Organization Name and Address
Systems, Science and Software
P. O. Box 1620
La Jolla, CA 92038

10. Work Unit No.

11. Contract or Grant No.
NAS3-21762

12. Sponsoring Agency Name and Address
National Aeronautics and Space Administration
Lewis Research Center
21000 Brookpark Road, Cleveland, OH 44135

13. Type of Report and Period Covered
Contractor Report
3/1979-10/1980

14. Sponsoring Agency Code
5532

15. Supplementary Notes

Project Manager, James C. Roche, NASA-Lewis Research Center, Cleveland, OH

16. Abstract

The SCATHA (Satellite Charging AT High Altitude), or P78-2 Satellite was launched early in 1979 specifically to study spacecraft charging in geosynchronous orbit. This contract called for analysis of results obtained from SCATHA using the NASCAP (NASA Charging Analyzer Program) computer code. NASCAP is a fully three-dimensional code capable of dynamically simulating the charging response of a detailed representation of a satellite exposed to a given plasma environment.

Two NASCAP models of SCATHA were constructed and used in simulations of charging events. The properties of the satellite's constituent materials were compiled (e.g., emission characteristics, conductivities, etc.) and representations of the plasma spectra observed experimentally were constructed. Armed with this data simulations of actual charging events observed on Day 87 and Day 89 (1979) of the emission, as well as simulations using test environments, were carried out.

Numerical models for the simulation of particle emitters and detectors, built into NASCAP, were used to analyze the operation of these devices on board SCATHA. The effect of highly charged surface regions (so-called "hot spots") on the charging of neighboring surfaces was examined. A model for effective conductivity within a photosheath was incorporated into NASCAP and used to interpret results from the on-board electric field experiment (SC-10).

Shadowing calculations were carried out for the satellite and a table of effective illuminated areas compiled.

An analytical treatment of the charging of a large object in polar earth orbit was carried out in order to obtain a preliminary indication of the response of the shuttle orbiter to such an environment.

17. Key Words (Suggested by Author(s))
Spacecraft Charging, SCATHA, NASCAP, Plasma Spectra, Computer Simulation, Hot Spot, Shuttle Orbiter, Spacecraft Materials, Secondary Emission, Photosheath, Active Control, Numerical Modeling

18. Distribution Statement
Publicly Available

19. Security Classif. (of this report)
Unclassified

20. Security Classif. (of this page)
Unclassified

21. No. of Pages
254

22. Price*

* For sale by the National Technical Information Service, Springfield, Virginia 22161

TABLE OF CONTENTS

TABLE OF CONTENTS (Continued)

TABLE OF CONTENTS (Continued)

LIST OF FIGURES

LIST OF FIGURES (Continued)

LIST OF FIGURES (Continued)

LIST OF FIGURES (Continued)

LIST OF FIGURES (Continued)

LIST OF FIGURES (Continued)

LIST OF FIGURES (Continued)

LIST OF FIGURES (Continued)

LIST OF TABLES

LIST OF TABLES (Continued)

SUMMARY

This report describes theoretical investigations performed to simulate the charging response of the SCATHA (Satellite Charging AT High Altitude) or P78-2 satellite in geosynchronous orbit. The focus for the investigations was a detailed three-dimensional model of the SCATHA spacecraft which was used with the NASCAP (NASA Charging Analyzer Program) computer code.

Two NASCAP models of SCATHA are described, and their material properties are characterized in detail. The charging response of individual materials and the full SCATHA models is described for a series of test environments and actual plasma environments observed by SCATHA in earth orbit. The results of NASCAP simulations of actual charging events are reported.

The operation of active control and particle detectors were also simulated using NASCAP. Analytical and computational models for the operation of the electron and ion guns are presented.

An analytical model of the influence of a small region of high potential was developed to simulate the effect of "hot spots" on a spacecraft, and the results were compared to the NASCAP model. Two code enhancements were implemented to improve the simulation of photosheath effects: one incorporates a model of effective surface conductivity in the photosheath, and the other allows the self-consistent calculation of the space fields in the photosheath for fixed spacecraft potentials. The latter option was used to aid in the interpretation of the SCATHA electric field experiment.

A table of effective illuminated areas of the SCATHA body was prepared as a supplement to the shadowing tables previously generated for selected SCATHA experiments.

An analytical treatment of the charging of a large object in polar earth orbit is presented and its implications for the operation of the shuttle orbiter are discussed.

1. INTRODUCTION

This report describes a portion of the work performed by Systems, Science and Software on Contract NAS3-21762, "Additional Application of the NASCAP Code". The report covers work in which the NASCAP computer code was used in conjunction with supplementary analytical models to analyze the charging effects of the natural space environment on the SCATHA spacecraft and to analyze the combined effects of this environment and of the charged condition of the spacecraft on the scientific instruments of SCATHA. This work is part of a continuing series of analyses designed to assist in the interpretation of the data collected by the SCATHA spacecraft, and to validate and verify the NASCAP computer code as a modeling tool for analysis of spacecraft charging. The development of a validated code for the analysis of spacecraft charging is one of the goals of the joint NASA/Air Force Spacecraft Charging Investigation program.

Much of the material contained in this report was originally prepared for monthly progress reports during the contract year. This document consolidates those reports and includes additional material to provide a unified and comprehensive description of the SCATHA modeling effort. It is assumed that the reader is familiar with the capabilities and general features of the NASCAP computer code, which is described in detail in References 1-3. Reference 4 provides a summary of the capabilities of the NASCAP program. The first description of the SCATHA model was presented at the 1978 Spacecraft Charging Technology Conference,[5] and a summary of some of the work discussed herein was presented at the 1979 Fall AGU Meeting.[6]

The NASCAP SCATHA model includes specification of the detailed geometrical, electrical, and material parameters of the spacecraft. Complete descriptions of two models are presented in Chapter 2, along with a summary of the SCATHA surface material properties. A discussion of the representation of the plasma environment used by NASCAP is given in Chapter 3.

Chapter 4 reports on a number of aspects of surface charging. These include the effect of the environment representation, material properties, the angular distribution of the incident particle flux and the effect of high energy particles on the charging and discharging of dielectrics.

In Chapters 5 and 6 the charging response of the entire SCATHA vehicle is discussed. Chapter 5 reports on the response of the four-grid model to a set of fictitious test environments, while in Chapter 6 the results of detailed simulations of actual charging events, using the one-grid model, on Days 187 and 89, 1979, are presented.

An important feature of the SCATHA vehicle operation is the ability to use charged particle beams to control the satellite potential. In discussions with AFGL experimenters, various features of the gun operations were chosen for detailed study. The results of these investigations are described in Chapter 7. The NASCAP code includes a DETECTOR mode which simulates fluxes to specified spacecraft surface locations by explicitly generating reverse particle trajectories. Chapter 8 summarizes the simulation of the response of the satellite particle detector experiments using the DETECTOR mode.

A simple analytical model was developed to illustrate the range of influence of an isolated highly charging insulating spot on the nearby spacecraft surfaces, both with and without photosheath effects. A description of these models is presented in Chapter 9. Photosheath effects away from the surface of the vehicle have also been modeled using a self-consistent treatment. This work is described in Chapter 9.

Shadowing tables for selected SCATHA experiments were described previously.[7] For analysis of the overall response of the vehicle, shadowing of body elements by booms and protruding experiments must be considered. Chapter 10 describes such body shadowing effects.

A physical model for the charging of objects large compared to the Debye length of the ambient plasma is developed in Chapter 12. The implications of this for the shuttle orbiter in polar earth orbit are discussed.

Finally, the major conclusions of the study are presented in Chapter 13, along with a number of recommendations for future investigations.

2. SCATHA MODEL DESCRIPTION

The NASCAP program allows the specification of the geometrical, material, and electrical properties of the SCATHA spacecraft in considerable detail. This chapter describes the NASCAP SCATHA models which were used to perform the charging calculations described in Chapters 4 and 5. The models are similar to a preliminary version described elsewhere.[5]

2.1 "FOUR-GRID" MODEL

Perspective views of the four-grid model are shown in Figures 2.1 and 2.2. The main body of the satellite is represented as a right octagonal cylinder, with the aft cavity visible in Figure 2.2. The 11.5 cm grid resolution allows the model to reproduce actual SCATHA geometrical features extremely well, as shown in Table 2.1. Note in particular that the treatment of booms in NASCAP allows the actual boom radii to be reproduced exactly. Figure 2.3 illustrates the computational space in which NASCAP solves Poisson's equation for this model. Monopole boundary conditions are imposed on the edges of the outermost grid, which is a rectangular prism of dimensions 12.8 × 12.8 × 25.6 m. The zone size increases by a factor of 2 in each of the four successive grids. This doubling of zone size, plus the requirements that booms parallel coordinate axes and intercept mesh points in all grids effectively force any long booms to pass through the center of the innermost mesh. Therefore, the model includes only the SC6, SC11, and two SC2 booms, with the orientations fixed at right angles to one another.

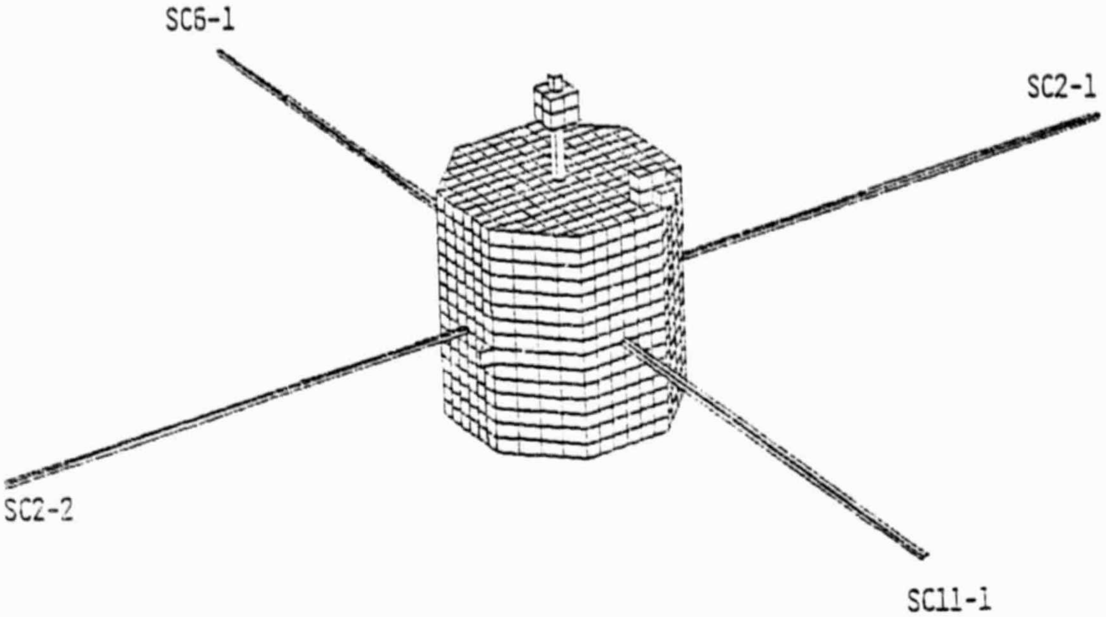

Figure 2.1. Four-grid SCATHA model: side view. The 50 m antenna and the SC1-4 boom are not included in this model.

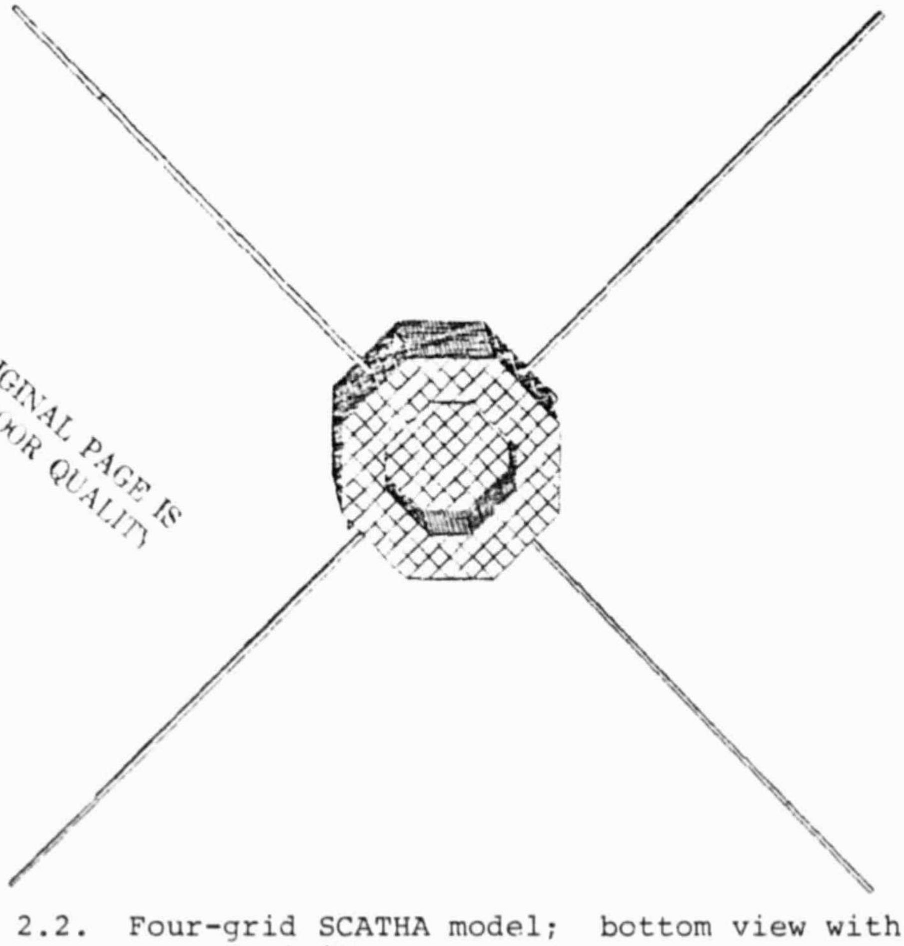

ORIGINAL PAGE IS OF POOR QUALITY

Figure 2.2. Four-grid SCATHA model; bottom view with aft cavity visible.

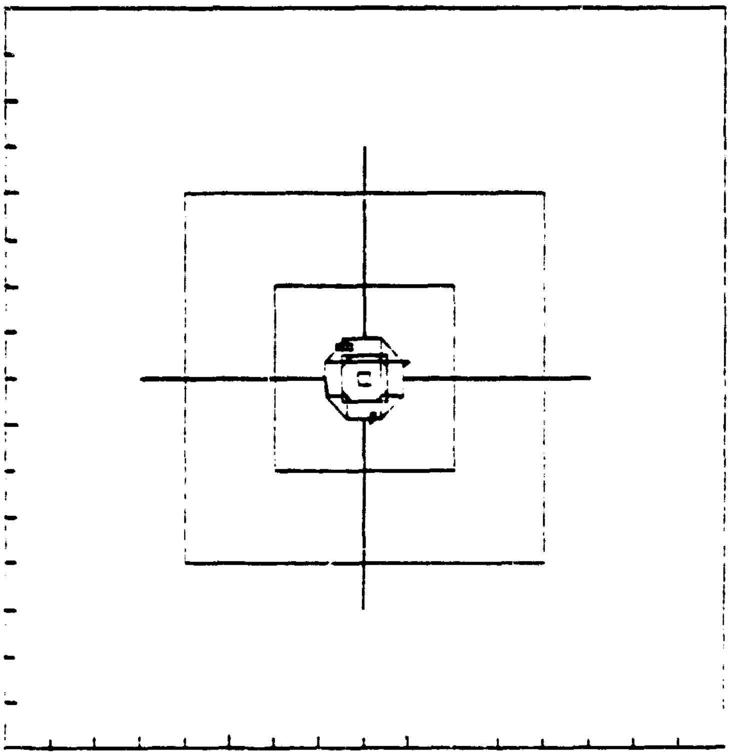

Figure 2.3. Computational space surrounding the four-grid SCATHA model, showing the nesting of the grids. The tic marks along the axes indicate the outer grid zone size; the zone size decreases by a factor of two in successive grids.

TABLE 2.1. COMPARISON OF ACTUAL SCATHA GEOMETRICAL FEATURES TO FOUR-GRID NASCAP MODEL

Zone Size = 4.54 in. (11.5 cm)

	SCATHA	MODEL
Radius	33.6 inches	32.0 inches
Height	68.7	68.0
Solar Array Height	29	27.2
Bellyband Height	12.0	13.6
SC9-1 Experiment	9.2 × 6 × 8	9.1 × 4.5 × 9.1
SC6-1 Boom	1.7 (radius) 118 (length)	1.7 113.2
Surface Area	2.16×10^4 sq.in.	2.11×10^4 sq.in.
Solar Array Area	1.23×10^4	1.15×10^4
Forward Surface Area	0.36×10^4	0.34×10^4

2.2 "ONE-GRID" MODEL

In addition to the four-grid model it is possible to represent the SCATHA satellite entirely within grid one, increasing the zone size to 19.6 cm. All four materials on the SSPM's are resolved but the booms are not to scale. However, this so-called "one-grid" model shows a similar charging response to the more detailed model above but uses considerably less computer time.

For this reason the one-grid model was used for the charging simulation using actual data measured in space by SCATHA (Chapter 5).

NASCAP generated material plots and perspective views are shown in Figures 2.5 through 2.13.

2.3 SURFACE MATERIALS

The models include the specification of 15 distinct exposed surface materials, each of which is specified by the values of 14 parameters. The surface materials are described in Table 2.2. Wherever possible, experimentally measured values for all parameters were used; where this has not been possible, suitable estimates based on the properties of similar materials were used. Table 2.3 gives the values of the material parameters which were used in the calculations reported herein.

The exposed materials in the four-grid model are illustrated in Figure 2.4, in which the locations of several SCATHA experiments are also shown. Experiments at the ends of the SCATHA booms were modeled as single boom segments whose radii were chosen to reproduce the exposed surface area of the actual experiment. NASCAP generated plots of exposed surface materials are included in Appendix A.

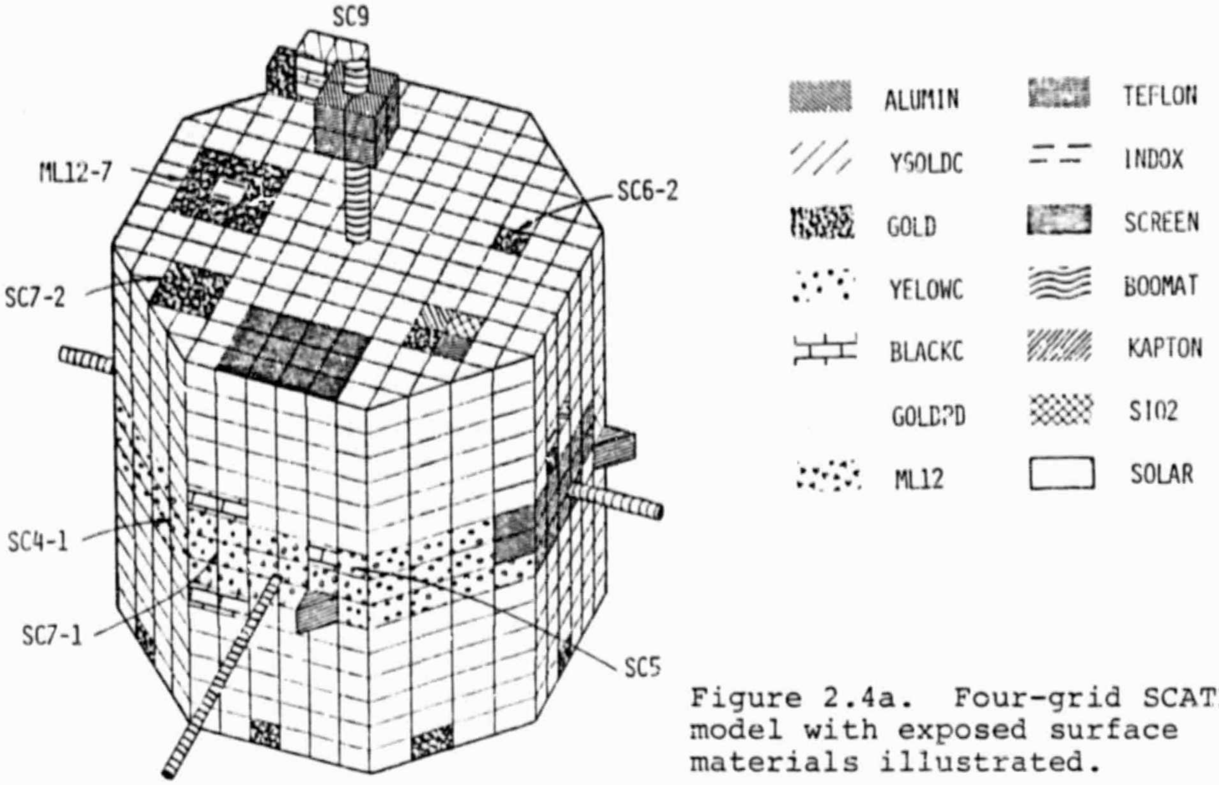

Figure 2.4a. Four-grid SCATHA model with exposed surface materials illustrated.

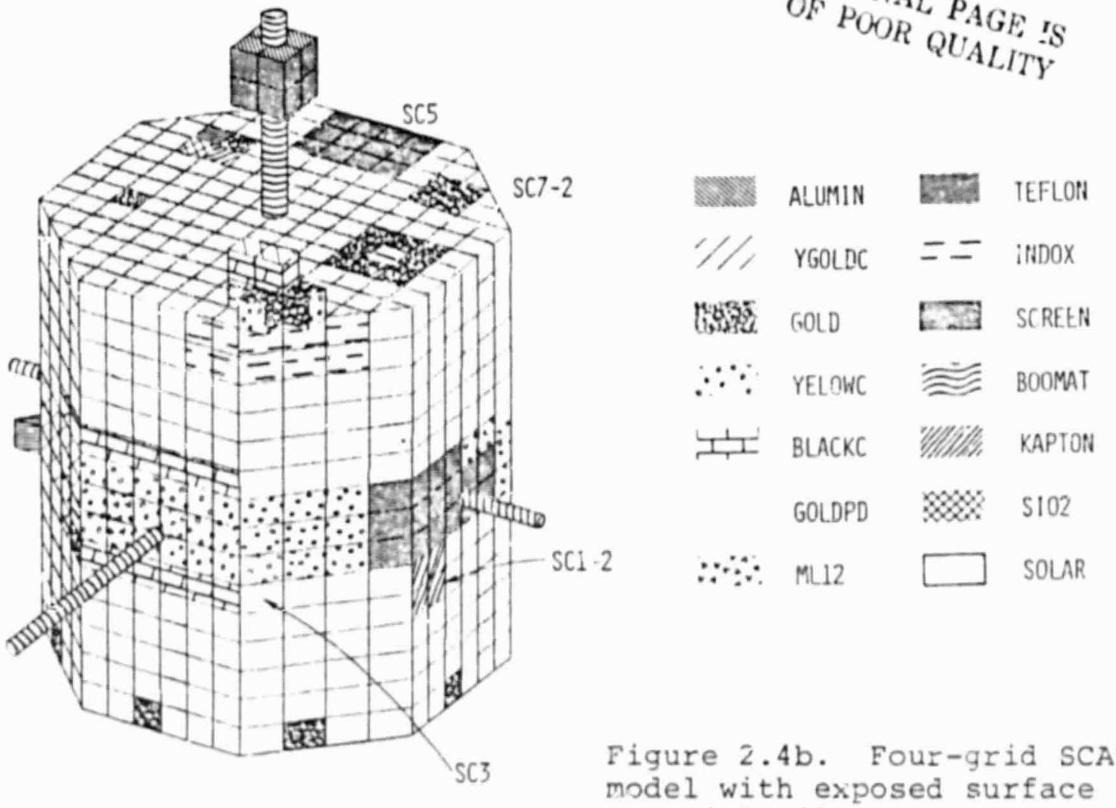

Figure 2.4b. Four-grid SCATHA model with exposed surface materials illustrated.

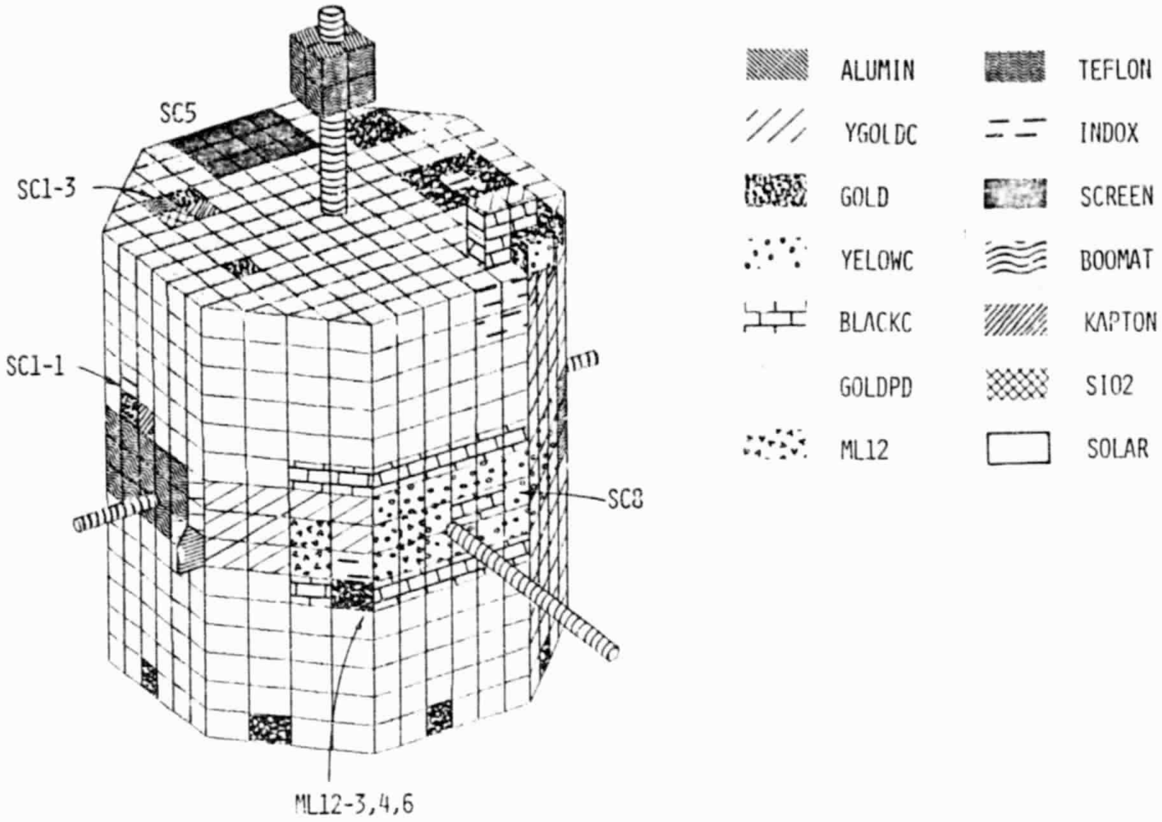

Figure 2.4c. Four-grid SCATHA model with exposed surface materials illustrated.

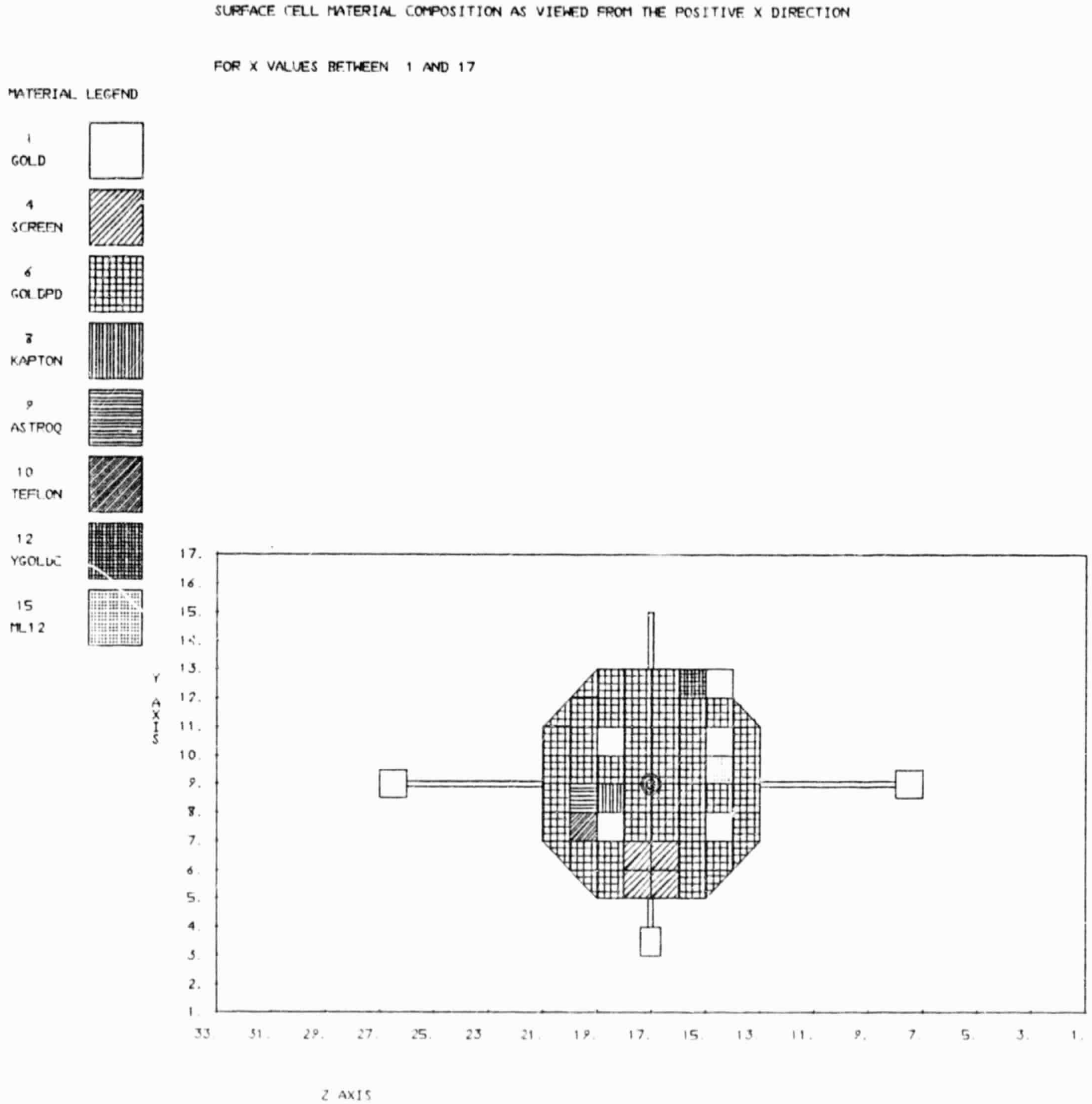

Figure 2.5. One-grid SCATHA model material plots.

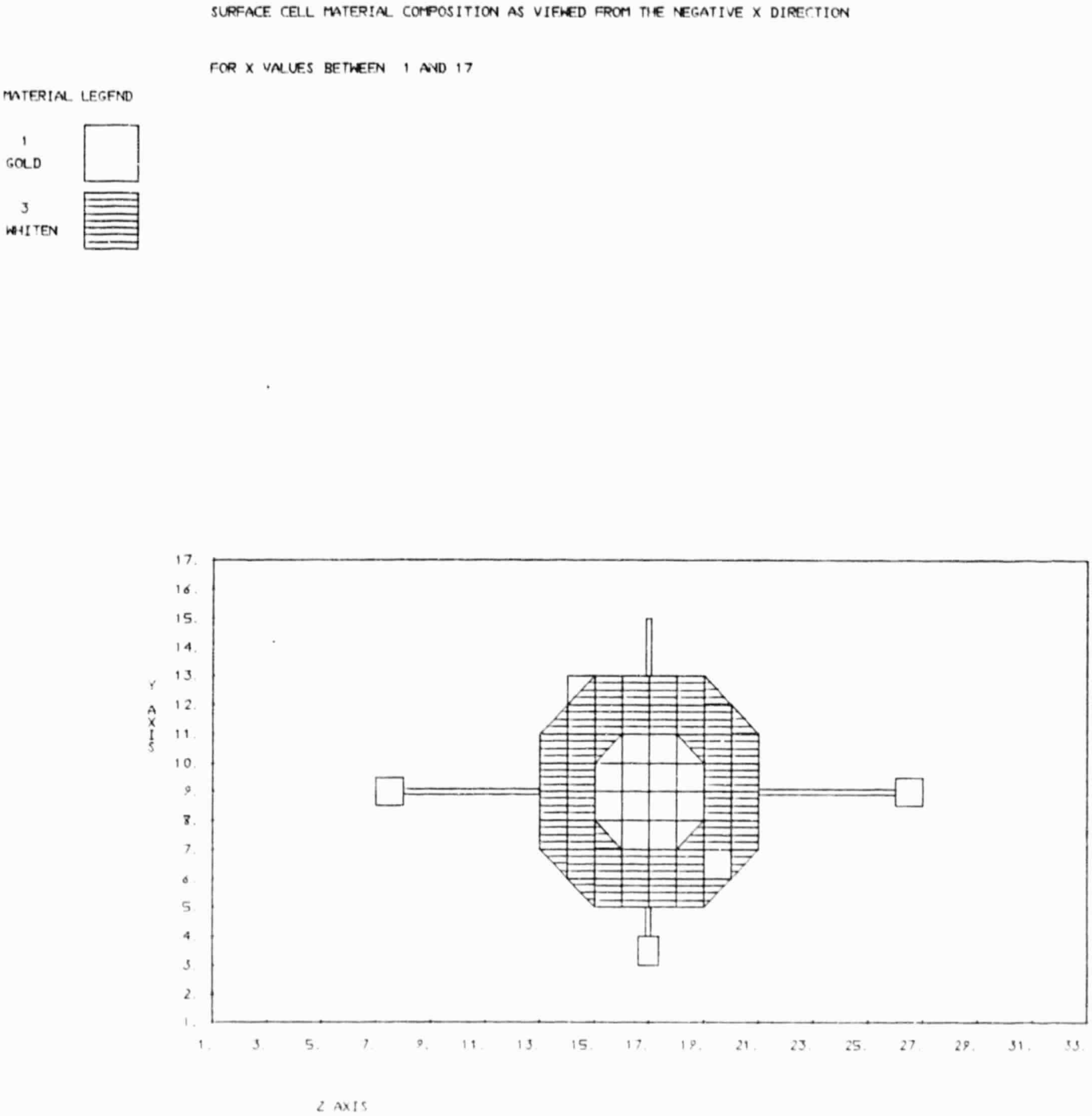

Figure 2.6. One-grid SCATHA model material plots.

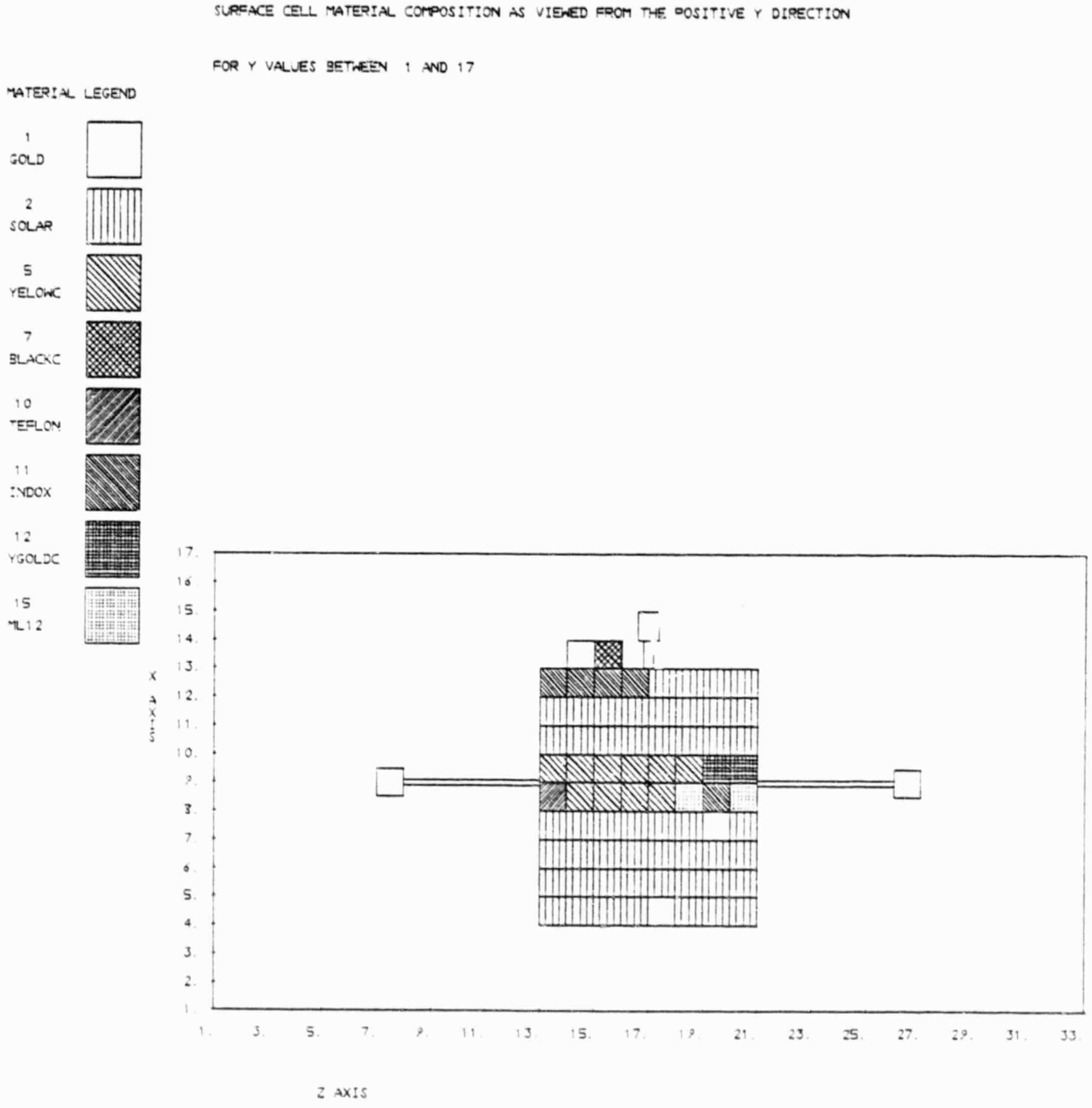

Figure 2.7. One-grid SCATHA model material plots.

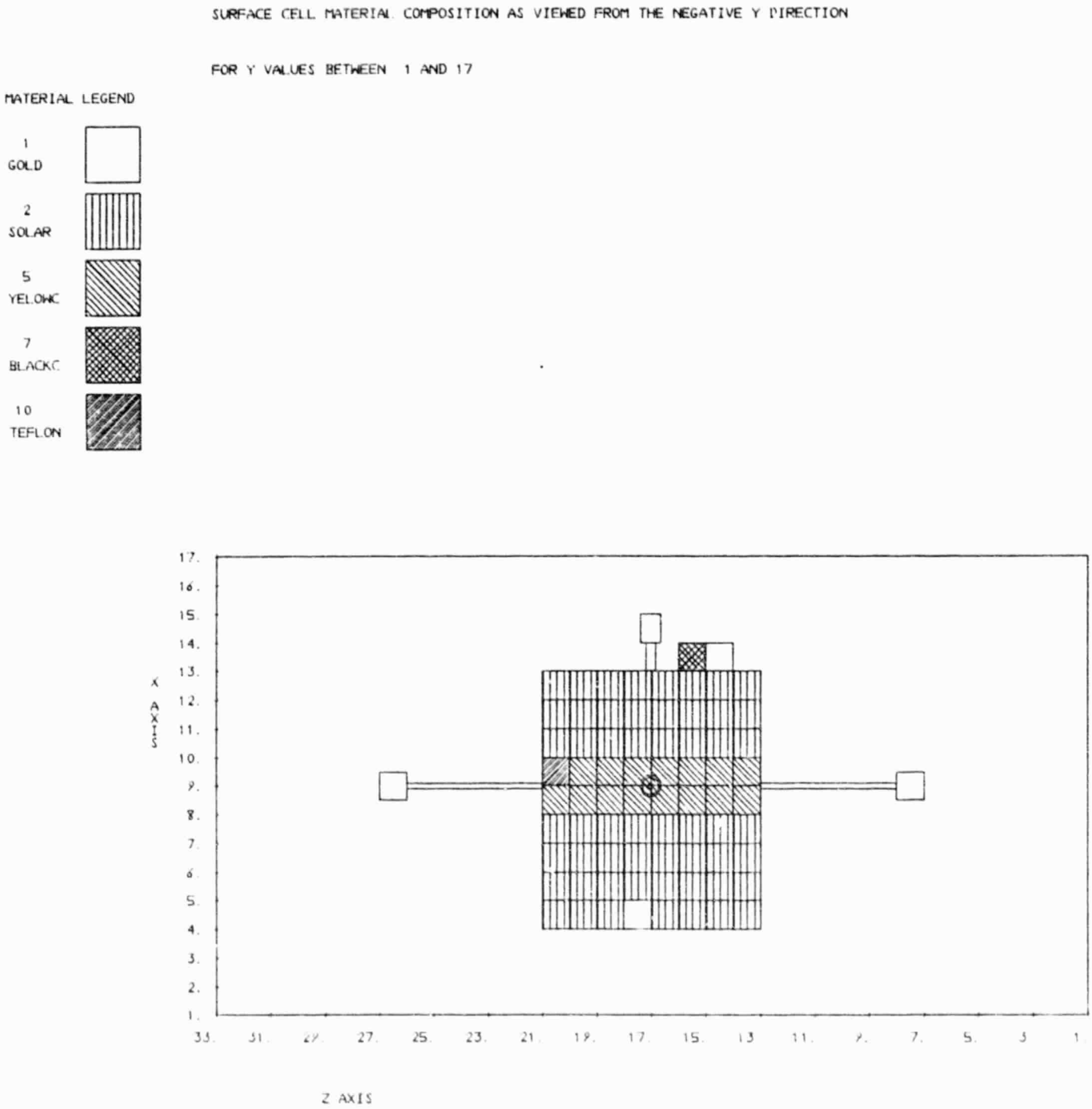

Figure 2.8. One-grid SCATHA model material plots.

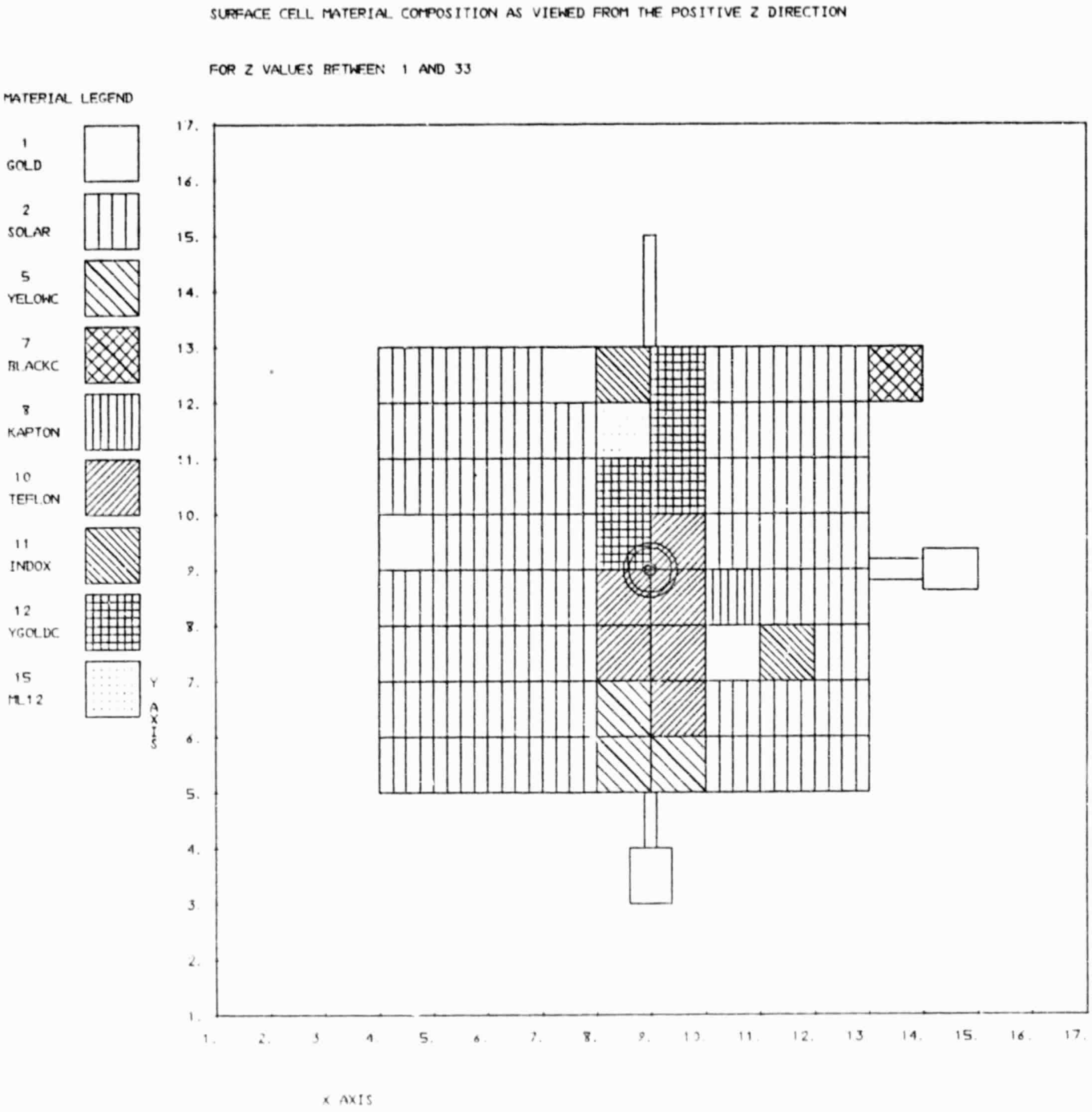

Figure 2.9. One-grid SCATHA model material plots.

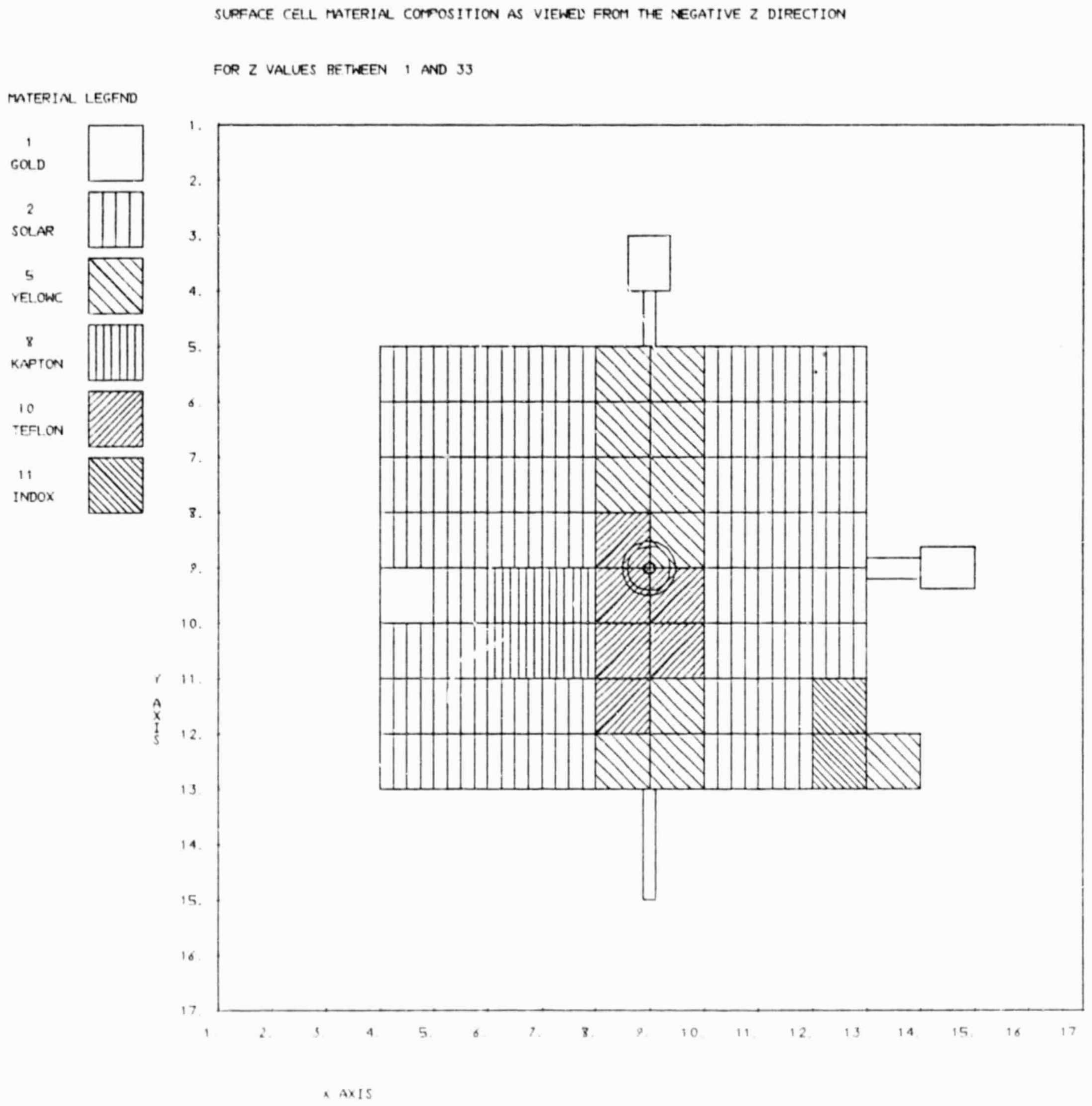

Figure 2.10. One-grid SCATHA model material plots.

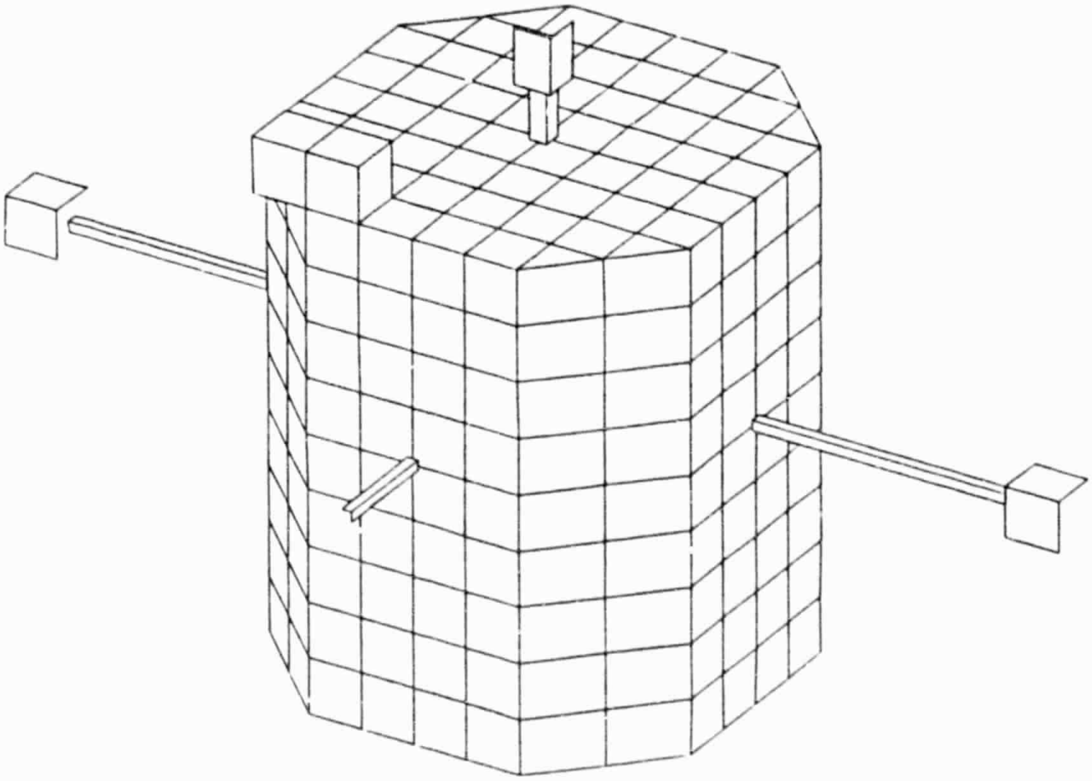

Figure 2.11. One-grid SCATHA model perspective plots.

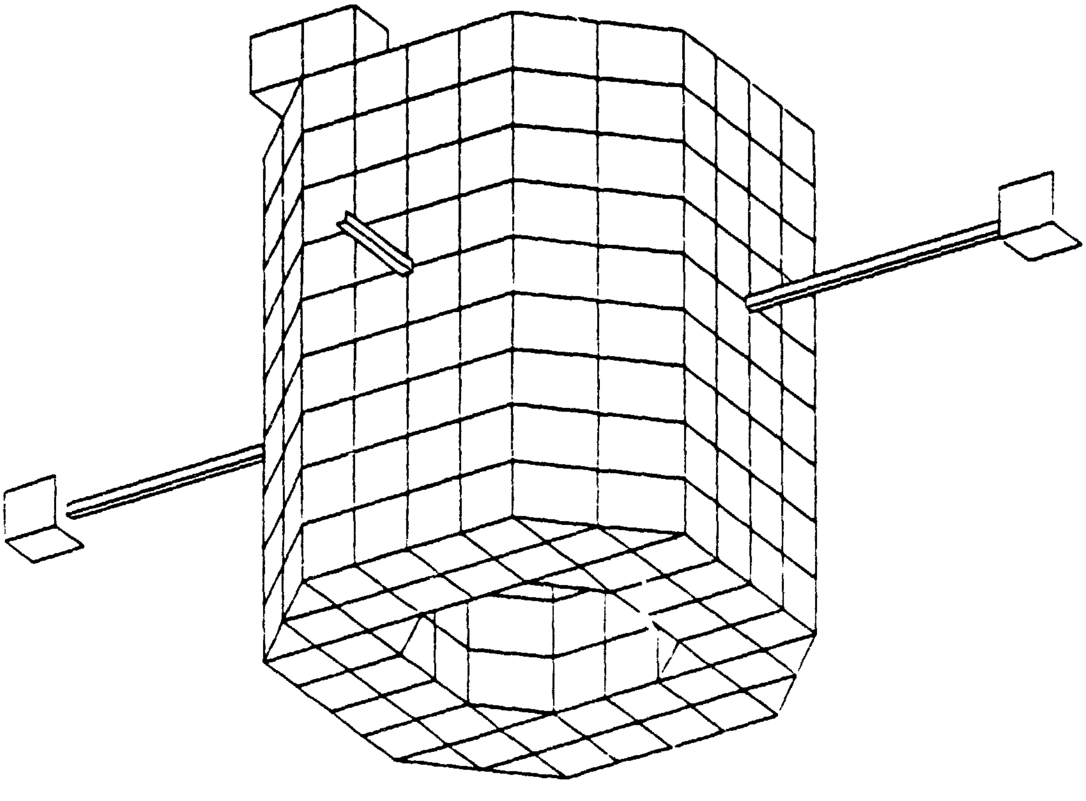

Figure 2.12. One-grid SCATHA model perspective plots.

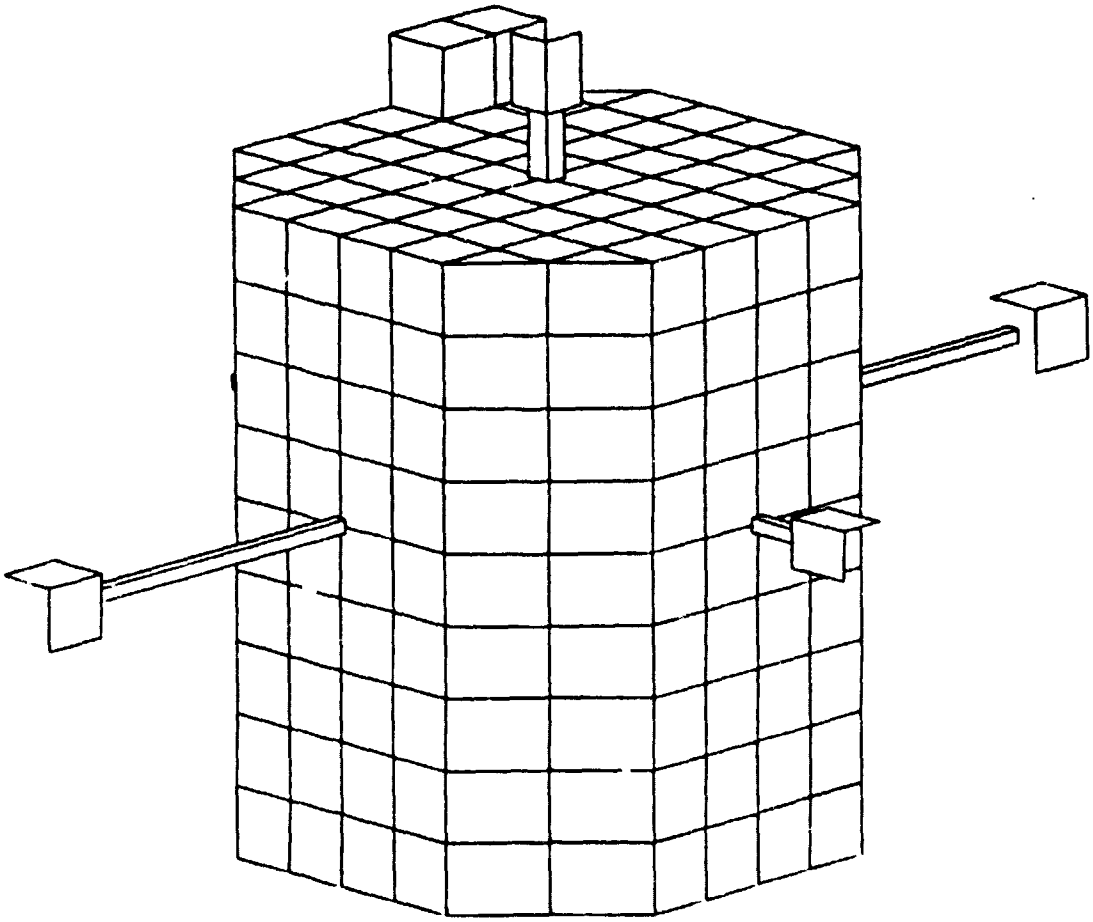

Figure 2.13. One-grid SCATHA model perspective plots.

TABLE 2.2. EXPOSED SURFACE MATERIALS

GOLD:	gold plate
SOLAR:	solar cells, coated fused silica
WHITEN:	non-conducting white paint (STM K792)
SCREEN:	SC5 screen material, a conducting fictitious material which absorbs but does not emit charged particles
YELOWC:	conducting yellow paint
GOLDPD:	88 percent gold plate with 12 percent conductive black paint (STM K748) in a polka dot pattern
BLACKC:	conductive black paint (STM K748)
KAPTON:	kapton
ASTROQ:	SiO_2 fabric
TEFLON:	teflon
INDOX:	indium oxide
YGOLDC:	conducting yellow paint (50 percent) gold (50 percent)
ML12:	ML12-3 and ML12-4 surface, a fictitious material whose properties are an average of the properties of the several materials on the ML12 surfaces
ALUM:	aluminum plate
BOOMAT:	platinum banded kapton

TABLE 2.3. MATERIAL PROPERTIES FOR EXPOSED SURFACES[a]

PROPERTY[b]	GOLD	SOLAR	WHITEN	SCREEN	BLACKC YELOWC	GOLDPD	KAPTON
1	-	3.80	3.50	-	-	-	3.50+00
2	1.00-03	1.79-04	5.00-05	1.00-03	1.00-03	1.00-03	1.27-04
3	∞	1.00-17	5.90-14	∞	∞	∞	1.00-16
4	7.90+01	1.00+01	5.00	1.00	5.00	7.01+01	5.00+00
5	8.80-01	2.05	2.10	0.00	2.10	1.03	2.10+00
6	8.00-01	4.10-01	1.50-01	1.00	1.50-01	7.20-01	1.50-01
7	8.8 +01	7.75+01	7.15+01	1.00+01	7.15+01	8.8 +01	7.15+01
8	9.20-01	4.50-01	6.00-01	1.50	6.00-01	9.20-01	6.00-01
9	5.35+01	1.56+02	3.12+02	0.00	3.12+02	5.35+01	3.12+02
10	1.73	1.73	1.77	1.00	1.77	1.73	1.77
11	4.13-01	2.44-01	4.55-01	0.00	4.55-01	4.13-01	4.55-01
12	1.35+02	2.30+02	1.40+02	1.00	1.40+02	1.35+02	1.40+02
13	2.90-05	2.00-05	2.00-05	0.00	2.00-05	2.90-05	2.00-05
14	-	1.00+19	1.00+13	-	-	-	1.00+16

	ASTROQ	TEFLON	INDOX	YGOLDC	ALUMIN	BOOMAT[c]	ML12
1	3.8	2.00	-	-	-	2.00+00	-
2	2.75-04	1.27-04	1.00-03	1.00-03	1.00-03	5.00-03	1.00-03
3	2.75-12	1.00-16	∞	∞	∞	1.00-15	∞
4	1.00+01	7.00	2.44+01	4.20+01	1.30+01	6.34+01	6.00
5	2.40	3.00	1.40	1.49	9.70-01	8.80-01	1.00
6	4.00-01	3.00-01	8.00-01	4.80-01	3.00-01	8.00-01	3.00-01
7	6.75+01	4.54+01	-1.00+00	-1.00+00	1.54	8.8 +01	-1.00+00
8	8.10-01	4.00-01	0.00	0.00	8.00-01	9.20-01	0.00
9	1.06+02	2.18+02	7.18	1.78	2.20	5.35+01	2.00
10	1.86	1.77	5.55+01	1.03	1.76	1.73	1.20+01
11	4.55-01	4.55-01	4.90	4.13-01	2.44-01	4.13-01	4.55-01
12	1.40+02	1.40+02	1.23	1.35+02	2.30+02	1.35+02	1.40+02
13	2.00-05	2.00-05	3.20-05	2.40-05	4.00-05	2.72-05	2.10-05
14	1.00+11	1.00+16	-	-	-	1.00+11	-

TABLE 2.3. (Continued)

[a] The materials are described in Table 2.2.

[b] The thirteen properties are as follows:

Property 1:	Relative dielectric constant for insulators (dimensionless).
Property 2:	Thickness of dielectric film or vacuum gap (meters).
Property 3:	Electrical conductivity (mho/m). The value ∞ indicates a vacuum gap over a conducting surface.
Property 4:	Atomic number (dimensionless).
Property 5:	Maximum secondary electron yield for electron impact at normal incidence (dimensionless).
Property 6:	Primary electron energy to produce maximum yield at normal incidence (keV).
Properties 7-10:	Range for incident electrons. <u>Either</u>: $\text{Range} = P_7 E^{P_8} + P_9 E^{P_{10}}$ where the range is in angstroms and for the energy in keV, <u>or</u> $P_7 = -1.$ to indicate use of an empirical range formula P_9 = density (g/cm^3) P_{10} = mean atomic weight (dimensionless).
Property 11:	Secondary electron yield for normally incident 1 keV protons.
Property 12:	Proton energy to produce maximum secondary electron yield (keV).
Property 13:	Photoelectron yield for normally incident sunlight (A/m^2).
Property 14:	Surface resistivity for insulators (ohms).

[c] The dielectric constant and thickness for the boom surfaces were chosen to reflect the *effective* capacitance to the underlying cable shield.

The model also includes six distinct underlying conductors: spacecraft ground, the reference band, and the four experimental mountings SC2-1, SC2-2, SC6-1, and SC6-2. Each of these conductors can be separately biased or floated with respect to spacecraft ground, and each conductor is directly capacitively coupled to spacecraft ground. The values employed for these capacitive couplings are given in Table 2.4; these values were chosen to represent the capacitance of dielectric spacers separating the conductors from ground.

To improve agreement between NASCAP predictions and experimental observations, the values of the material parameters are continually being updated, as better information becomes available. In particular some effort has been applied to the problem of secondary emission due to the impact of both electrons and ions at the spacecraft surface.

TABLE 2.4. CAPACITIVE COUPLINGS EMPLOYED WITH SCATHA MODEL

Conductor	Capacitance to Ground (pf)
2: SC2-1	30
3: SC2-2	30
4: SC6-1	240
5: SC6-2	30
6: Reference Band	250

2.4 ELECTRON-INDUCED SECONDARY EMISSION

The formulation of secondary emission due to incoming electrons has been improved by the use of better stopping power data. The secondary electron yield δ for a primary beam normally incident is directly proportional to the stopping power S_o at the incident energy.

$$\delta = CS_o \int_0^R f(x)\ e^{-\alpha x}\ dx$$

where $f(x)$ describes the change in stopping power as a function of depth x, and R is the "range" of the primary electron.

By fitting S_o to ab-initio calculations by Ashley, *et al.*[11] much more physical values of δ were obtained for materials like kapton, especially at energies above 10 keV where they were previously too high (Figure 2.14).

The stopping power is fit in such a way as to force the range into a bi-exponential form.

$$R(E) = b_1 E^{n_1} + b_2 R^{n_2}$$

$$\therefore \quad S_o(E) = \left(n_1 b_1 E^{n_1 - 1} + n_2 b_2 E^{n_2 - 1}\right)^{-1}$$

The parameters $n_1 b_1 n_2 b_2$ are given in Table 2.5 for a number of materials.

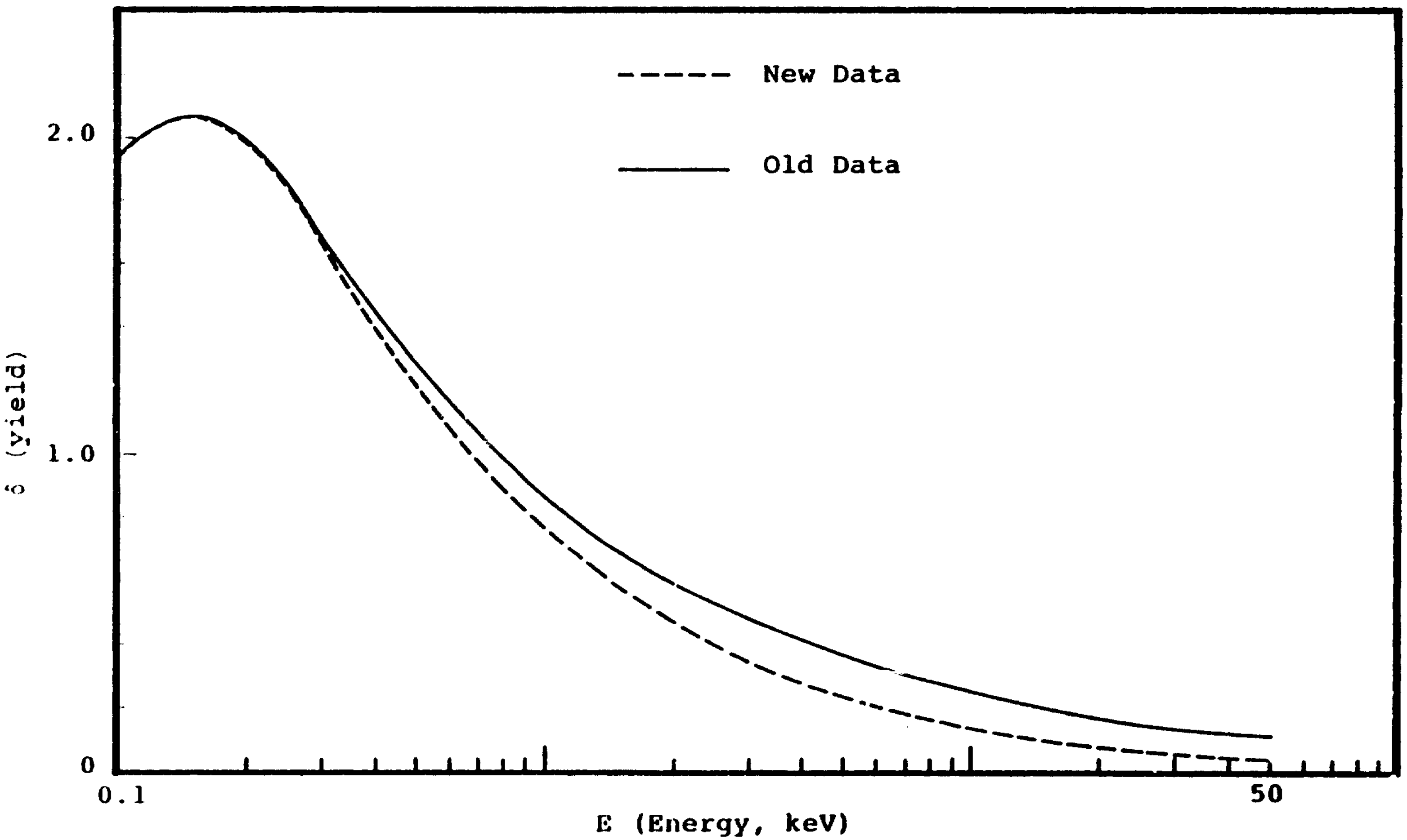

Figure 2.14. Comparison of updated and original secondary yields for kapton.

TABLE 2.5. FOUR PARAMETER STOPPING POWER FITS

$$S = n_1 b_1 E^{n_1-1} + n_2 b_2 E^{n_2-1}{}^{-1}$$

Material	b_1	n_1	b_2	n_2
Au	88.79	0.92	53.48	1.73
Ag	84.46	0.82	79.43	1.74
Al	153.7	0.80	220.0	1.76
SiO_2	116.3	0.81	183.1	1.86
Polystyrene	88.43	0.67	371.7	1.79
Kapton	71.48	0.60	312.1	1.77
Teflon	45.37	0.40	217.6	1.77
Solar*	77.50	0.45	156.1	1.73

*Stopping power of Al_2O_3 used.

2.5 ION-INDUCED SECONDARY EMISSION

The NASCAP model assumes that all positively charged species in the plasma environment are protons H^+. Measurements made in geosynchronous orbit indicate in fact that often up to 80 percent of the ions present are O^+ rather than H^+. This observation has called into question the ion-impact induced, secondary electron current, calculated by the code assuming a purely proton environment.

Secondary emission of electrons following ion-surface impact can occur via two mechanisms.

a. Potential Emission

This occurs via transfer of ion potential energy to lattice electrons at metal surfaces. Electrons tunnel into the potential well formed by the adsorption of the ion on the surface, neutralizing the ion, which then auto-ionizes.

It is a low energy phenomenon (<20 eV) and is unimportant in most of the energy regime associated with NASCAP (0-50 keV).

b. Kinetic Emission

Here emission results from the direct transfer of ion-kinetic energy to lattice electrons, and depends, in a complicated way, on the projectile/target atomic collision cross-section. It is the dominant mechanism in the energy range of interest.

The yield for both mechanisms does not appear to depend in any predictable way upon atomic number. The mechanism for potential emission is almost chemical in nature and depends much more upon electronic structure than nuclear mass. The most identifiable trend appears to be an increasing yield for projectile ions having greater electron affinities.

While the collision cross-section central to kinetic emission increases with atomic number of the projectile ion, the yield of escaping secondary electrons involves a trade-off between factors such as the efficiency of energy transfer per collision and the depth of penetration of the ion. This is rather poorly understood and experimental studies with rare gas ions impinging on clean metal surfaces show an irregular dependence of yield upon atomic number. For example, the energy-yield curves for Kr and Xe incident on Mo cross twice within the range 6-10 keV.

Conclusions

A table of secondary yields for ions of 1 keV incident on Mo is shown below.

Ion	Yield (at 1 keV)
H^+	0.250
He^+	0.276
O^+	0.178

In this case the yields for H^+ and O^+ are of a similar magnitude. Very little additional data is available. The data that is available is often subject to large errors because of the sensitivity of measurements to the nature of the test surface. This coupled with the fairly large uncertainties in the measurement of O^+/H^+ ratios in space at any particular time leads us to the conclusion that adjustment of the code and/or data to take the presence of O^+ into account is not justified. The magnitude of the adjustments to be made are smaller than the additional uncertainties that would be introduced.

3. REPRESENTATION OF THE PLASMA ENVIRONMENT

The NASCAP code recognizes plasma spectra in three forms: Maxwellian, double Maxwellian and a tabular form as described in Appendix C. The tabular data is integrated using the DIRECT mode.

Measurements made on board SCATHA have provided information about the spectrum of the plasma environment in the form of tabulations of the distribution function, for both electrons and ions, in the energy range 10^2 to 10^5 eV. This data is based on observations of energy flux, made by the SC9 detector, averaged over a 16 second period, and so has certain associated limitations; i.e.,

a. When the satellite is charged the spacecraft potential affects the energy of charged particles reaching the surface. For example if the spacecraft potential is -2000 V, protons are attracted to it and their energy is increased by 2000 eV at the surface, compared to infinity. In the same way electrons are repelled so that their energy is reduced by 2000 eV at the surface, and those electrons with initially less than 2000 eV of energy do not reach the surface at all.

This distorts the distribution function observed at the surface. While the shape of the distribution function $f(E)$ is unaffected by spacecraft potential, the energies associated with each value are affected. The particle repelled by the potential ϕ has $q \times \phi$ less energy at the surface than it did at infinity (q is the charge on the particle). Hence instead of associating the value of the distribution function $f_\infty(E)$ with energy E, the value is associated with particles of energy $E - q\phi$, i.e.,

$$f_\infty(E) = f_s(E - q\phi)$$

Knowing the spacecraft potential, this shift in energies is easily corrected for, providing the repelled species can reach the surface at all. However, those particles with energies at infinity less than $q\phi$ cannot and so there is no distribution function information measured at these energies.

The lack of information for the repelled species (almost always electrons), below the spacecraft potential, represents a major limitation of the data as measured. This limitation does not apply to the attracted species (ions) since particles of all energies reach the spacecraft.

b. The energy flux is weighted by the energy

$$\langle \text{Energy Flux} \rangle \int_0^\infty E^2 \, f(E) \, dE$$

Measurements at low energies have a lower intensity and poorer signal to noise ratio. Hence the estimates of distribution function derived from these measurements are less reliable at the lowest energies.

NASCAP requires spectral information in the form of a distribution function at infinity. This presents no difficulty for the attracted species but, for reasons discussed above, can lead to complications for the repelled species.

3.1 DIRECT INTEGRATION

In particular, the absence of spectral information concerning the repelled species for energies below the spacecraft potential has prevented a successful simulation involving direct integration of the observed data points. In principle, the missing data could be replaced by an extrapolation of the known data. This requires some assumption about its functional form and a fit to this form. Two approaches were tried.

a. The whole of the known data was fit to a Maxwellian form.

b. The known data of lowest energy was fit to a Maxwellian form.

The former approach was unsuccessful because the effective temperature of a Maxwellian fit increases with energy (i.e., the known data has a high energy non-Maxwellian "tail"). Thus the fit had a higher temperature than that appropriate for the extrapolated energy range. Figure 3.1 shows this as Case "C". The higher temperature leads to a lower density than would be expected by smooth extrapolation of the known data (Case "B"), and hence to anamolously low values for the distribution function in the extrapolated region. Such a distribution leads to false multiple equilibrium potentials.

The second approach, fitting only the data at energies close to the spacecraft potential, can lead to unphysically high values for the density and hence anamolously high values of the distribution function in the extrapolated region (Case "A"). This problem arises because the fit is based on an unrepresentatively small sample of points.

Stable predictions were obtained using direct integration of the data when only the high energy points were used, and all of the remainder replaced by a fit to these points. Under these circumstances, it is just as reasonable to replace the whole spectrum with a suitable analytic representation instead.

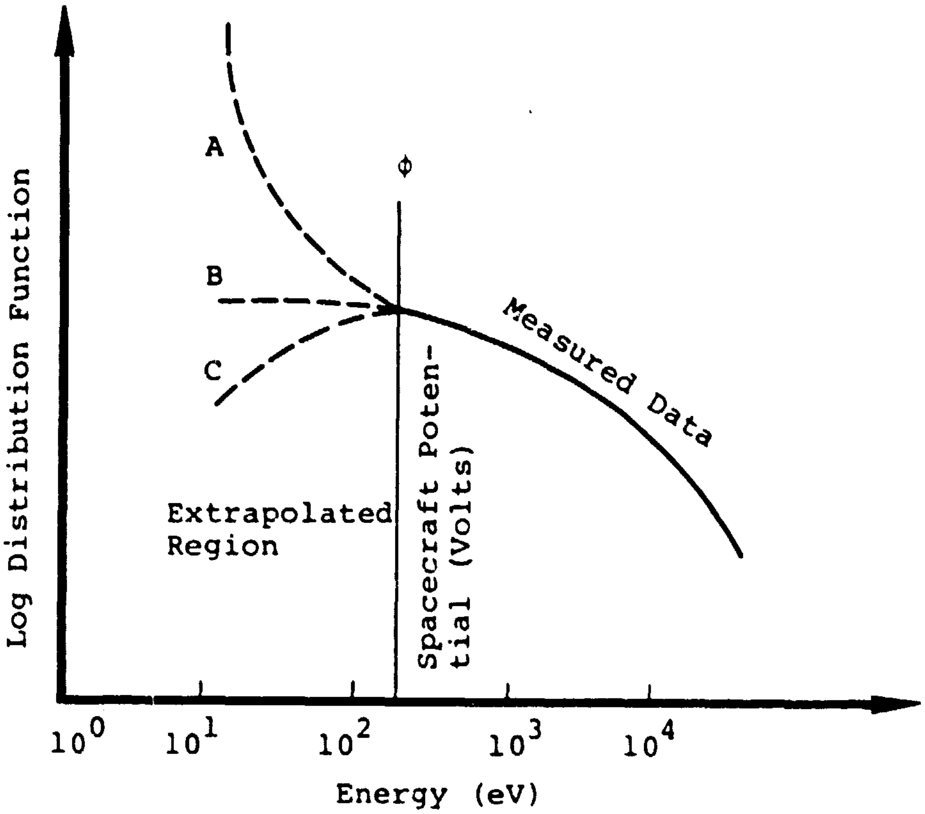

Figure 3.1. Extrapolations of measured data beyond the spacecraft potential for the repelled species.

3.2 FITTING OF THE DATA

Two types of fit to the data were made.

a. Single Maxwellian - fitted by moments (Appendix D).

b. Double Maxwellian - fitted by least squares analysis.

In general, the double Maxwellian fits were better able to represent the non-Maxwellian character of the data (Figures 3.2 and 3.3). Even though the fits were good from 100 eV to 100,000 eV, the low energy components of the double Maxwellians were often unphysical with very high densities and low temperatures. This was particularly true for the electrons in cases where the satellite was charged to several thousand volts negative. Under these conditions only the very end of a Maxwellian component with a temperature, say one-tenth the spacecraft potential, contributes to the flux at the surface. Such contributions can only be considered as noise.

Increasing the "cutoff", below which data points are ignored, to 1000 eV greatly improves the physical picture provided by the fit. This, coupled with an enforced lowest value of at least half the spacecraft potential for the temperature, leads to a series of double Maxwellian fits that were both physical and accurate in all energy regions (Table 3.1).

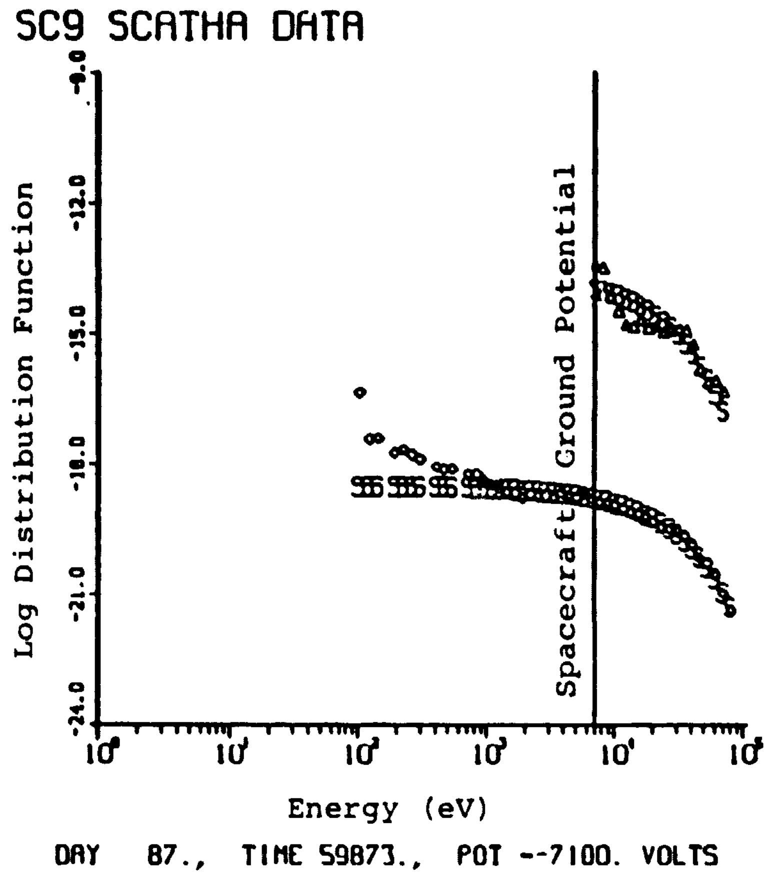

Figure 3.2. Comparison of single Maxwellian fit (S) with observed ion (Δ) and electron (◇) distribution functions.

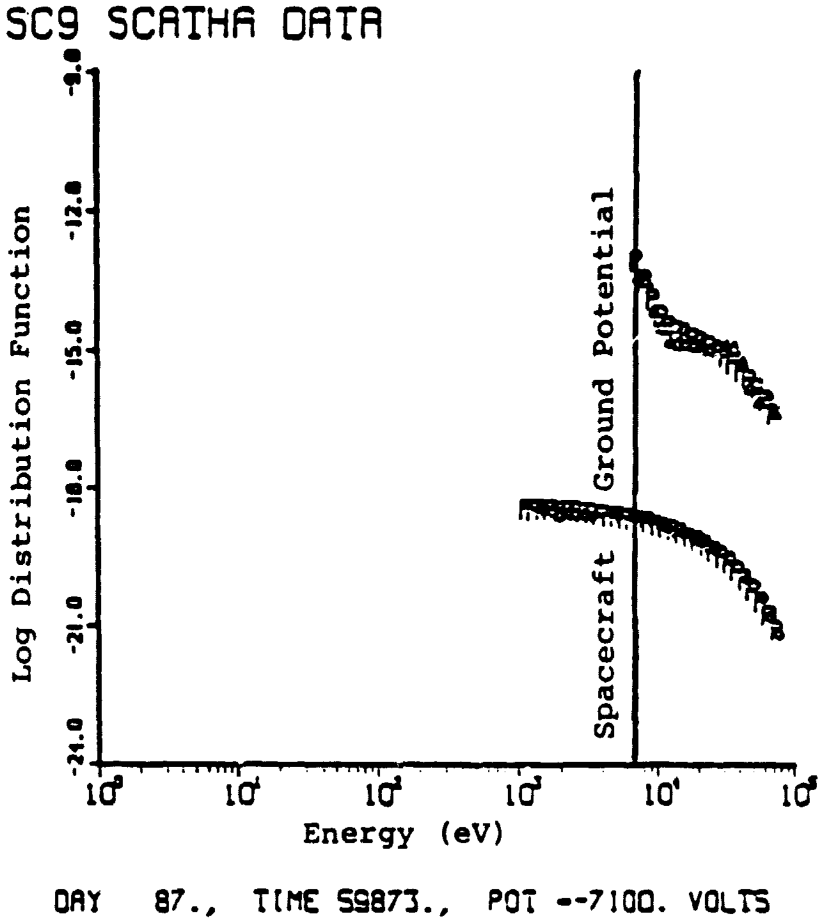

Figure 3.3. Comparison of double Maxwellian fit (P) with observed ion (Δ) and electron (◇) distribution functions.

TABLE 3.1 NEUTRALIZED FITS TO DAY 87 ECLIPSE ENVIRONMENTS

N1 = density of first component in m^{-3}.

T1 = temperature of first component in eV.

N2 = density of second component in m^{-3}.

T2 = temperature of second component in eV.

```
ELECTRONS AT 59473. N1=   1.9+05 T1=  800. N2=   6.1+02 T2= 9000.
IONS      AT 59473. N1=   5.5+04 T1= 3100. N2=   4.8+04 T2=13000.

ELECTRONS AT 59673. N1=   4.7+05 T1= 2000. N2-   6.3+03 T2= 7000.
IONS      AT 59673. N1=   1.1+05 T1= 2400. N2=   1.5+05 T2=15000.

ELECTRONS AT 59753. N1=   8.0+06 T1= 1600. N2=   7.4+04 T2= 7000.
IONS      AT 59753. N1=   3.5+05 T1= 3500. N2=   1.3+05 T2=28000.

ELECTRONS AT 59813. N1=   4.3+04 T1= 5850. N2=   7.1+04 T2=11000.
IONS      AT 59813. N1=   2.0+G4 T1=  700. N2=   4.3+04 T2=27000.

ELECTRONS AT 59853. N1=   2.2+04 T1= 5100. N2=   1.2+05 T2=11000.
IONS      AT 59853. N1=   2.1+04 T1=  600. N2=   3.8+04 T2=16000.

ELECTRONS AT 59873. N1=   2.1+04 T1= 4650. N2=   2.9+05 T2=12000.
IONS      AT 59873. N1=   3.7+04 T1= 1000. N2=   9.4+04 T2=14000.

ELECTRONS AT 59913. N1=   4.5+05 T1= 4000. N2=   6.6+04 T2=11000.
IONS      AT 59913. N1=   1.2+05 T1= 1900. N2=   9.6+04 T2=15000.

ELECTRONS AT 59933. N1=   6.7+05 T1= 1810. N2=   3.5+05 T2= 9000.
IONS      AT 59933. N1=   1.1+05 T1= 1700. N2=   3.2+05 T2=10000.

ELECTRONS AT 59973. N1=   1.0+06 T1= 2840. N2=   2.5+05 T2= 9000.
IONS      AT 59973. N1=   4.0-03 T1=  100. N2=   5.5+05 T2= 4000.

ELECTRONS AT 60013. N1=   1.5+05 T1= 1600. N2=   2.2+05 T2=10000.
IONS      AT 60013. N1=   7.4+04 T1= 2000. N2=   8.0+04 T2=29000.

ELECTRONS AT 60053. N1=   2.0+05 T1= 2000. N2=   2.7+05 T2= 9000.
IONS      AT 60053. N1=   7.0+04 T1= 1200. N2=   1.3+05 T2=30000.

ELECTRONS AT 60133. N1=   3.9+05 T1= 1900. N2=   3.4+05 T2=11000.
IONS      AT 60133. N1=   6.8+04 T1= 3400. N2=   2.2+05 T2=20000.

ELECTRONS AT 60213. N1=   4.2+05 T1= 2000. N2=   2.3+05 T2= 9000.
IONS      AT 60213. N1=   1.8+04 T1=  800. N2=   2.4+05 T2=16000.

ELECTRONS AT 60293. N1=   4.1+05 T1= 3200. N2=   3.4+05 T2= 9000.
IONS      AT 60293. N1=   1.2+05 T1= 2200. N2=   1.8+05 T2=18000.

ELECTRONS AT 60421. N1=   2.1+05 T1= 1550. N2=   2.1+05 T2= 7000.
IONS      AT 60421. N1=   9.2+04 T1= 2300. N2=   1.7+05 T2=15000.

ELECTRONS AT 60493. N1=   1.8+05 T1= 1800. N2=   2.7+05 T2= 7000.
IONS      AT 60493. N1=   1.0+05 T1= 1800. N2=   1.9+05 T2=16000.

ELECTRONS AT 60593. N1=   5.7+05 T1= 2650. N2=   8.4+04 T2=12000.
IONS      AT 60593. N1=   1.0+05 T1= 1000. N2=   2.0+05 T2=18000.

ELECTRONS AT 60633. N1=   6.4+05 T1= 3150. N2=   1.1+05 T2=17000.
IONS      AT 60633. N1=   1.4+05 T1= 1000. N2=   2.0+05 T2=15000.

ELECTRONS AT 60653. N1=   5.4+05 T1= 3110. N2=   1.0+05 T2=20000.
IONS      AT 60653. N1=   1.3+05 T1= 1300. N2=   1.4+05 T2=19000.

ELECTRONS AT 60673. N1=   5.9+05 T1= 3300. N2=   1.3+05 T2=18000.
IONS      AT 60673. N1=   1.5+05 T1= 1100. N2=   1.8+05 T2=16000.
```

```
ELECTRONS AT 60693. N1=   4.9+06 T1= 4050. N2=   1.7+05 T2=19000.  ELECTRONS AT 62093. N1=   5.7+06 T1= 3150. N2=   1.8+06 T2= 8000.
IONS      AT 60693. N1=   2.1+05 T1= 1200. N2=   1.4+05 T2=18000.  IONS      AT 62093. N1=   2.2+06 T1= 2400. N2=   2.5+06 T2=17000.

ELECTRONS AT 60753. N1=   5.0+05 T1= 3950. N2=   1.4+05 T2=18000.  ELECTRONS AT 62133. N1=   6.3+06 T1= 2000. N2=   1.7+06 T2= 8000.
IONS      AT 60753. N1=   1.3+05 T1= 2000. N2=   1.6+05 T2-20000.  IONS      AT 62133. N1=   2.9+06 T1= 3600. N2=   2.2+06 T2=21000.

ELECTRONS AT 60833. N1=   3.7+06 T1= 3100. N2=   1.3+06 T2=16000.  ELECTRONS AT 62133. N1=   6.3+05 T1= 2000. N2=   1.7+06 T2= 8000.
IONS      AT 60833. N1=   2.0+06 T1= 1600. N2=   1.7+06 T2=19000.  IONS      AT 62133. N1=   2.9+06 T1= 3500. N2=   2.2+05 T2=21000.

ELECTRONS AT 60893. N1=   2.3+06 T1= 2700. N2=   1.2+05 T2=13000.  ELECTRONS AT 62233. N1=   4.7+06 T1= 1900. N2=   9.3+04 T2= 8000.
IONS      AT 60893. N1=   1.3+06 T1= 1900. N2=   1.3+06 T2=22000.  IONS      AT 62233. N1=   1.5+06 T1= 5000. N2=   9.8+04 T2=22000.

ELECTRONS AT 60973. N1=   2.7+06 T1= 3250. N2=   1.5+05 T2=14000.  ELECTRONS AT 62353. N1=   4.7+06 T1= 1500. N2=   1.7+05 T2= 8000.
IONS      AT 60973. N1=   1.5+05 T1= 1600. N2=   1.6+06 T2=22000.  IONS      AT 62353. N1=   0.0     T1=    0. N2=   2.8+06 T2= 6000.

ELECTRONS AT 61033. N1=   1.8+05 T1= 3900. N2=   1.0+05 T2=15000.  ELECTRONS AT 62393. N1=   7.9+06 T1= 1500. N2=   4.3+05 T2= 8000.
IONS      AT 61033. N1=   7.4+04 T1= 1500. N2=   1.0+06 T2=19000.  IONS      AT 62393. N1=   3.7+05 T1= 4800. N2=   1.4+05 T2=30000.

ELECTRONS AT 61073. N1=   1.9+06 T1= 5100. N2=   1.3+06 T2=16000.  ELECTRONS AT 62413. N1=   9.0+06 T1= 1900. N2=   4.5+06 T2= 8000.
IONS      AT 61073. N1=   8.4+04 T1= 2200. N2=   1.1+05 T2=24000.  IONS      AT 62413. N1=   4.2+06 T1= 2500. N2=   1.7+06 T2=22000.

ELECTRONS AT 61133. N1=   4.2+05 T1= 2750. N2=   1.4+06 T2=13000.  ELECTRONS AT 62593. N1=   1.7+06 T1= 1100. N2=   2.3+06 T2= 9000.
IONS      AT 61133. N1=   2.1+06 T1= 1100. N2=   1.3+05 T2=24000.  IONS      AT 62593. N1=   8.5+04 T1= 1200. N2=   1.1+05 T2=23000.

ELECTRONS AT 61193. N1=   4.3+06 T1= 2600. N2=   2.1+06 T2=12000.  ELECTRONS AT 62693. N1=   3.2+06 T1= 1600. N2=   2.2+06 T2= 9000.
IONS      AT 61193. N1=   2.6+05 T1= 1400. N2=   1.6+05 T2=19000.  IONS      AT 62693. N1=   1.2+05 T1= 2200. N2=   1.3+05 T2=30000.

ELECTRONS AT 61313. N1=   4.6+05 T1= 2500. N2=   2.1+06 T2=12000.  ELECTRONS AT 62753. N1=   4.4+06 T1= 2000. N2=   1.8+06 T2=12000.
IONS      AT 61313. N1=   1.9+05 T1= 1600. N2=   1.0+06 T2-30000.  IONS      AT 62753. N1=   1.2+06 T1= 2000. N2=   1.7+05 T2=15000.

ELECTRONS AT 61393. N1=   4.4+06 T1= 1800. N2=   2.6+05 T2=10000.  ELECTRONS AT 62813. N1=   4.8+05 T1= 2100. N2=   9.2+04 T2=13000.
IONS      AT 61393. N1=   1.4+05 T1= 2200. N2=   1.7+05 T2=20000.  IONS      AT 62813. N1=   1.4+05 T1= 2300. N2=   1.3+06 T2=27000.

ELECTRONS AT 61453. N1=   4.1+05 T1= 1800. N2=   3.0+05 T2= 9000.  ELECTRONS AT 62933. N1=   4.4+06 T1= 2200. N2=   1.2+06 T2=11000.
IONS      AT 61453. N1=   1.5+06 T1= 1500. N2=   1.6+06 T2=24000.  IONS      AT 62933. N1=   1.8+06 T1= 2900. N2=   8.2+04 T2=30000.

ELECTRONS AT 61513. N1=   4.4+06 T1= 1700. N2=   3.7+05 T2= 9000.  ELECTRONS AT 63053. N1=   3.8+05 T1= 2300. N2=   1.7+06 T2=12000.
IONS      AT 61513. N1=   2.0+06 T1= 2200. N2=   1.7+05 T2=23000.  IONS      AT 63053. N1=   1.4+06 T1= 2500. N2=   1.2+05 T2=30000.

ELECTRONS AT 61573. N1=   5.6+05 T1= 1550. N2=   3.7+06 T2= 9000.
IONS      AT 61573. N1=   2.3+06 T1= 2200. N2=   1.9+05 T2=23000.

ELECTRONS AT 61633. N1=   3.2+06 T1= 2650. N2=   3.0+05 T2=10000.
IONS      AT 61633. N1=   1.4+05 T1= 3100. N2=   1.4+06 T2=24000.

ELECTRONS AT 61653. N1=   2.3+06 T1= 2450. N2=   2.4+05 T2=10000.
IONS      AT 61653. N1=   8.7+04 T1= 2200. N2=   1.4+05 T2=28000.

ELECTRONS AT 61953. N1=   3.8+06 T1= 3700. N2=   3.0+05 T2= 9000.
IONS      AT 61953. N1=   1.2+06 T1= 3100. N2=   1.7+06 T2=30000.

ELECTRONS AT 62013. N1=   5.2+05 T1= 4350. N2=   2.6+06 T2= 9000.
IONS      AT 62013. N1=   2.7+05 T1= 2400. N2=   2.2+06 T2=30000.

ELECTRONS AT 62033. N1=   3.3+06 T1= 3710. N2=   1.5+05 T2= 9000.
IONS      AT 62033. N1=   0.0     T1=    0. N2=   3.0+06 T2= 4000.

ELECTRONS AT 62073. N1=   4.0+05 T1= 3255. N2=   1.7+05 T2= 8000.
IONS      AT 62073. N1=   1.3+05 T1= 1600. N2=   2.2+05 T2=15000.
```

TABLE 3.1. NEUTRALIZED FITS TO DAY 87
ECLIPSE ENVIRONMENTS
(CONTINUED)

3.3 CHARGE NEUTRALIZATION

While the fits accurately represent both the ion and electron data points as observed, the electron densities tend to be as much as a factor of ten higher than the ion densities at the same time. This implies that the plasma surrounding the spacecraft is highly non-neutral. This unphysical result may be due to a systematic error in the measurement of energy flux for one of the species. Independent measurements indicate that the ion densities are the best choice for the correct value. To neutralize the plasma we renormalize the electron densities so that they are equal to the ion densities. This would be a simple matter if the ions were all protons (as the conversion to distribution function assumes). However, measurements by Kaye, et al.[12] show that O^+ is often the dominant species. This does not affect the fluxes as calculated by NASCAP because the code also assumes all the ions are protons and so the error is cancelled out. However, a factor of $(\text{mass})^{-1/2}$ is carried over into the values of the distribution function and hence the estimate of density N. For a pure O^+ environment an electrically neutral plasma would have $N^- = (16)^{1/2} N^+$ as calculated assuming that all ions were protons; i.e.,

$$N^+ = 0.25\, N^-$$

If only a fraction α are oxygen

$$N^+ = [0.25\alpha + (1-\alpha)]\, N^-$$

$$N^- = N^+/(1 - 0.75\alpha) \; .$$

To correct the values of the density for the electrons the values of N_1^- and N_2^- obtained by the fitting procedure were multiplied by the factor f.

$$f = \frac{\left(N_1^+ + N_2^+\right)}{\left(N_1^- + N_2^-\right)\left(1 - 0.75\right)}$$

Hence we arrive at the final representation of the environment, shown for Day 87, 1979, in Table 3.1.

4. SCATHA MATERIALS CHARGING RESPONSE

To examine the sensitivity of the charging response to the method of fitting, and compare the fits with directly integrated tabulated data, the NASCAP support code, MATCHG, was used to study just one material. The material chosen was "SOLAR", the solar cell cover glass that forms most of the exposed surface area of the SCATHA satellite. The silica cover glass is coated with a non-reflective MgF_2 layer and we assume that is has the same material properties (e.g., secondary emission yield, etc.) as MgF_2. The MATCHG predicted equilibrium potentials for a sphere covered with "SOLAR" charging under the influence of the three different representations of the environment are compared in Table 4.1. The parameters associated with these representations are summarized in Tables 4.2 and 4.3.

TABLE 4.1. CHARGING RESPONSE (kV) OF SOLAR AS A FUNCTION OF ENVIRONMENT REPRESENTATION

Environment	59813	59873	61073	59873 (Neutral)
Single Maxwellian	-14.5	-22.3	-17.2	-12.1
Double Maxwellian	-17.6	-20.3	-18.9	-
Direct Integration	-16.2	-22.6	-17.9	-
Satellite Potential	- 1.9	- 7.1	- 4.8	- 7.1

TABLE 4.2. SINGLE MAXWELLIAN FITS TO DAY 87 MEASURED DISTRIBUTION FUNCTIONS

Time (sec)		Species	Density (10^6 m^{-3})	Temperature (keV)
59813	(uncorrected)	Electrons	0.79	8.7
59813		Ions	0.086	12.0
59873	(uncorrected)	Electrons	0.98	12.0
59873		Ions	0.15	9.9
61073	(uncorrected)	Electrons	0.95	11.0
61073		Ions	0.20	12.0
59873	corrected for O^+	Electrons	0.28	12.0
59873		Ions	0.15	9.9

TABLE 4.3. DOUBLE MAXWELLIAN FITS TO DAY 87 MEASURED DISTRIBUTION FUNCTIONS (UNCORRECTED FOR O^+)

Time (sec)	Species	Density (10^6 m^{-3})	Temperature (keV)	Density (10^6 m^{-3})	Temperature (keV)
59813	Electrons	0.29	5.9	0.48	11.0
59813	Ions	0.020	0.70	0.043	27.0
59873	Electrons	0.062	4.7	0.87	12.0
59873	Ions	0.037	1.0	0.096	14.0
61073	Electrons	0.64	5.1	0.45	16.0
61073	Ions	0.084	2.2	0.11	24.0

Agreement between the two fits and the directly integrated spectra are very good. The direct integration is only possible because a single Maxwellian fit to the known data is used to fill in the part cut out by the spacecraft potential. Furthermore, a much more stable result is obtained when in addition the first 2000 eV of known data for both the ions and electrons is replaced by the Maxwellian fit. The points replaced are highly non-Maxwellian. This could be a real phenomenon or it may be due to the poor signal/noise ratio inherent in measurements of energy flux at low energies. In either case, including it leads to erratic changes in the calculated net current and prediction of more than one equilibrium potential. These additional predicted potentials occur at unphysically low values and are almost certainly false.

Included in Table 4.1 are the spacecraft ground potentials observed on the SCATHA satellite when the distribution function data was being measured. MATCHG predicts considerably more charging than observed. There are at least three reasons for this:

1. The satellite is not a sphere covered in SOLAR.
2. In space the charging environment is not constant, particularly at the times when our test spectra were measured. MATCHG assumes a steady charging environment.
3. The measured distribution functions are highly non-neutral (see Tables 4.2 and 4.3). This is rather unphysical and as explained in Chapter 3, indicates a systematic deficiency in the measurement in the density of at least one of the species.

The equilibrium potential predicted with the environment corrected for the presence of O^+ is much closer to the observed satellite potential.

4.1 THRESHOLD EFFECT

The three environments chosen all charge the SOLAR material to high potentials in all representations. For environments with only a small tendency to charge the material, very small changes in the representation of the plasma can lead to qualitatively very different charging predictions.

Figure 4.1 shows the effect of varying the electron temperature parameter in the 59873 single Maxwellian representation. There is a definite threshold for charging that occurs at $T = 6.9$ keV. Below this temperature, no charging is predicted, while only 0.3 keV above it, at $T = 7.2$ keV, a potential of 4.3 keV[*] is forecast. Such small changes in temperature are well within experimental error for measurement and fitting procedures. For "borderline" environments close to the charging threshold quite different predictions are possible according to the representation employed.

A similar phenomenon is presented when we examine the effect of changing important material parameters on charging. Figure 4.2 shows a threshold for charging in the 59873 environment (as given in Table 4.2), when the maximum secondary electron yield $\delta_{max} = 3.1$. Above this value the net current is positive at zero potential and the spacecraft never negatively charges, while below 3.1 rapid charging to several keV negative is predicted. The usual value used by MATCHG of 2.05 is well into the stable charging range. However, in borderline cases small changes and errors in material properties can lead to significantly different predicted potentials.

Another factor that can affect charging is the angular distribution of the incident fluxes.

---

[*] The particularly high value of 4.3 keV predicted here is due to the non-neutrality of the plasma.

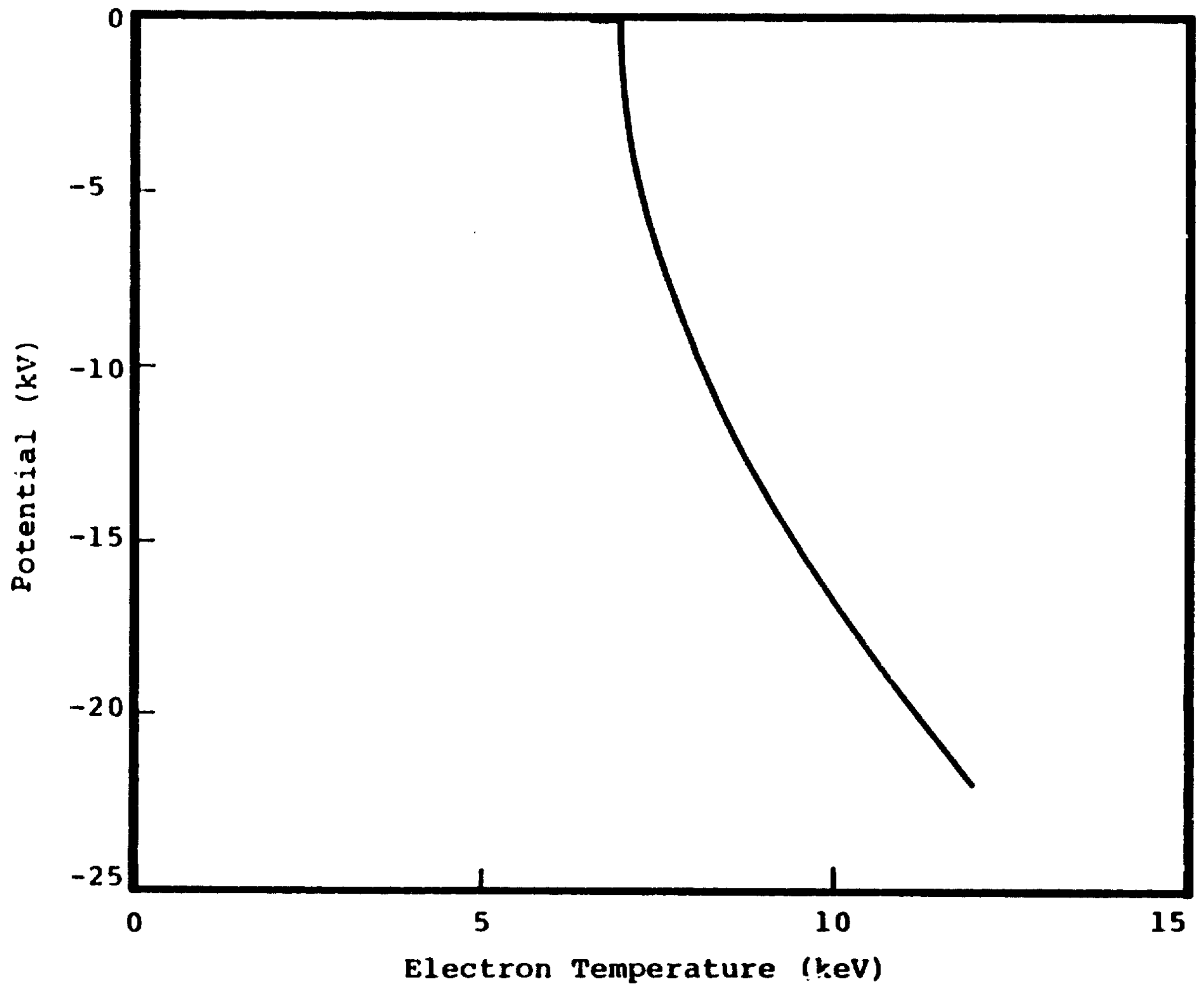

Figure 4.1. Charging characteristics of a solar sphere as a function of electron temperature.

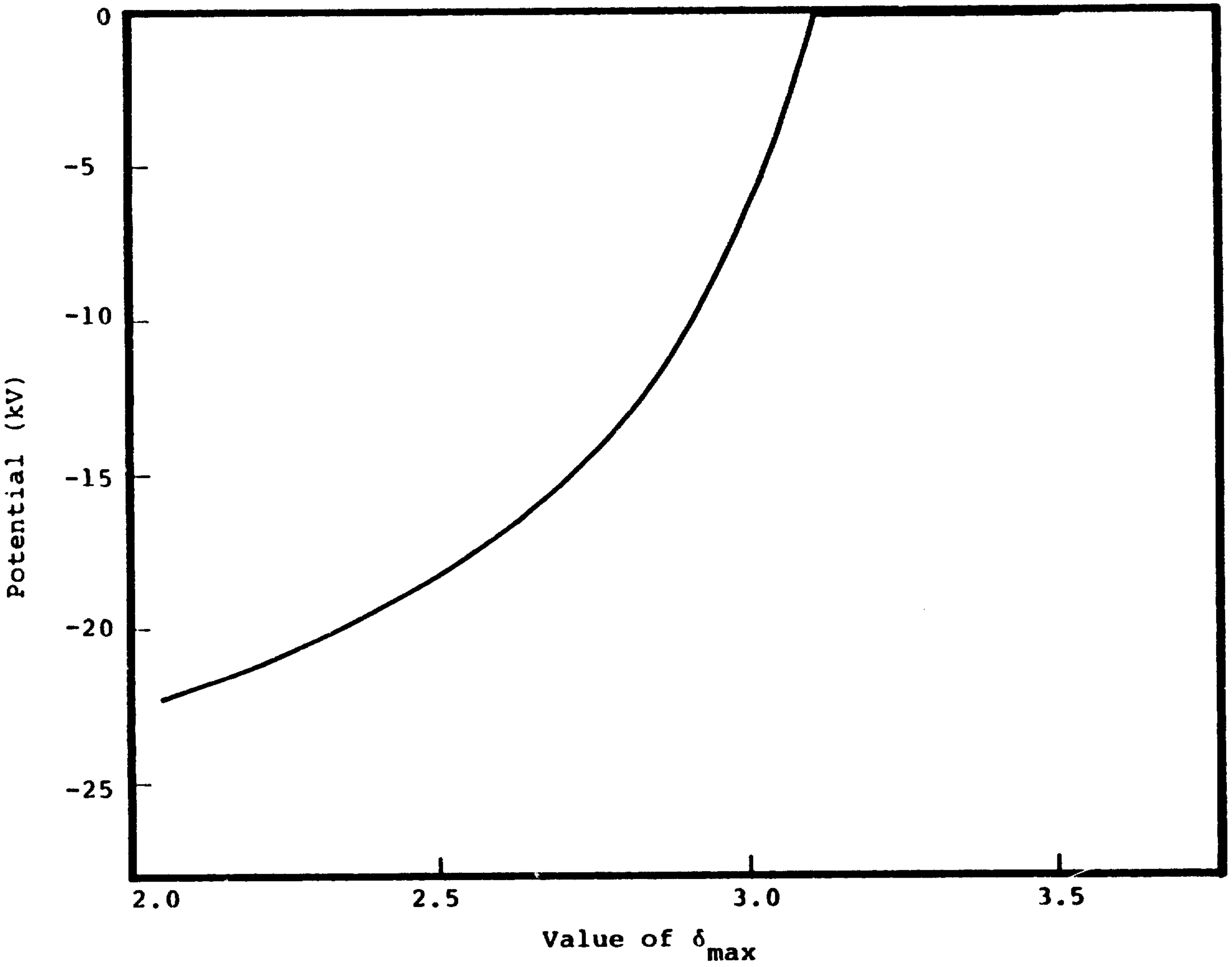

Figure 4.2. Charging characteristics of a solar sphere as a function of secondary emission yield (δ_{max}).

4.2 ANISOTROPIC FLUX

The SC5 detector on the "belly band" of the SCATHA satellite measures the angular distribution of the energy flux of the surrounding plasma in the plane of satellite rotation (Figure 4.3). For an isotropic plasma the flux is constant over a rotation giving a circular radial plot (Figure 4.4). For an anisotropic flux (i.e., one having particles aligned preferentially in one direction) the measured plot is distorted. The degree of distortion increases with the degree of anisotropy.

The most extreme case consists of a narrow beam lying in the plane of rotation. As the satellite rotates, the angle of incidence of the beam, θ_o, oscillates between 0 and $\pi/2$. To investigate the effect of anisotropy on spacecraft charging, we simulated this situation using MATCHG to calculate the potential of an aluminum plate under the influence of a beam with an oscillating angle of incidence θ_o.

The secondary emission yields and the backscatter all increase with increasing angle of incidence, and we expect the aluminum to be driven more positive at high angles and more negative at low angles of incidence. Figure 4.5 shows a plot of potential against time (angle) confirming our expectations.

When the charging response is fast compared to the period of the oscillations, we see the potential of the plate oscillate in time with the angle of incidence of the beam. The faster the charging response (or slower the rotation), the greater the amplitude of the oscillations. For a very fast oscillation, the plate would respond only to an average environment and no oscillations would be seen. The initial oscillations are erratic and more pronounced before settling into a regular pattern. This behavior reflects the two influences on the net current to the plate; potential and θ_o.

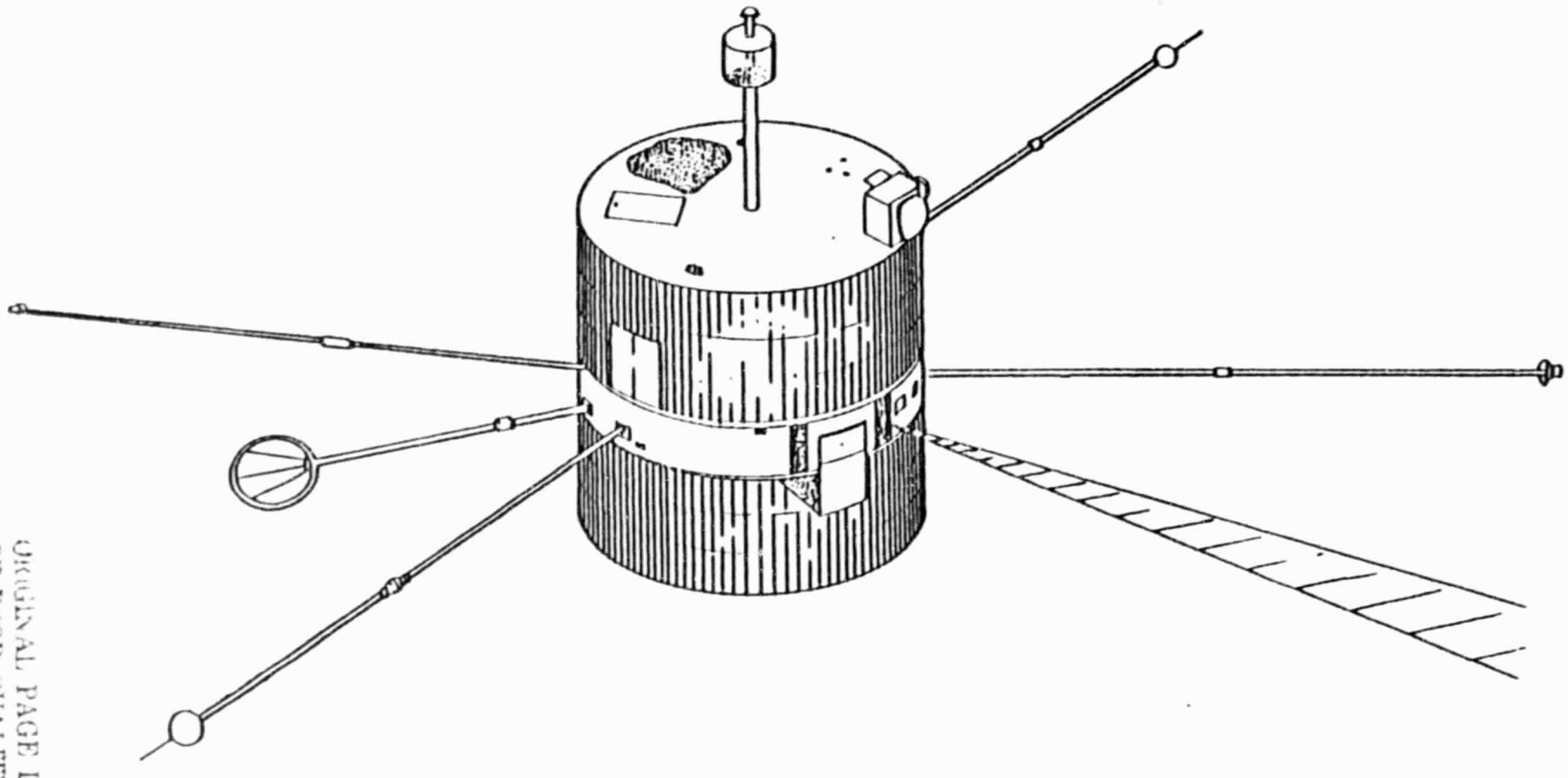

Figure 4.3. SC5 measures the angular distribution of the flux in the plane of rotation of the SCATHA satellite.

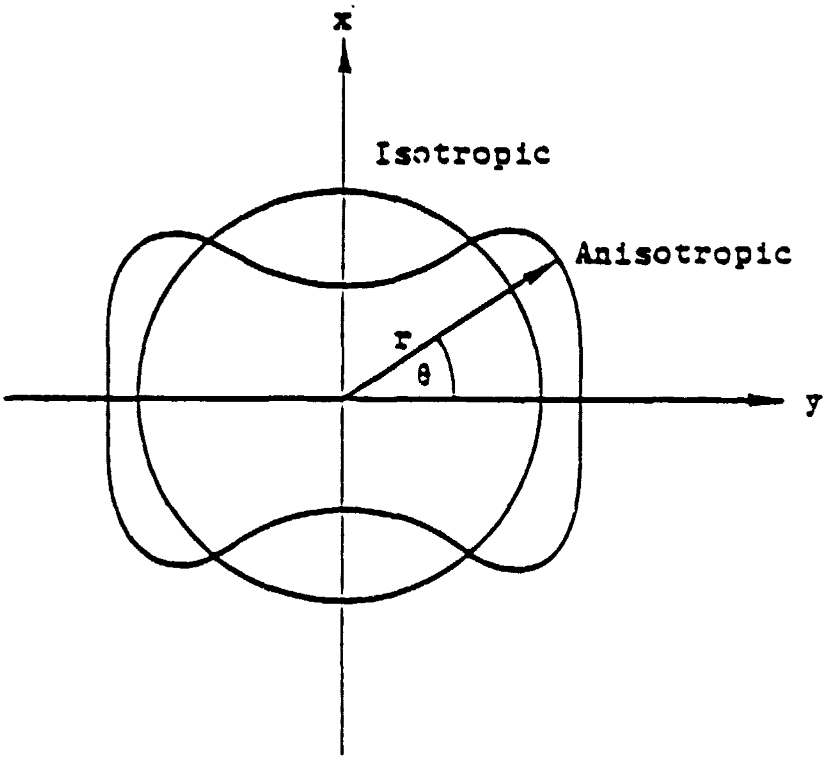

Figure 4.4. Representation of the angular distribution in the rotation plane. r represents the magnitude of the flux at angle θ.

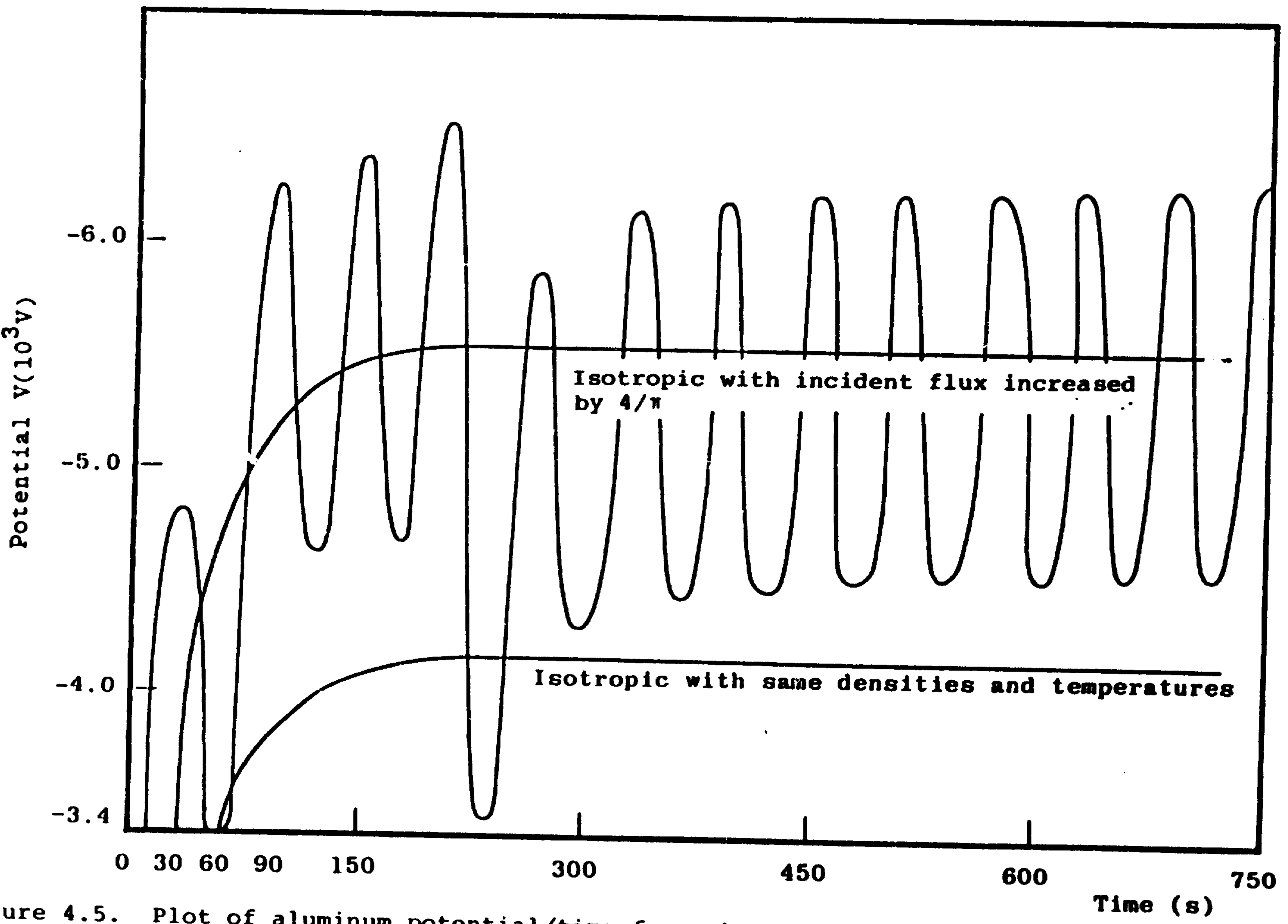

Figure 4.5. Plot of aluminum potential/time for a beam rotating at 3 deg/sec, Ion Density = Electron Density = 2 × 10^6 m^{-3}, Ion Temperature = 1 keV, Electron Temperature = 5 keV.

Initially, these may be out of phase leading to transient potentials that are too high or low.

The mean of the oscillating potential is not the same as that for an isotropic plasma of the same density and temperature. This is because of different incident currents arising out of distributions with the same flux normalization. A directional beam lying in the rotation plane has but one angle of incidence, θ_o, so the incident current is proportional to $\cos\theta$. The mean incident current is thus the mean of $\cos\theta$.

$$\text{Beam:} \quad \bar{I}_B \; \alpha \int_0^{\pi/2} \cos\theta \, d\theta \Big/ \int_0^{\pi/2} d\theta = \frac{2}{\pi}$$

For an isotropic distribution an angle of incidence θ_o in the rotation plane has associated with it all other angles of incidence due to particles arriving from above and below it. The average of these is $\sin\theta$. Thus the current from an isotropic distribution is proportional to $\cos\theta$ and $\sin\theta$, and the mean is the mean of $\cos\theta \sin\theta$:

$$\text{Isotropic:} \quad \bar{I}_i \; \alpha \int_0^{\pi/2} \cos\theta \sin\theta \, d\theta \Big/ \int_0^{\pi/2} \sin\theta \, d\theta = \frac{1}{2}$$

Thus, the beam current exceeds the isotropic by a factor of $4/\pi \sim 1.27$.

This illustrates some important points regarding the measurement of flux distributions in space:

1. If a detector measures an average flux over a rotation and assumes that it arises from an isotropic plasma, the actual current will be underestimated by an amount that will increase with the increasing directionality of the true angular distribution (reaching a maximum of $4/\pi$ for a beam).

2. If a detector measures actual average current, then in the same way flux (density) will be overestimated.
3. If a detector measures the angular distribution of the flux, information in both the perpendicular and parallel directions must be known, or implied to infer densities and currents.
4. For a "loss-cone" (negative aligned component) the reverse of 1 and 2 apply.

4.3 RADIATION-INDUCED BULK CONDUCTIVITY

In addition to the electron flux with energy below 100 keV, electrons with energies up to 5000 keV have been observed by detectors on board SCATHA. This high energy radiation makes an insignificant contribution to the total incident electron current but nevertheless can influence differential charging of insulators on a spacecraft

When high energy radiation, such as a 300 keV electron, passes through an insulator such as kapton, electrons can be promoted into the normally empty conduction bands and increase the bulk conductivity σ. Frederickson[13] has represented this by the equation

$$\sigma = \kappa\dot{D} + \sigma_o$$

where $\dot{D}$ is the radiation dose rate and κ is the coefficient that depends upon the nature of the material. σ_o is the conductivity in the absence of radiation. As the flux and hence dose rate increases, the radiation-induced conductivity increases. For a sufficiently high flux this could limit the potential differences that can build up between an insulator and the underlying conductor.

To investigate this question we use MATCHG to predict the potential of 0.005 inches (1.27×10^{-4} m) thick kapton subject to the single Maxwellian representation of the 59873 environment, with a range of values for the bulk conductivity.

The results are shown in Table 4.4. The fluxes corresponding to each value of σ can be estimated using an experimental result of Treadaway et al.[14] He found that a 0.002 inch (5.08×10^{-4} m) kapton film subjected to a 0.05 pA cm^{-2} beam of 300 keV electrons accompanied by a 0.2 nA cm^{-2} beam of 10 keV electrons charged to -1600 (±300) V. Simulating this experiment with MATCHG implied a value of 4.67×10^{-14} mhos m^{-1} for the bulk conductivity σ. Assuming that σ_o is insignificant we can estimate κ.

$$\sigma = \kappa \dot{D}$$

The dose rate $\dot{D}$ arises from 5×10^{-8} A m^{-2} of 300 keV electrons, i.e., a flux of 1.67×10^{4} electrons cm^{-2} s^{-1} sr^{-1} keV^{-1}. This is equivalent to a dose rate of 1.2 rads s^{-1}.

$$\kappa = 4.0 \quad 10^{-14} \text{ mhos } m^{-1} \text{ rad}^{-1} \text{ s}$$

This value is rather higher than Frederickson's estimate of 10^{-15}-10^{-16} mhos m^{-1} rad^{-1} s.[15]

As we can see from Table 4.4, as soon as the dose reaches $\sim 10^{2}$ electrons cm^{-2} s^{-1} keV^{-1} there is a significant drop in the potential difference that the kapton film can support. Since a 0.005 inch layer of kapton is typical of the insulating materials found on satellites, this result suggests that in environments with doses higher than 10^{2} electrons cm^{-2} s^{-1} sr^{-1} keV^{-1}, the radiation induced conductivity may play a significant role in preventing acute differential charging and hence discharges.

Figure 4.6 shows a plot of the data in Table 4.4. The vertical lines are drawn to represent the typical values for 200 keV flux on days 146, 87 and 114.[16] Days 146 and 114 are examples of the lowest and highest extremes documented so far. We see that fluxes in the range where radiation induced conductivity appears to be important are common.

It will be interesting to discover, as more data becomes available, if there is any correlation between the high energy flux and discharges on board SCATHA.

TABLE 4.4. THE EFFECT OF RADIATION-INDUCED CONDUCTIVITY ON THE CHARGING OF 0.005 INCH (1.27 × 10^{-4} m) KAPTON FILM AS PREDICTED BY MATCHG

300 keV Incident Current pA cm^{-2}	Differential Flux (F) Electrons cm^{-2} $s^{-1} sr^{-1} keV^{-1}$	Conductivity σ	Potential* Volts
0	0	0	-15500
0.003	1.0×10^{1}	2.8×10^{-17}	-15300
0.03	1.0×10^{2}	2.8×10^{-16}	-13700
0.05	1.67×10^{2}	4.67×10^{-16}	-12800
0.5	1.67×10^{3}	4.67×10^{-15}	- 5600
5.0	1.67×10^{4}	4.67×10^{-14}	- 1000
50.0	1.67×10^{5}	4.67×10^{-13}	- 100
500.0	1.67×10^{6}	4.67×10^{-12}	- 0

*Environment at 59873 Day 87 used.

$n_e = 0.28\ cm^{-3}$ $T_e = 12$ keV

$n_i = 0.15\ cm^{-3}$ $T_i = 9.9$ keV

$\sigma = \kappa F$

$\kappa = 2.8 \times 10^{-22}$ mhos m $electron^{-1}$ s sr keV

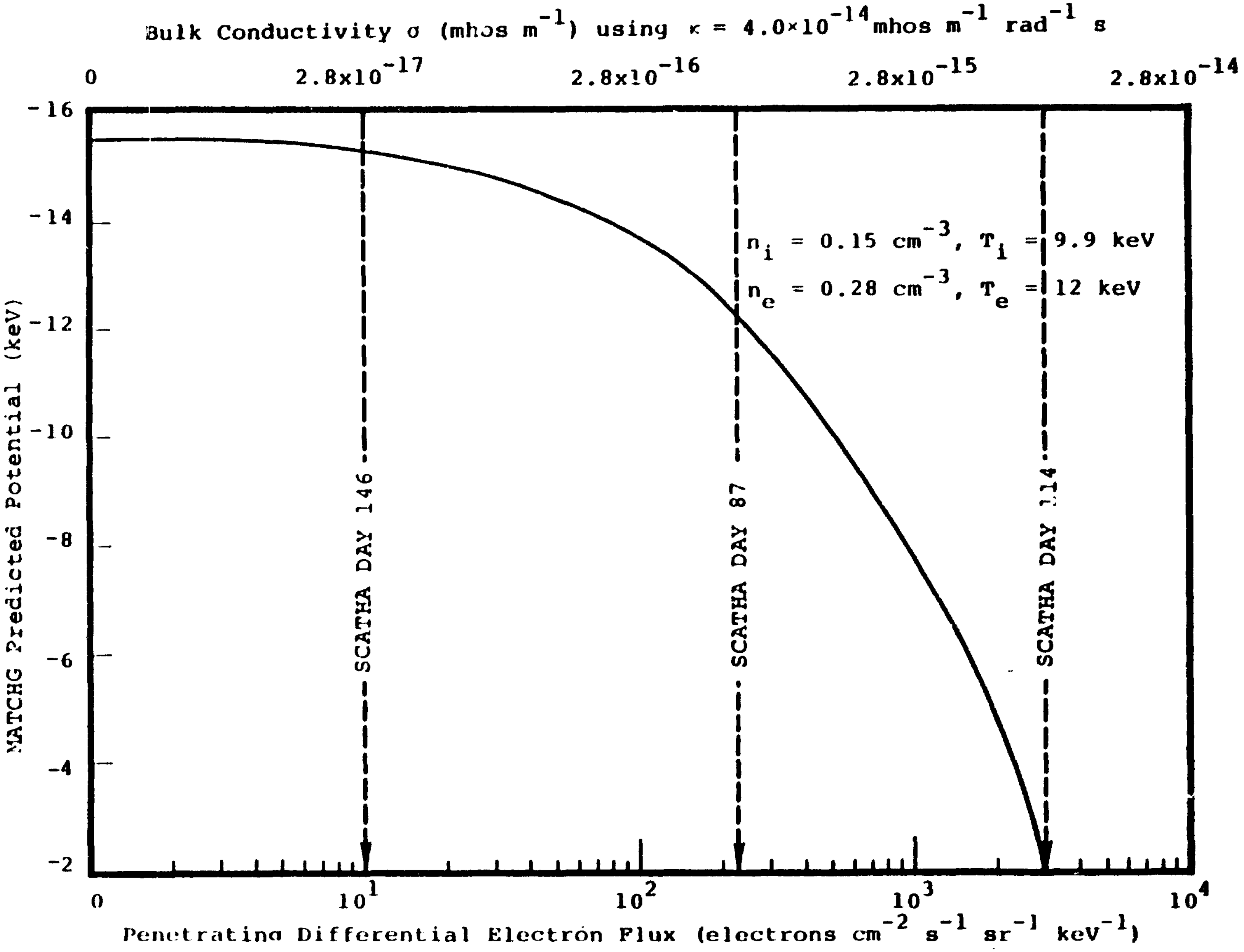

Figure 4.6. Plot of equilibrium potential of 5 mil kapton coating a grounded conductor versus bulk conductivity.

5. SCATHA CHARGING SIMULATIONS USING TEST DATA

This chapter comprises descriptions of SCATHA charging simulations in several typical, but fictitious, environmental conditions at geosynchronous orbit.* Charging in eclipse using the "high" and "moderate" double Maxwellian plasmas is described in Section 5.1 and 5.2, respectively. Sunlight charging simulations are discussed in Section 5.3. The induced charging event on day 89 is of special interest due to the SC2 failure and telemetry upset which occurred; modeling of the SCATHA charging response during this event is discussed in Section 5.4.

The four grid SCATHA model as described in Chapter 2 was used for all of the simulations reported here. The spherical probe current collection model and the "NORMAL" secondary yield formulation were used throughout. Monopole boundary conditions were imposed at the outer (fourth) grid boundary, and simulations were begun with the spacecraft uncharged, unless otherwise indicated.

5.1 ECLIPSE CHARGING IN HIGH TEMPERATURE ENVIRONMENT

The charging simulation described in this section used a high temperature double Maxwellian ambient plasma model given in Table 5.1. The spacecraft response followed a pattern typical for a highly charging environment: rapid overall charging to several kilovolts followed by much slower development of differential charging. Figures 5.1 and 5.2 illustrate the potential contours after three seconds of charging, when the overall charging to -6.4 kV is complete. Differential charging was then followed for 3200 seconds: Figures 5.3 and 5.4 illustrate the final potential contours.

---

*These computations were carried out early in the program, prior to the updating of material properties shown in Table 2.3. The conclusions remain valid, however.

TABLE 5.1. TYPICAL GEOSYNCHRONOUS ENVIRONMENTS SPECIFIED FOR SCATHA CHARGING STUDIES

	SINGLE MAXWELLIAN				DOUBLE MAXWELLIAN								
	$n_e = n_i$	T_e	T_i		n_{e1}	n_{e2}	T_{e1}	T_{e2}		n_{i1}	n_{i2}	T_{i1}	T_{i2}
LOW T	1.1	1.8	8		.85	.25	1	4		.25	.85	.3	9
MODERATE T	1.5	2.8	7		.9	.6	1.5	4.4		.9	.6	.43	10
HIGH T	.2	8	13		.06	.14	1.2	10		.06	.14	2	16

Densities in cm^{-3}

T in keV

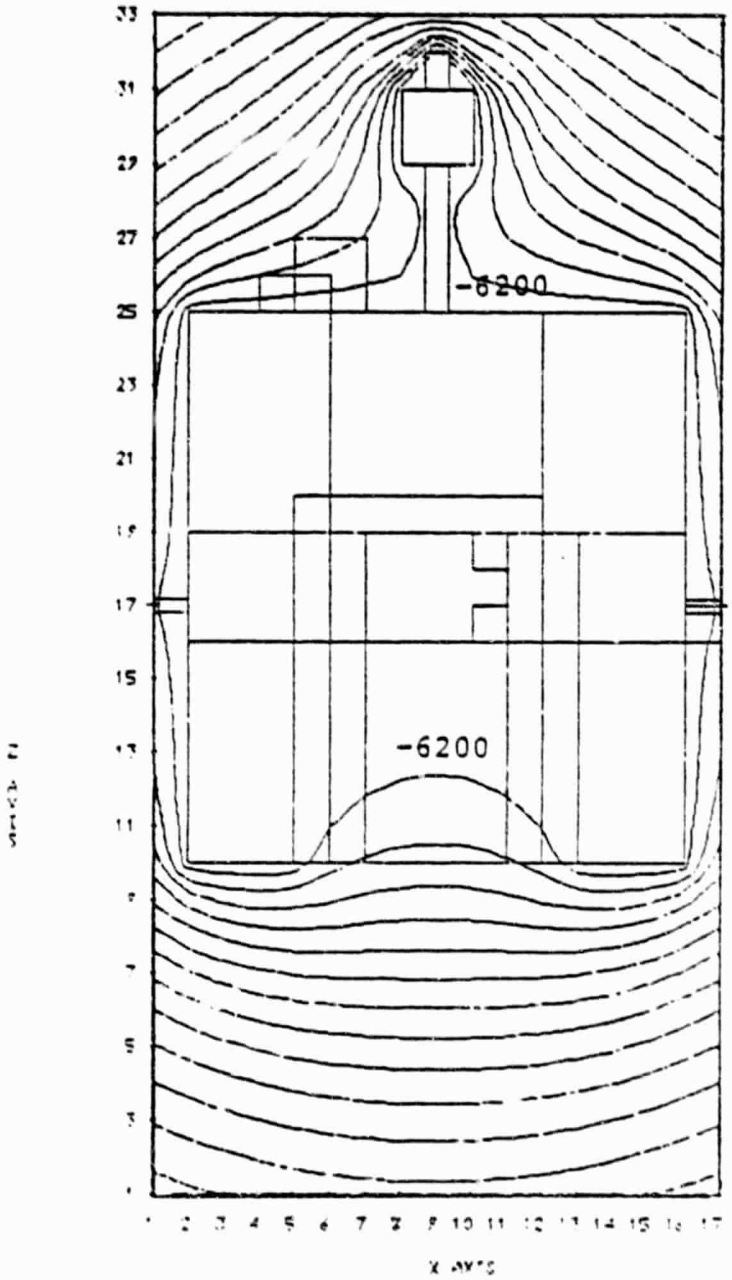

SCATHA IN
ECLIPSE

HIGH T
DOUBLE MAXWELLIAN
ENVIRONMENT

S/C GROUND
= -6300 V

CONTOUR STEPS
= 200 V

Figure 5.1. SCATHA potential contours Time = 3 seconds.

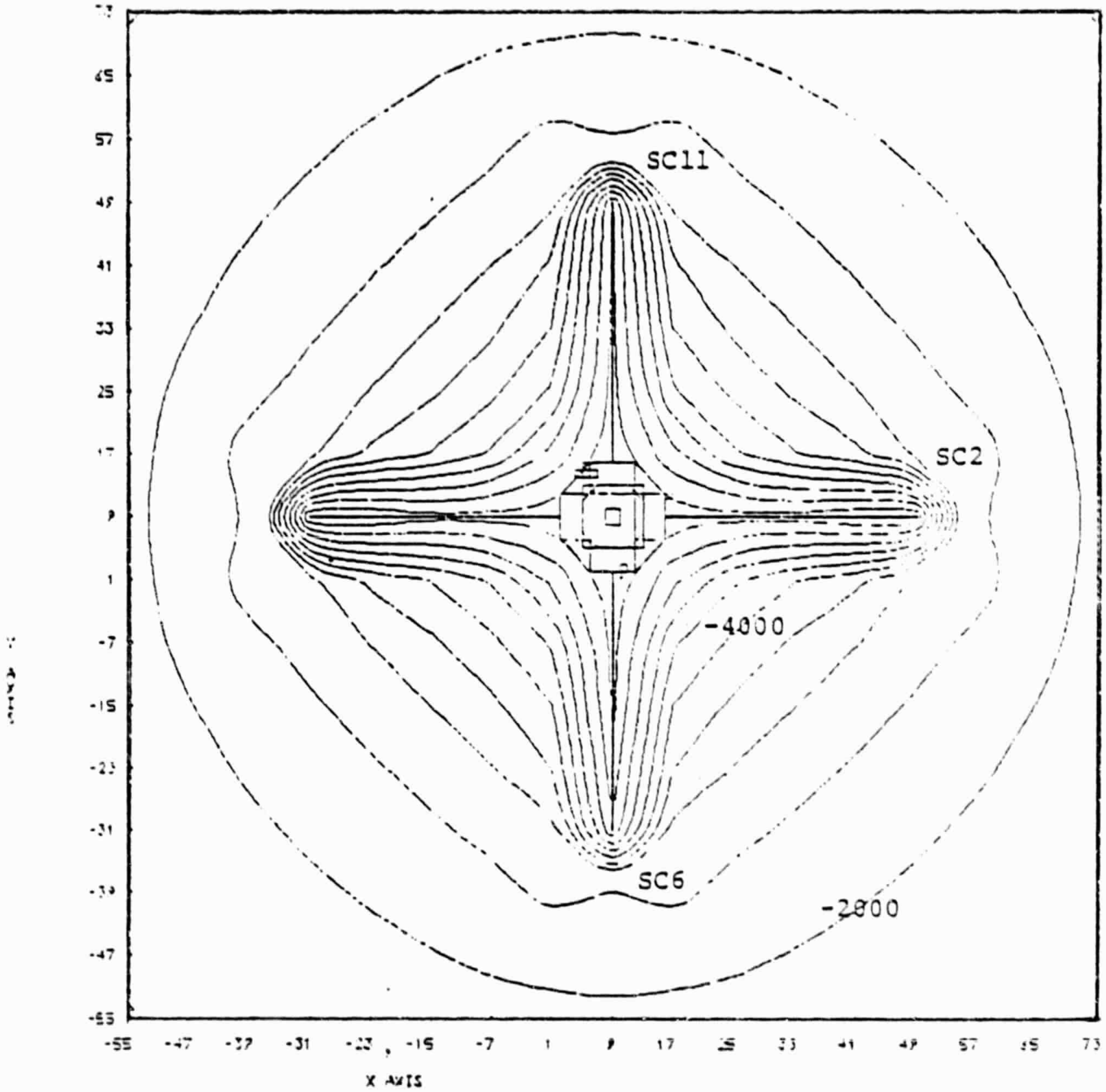

SCATHA IN ECLIPSE; S/C GROUND = -6200 V; CONTOUR STEPS = 500 V.

Figure 5.2. SCATHA potential contours. Time = 3 seconds.

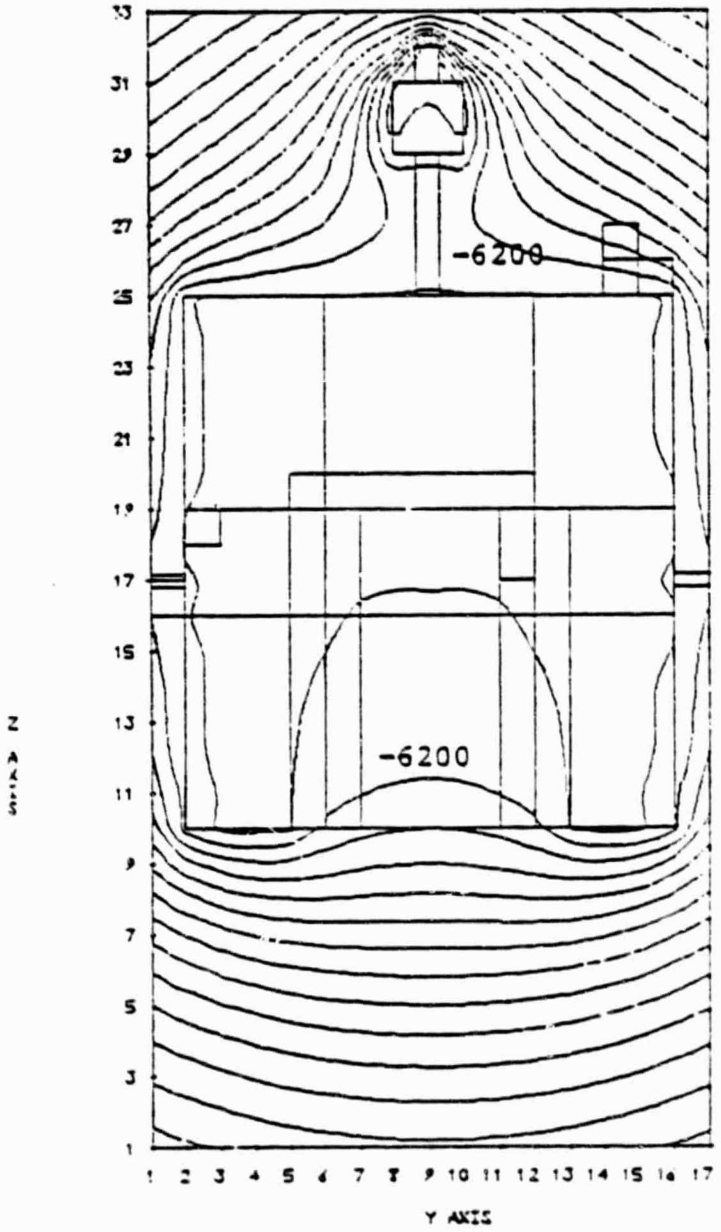

SCATHA IN
ECLIPSE

HIGH T
DOUBLE MAXWELLIAN
ENVIRONMENT

S/C GROUND
= -6400 V

CONTOUR STEPS
= 200 V

Figure 5.3. SCATHA potential contours. Time = 3230 seconds.

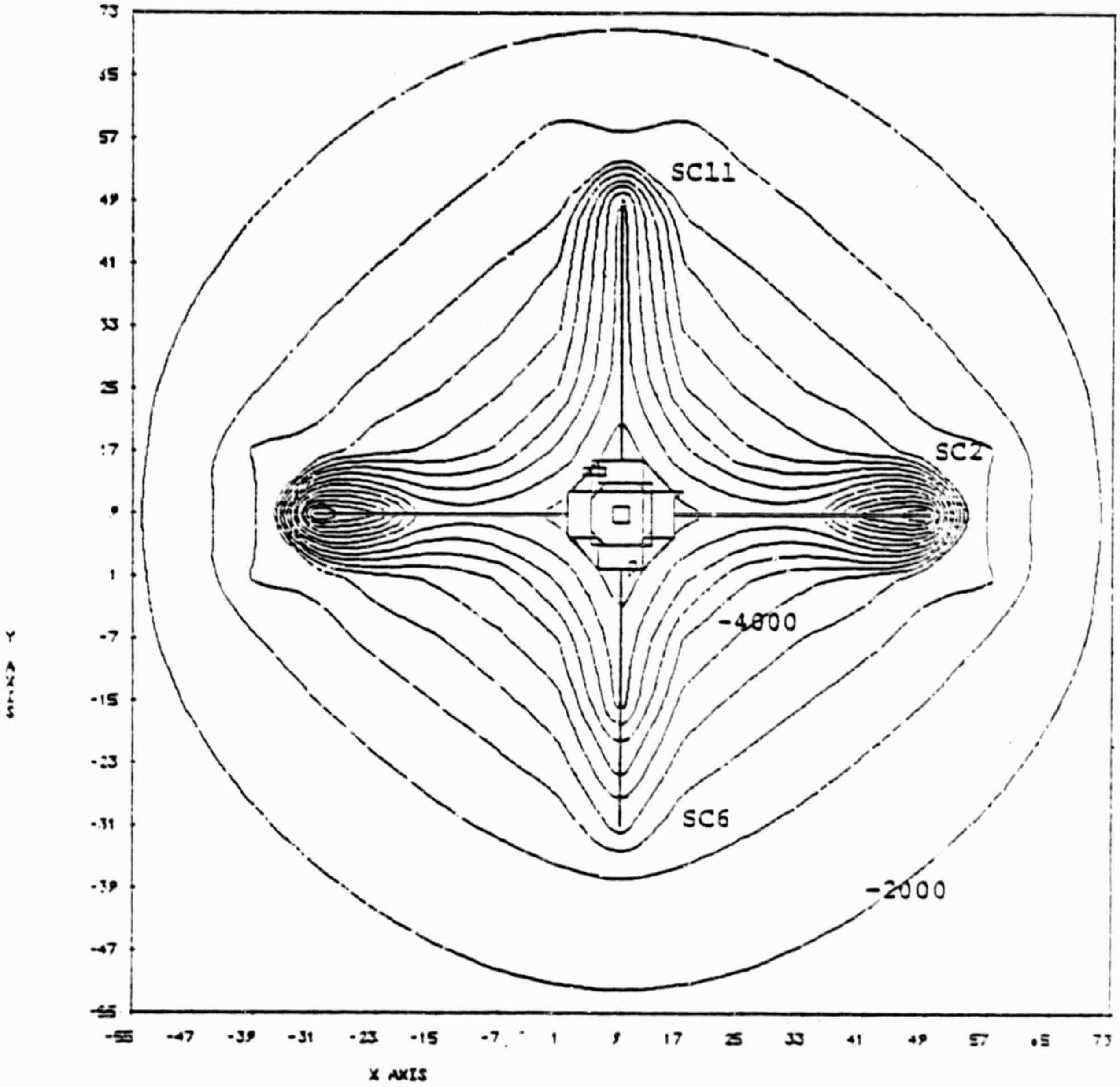

SCATHA IN ECLIPSE; S/C GROUND = -6400 V; CONTOUR STEPS = 500 V.

Figure 5.4. SCATHA potential contours. Time = 3230 seconds.

Two types of differential charging occur during this period. The first involves development of electric stresses internal to insulating materials whose surfaces charge relative to underlying conductors. Maximum stresses of this type were 3×10^6 V/m for TEFLON insulating patches on the bellyband; far below breakdown thresholds for this material. Differential charging along adjacent satellite surfaces can also occur. In this simulation, the segments at the ends of the SC2 and SC6 booms representing experiment mountings were allowed to float with respect to spacecraft ground. As a result, differential charging of surfaces near these boom ends becomes severe, as the SC6 tip (GOLD) reaches -3.5 kV and the SC2 tips (BLACKC) charge to -9 kV. (The SC11 boom remains nearly an equipotential since the magnetometer experiment at its end is not distinguished in the model.) The large surface potential gradients near boom tips are clearly visible in Figure 5.4: these are the most likely sites for surface flashovers identified in this simulation. The development of differential charging during the simulation is illustrated graphically in Figure 5.5.

5.2 ECLIPSE CHARGING IN MODERATE TEMPERATURE ENVIRONMENT

The charging simulation described in this section used the moderate temperature double Maxwellian ambient plasma model given in Table 5.1. The expected spacecraft response is quite different from that described in the preceding section: little overall charging is expected since equilibrium potentials for much of the surface material (GOLD, GOLDPD, SOLAR) are near zero. The satellite surfaces charge differentially (hence slowly) from the outset: potential contours after 2300 seconds are shown in Figures 5.6 through 5.8. Even though the charging environment is not severe, local charge buildup near some surfaces can lead to large differential charging, such as near the KAPTON surface of the SC1 experiment in Figure 5.6, and along the SC2 booms in Figure 5.7.

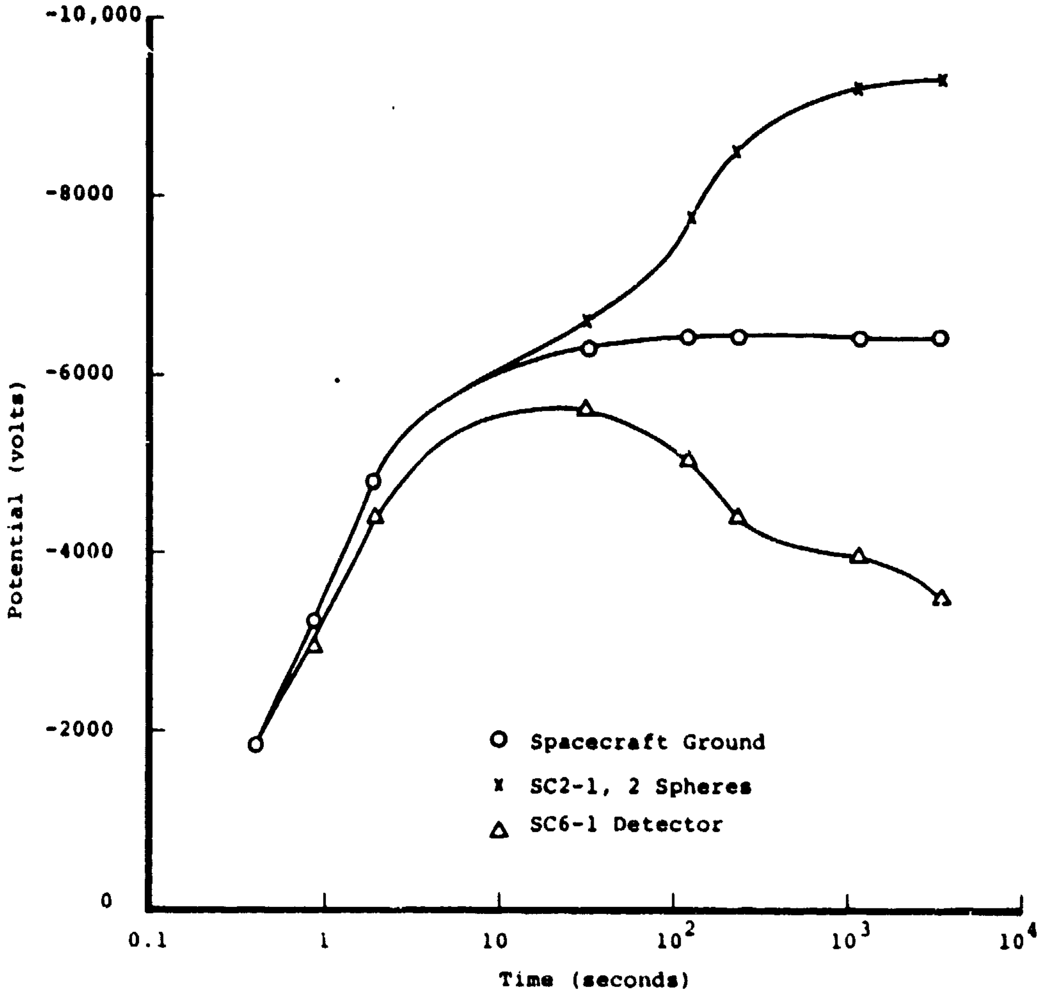

Figure 5.5. Potentials versus time for SCATHA model in high temperature ambient plasma.

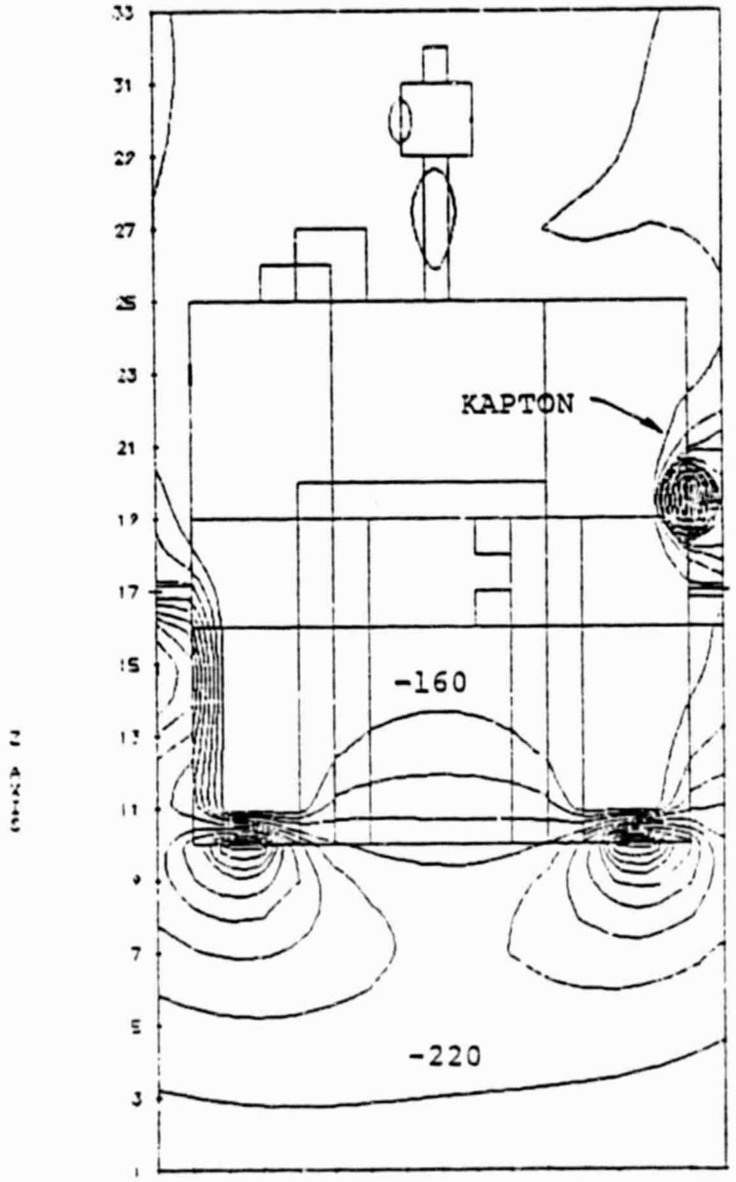

SCATHA IN
ECLIPSE

MODERATE T
DOUBLE MAXWELLIAN
ENVIRONMENT

CONTOUR STEPS
= 20 V

Figure 5.6. SCATHA potential contours.

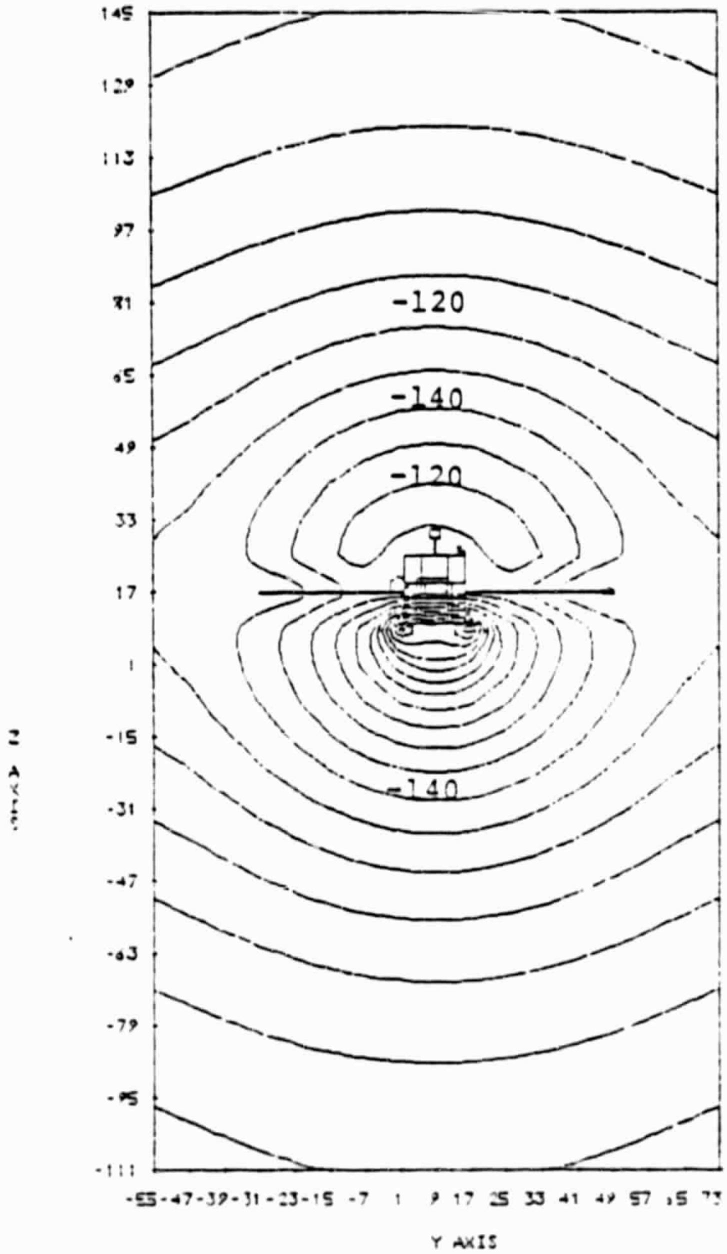

SCATHA IN
ECLIPSE

MODERATE T
DOUBLE MAXWELLIAN
ENVIRONMENT

CONTOUR STEPS
= 10 V

Figure 5.7. SCATHA potential contours.

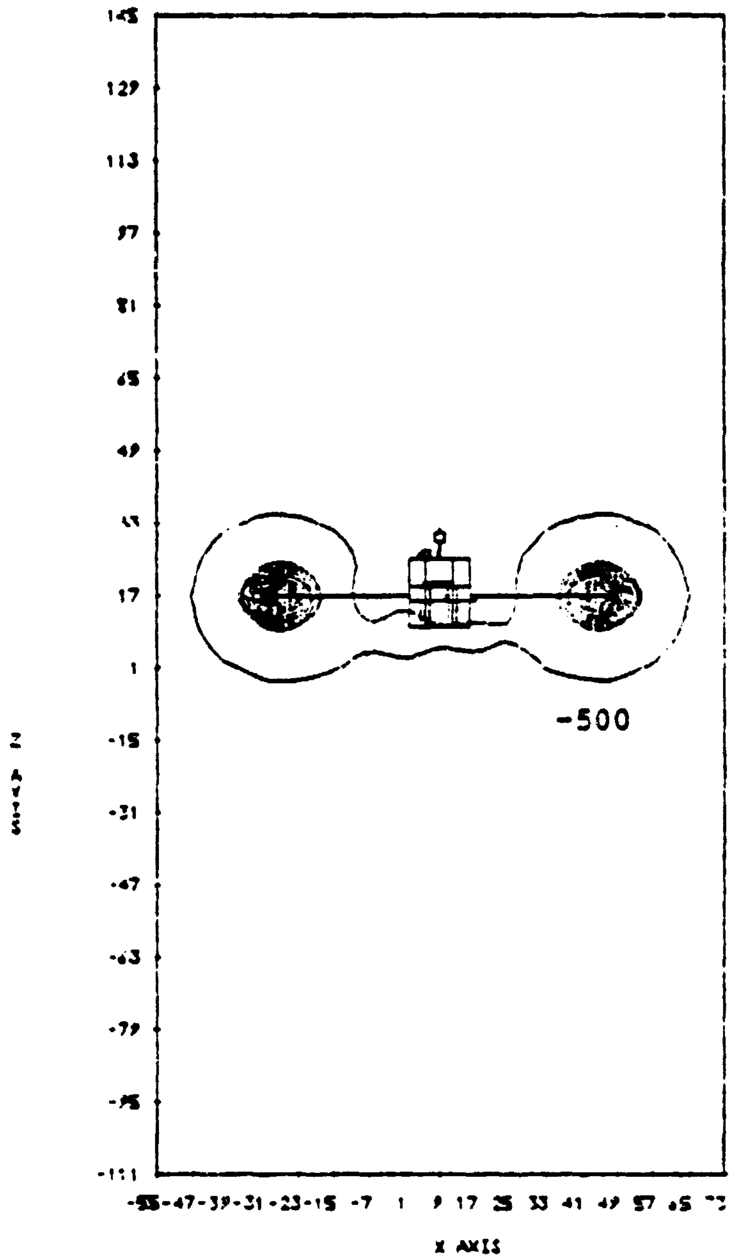

SCATHA IN
ECLIPSE

MODERATE T
DOUBLE MAXWELLIAN
ENVIRONMENT

CONTOUR STEPS
= 200 V

Figure 5.8. SCATHA potential contours.

Charging of the non-conducting white paint (WHITEN) covering the aft surface has important consequences. Fringing fields from the aft surface result in the suppression of low energy emission from neighboring solar cells and the cavity, so that the ground conductor has charged to -143 volts at the time shown. The WHITEN surface has reached -390 volts; further charging is limited by bulk conductivity. The dipolar character of the potential is clearly displayed in Figure 5.8. The reference band conductor (GOLD) reached a potential of -213 volts, nearer the WHITEN potential than the ground conductor due to its proximity to the aft surface. The drift of the reference band away from plasma ground due to fringing fields will obviously have an impact on SSPM measurements which attempt to use the reference band as a measure of zero potential; this point is discussed further in the next section.

5.3 SUNLIGHT CHARGING SIMULATIONS

Two simulations of charging response in sunlight are described in this section. Since the differential charging timescale for most SCATHA materials is typically $\sim 10^3$ seconds, the satellite reaches equilibrium in response to solar illumination averaged over many rotations, and the SPINNER model in NASCAP is appropriate. In this mode, both a sun direction and a spin axis are specified, and the photocurrent expected from each surface cell is calculated on the basis of the averaged applied solar illumination. Although the relatively fast response of instruments such as the SSPM experiments could not be correctly modeled in this fashion, the SPINNER mode does serve as a convenient and economical procedure for studying ex ted equilibrium charging response.

The results of the first set of calculations are illustrated in Figures 5.9 and 5.10. These potential contours result from charging in the high temperature single Maxwellian environment, using the SPINNER model in sunlight;

over 5000 seconds have elapsed in the simulation. The sun direction was taken to be perpendicular to the SCATHA spin axis, so that only the forward, aft, and cavity surfaces remain in darkness. Fringing fields from the aft surface are not sufficient to cause charging of the ground conductor: it remained at +4 volts throughout the simulation. All the boom surfaces also stayed at small positive potentials. The charge accumulation of the WHITEN aft surfaces again leads to an overall dipolar field, as shown in Figures 5.9 and 5.10. The latter figure is particularly striking, showing the positive potentials near the booms distorting the negative potentials emanating from the aft region. Although the ground conductor remains discharged in this case, the solar cells on the lower portion of the satellite charged to as much as -20 volts, and the reference band charged to -34 volts. These results indicate that even in sunlight, SSPM measurements may not be accurately referenced to plasma ground.

Potential contours during discharge of the SCATHA model from high negative potentials are shown in Figures 5.11 through 5.14. Solar illumination was applied using the SPINNER model (sun again incident perpendicular to the spin axis) after the satellite was charged in eclipse in the high temperature double Maxwellian plasma. As the discharge in sunlight begins, local regions of strong differential charging persist as the overall net charge is dissipated. Some surfaces reach positive potentials of up to 2 kV due to the transient persistence of differential charging. Figures 5.11 and 5.12 show the potential contours after 1 second of sunlit discharging, when the persistence of differentially charged regions is still clear. After 40 seconds of discharging, as illustrated in Figures 5.14 and 5.15, much of the differential charging has been removed. The SC6 boom is returning from a high positive potential to near plasma ground by collecting ambient electron current from the plasma, a relatively

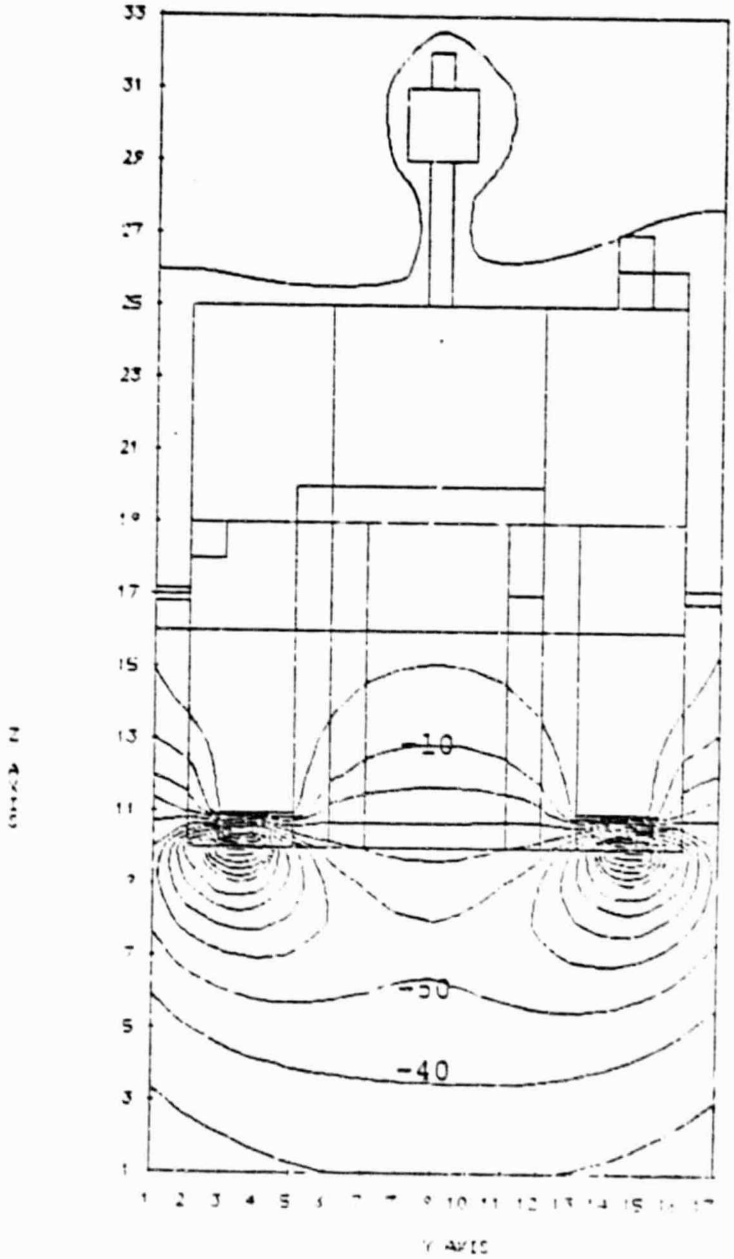

SCATHA IN
SUNLIGHT

HIGH T
SINGLE MAXWELLIAN
ENVIRONMENT

CONTOUR STEPS
= 10 V

Figure 5.9. SCATHA potential contours.

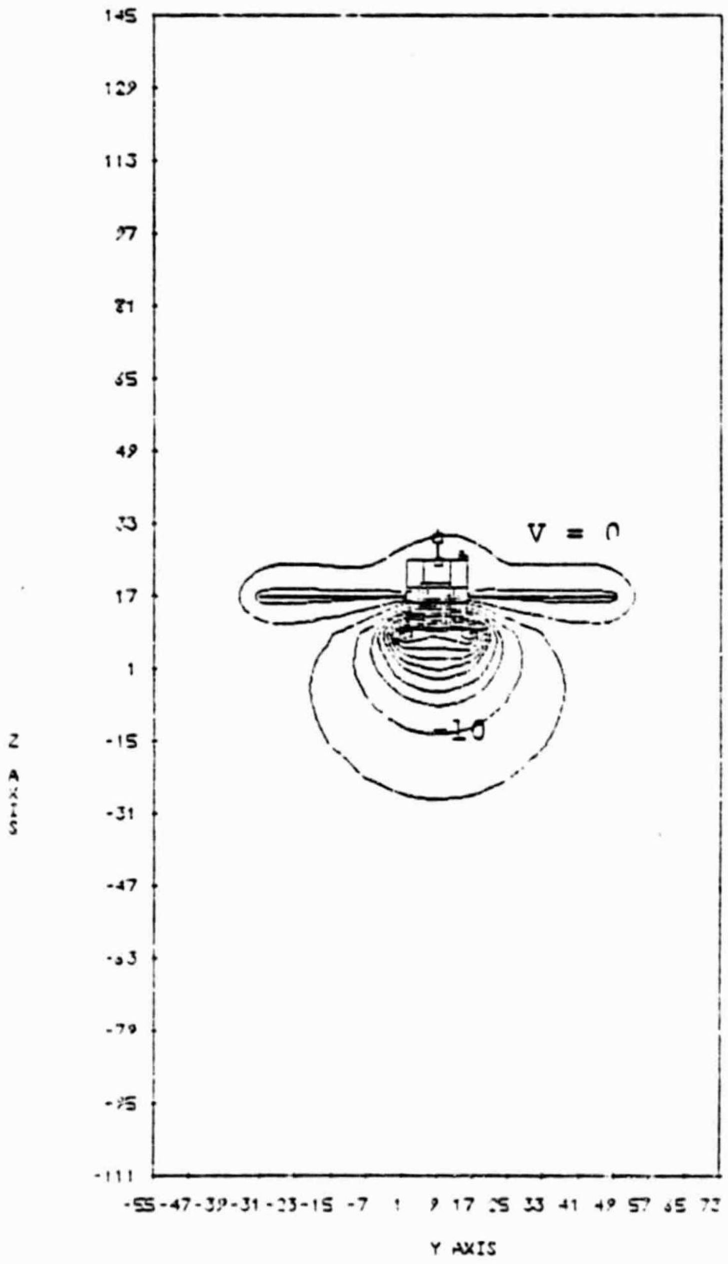

SCATHA IN
SUNLIGHT

HIGH T
SINGLE MAXWELLIAN
ENVIRONMENT

CONTOUR STEPS
= 5 V

Figure 5.10. SCATHA potential contours.

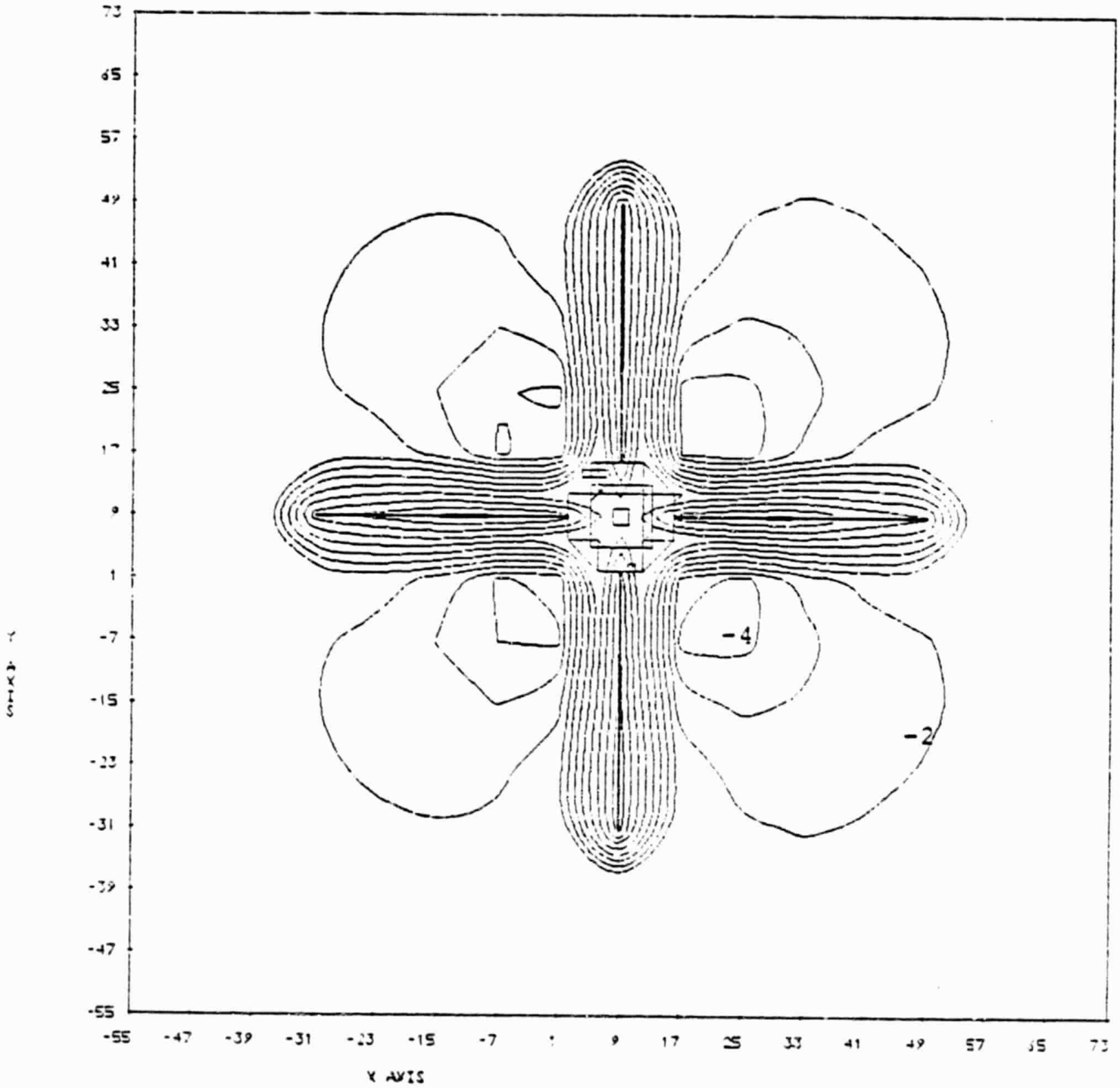

SCATHA IN SUNLIGHT; HIGH T SINGLE MAXWELLIAN ENVIRONMENT; CONTOUR STEPS = 1 VOLT.

Figure 5.11. SCATHA potential contours.

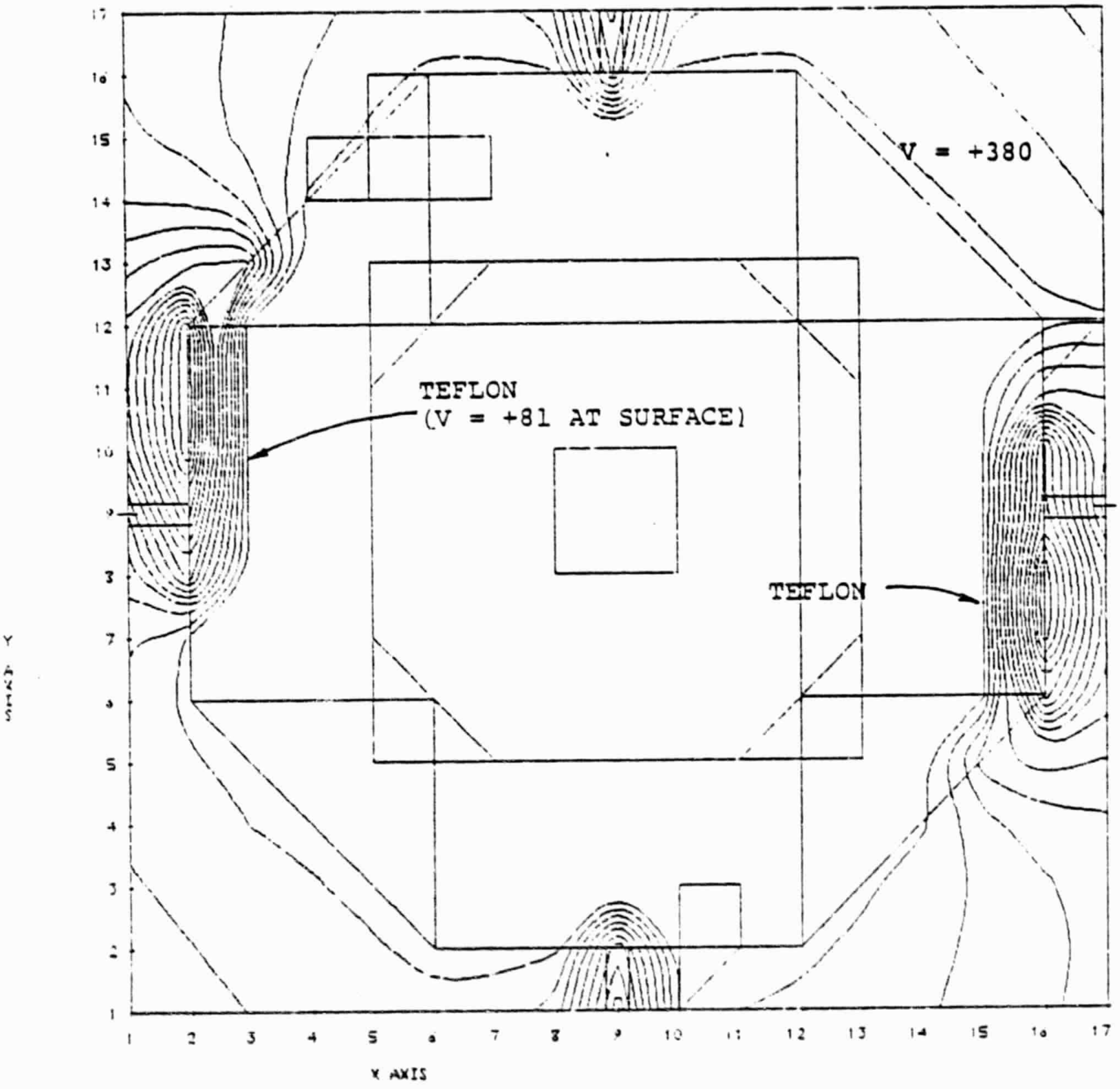

SCATHA DISCHARGING IN SUNLIGHT; CONTOUR STEPS = 20 V.

Figure 5.12. SCATHA potential contours. Time = 1 second after entering sunlight.

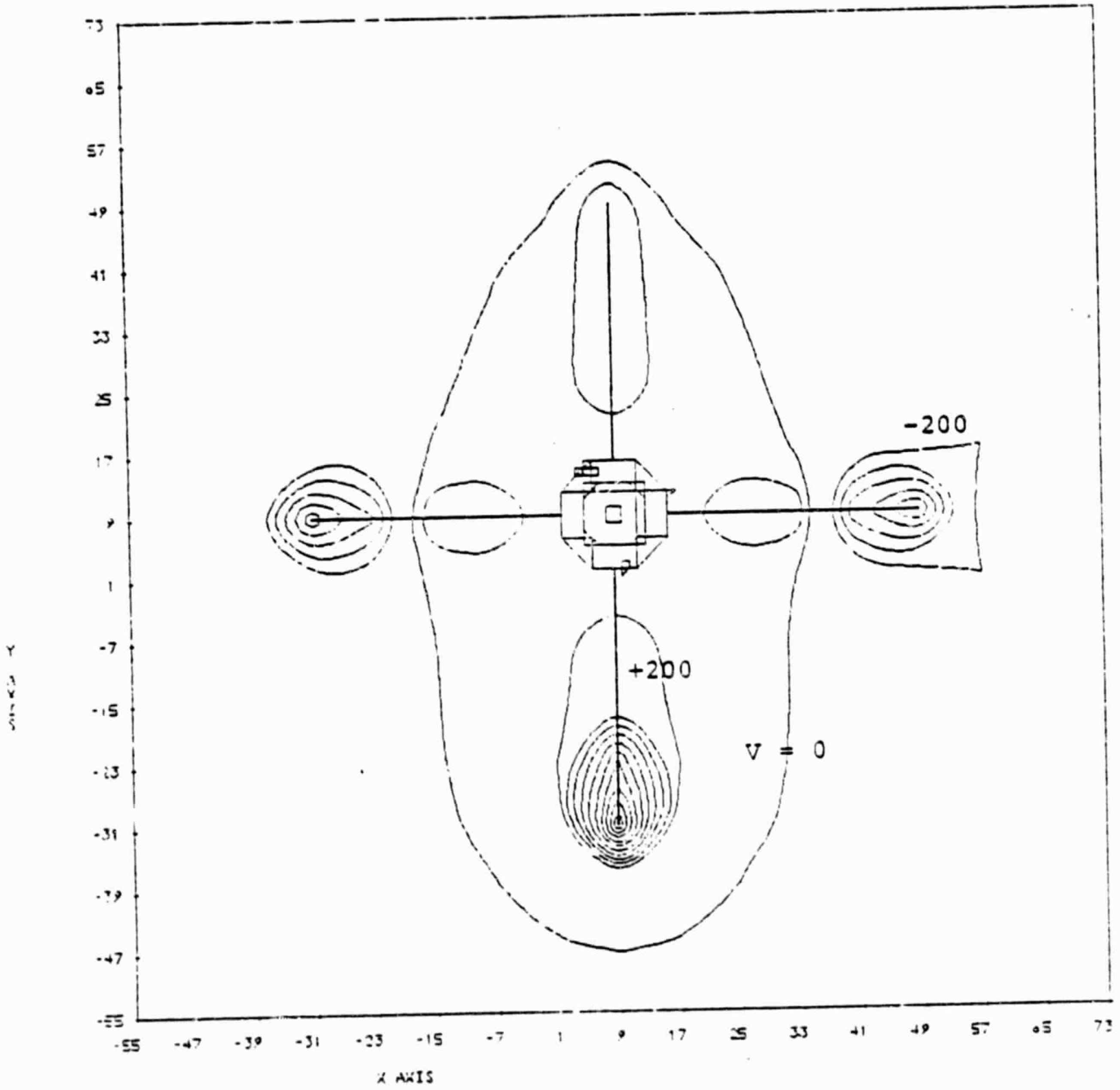

SCATHA DISCHARGING IN SUNLIGHT; CONTOUR STEPS = 200 V.

Figure 5.13. SCATHA potential contours. Time = 1 second after entering sunlight.

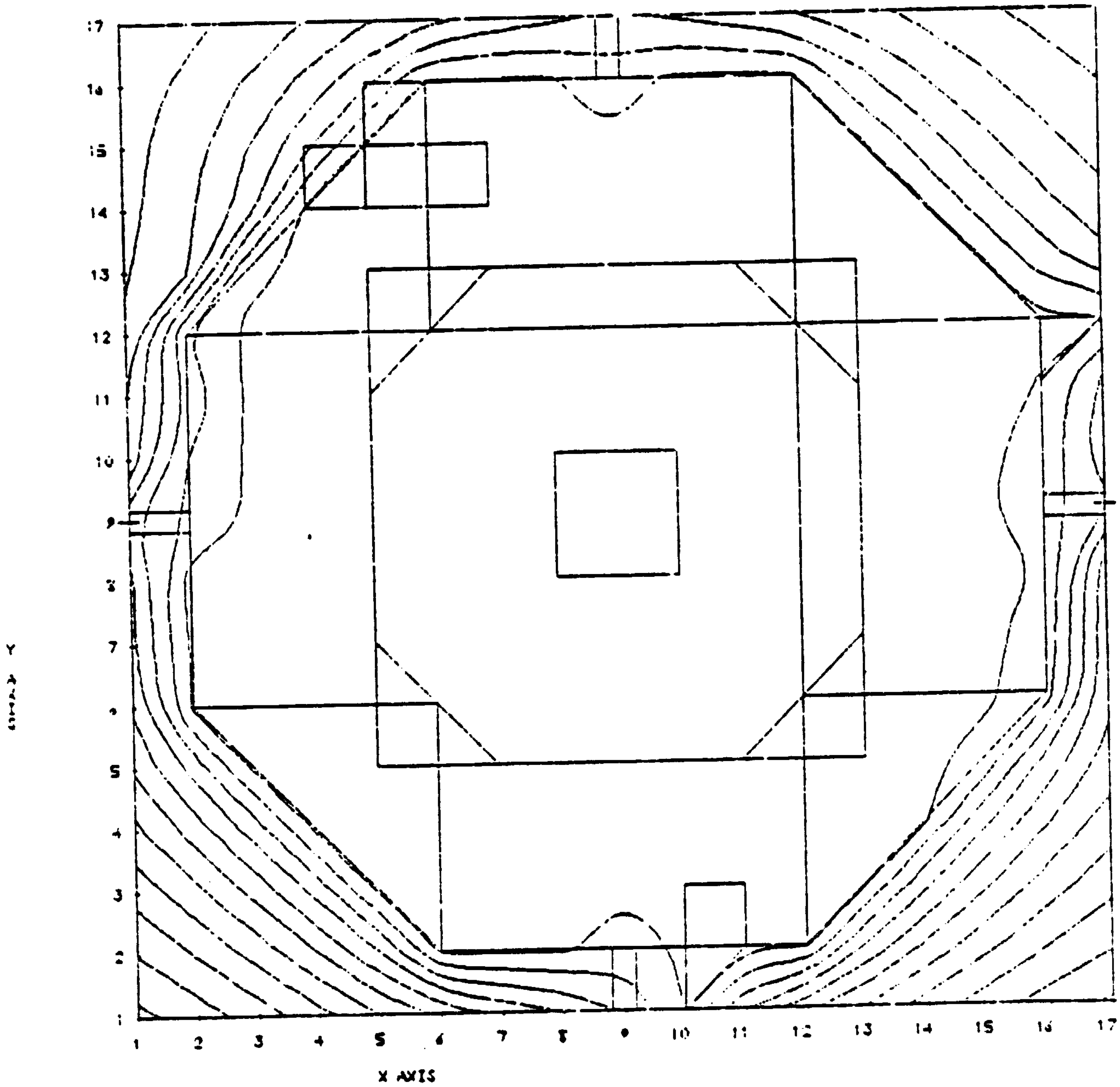

SCATHA DISCHARGING IN SUNLIGHT; CONTOUR STEPS = 1 V.

Figure 5.14. SCATHA potential contours. Time = 40 seconds after entering sunlight.

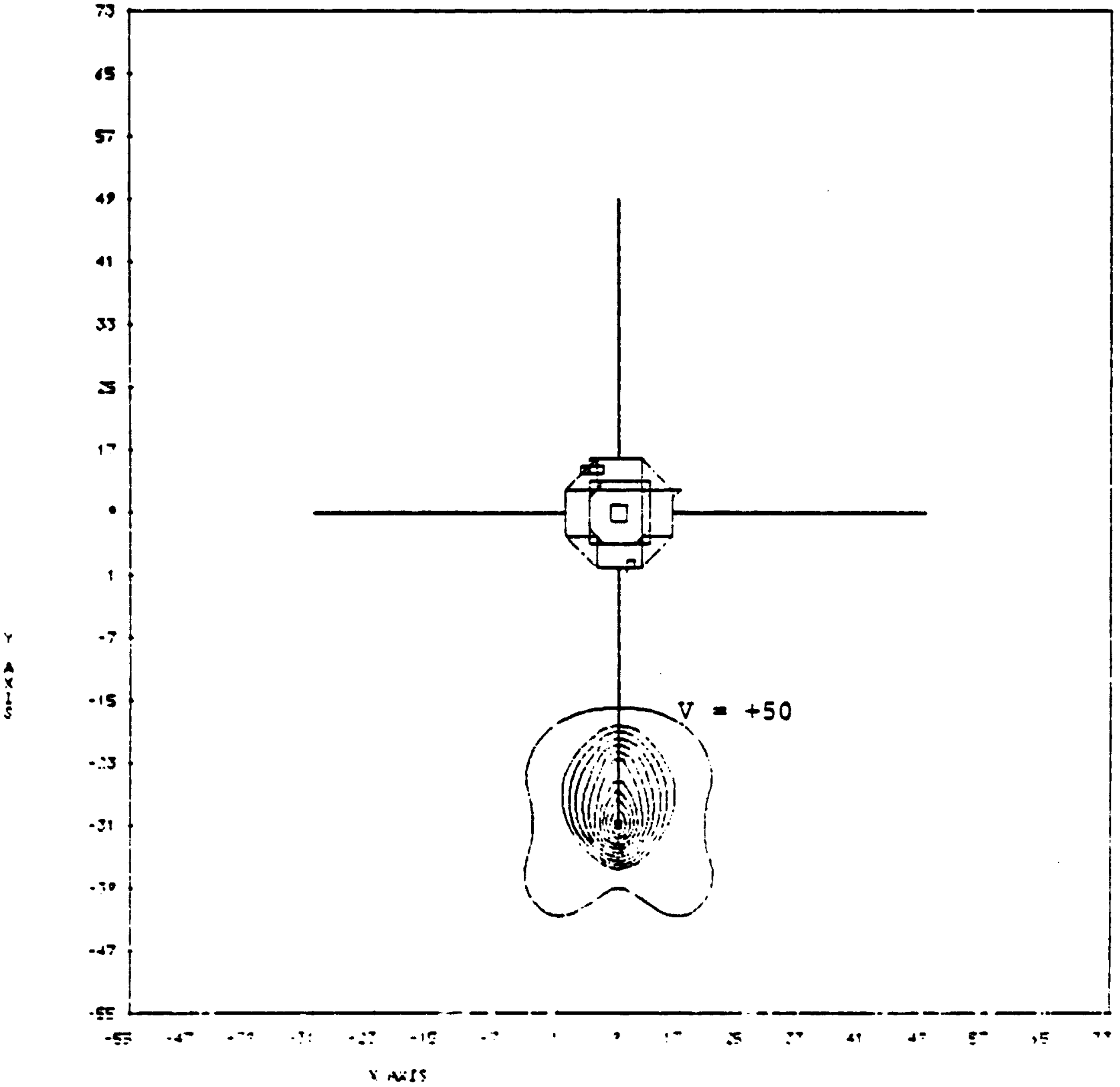

SCATHA DISCHARGING IN SUNLIGHT; CONTOUR STEPS = 50 V.

Figure 5.15. SCATHA potential contours. Time = 40 seconds after entering sunlight.

slow process. This simulation graphically illustrates the complicated dynamics involved in the SCATHA exit from eclipse. Since many of the interesting processes occur on a timescale of less than a full rotation of the satellite, the SPINNER model used has undoubtedly distorted the actual time sequences somewhat.

6. SCATHA CHARGING SIMULATIONS USING EXPERIMENTAL DATA

6.1 DAY 87, 1979

The SCATHA vehicle charged rapidly shortly after going into eclipse on Day 87, 1979, following an injection event.

The detectors on board SCATHA have transmitted a wealth of information on the plasma environment and corresponding spacecraft potential during this event. Armed with this information, and an accurate representation of the spacecraft, we have been able to make the first direct comparison between the charging behavior predicted by NASCAP, and that actually observed for a real satellite in space. We have also been able to show that the physical model upon which NASCAP rests is a sound one.

The environments used in this simulation were those described in Chapter 3, and shown in Table 3.1. The representation of the SCATHA satellite used was the "one-grid" model described in Chapter 2.

The potential reached by a spacecraft bathed in a plasma environment depends on at least three factors.

1. The nature of the environment (temperature and density).
2. The time it has been exposed to the environment. (Charging or discharging is not instantaneous.)
3. The potential of the spacecraft prior to the introduction of the new environment.

To properly simulate the response of the spacecraft to the charging environment, NASCAP takes all of these factors into account. After each cycle, the time elapsed is checked, and the environment parameters used updated to the most recent time for which data was measured. The data points are typically 60 seconds apart.

The results are shown in Figure 6.1. The NASCAP simulation reproduces the two major jumps in potential, but misses the remaining two minor jumps. Quantitative agreement is excellent considering the sensitivity of the NASCAP predictions to the values of the material properties used. The NASCAP simulation is slower to respond to changes in environment than the real satellite, because the environment changes occur in ~60 second steps rather than the continuous adjustment experienced in space.

In addition, the slow discharge rate predicted, following the two charging pulses, would have been faster if shorter computational timesteps had been used.

The Day 87 simulation is the first real test of both NASCAP and the physical model on which it is based. The remarkable agreement between the NASCAP predicted potentials and those actually observed on a real satellite in an actual space environment, shown in Figure 6.1, confirms their validity. We can now say with confidence that the physical processes which control spacecraft charging are understood.

6.2 DAY 89, 1979

The SCATHA SC4-2 electron gun was operated at a variety of current-voltage combinations during pass 89-4. These gun operations induced a complex response by the spacecraft ground, the insulating surface potentials on the SSPM's, and the SC2 probes. Below we will describe a qualitative picture of the beam dynamics, the satellite environment, and the charging processes which occurred during pass 89-4.

6.2.1 Overview and Spacecraft Ground Potential

The beam dynamics of the electron gun are examined in detail in Chapter 7. The electron gun emits monoenergetic electrons from an area of approximately 1 cm^2, at currents

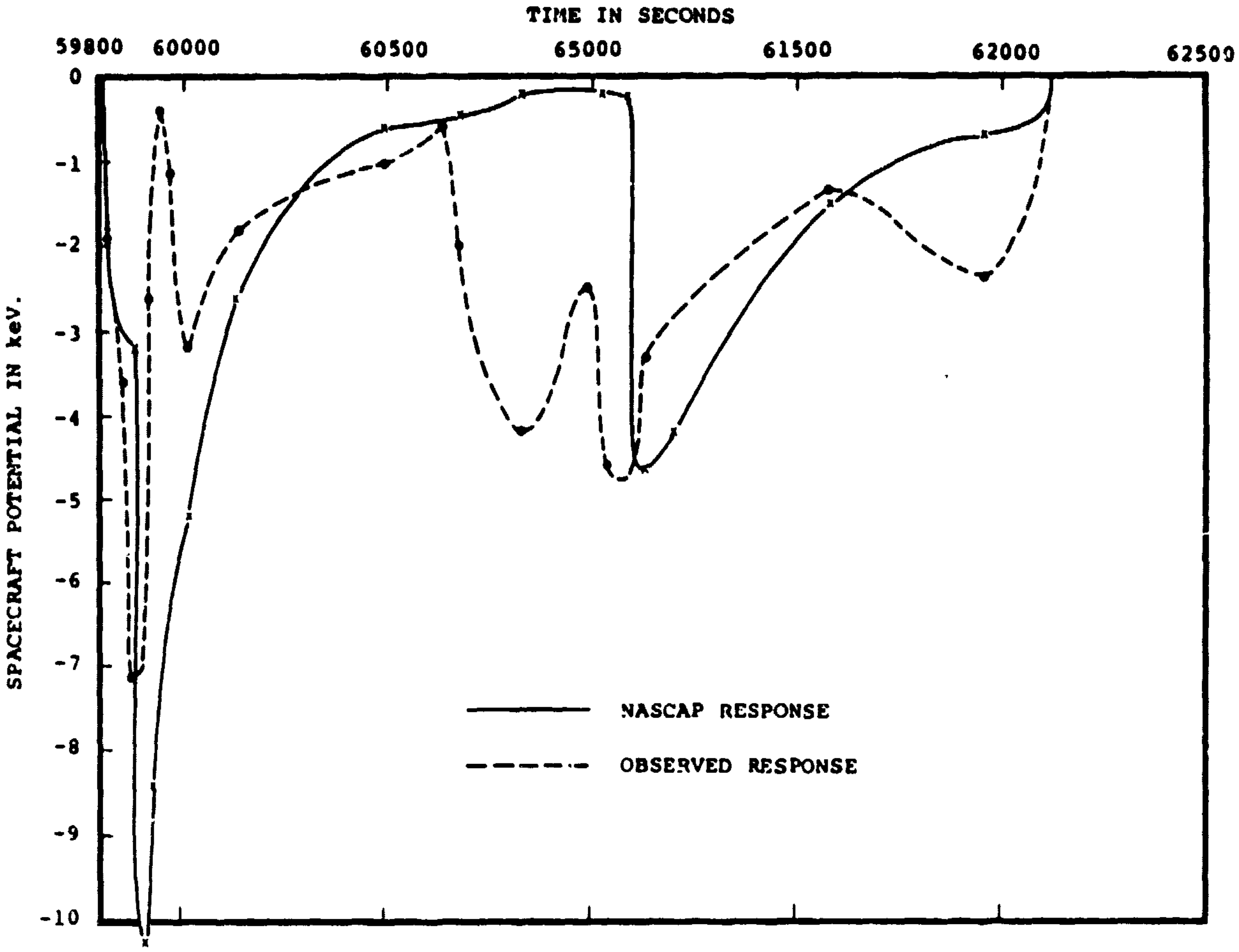

Figure 6.1. NASCAP simulated SCATHA charging response for Day 87 eclipse.

ranging from 0.01 to 13 mA, and voltages ranging from 0.3 to 3.0 keV. Such a beam is not heavily space charge limited: for a 1 kV, 1 mA mode the Child-Langmuir limiting distance is 8 cm, much larger than the beam diameter. However, the escaping beam is significantly spread by its self-field and by the satellite field. Electrons returning to the vehicle do so after excursions large compared to the satellite radius, and the beam returns isotropically to a first approximation.

The relative magnitude of the important charging currents is illustrated in Table 6.1. Since the escape of photoelectrons from the vehicle will be effectively prevented as soon as the ground charges positively, the range of currents available should be sufficient to charge the vehicle to the beam potential in all except perhaps the 0.01 mA case. Observations of the actual vehicle potential, as monitored by SC10, confirm this prediction.

TABLE 6.1. SATELLITE ENVIRONMENT

PHOTOCURRENT

$J_{PH} \sim 2 \text{ nA/cm}^2$

AMBIENT THERMAL ELECTRON CURRENT

$J_{TH} \sim 0.1 \text{ nA/cm}^2 \ (\theta_E = 1 \text{ keV}, n_e = 1 \text{ cm}^{-3})$

RETURNING BEAM CURRENT

$A_{SAT} \sim 20 \text{ m}^2$

I_{BEAM}	.01	0.1	1.0	6.0	mA
J_{BEAM}	.05	0.5	5.0	30.0	nA/cm^2

The observation that beam currents of 0.1 mA suffice to control the satellite ground place limits on the magnitude of any low energy electron component in the ambient plasma. As the satellite charges positively, the collected low energy electron current density for a Maxwellian distribution is given by

$$J_{low} = J_o \left(1 + \frac{V}{\theta}\right) \stackrel{\sim}{=} ne \left(\frac{\theta}{2\pi m}\right)^{1/2} \left(\frac{V}{\theta}\right)$$

$$= 2.7 \times 10^{-12}\, n \left(\frac{V}{\theta^{1/2}}\right) \text{ A/cm}^2 \qquad (6.1)$$

where V is the satellite potential in volts, n the low energy density in cm^{-3} and θ the low energy temperature in eV. For $V = 3$ kV, requiring $J_{low} << 0.5 \times 10^{-9}$ A/cm^2 (see Table 6.1) gives

$$\left(\frac{n}{\theta^{1/2}}\right) << 6 \times 10^{-2} \qquad (6.2)$$

Thus if $n \sim 0.1$ cm^{-3}, $\theta >> 3$ eV, and if $\theta \sim 1$ eV, $n << 0.06$ cm^{-3}. Low energy electron components which violate the inequality in Eq. (6.2) would have prevented the beam current from charging the vehicle to near the beam voltage.

6.2.2 Charging Response of Insulating Surfaces

The surface potential monitors on SCATHA show a complex response to the range of beam currents employed on Pass 89-4. Here we focus on a general description of the response of loosely coupled insulating surfaces — these general considerations will be applied to the specific responses of the SSPM kapton sample and to the SC2 probe responses in Sections 6.2.3 and 6.2.4.

C-2

The net electron flux to an insulating surface is given by

$$J_{NET} = -J_{TH} - J_{BEAM} + J_{SEC} + J_{PH} \quad (6.3)$$

where

J_{TH} = incident ambient flux less backscatter

J_{BEAM} = returning beam flux

J_{SEC} = resulting secondaries (from ambient and beam electrons)

J_{PH} = photoelectron flux

Absolute values are used for the J's with the signs indicating the direction of the charging they induce. The J_{BEAM} term can dominate or be comparable to J_{PH}, as indicated in Table 6.1. Since J_{SEC} and J_{PH} are characterized by temperatures of a few eV, the escape of secondary and photoelectrons is completely controlled by the sign of the surface electric fields. Ion and conductivity currents are small and can be ignored for the purposes of this discussion.

A qualitative picture of secondary electron production must be kept in mind to develop a model of insulating surface response. The typical behavior of secondary electron yield as a function of incident electron energy is illustrated in Figure 6.2. In region I, the surface will tend to charge positively. The extent of positive charging is limited by the suppression of secondary electron escape as the surface field becomes electron attracting. When $E_{KIN} > E_2$, the surface charges negatively until $E_{KIN} = E_2$. The value of E_2 is dependent on the angular distribution of incoming electrons.

The net flux to a surface will be dominated by different terms in Eq. (6.3), depending on both the relative magnitudes of these terms and on the surface electric fields.

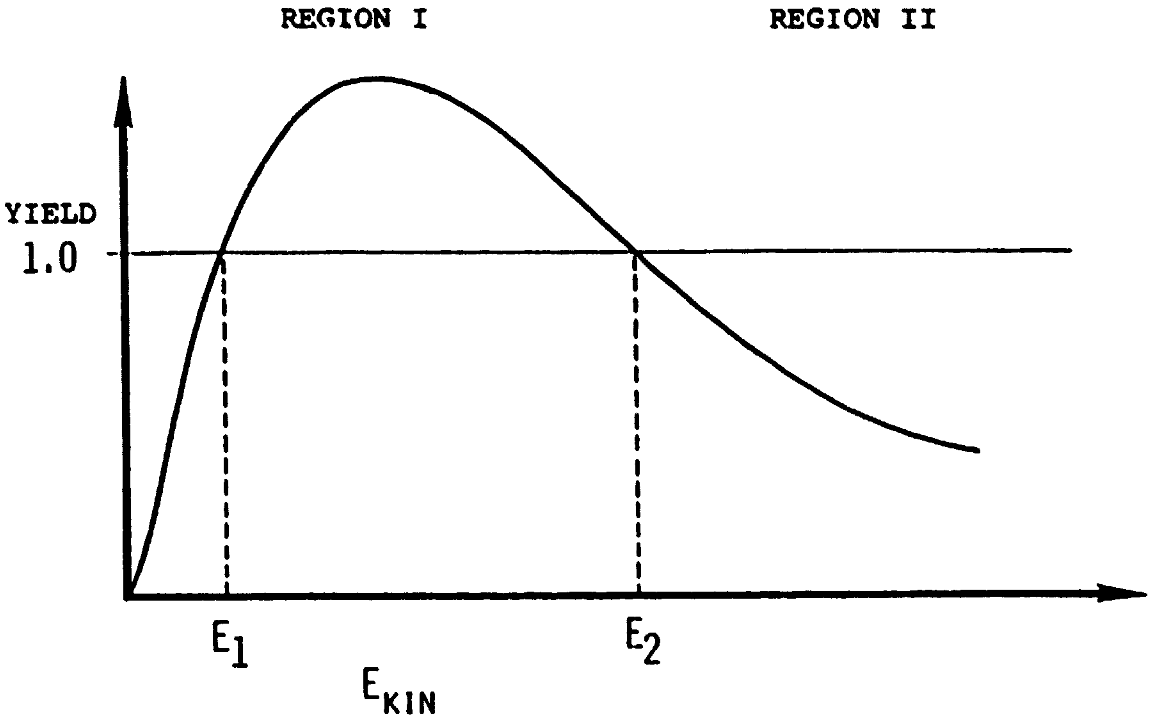

REGION I: POSITIVE CHARGING

REGION II: NEGATIVE CHARGING UNTIL SURFACE POTENTIAL ADJUSTS SO THAT $E_{KIN} = E_2$

Figure 6.2. Effect of incoming electron kinetic energy on secondary emission and charging.

Figure 6.3 illustrates the various possibilities for an insulating surface surrounded by conducting satellite ground. Case I occurs when the satellite and the insulator are charged to the same positive potential, so that surface fields are attracting and secondaries and photoelectrons do not escape. The surface then charges negatively with respect to V_{SAT}. The other extreme case, Case IV, occurs when the surface has charged towards zero enough to reverse the field on the surface and cause escape of low energy electrons. Now the net flux is positive and the surface will tend to charge towards V_{SAT}. Neither Case I nor Case IV represents a stable equilibrium.

Equilibrium can be reached in two different ways, as shown in Cases II and III. If $E_{KIN} < E_2$ <u>or</u> $J_{BEAM} < J_{PH}$, then equilibrium will be reached as enough low energy electrons escape to balance the incident electron currents. Case II represents such an equilibrium situation, where $V < V_{SAT}$ and the surface field is reduced enough to limit the required fraction of low energy electrons, F. As the surface moves in and out of sunlight, J_{PH} will change and the surface potential will move correspondingly to adjust F. Thus oscillations in surface potential with satellite rotation are expected for Case II. If the beam flux dominates J_{PH}, and if $E_{KIN} > E_2$, then limiting of low energy electrons cannot lead to current balance. Instead, as in Case III, the surface potential adjusts until $E_{KIN} = E_2$. Transitions between Case II and Case III are expected when $J_{BEAM} \sim J_{PH}$ and the surface moves in and out of sunlight.

Equilibrium in Case II will be reached when the surface fields are nearly zero, since low energy electrons are totally limited with fields of only a few volts per meter. Thus the equilibrium voltage results from a purely geometric consideration: when does field reversal occur for the insulator neighboring a conductor? A NASCAP model using a

INSULATING SURFACE POTENTIALS

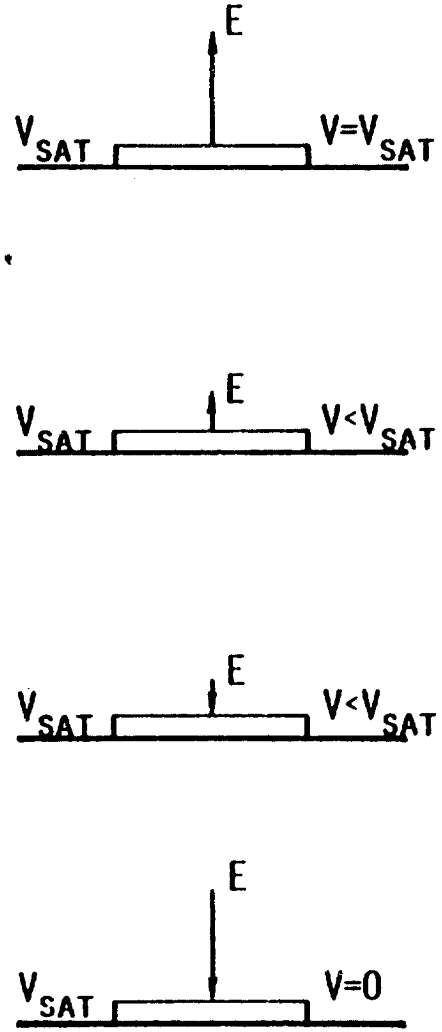

CASE I

$J_{NET} \sim -J_{TH} - J_{BEAM} < 0$

J_{SEC}, J_{PH} TOTALLY LIMITED

CASE II

$J_{NET} = 0 \simeq -J_{TH} - J_{BEAM} + F(J_{SEC} + J_{PH})$

EITHER $J_{BEAM} < J_{PH}$ OR $E_{KIN} < E_2$

CASE III

$J_{NET} = 0 = -J_{BEAM} + J_{SEC}$

BEAM CURRENT DOMINATES

$J_{BEAM} >> J_{TH}$, J_{PH} AND $E_{KIN} > E_2$

CASE IV

$J_{NET} = -J_{TH} - J_{BEAM} + J_{SEC} + J_{PH} > 0$

ALL LOW ENERGY ELECTRONS ESCAPE

Figure 6.3. Current collection by an insulator backed by a conductor.

30 cm rectangular insulating region on a conducting plate charged to 3000 volts predicted this reversal to occur at 500 volts differential. However, it is impossible to obtain sufficient resolution using NASCAP to correctly resolve the sharp gradient in charge distribution near the metal/insulator interface. A model problem is illustrated in Figure 6.4 which can be solved approximately to evaluate the field reversal potential. For a conducting annular ring with inner and outer radius A and B respectively, field reversal occurs when the differential potential at the center, ΔV, is bounded by

$$\frac{V_{SAT}}{3}\left(\frac{A}{B}\right) < \Delta V < \frac{2V_{SAT}}{3}\left(\frac{A}{B}\right) \tag{6.4}$$

For a 30 cm insulator on a 1 m radius satellite, we find $150 < \Delta V < 300$ volts.

6.2.3 SSPM Response

In this section we discuss the response of the large kapton sample during pass 89-4. This sample exhibited both the largest range and the most consistent pattern of charging responses during the gun operations.

For all but two modes in sunlight, the kapton surface stayed within 100 volts of spacecraft ground. These are all examples of equilibrium occurring by the Case II mechanism described above.

When the beam energy was 3 kV, then the returning beam electrons had greater kinetic energy than the second crossover for their angular distribution. This made the large kapton sample charge substantially negative with respect to spacecraft ground when the beam current density was greater than the photocurrent density. Such was the case for 3 keV 6 mA beam in sunlight and the 3 keV 0.1 mA beam in eclipse.

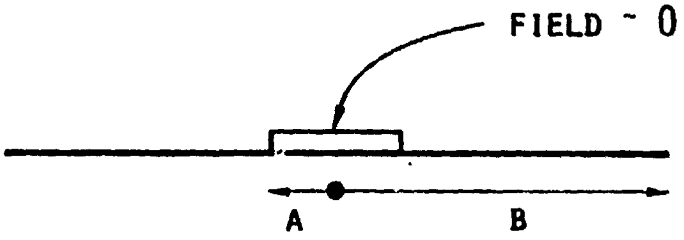

$$\frac{V_{SAT}}{3}\left(\frac{A}{B}\right) < V < \frac{2V_{SAT}}{3}\left(\frac{A}{B}\right)$$

Figure 6.4. Field reversal for an insulator and conductor featuring an annular ring.

SSPM voltage profiles for these two examples are shown in Figures 6.5 and 6.6. Note the absence of spin period fluctuations in 6 mA example but their presence, albeit weak, for the 0.1 mA case. The origin of these fluctuations is in magnetic field effects on the longer beam excursions in the low current case (see Chapter 7).

The validity of this surface electric field determining current balance model is shown dramatically when the electron beam was run in the 3 keV 0.1 mA mode while the satellite was in sunlight. In this case when the sample is exposed to the sun, the photocurrent is much greater than the returning beam current, causing the current balance to be reached as in Case II, with the surface nearly at spacecraft ground. However, as the sample rotates into shadow, the photocurrent disappears and the sample is in a charging beam environment and responds accordingly. This strongly spin modulated charging is shown in Figure 6.7.

Not only can one see sunlight effects for the 3 keV charging modes, but there is substantial spin modulation in the 1.5 keV 0.1 mA and 1.0 mA modes. This is shown in Figure 6.8. While the precise mechanism for this modulation is not known, two features of the voltage profile are important. First, the sample never charges more than 100 volts negative with respect to spacecraft ground. This indicates that the beam energy is near or below the second crossover, E_2, and the sample behaves as in Case II. The second, and extremely important feature, is that the response is independent of beam current, indicating that purely geometrical effects determine the electric field structure. This is common to the Case II responses; that is, the voltage is not very sensitive to beam parameters.

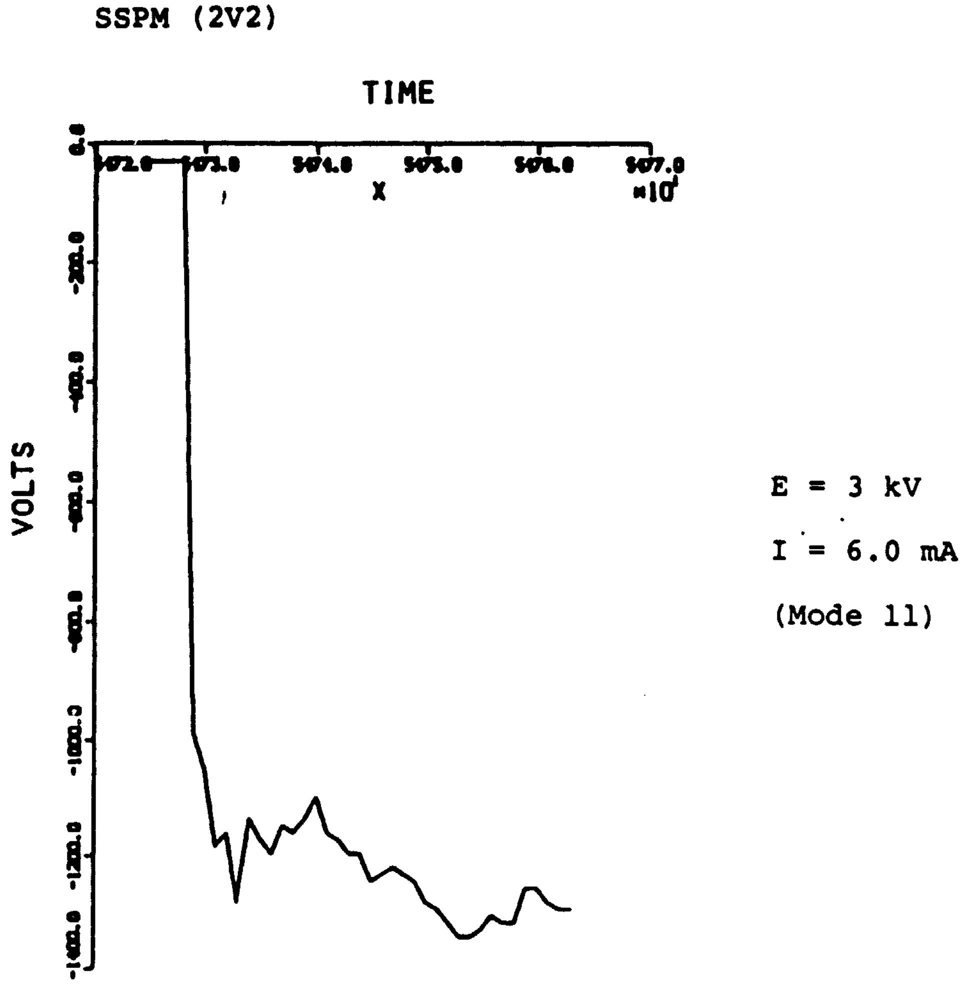

Figure 6.5. SSPM voltage for 3 kV 6 mA beam in sunlight.

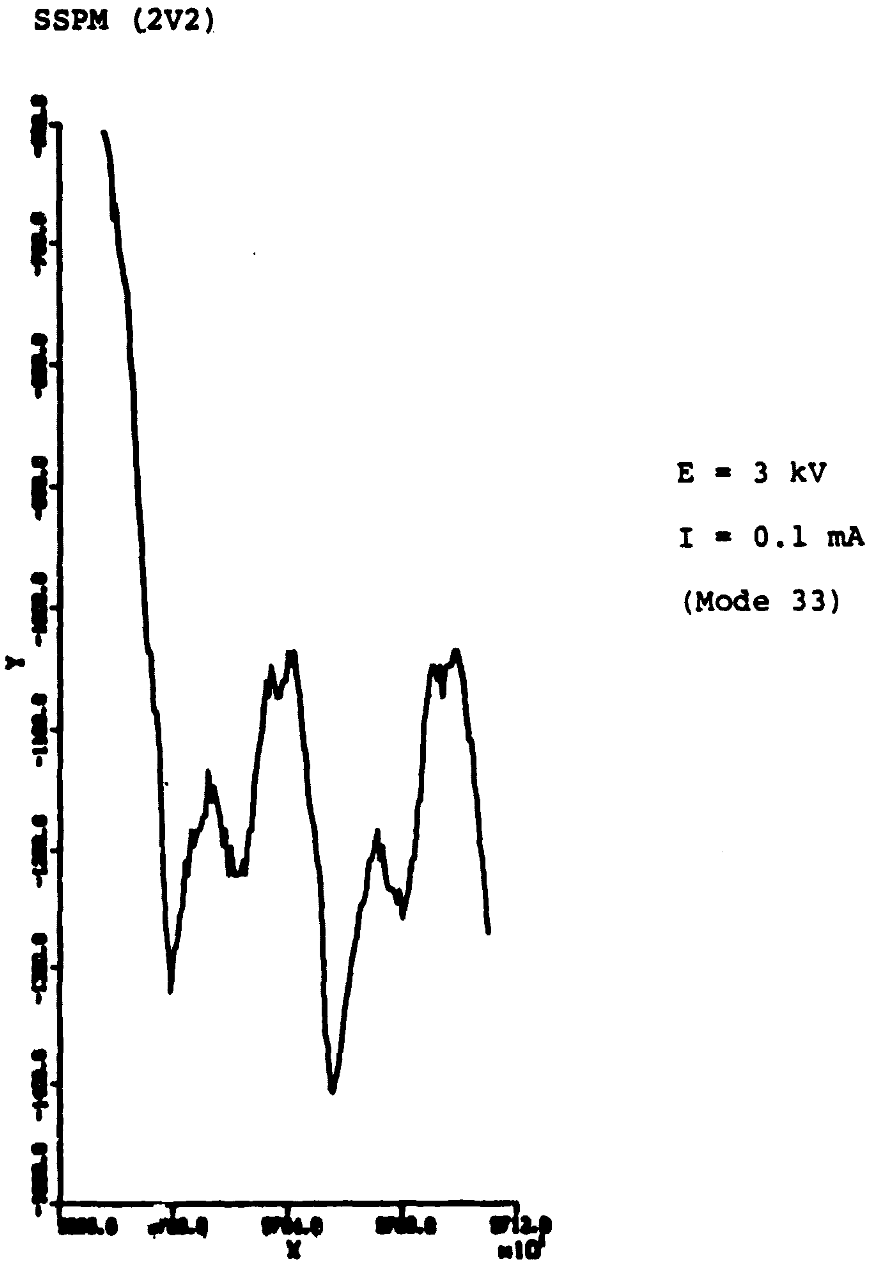

Figure 6.6. SSPM voltage for 3 kV 0.1 mA beam in eclipse.

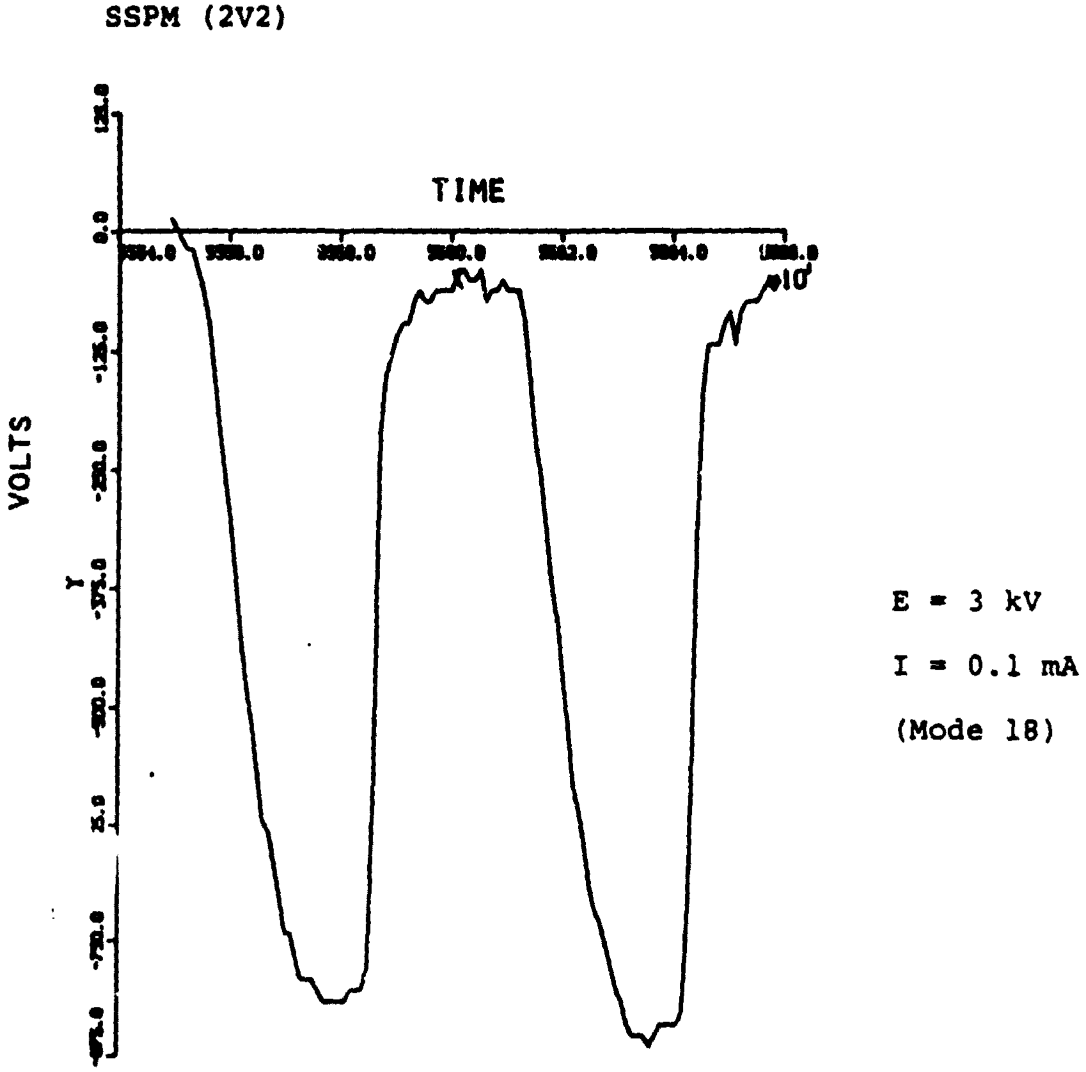

Figure 6.7. SSPM voltage for 3 kV 0.1 mA beam in sunlight.

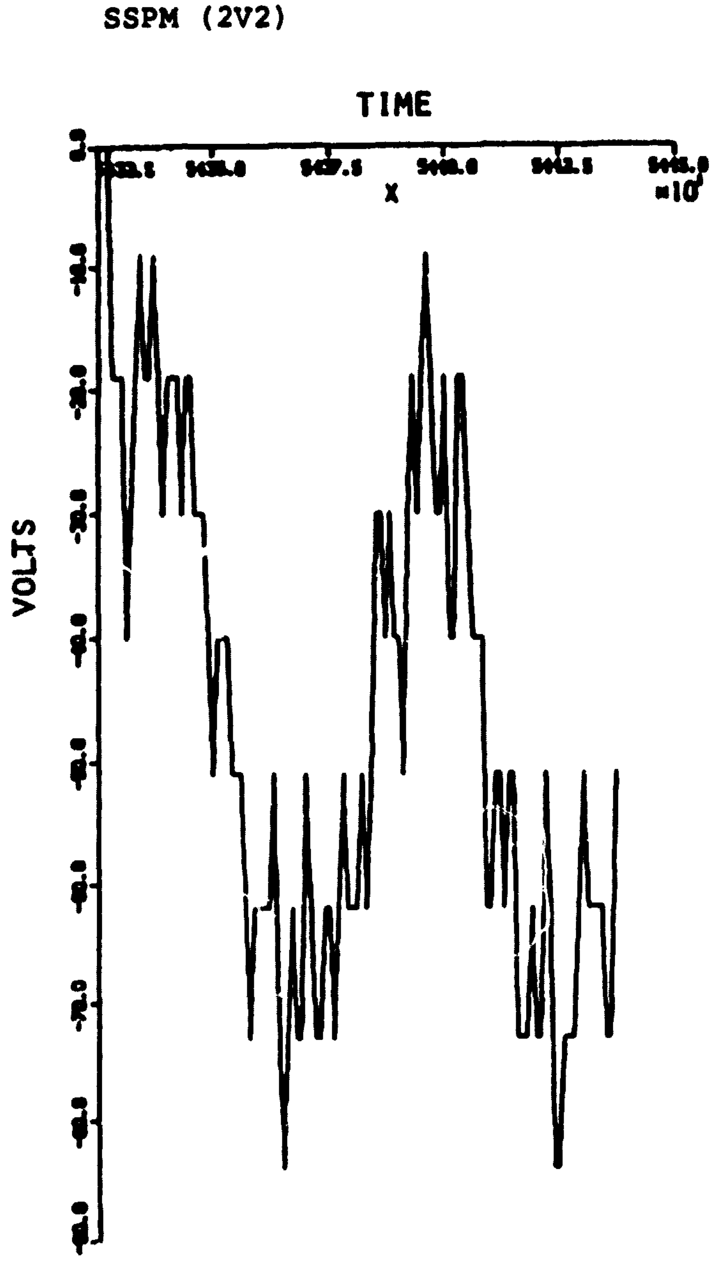

E = 1.5 kV

I = 0.1, 1.0 mA

(Modes 5, 6)

Figure 6.8. SSPM voltage for 1.5 kV 0.1, 1.0 mA beam in sunlight.

6.2.4 SC2 Response

The response of the SC2-1 and SC2-2 probes to the electron beam operations are shown in Figures 6.9 and 6.10. The plots stop at the failure during the first 3 keV 6 mA gun operation. Certain features stand out dramatically. First is the similarity of the response with beam energies of 0.5 and 1.5 keV for all beam currents. In all these cases the spheres were $\sim$350 V negative relative to the spacecraft. Indeed there is less than 40 volts total spread for modes 5, 6, 7, and 8 observed on SC2-2. This agrees well with a field limited behavior as described in Case II, where the potentials are determined by geometrical field effects. The 300 volt beam, of course, could not produce a greater than 300 volt differential.

When the 3 keV 6 mA mode came on we see that the SC2-2 charged rapidly 100 volts more negative, then started to drift further negative at a rate of about 20 volts per second. This type of behavior is typical of differential induced charging: that is, where the development of differential charging produced saddle point inhibits secondary electrons from escaping a surface which would normally be in equilibrium, and as a result the surface slowly charges more negatively. This is shown in Figure 6.11. (The sudden zero potential reading is due to a data dropout.)

Certain features of the data are not well understood. In particular the magnitude of the shadow pulse for the 300 eV gun operation is dramatically large compared to the magnitude at other times. One possible explanation is that the 100 volt incident electrons may be near or below E_1 and as such do not dominate the dark current collection. Thus the spheres respond to the weak ambient environment as opposed to the electron beam. This is an area which needs to be studied further.

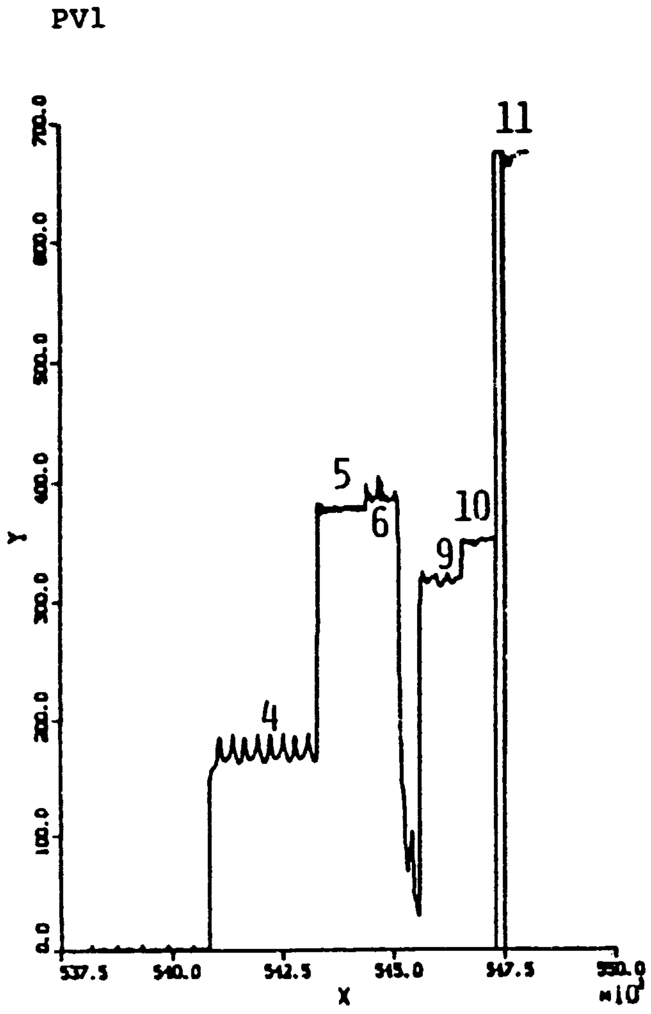

MODE	E (kV)	I (mA)
4	0.3	0.1
5	1.5	0.1
6	1.5	1.0
9	0.5	1.0
10	0.5	6.0
11	3.0	6.0

Figure 6.9. SC2-1 response to beam operations.

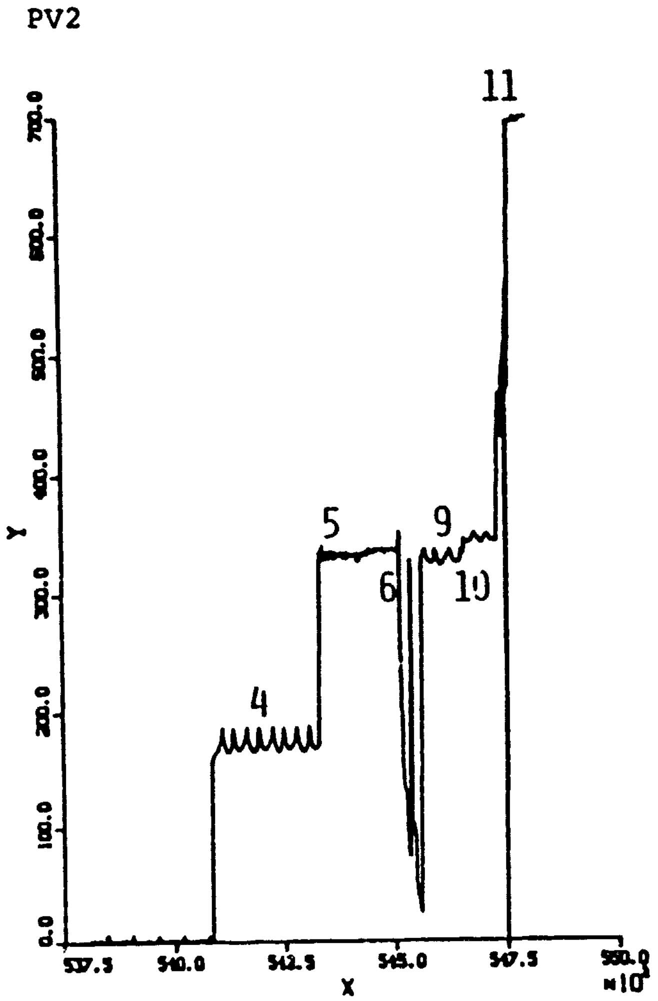

MODE	E (kV)	I (mA)
4	0.3	0.1
5	1.5	0.1
6	1.5	1.0
9	0.5	1.0
10	0.5	6.0
11	3.0	6.0

Figure 6.10. SC2-2 response to beam operations.

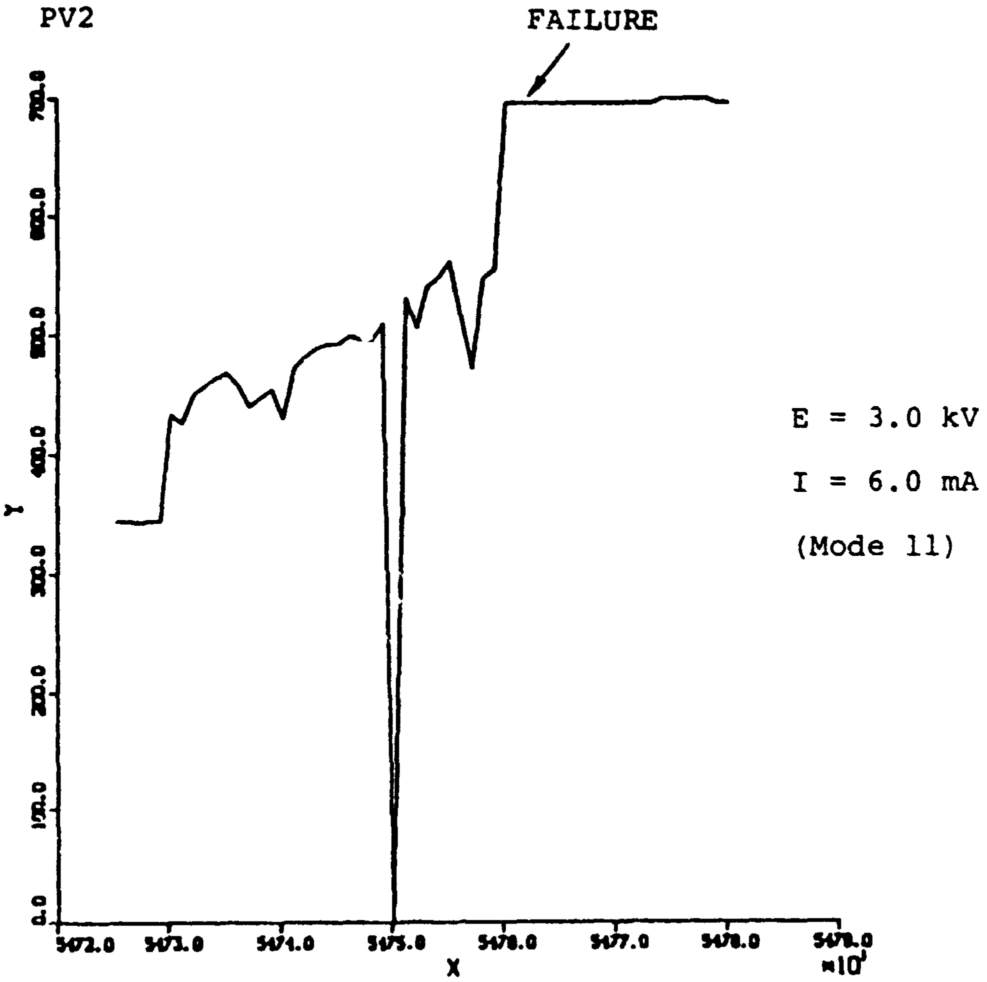

Figure 6.11. PV2 response during beam operations.

6.2.5 Speculation About the SC-2 Failures

From the SSPM response it is clear that the 3 keV 6 mA beam was sufficient to charge kapton to about 1500 volts negative with respect to satellite ground. Since the booms were kapton covered and the spheres were observed at no more than 500 volts negative, there probably was a 1000 volt differential between the booms and the spheres. Consequently, albeit a lower differential than associated with surface discharges in the laboratory, a kilovolt differential with the appropriate polarity to inject electrons onto the spheres existed just prior to their failure. The role of sunlight in triggering such a discharge is not apparent, but the conclusion that differential charging induced discharges led to the SC2 failures seems warranted.

7. ACTIVE CONTROL SIMULATIONS

The SCATHA spacecraft includes two experiments designed to achieve active control of the vehicle potential: the SC4-1 electron gun and the SC4-2 ion gun. In consultation with the SC4 experimental team at the Air Force Geophysics Laboratory, specific features of the beam operations observed during flight testing were identified as of special interest, and simulations were performed to elucidate the nature of these operations. Sections 7.1 and 7.2 provide estimates of the current-voltage characteristics for the SC4-1 electron gun, and also assesses the expected magnitude and characteristics of the expected return currents. Section 7.3 presents an analysis of the observed inability of the electron gun to completely discharge the vehicle during a natural charging event. Analysis of the operation of the ion gun is complicated by the fact that the gun operates in a regime wherein the emission is highly space charge limited. The current version of NASCAP does not include such effects. A simple model of the operation of the ion gun is presented in Section 7.4.

7.1 SIMULATION OF SCATHA ELECTRON GUN OPERATION

The electron gun on board SCATHA operates in a regime of low current and moderately high voltage. By this we mean that the one-dimensional Child's law limiting distance is large compared to the beam radius. Since the beam radius is only 0.5 cm, the beam dynamics are multi-dimensional as demonstrated by the 1-D limiting distance in Table 7.1. Unfortunately, the deviations from one-dimensional behavior make any direct analysis intractable. Simulations of the beam electrostatic self interactions have shown that the deviation from one-dimensional behavior is dramatic, and cannot be treated in a perturbative fashion. Indeed, since the self forces expand the beam quite rapidly, any similarity to

TABLE 7.1. ELECTRON BEAM PARAMETERS AND CORRESPONDING 1-D CHILD'S LAW LIMITING DISTANCE

V (volts)	I (mA)	1-D Limiting Distance (cm)
3000	6.0	8
	0.1	60
	0.01	100
1500	12.0	3

one-dimensional behavior is rapidly lost even in the most heavily space charge dominated cases.

For the purposes of analyzing satellite response, we must determine certain important features of the beam dynamics. The first is the extent of particle excursions. For all cases some beam particles join the surrounding plasma. However, the variation of satellite potential with beam current indicates that, for the higher beam currents, nearly all the beam electrons return to the satellite. The data presented in Table 7.2 indicates that the ambient plasma current collected by the satellite when charged to +3000 volts cannot be larger than 0.1 ma. Thus, for the 6 ma beam, over 5.9 ma must return to the satellite. The typical orbit length and excursion time is necessary to estimate magnetic field effects and returning beam current density. The mean orbit length is determined primarily by the self space charge of the beam for all but the lowest currents, where magnetic field effects are important.

Equally as important, but far more difficult to predict, is the returning beam density and angular distribution as a function of position on the spacecraft. When integrated with material surface response functions, this would enable a three-dimensional charging analyzer program (e.g., NASCAP) to predict the satellite surface potentials. What makes this

TABLE 7.2. SATELLITE POTENTIAL AS A FUNCTION OF CURRENT FOR 3 keV ELECTRON BEAM

I (ma)	V_{sat}
0.01	0
0.1	3000
6.0	3000

difficult is not any subtle nuances of the physics; everything can, in principle, be determined using the Lorentz force and Poisson's equation. However, even for the 1.5 keV, 13 ma beam, the excursions are more than an order of magnitude larger than the satellite. Thus, the calculation of the self-consistent charge densities and particle orbits with sufficient accuracy to predict current variations along the surface is a substantial numerical problem. For the longer length orbit, in particular for the 3 keV, 6 ma case, the problem is simply intractable by straightforward simulation.

In order to estimate particle orbits, we have developed a very simple model which accounts for self space charge in a perturbative fashion. The model, which is described in detail below, becomes more accurate for larger orbits. To demonstrate its validity, we have compared it with a two-dimensional simulation of a 1.5 keV, 13 ma beam emitted normally from a 1.8 meter radius sphere. (The sphere size was chosen to approximate the capacitance of the SCATHA spacecraft.)

7.1.1 Simulation of the 1.5 keV, 12 ma Electron Gun

The 2-D simulation was done using a finite element Poisson's code in conjunction with time-dependent particle pushing. The satellite potential was fixed at 1.5 keV. The mesh outer boundary was at 21.8 meter radius and the boundary potential was fixed at zero. While the sensitivity of the calculations to the boundary location was not examined, the fact that most trajectories were well within the mesh suggest the boundary location was acceptable. The computational mesh is shown in Figure 7.1. The calculation was started with no space charge in the mesh. As particles were emitted, they rapidly developed a space charge field across the beam which spread the beam dramatically. This is shown in Figure 7.2. The slow electrons at the beam head further enhanced this spreading, leading to a major accumulation of space charge 10 meters out from the satellite. Figure 7.3 shows a superposition of all the orbits for t = 0 to 10 μsec. Figure 7.4 shows the electrostatic potentials at that time.

Although the actual space charge barriers oscillate, the calculation was stopped at 15 μsec and a single set of representative orbits were calculated. These are shown in Figure 7.5. They consist of several trajectories corresponding to different initial positions across the beam width. (Since the calculations were performed in R-Z geometry without angular momentum about the Z axis, particles could cross the Z axis. When this occurs, they appear to be reflected from the axis, since a position (-r,z,0°) is equivalent to (+r,z,180°) and thus $(-r,z) \rightarrow (r,z)$ in the R-Z code.) Several important features are seen from those trajectories. First, the beam spreads farther than it propagates. This implies that the self-expansion forces are dominant in determining beam dynamics. Secondly, the particles all miss the sphere on the first orbit. Two-thirds of the beam finally hit the sphere after an orbit of ∿450° and ∿12 μsec. The remaining third appeared to be in a far longer orbit. This implies that single pass theories will overestimate the extent of excursions. Since only about one percent of the beam can actually escape, the potentials and orbits presented here have substantial uncertainties and are, at best, qualitative in nature. To provide more accurate results would require exorbitant amounts of computer time.

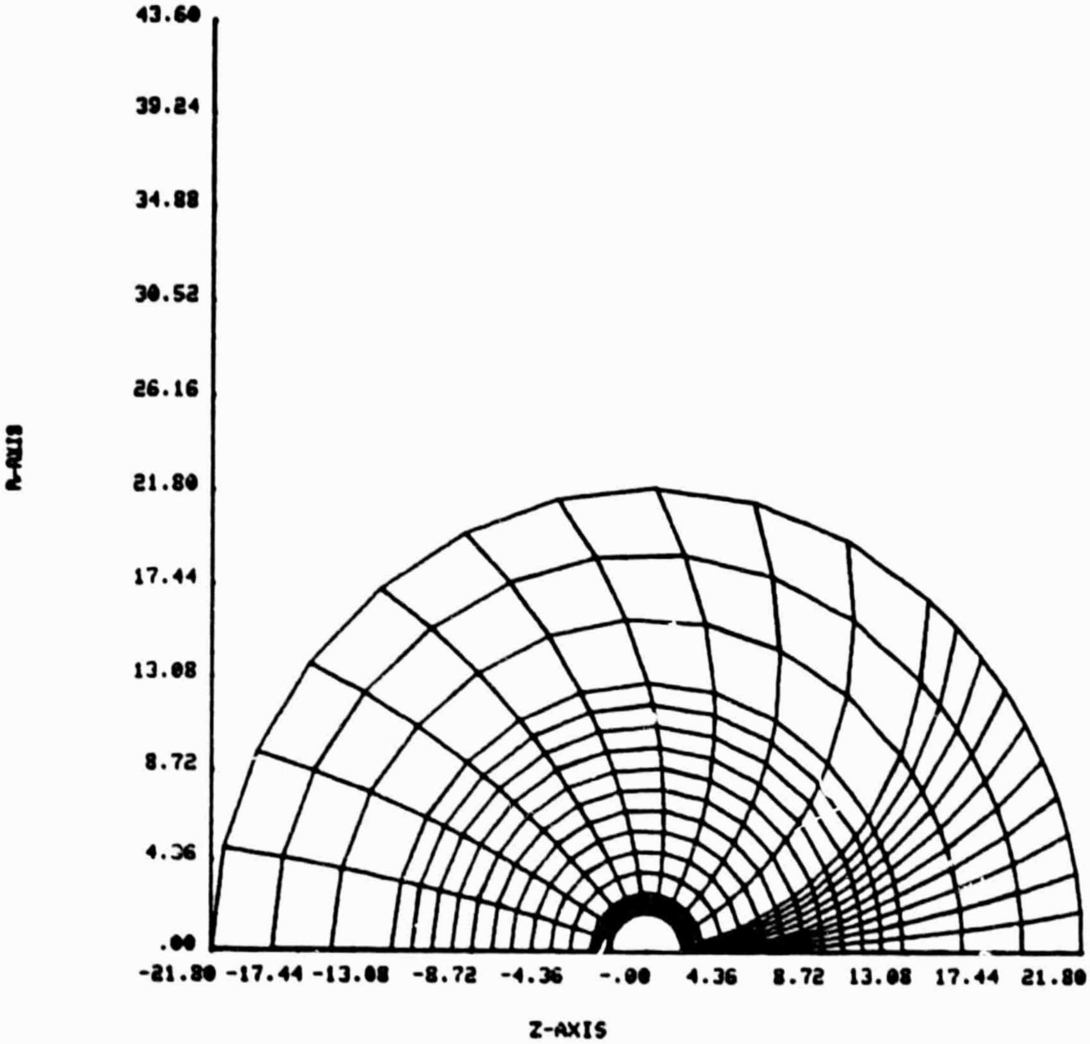

Figure 7.1. Computational mesh for 2-D (R-Z) simulation of 1500 eV, 13 ma electron beam.

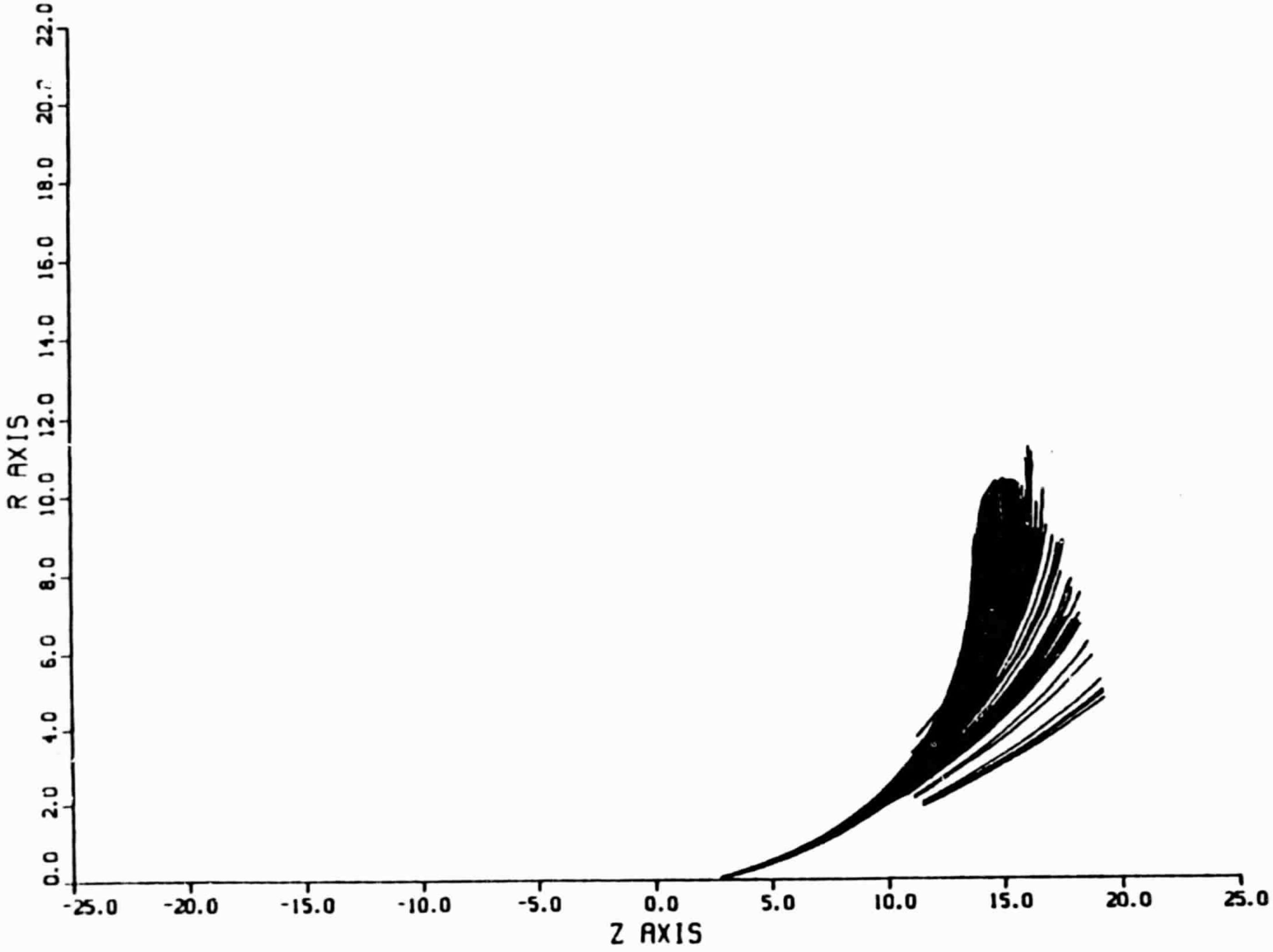

Figure 7.2. Initial spread of 1500 eV, 13 ma electron beam.

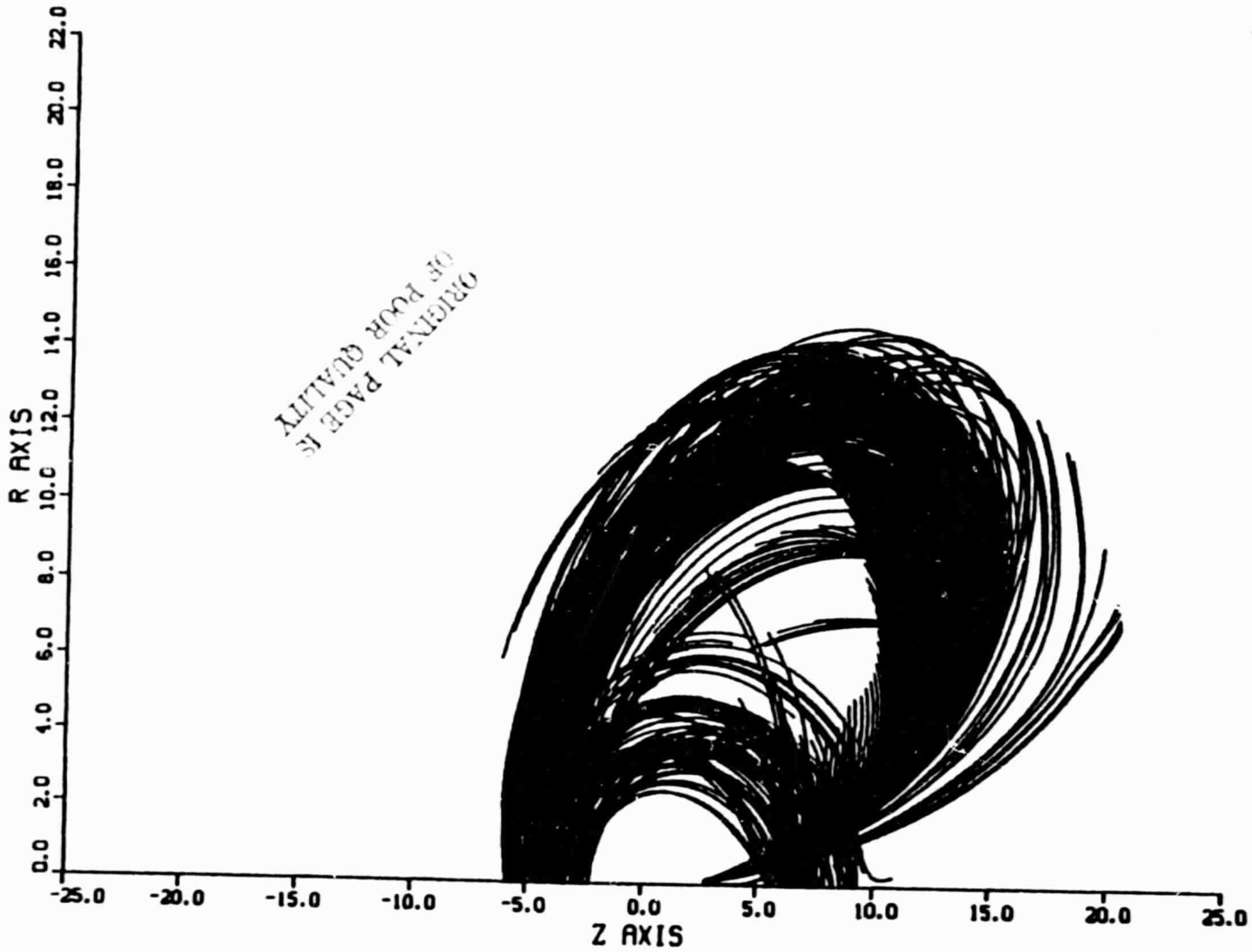

Figure 7.3. Superposition of electron trajectories for 1500 eV, 13 ma electron beam, 0-10 μsec.

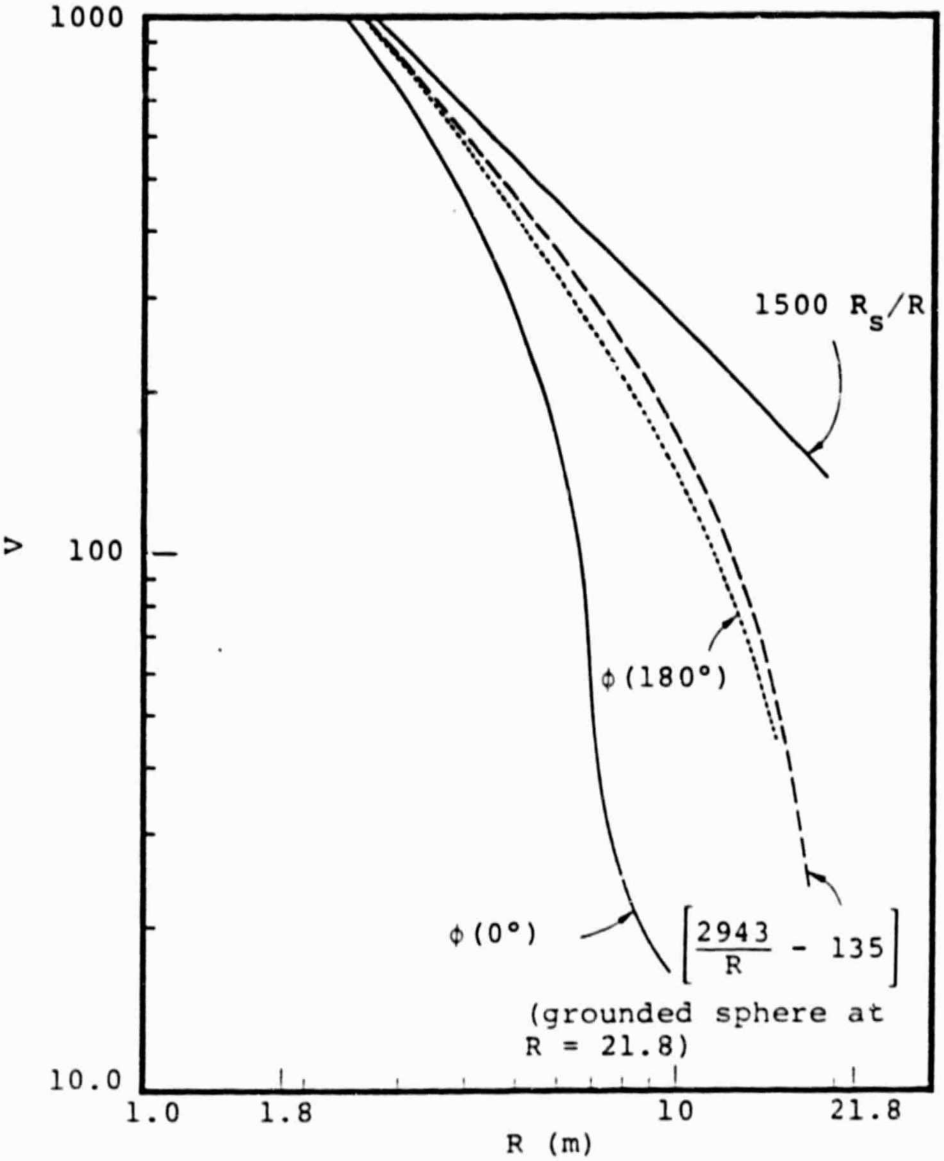

Figure 7.4. Electrostatic potentials after ∿10 μsec of gun operations at 13 ma, 1500 eV. Shown are (A) Coulomb potential (upper solid curve); (B) Laplace potential between 1.8 m and 21.8 m spheres (dashed curve); (C) potential opposite the beam direction (dotted curve); and (D) potential in the beam direction (lower solid curve). The "space charge barrier," defined as the maximum difference between (B) and (D), is ∿240 volts at a radius of ∿7 meters.

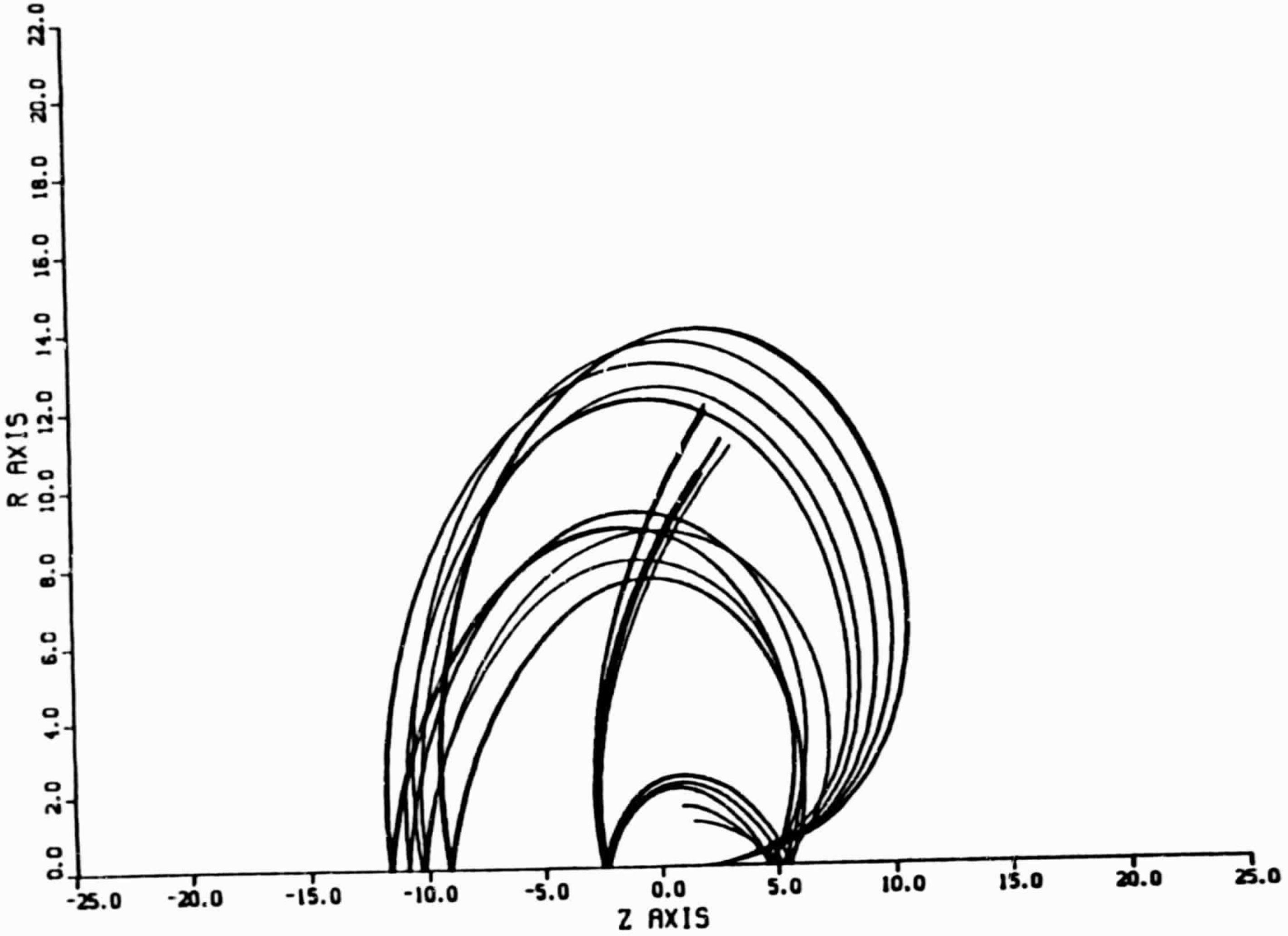

Figure 7.5. Electron trajectories in the potential of Figure 7.4.

7.1.2 A Perturbative Model

As the beam voltage increases and the current decreases, the numerical difficulties multiply so rapidly that even the simplistic type of calculations presented here become prohibitive.

Thus, we are forced to resort to simpler models of the beam-space charge interactions. From the current densities in the beam, one can see that the strongest forces in the system are the 1/r field from the sphere, and the beam expansion forces. From Gauss's law these can be seen to be

$$(F_{\exp})_{\max} \simeq \frac{I}{2\pi r V \varepsilon_0} \simeq \frac{12\times 10^{-3}}{\pi\cdot 10^{-2}\; 2.3\times 10^{7}\; 8.8\times 10^{-12}} = 1900 \text{ V/m}$$

$$(F_r)_{\max} \simeq \frac{1500}{1.8} = 800 \text{ volts/meter} .$$

The self-retarding fields can be estimated from the numerical results (Figure 7.4) by taking the maximum potential difference due to the space charge barrier and dividing it by the distance to it:

$$(F_{ret}) \simeq [V\, R_s/R_1 - V_{sc}(R_1)]/R_1$$

$$\simeq \frac{240}{7-1.8} \simeq 45 \text{ volts/meter} .$$

By including the first two forces in the particle dynamics and approximating the effect of the third by decreasing the initial velocity, we have constructed a computational algorithm that successfully estimates the extent of particle orbits. Since the kinetic energy is not returned to the particles as they are deflected from the space charge barrier, the orbits are qualitatively incorrect as these particles return to the vicinity of the sphere. The radial force is estimated via a paraxial theory and is applied only while the particle has substantial velocity in the initial beam direction. From the orbits of the outermost beam particles, the height of the space charge barrier is estimated by integrating the free charge Green's function as if the beam were a uniform disk. The uniform cross-section approximation is valid only during the initial paraxial phase. (Uniform density is a self-similar solution to the paraxial beam expansion problem.) The calculation is performed iteratively until the height of the space charge barrier predicted is equal to the energy initially extracted from the beam. The resultant electron orbit for the 1.5 keV, 12 ma case is shown in Figure 7.6. While not in good agreement as the particle returns to the sphere, the overall orbit extent is quite good. This procedure should improve for higher voltage, lower current beams where

$$F_{1/r} >> F_{exp} >> F_{ret} \quad .$$

The predicted transit time was 8 microseconds. The transit time is important in determining the effect of magnetic fields. For pass 89-4, 1979, the approximate field strength was 100γ or 10^{-3} Gauss. This corresponds to an electron ω_c of

$$\omega_{ce} = \frac{eB}{mc} \simeq 2 \times 10^4 \text{ rad/sec} \ .$$

Consequently, the effect of the magnetic field on the orbits is negligible, $\omega_{ce}\tau \simeq 0.2$ radians at most.

We have applied this model to cases of 3 keV, 6 ma and 3 keV, 0.1 ma electron beams. Resultant orbits are plotted in Figures 7.7 and 7.8. The 6 ma beam was limited by its own space charge some 50 meters from the satellite. The particle transit time is approximately 30 microseconds. For these particles $\omega_{ce}\tau$ is 0.6 radians which is only enough to make

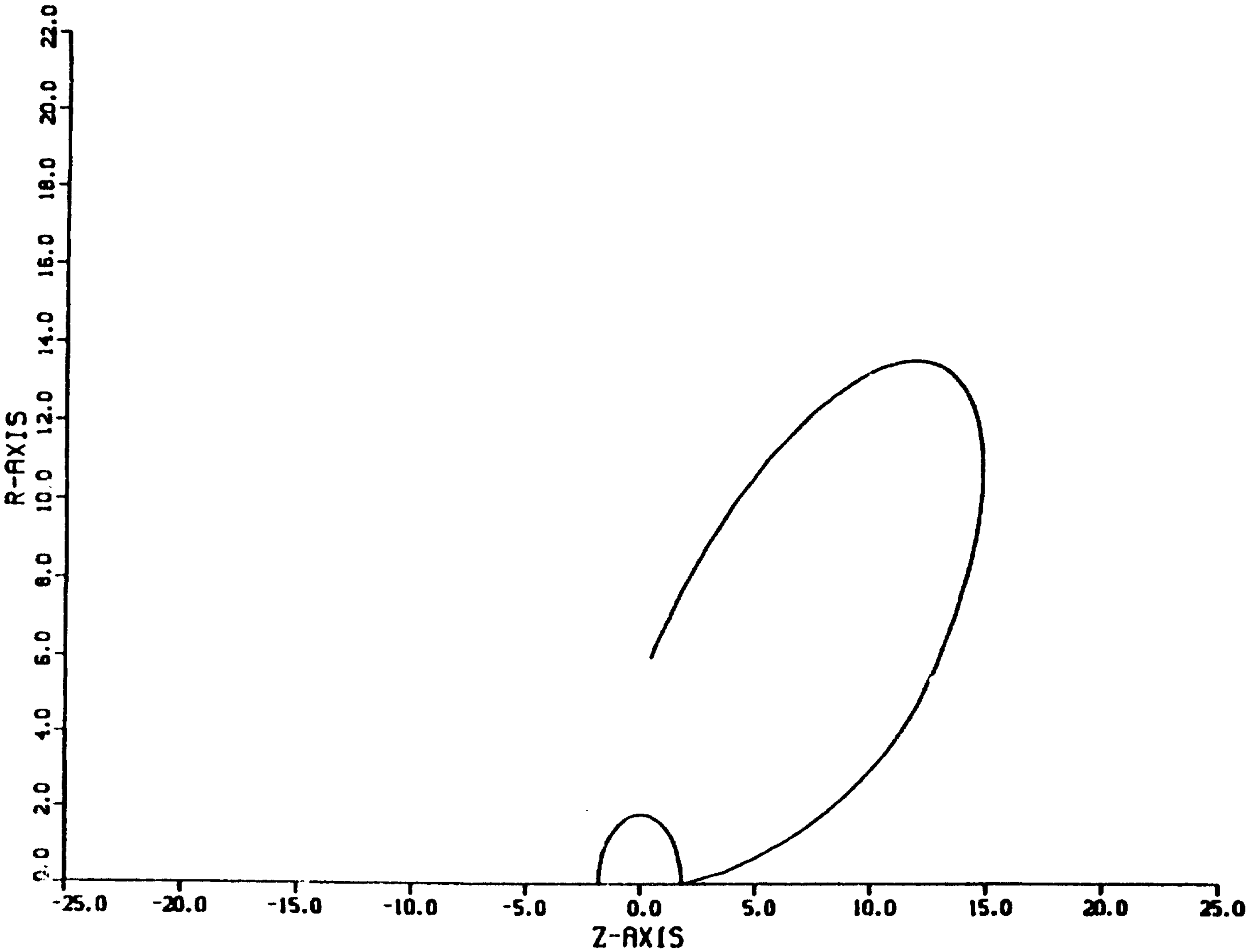

Figure 7.6. Approximate electron orbit for 1500 eV, 12 ma case.

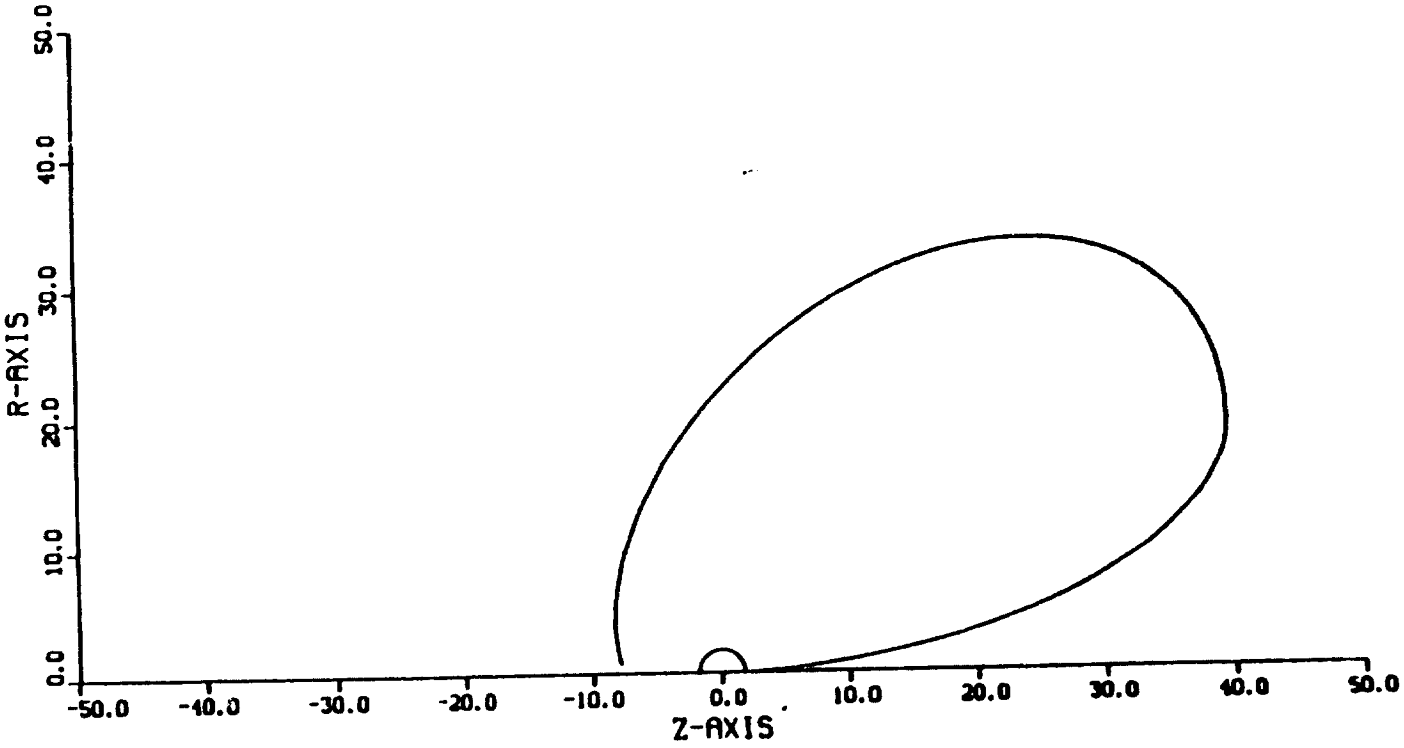

Figure 7.7. Approximate electron trajectories for 3 keV, 6 ma case.

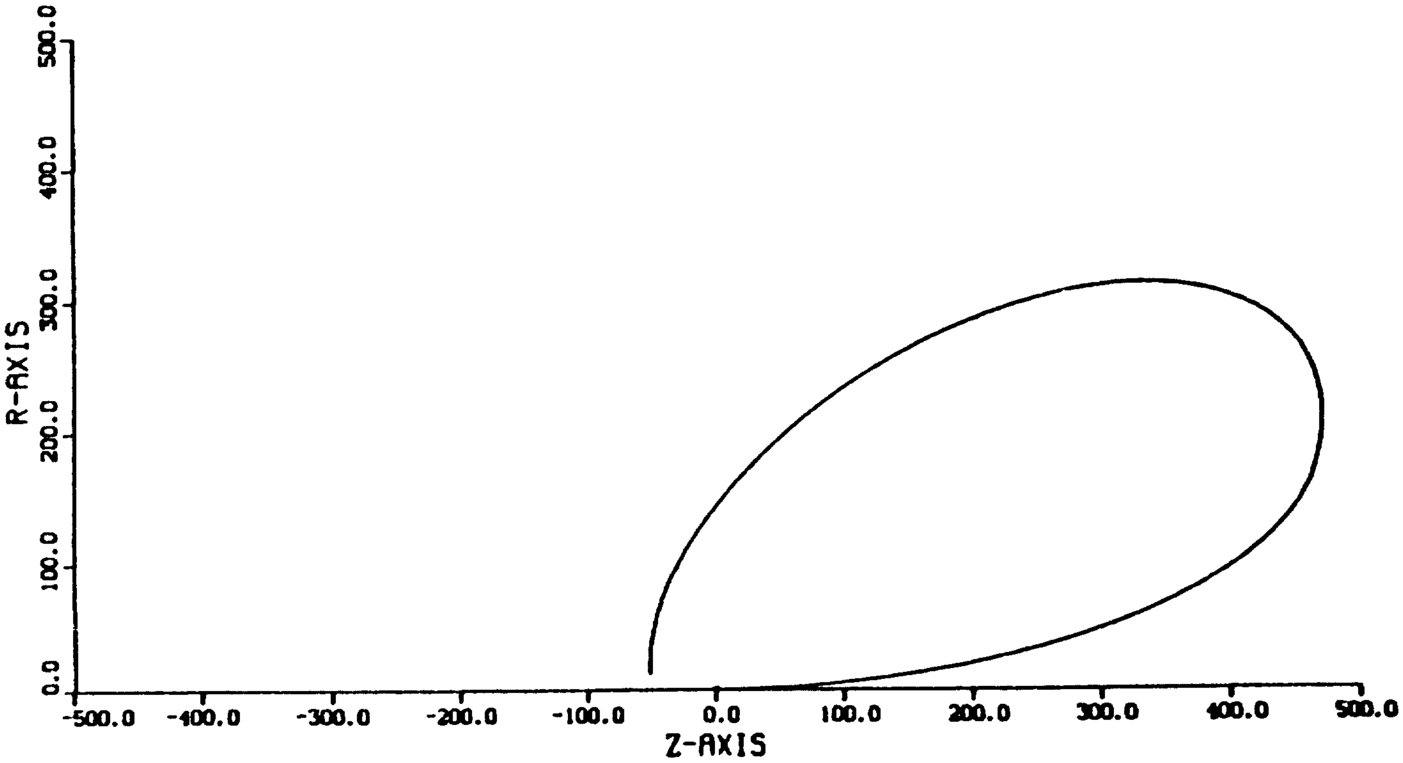

Figure 7.8. Approximate electron trajectories for 3 keV, 0.1 ma case in the absence of a magnetic field.

very small deviations in the orbit. Figure 7.9 shows the trajectories assuming B is normal to the plane of the orbit. The effects are barely discernible. However, for the 0.1 ma beam, the magnetic field dominates. Indeed, in the low current limit the beam is magnetically limited for most orientations. Figure 7.10 shows an example of a magnetically limited orbit.

7.1.3 Conclusions

The computer results suggest that, to a reasonable approximation for all but the lowest current cases, the beam electrons return to the sphere uniformly. If, in addition, we make the further simplification that the outgoing beam is spherically uniform, we can use the Langmuir-Blodgett theory of a spherical diode[23] to make a simple estimate of the excursion distance and time of the beam electrons.

Under the above assumptions, the beam current (approximated as 100 percent returning), beam energy, and travel distance are related by

$$2i = 2.93 \times 10^{-5} V^{3/2} \Big/ (-\alpha)^2$$

where the factor of 2 accounts for the beam's contributing space charge both leaving and returning, and $(-\alpha)^2$ is a function of the ratio of spacecraft radius, r_s, to beam excursion radius, r_B, given tabularly by Langmuir and Blodgett. The mean beam excursion time, Δt, is found by requiring the total beam space charge to equal the spacecraft charge:

$$i\Delta t = 4\pi\varepsilon_o V \left(\frac{1}{R_s} - \frac{1}{R_B}\right)^{-1} .$$

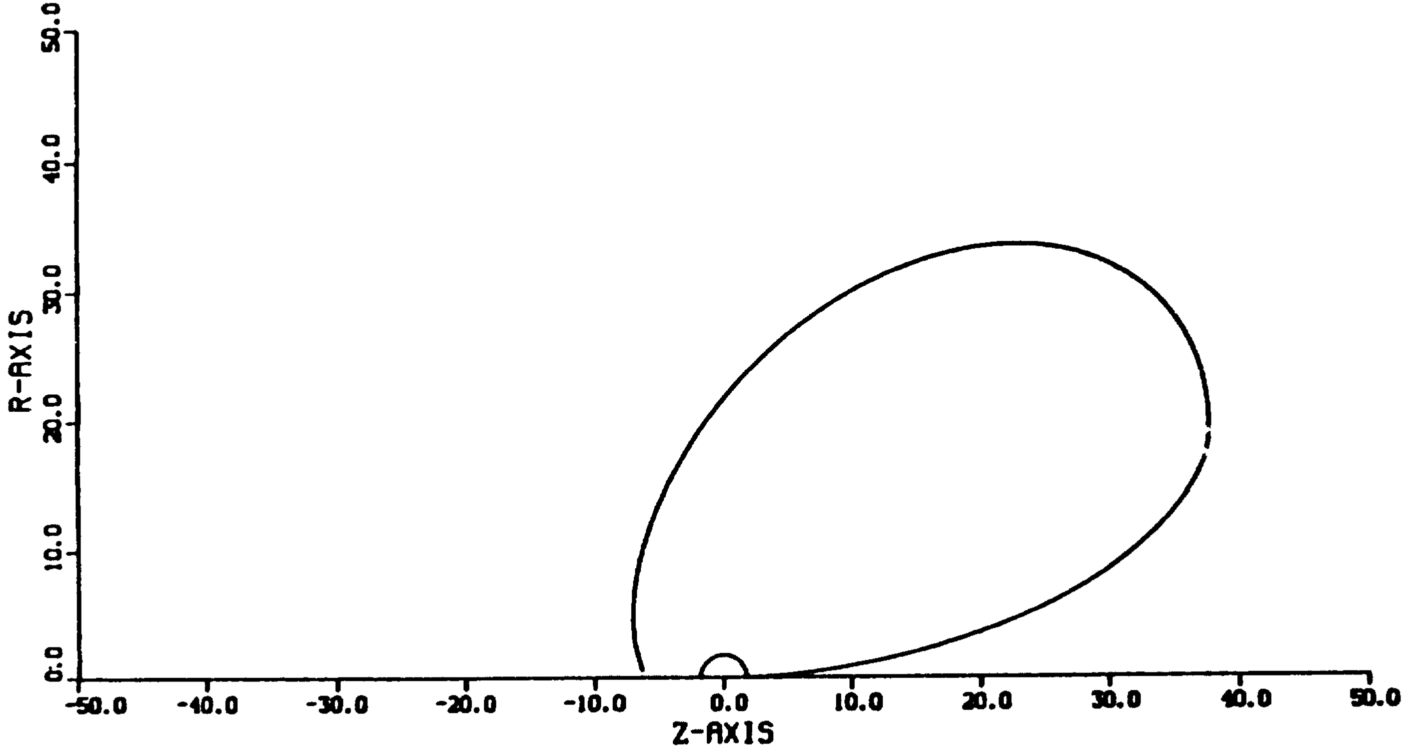

Figure 7.9. Approximate electron trajectories for 3 keV, 6 ma case with magnetic field.

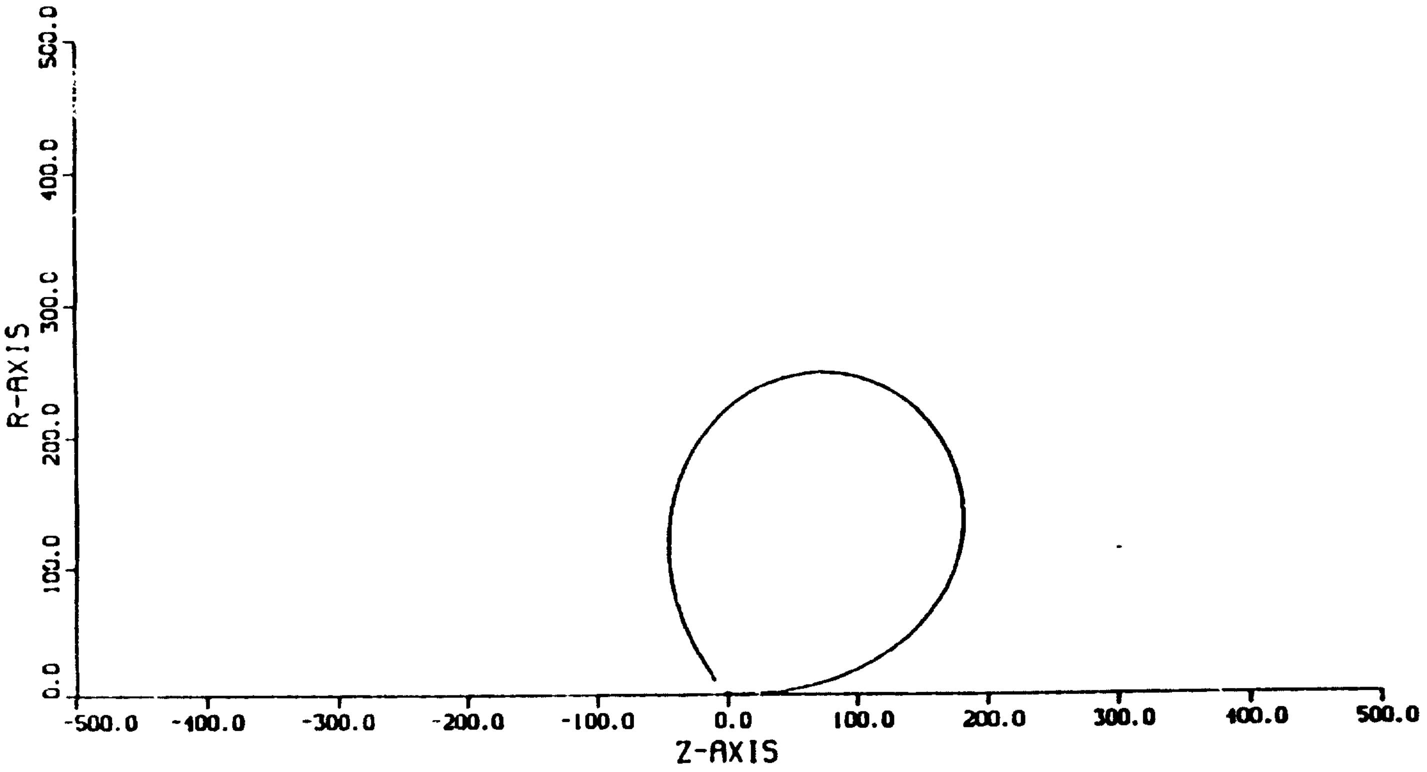

Figure 7.10. Approximate electron trajectories for 3 keV, 0.1 ma case in the presence of a magnetic field.

Table 7.3 presents the excursion distance and time for several cases calculated by all three methods. We see that the perturbative method, described in the previous section, compares quite well with the simulation and should be an excellent estimate for the low current high voltage beams. However, the Langmuir-Blodgett based estimates are good to a factor of two and are a ready method for predicting excursion times.

TABLE 7.3. EXCURSION DISTANCES FROM A CONDUCTING SPHERE CALCULATED VIA SIMULATION, PERTURBATIVELY AND USING THE LANGMUIR-BLODGETT ESTIMATE

V	I(ma)	R_{max} (R-Z) Simulation	R_{max} Perturbation	R_{max} (L-B)	$\Delta t(\mu sec)$
1500	12	17	18	29	25
3000	6		44	90	100
	1			290	600
	.1		540	$\sim$1000	$\sim$6000
300	.1			135	150

Comparing these excursion times to the gyroperiod $2\pi/\omega_c \sim$ 300 μsec, we see that space charge effects dominate magnetic field effects for currents above 1 ma for a 3 kV beam, and currents as low as 0.1 ma for a 300 volt beam. Interestingly, only for the 3 kV, 0.1 ma case were magnetic field effects visible in the SSPM response.

7.2 CURRENT-VOLTAGE CHARACTERISTICS OF THE SCATHA SPACECRAFT

Ambient current levels versus satellite potential have been obtained for a simple SCATHA model. The results are very sensitive to the environmental description employed. Two cases were considered which should bracket the actual environment: (1) a low energy dense plasma, described by single ion and electron Maxwellian distributions with $n_e = n_i = 10 \text{ cm}^{-3}$, $T_e = T_i = 2$ eV; and (2) a high energy plasma, also Maxwellian, with $n_e = n_i = 0.2 \text{ cm}^{-3}$, $T_e = 8$ kV, $T_i = 13$ kV. NASCAP was used to calculate ambient current to the four-grid model of the satellite assuming uniform charging in eclipse. The current versus voltage characteristics are shown in Figure 7.11. The area between the two curves represents the range of possible I-V characteristics expected. As discussed above, when the beam current reaches the level of the ambient current, the satellite potential will be controlled at beam potential and the return current will increase sharply. The curve for the low energy plasma certainly overestimates the ambient current due to the probe model employed for collection. It is therefore encouraging that the beam current available, 1 μA to 13 mA, includes the spectrum of expected I-V characteristics.

The results in Figure 7.11 were obtained for the satellite in eclipse. In sunlight, the ambient current is dominated by photoemission. NASCAP was used to predict the net current in sunlight, and the results vary between 60 μA for a uniformly negatively charged (or discharged) satellite to 18 μA for a differentially charged satellite (with the conductors held negative). Photoemission is of course completely limited when the satellite charges to positive potential.

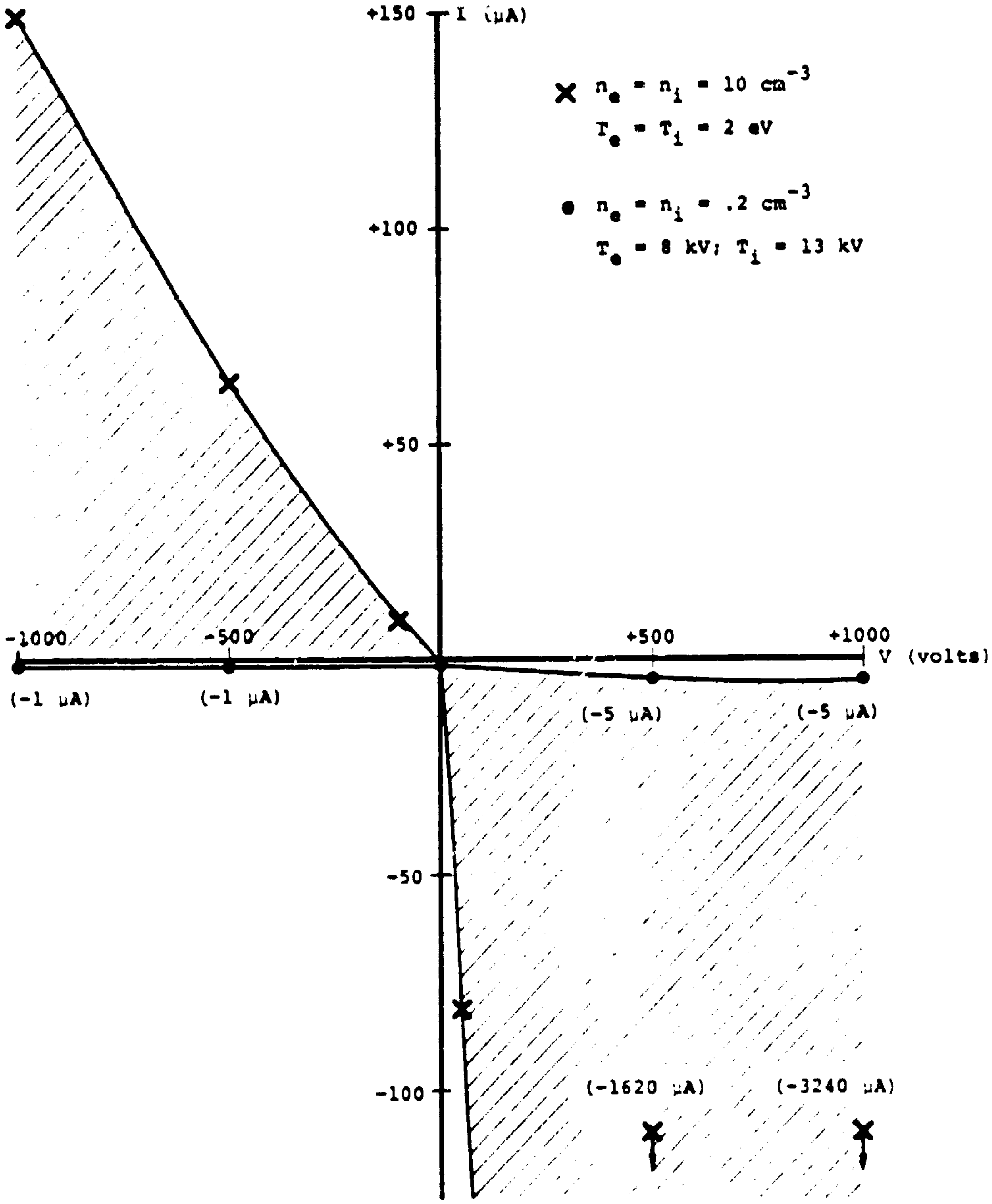

Figure 7.11. Current versus voltage for uniformly charged SCATHA model in eclipse.

7.3 POTENTIAL BARRIER FORMATION ABOVE THE SC4-1 GUN

When SCATHA encountered a magnetospheric substorm which charged the vehicle to -6 kV, an attempt was made to reduce the charging using the SC4-1 electron gun operating at 150 volts and 1 mA. The attempt was only partially successful, in that it was possible to drive the vehicle potential only to -1 kV, but not higher. One reason for the inability of the gun to completely discharge the satellite could be the formation of a potential barrier above the electron gun which would prevent the emitted electrons from escaping. In a strongly charging environment, the ground conductor at -1 kV around the gun aperture will be a region of relatively high potential, so the formation of a barrier is at least plausible. We have used the NASCAP code in an analysis of three questions regarding this hypothesis:

1. Will such a barrier form?
2. How much time is required to form a barrier?
3. Where will the barrier cause returned particles to hit the vehicle?

We began a simulation using the four-grid SCATHA model which had been charged in eclipse using a high temperature double Maxwellian environment described in Chapter 4; the ground potential was -6410 volts. We then fixed the ground conductor to -1000 volts while maintaining any existing differential charging; the resulting potential contours are shown in Figure 7.12. The SC4-1 electron gun is located on a conducting region of the bellyband, so that ejected electrons are emitted at -1 kV less the gun potential. Initially, the external fields above this region are repelling, so that all 150 volt electrons could escape. The exposed dielectrics were well above their equilibrium potentials in this environment since they followed the +5 kV jump in the ground conductor. The ground conductor was then held at -1 kV while the exposed dielectrics and other conductors

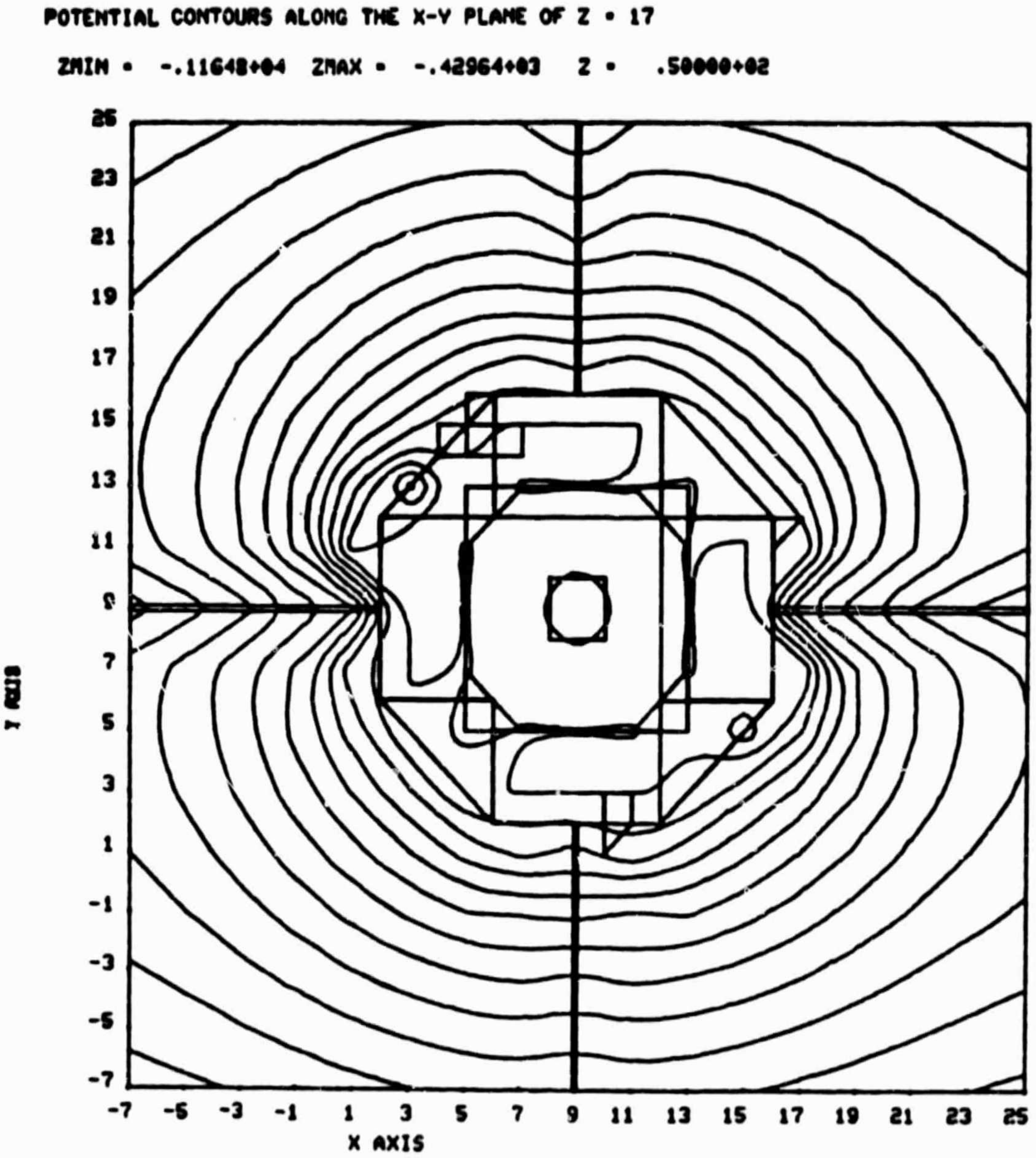

Figure 7.12. Potential contours at beginning of simulation. In Figures 7.12 through 7.19, the SC4-1 gun location is X = 3, Y = 4, Z = 17.

differentially charged. A barrier above the SC4-1 gun then slowly formed, chiefly as a result of the charging of both the neighboring solar cell covers and the booms.

The potential contours after 395 seconds of charging are shown in Figure 7.13, and the associated trajectories of emitted electrons are shown in Figures 7.14 and 7.15. A barrier of approximately 141 volts existed at this stage, enough to deflect the trajectories significantly but not to cause any particles to return. After 415 seconds, the barrier height increased to 144 volts. Now 40 percent of the emitted electrons returned to the vehicle, as shown in Figures 7.16 and 7.17. Notice that many particles escape by glancing off the barrier, since the barrier height diminishes rapidly away from the bellyband. By 435 seconds, the barrier increased to about 150 volts, and 80 percent of the particles returned to the vehicle, as shown in Figures 7.18 and 7.19.

Emitted electrons which return travel along the bellyband, away from the region of high negative potential generated by the SC1 teflon mask. These electrons cannot pass the potential barrier around the SC6 boom, and they return to the vehicle on the bellyband between the SC4-1 gun and the SC6 boom or on the solar cells above this region.

The <u>total</u> time for the barrier to form in the above simulation was 8 minutes. However, this time is very sensitive to the initial charging conditions, which is in turn sensitive to the material properties, and these are poorly known. The "switching time" for a change from under 25 percent current returned to over 75 percent returned is about 30 seconds. Both the above times scale inversely with the assumed ambient density, which was 0.2 cm^{-3} in the above case. Space charge limiting of the emitted beam (neglected above) could also allow more rapid barrier formation due to local charging of solar cells near the SC4-1 gun.

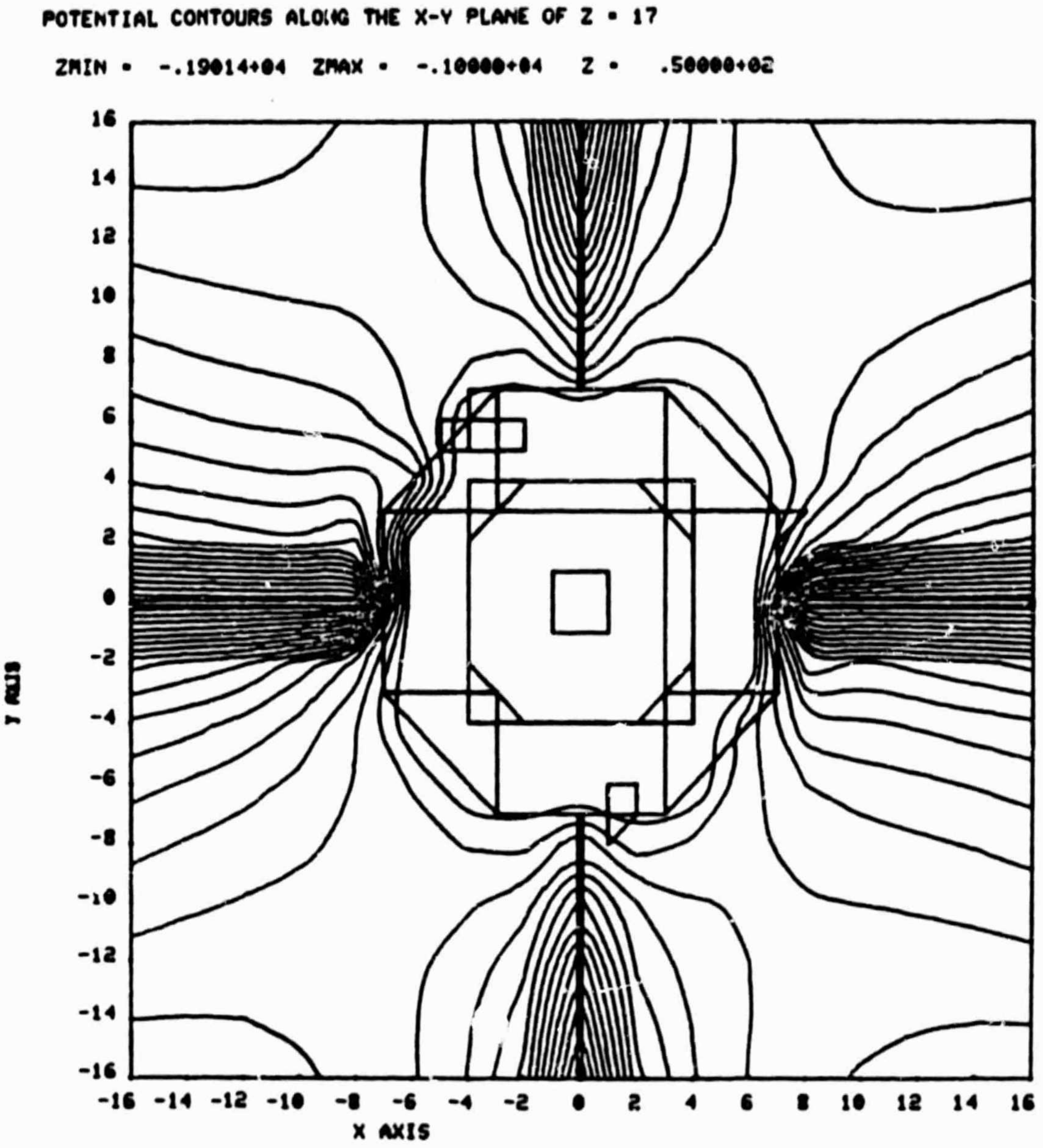

Figure 7.13. Potential contours after 395 seconds. Note the potential barrier above the SC4-1 gun location.

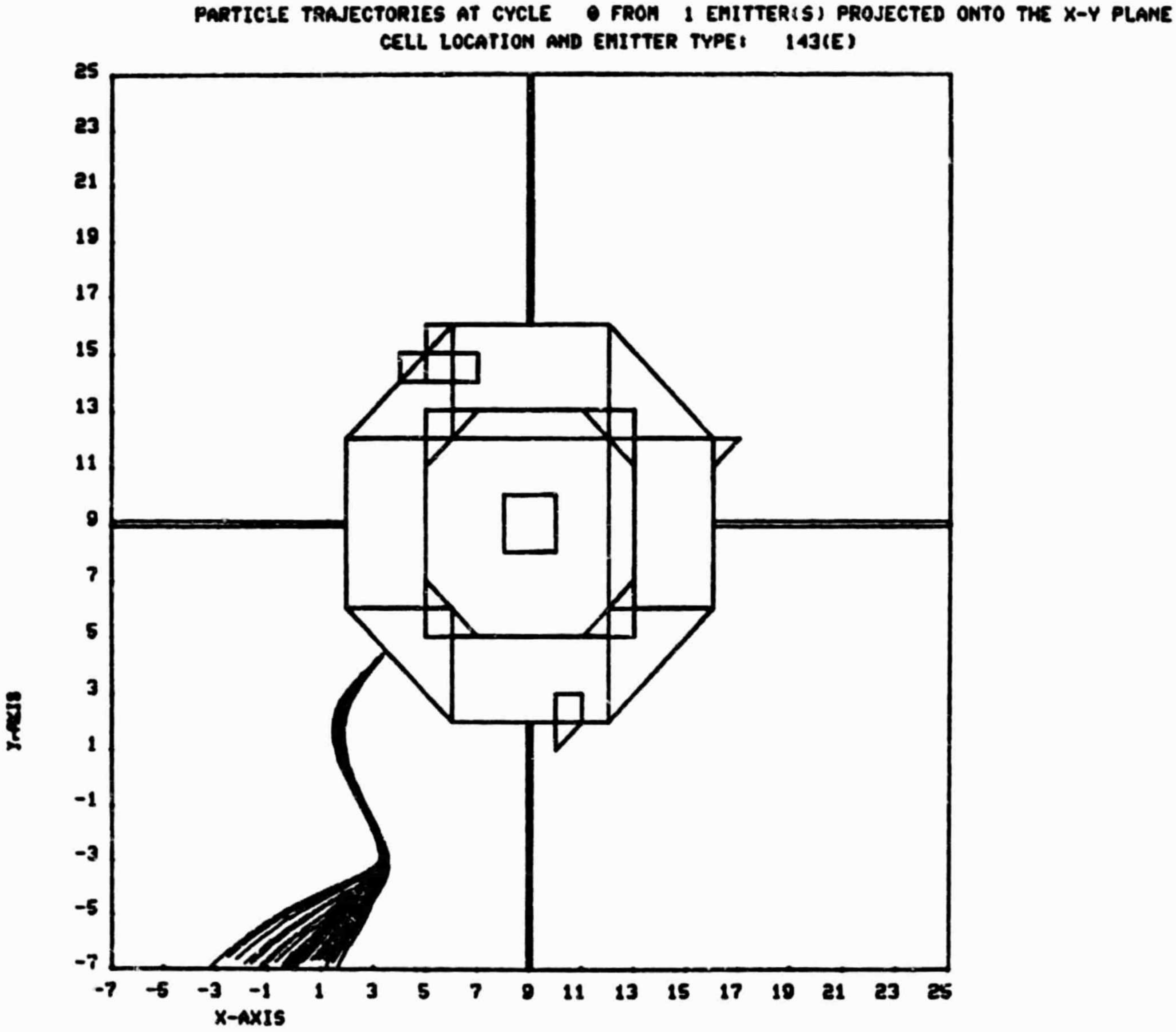

Figure 7.14. Trajectories of 150 volt electrons from SC4-1 gun after 395 seconds. All particles escape.

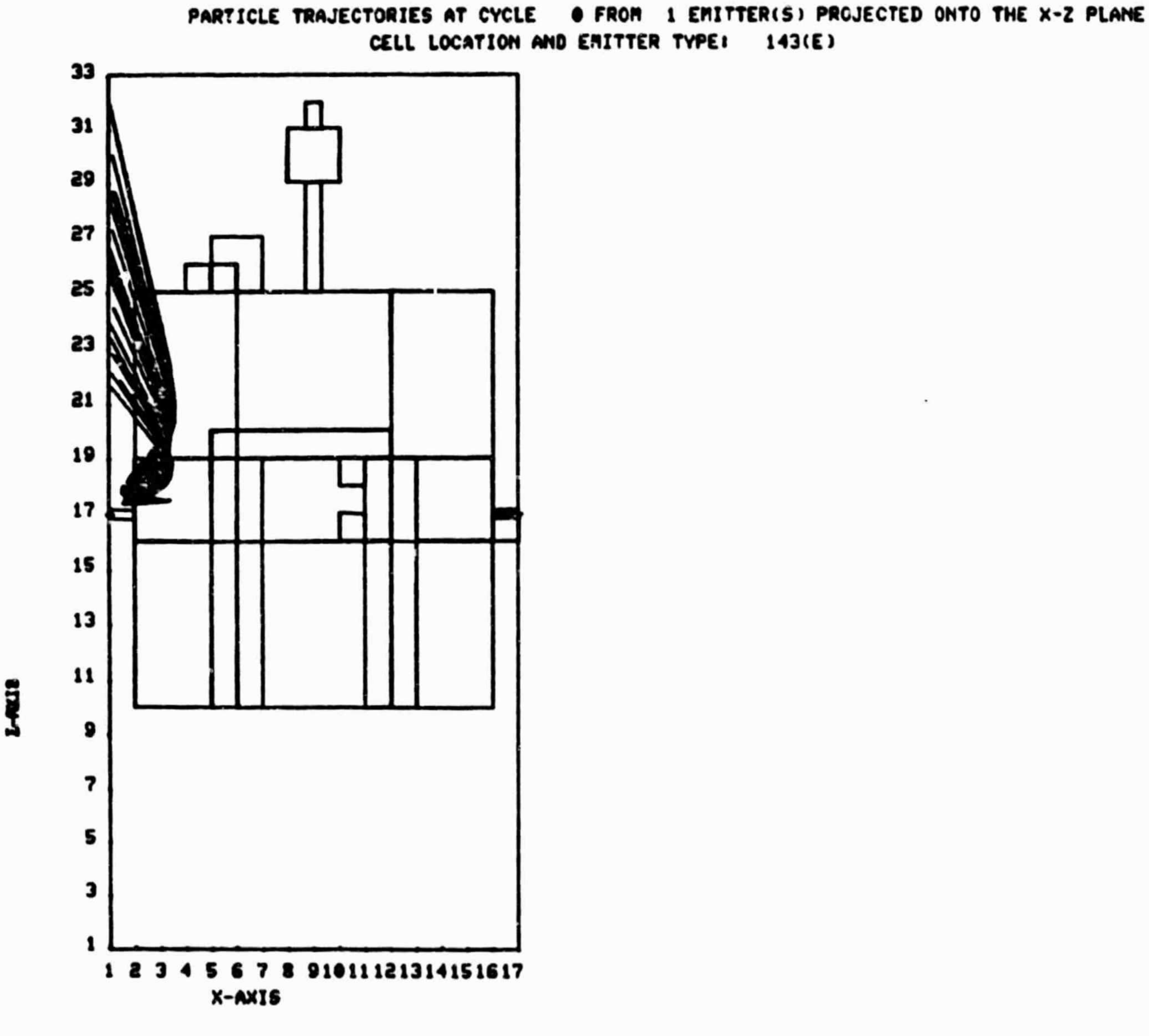

Figure 7.15. Trajectories of 150 volt electrons from SC4-1 gun after 395 seconds. All particles escape.

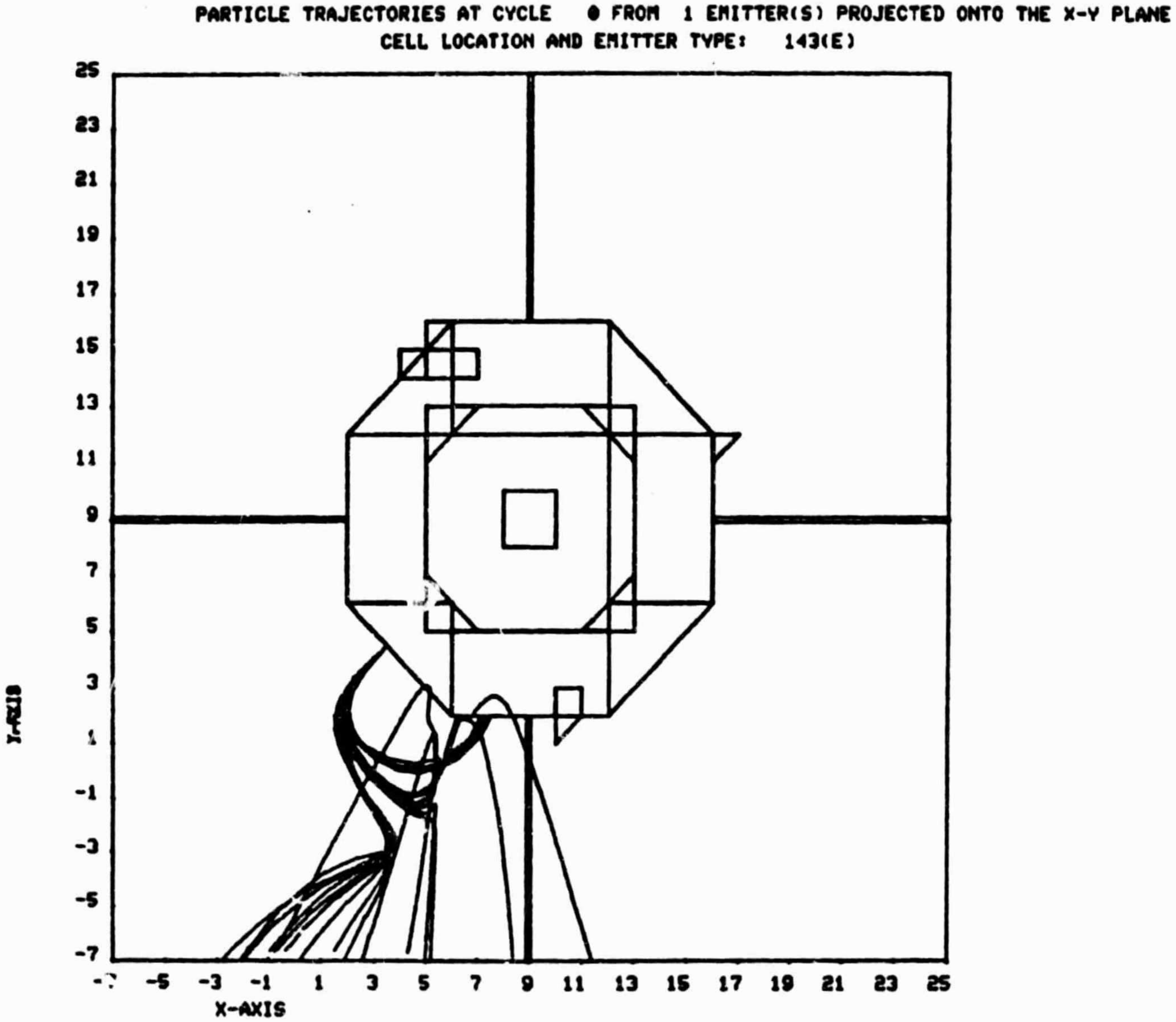

Figure 7.16. Trajectories of 150 volt electrons from SC4-1 gun after 415 seconds. Forty percent of emitted particles return.

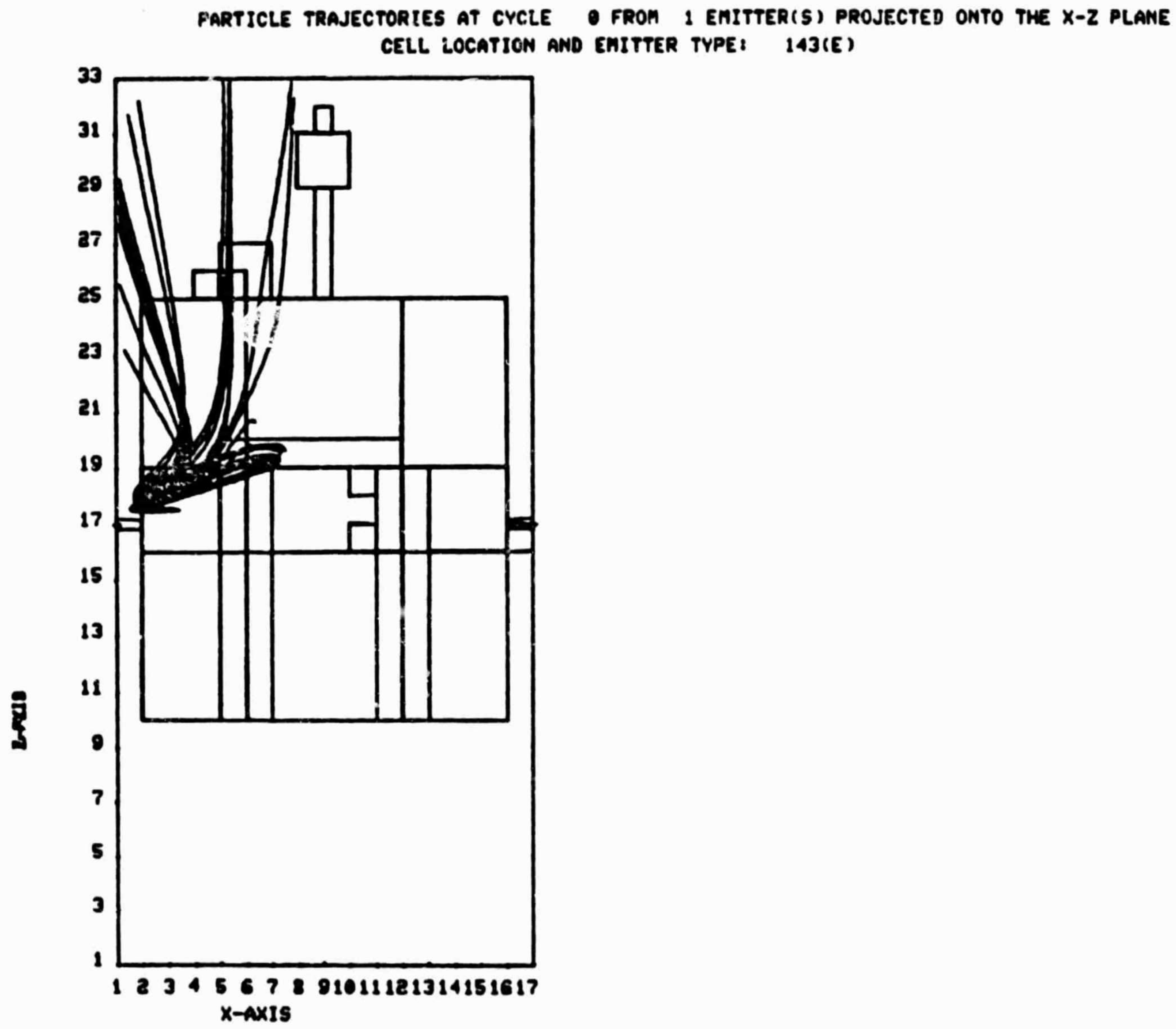

Figure 7.17. Trajectories of 150 volt electrons from SC4-1 gun after 415 seconds. Forty percent of emitted particles return.

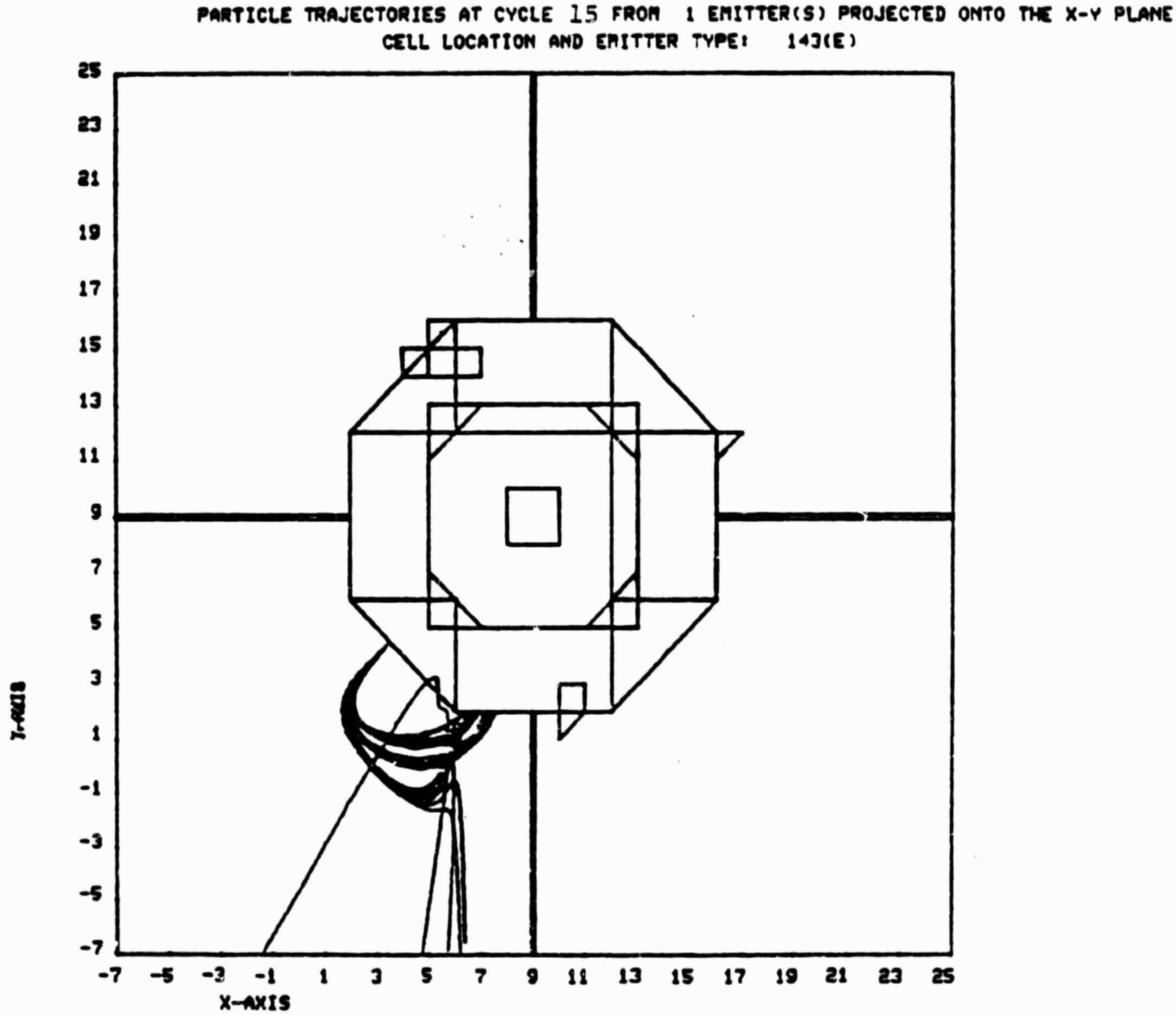

Figure 7.18. Trajectories of 150 volt electrons from SC4-1 gun after 435 seconds. Eighty percent of emitted particles return.

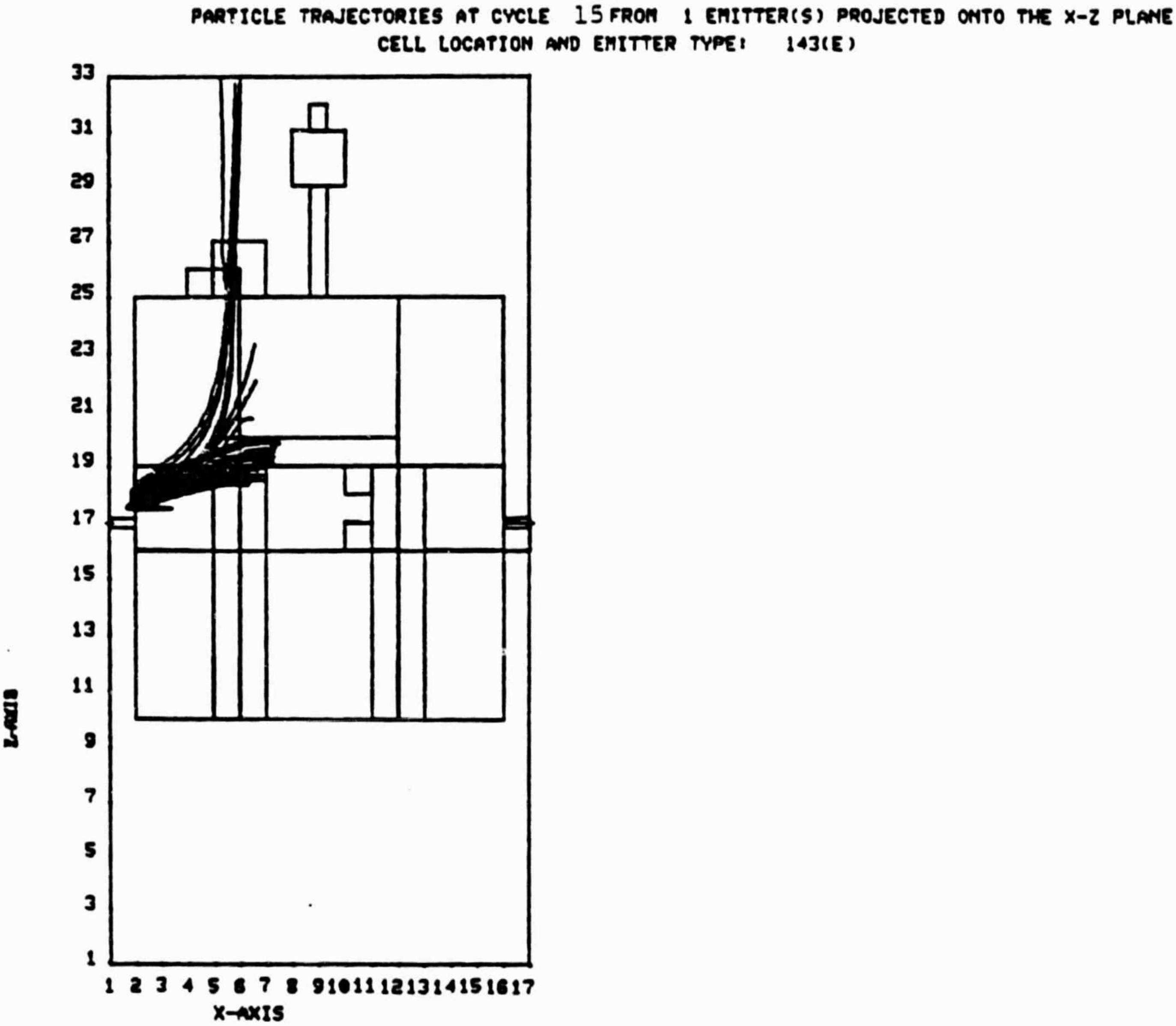

Figure 7.19. Trajectories of 150 volt electrons from SC4-1 gun after 435 seconds. Eighty percent of emitted particles return.

7.4 SPACE CHARGE LIMITED ION BEAM EMISSION

One of the experiments on board the SCATHA satellite is a plasma discharge ion emitter. The working gas is Xenon, whose large mass makes the unneutralized beam extremely space charge limited at the operating voltages and currents. In this section we present an analysis of the emitter based upon simple space charge limited diode theory. While the model developed has a large number of limitations, the satellite voltages it predicts are in rough agreement with experiment. The model identifies the relevant physical mechanisms of beam emission and thus is useful in planning more elaborate multidimensional calculations.

7.4.1 Model Description

We assume the emitter to be a 1.27 cm diameter disk held at spacecraft ground. The beam is assumed to be monoenergetic with the ion velocities all normal to the emitting surface. Ion energy is 1100 eV. At the three current levels evaluated (2 mA, 0.3 mA, 0.08 mA) the limiting distances are much shorter than the assumed plasma Debye length of 700 cm. This length corresponds to a $\theta = 1$ eV, $n_e = 1\ \text{cm}^{-3}$ background plasma. As will be shown, the results are not sensitive to the estimates of the background plasma.

The severe limiting is used to divide space into two regions. The first region is between the emitter and the limiting layer. The second is outward from the limiting layer, which is a virtual anode for ion emission into the plasma. In Figure 7.20 we illustrate qualitatively the behavior of the potential along a line normal to the emitter surface.

In Region 1 the ion beam forms a potential barrier which reflects the beam back to the emitting surface. Since

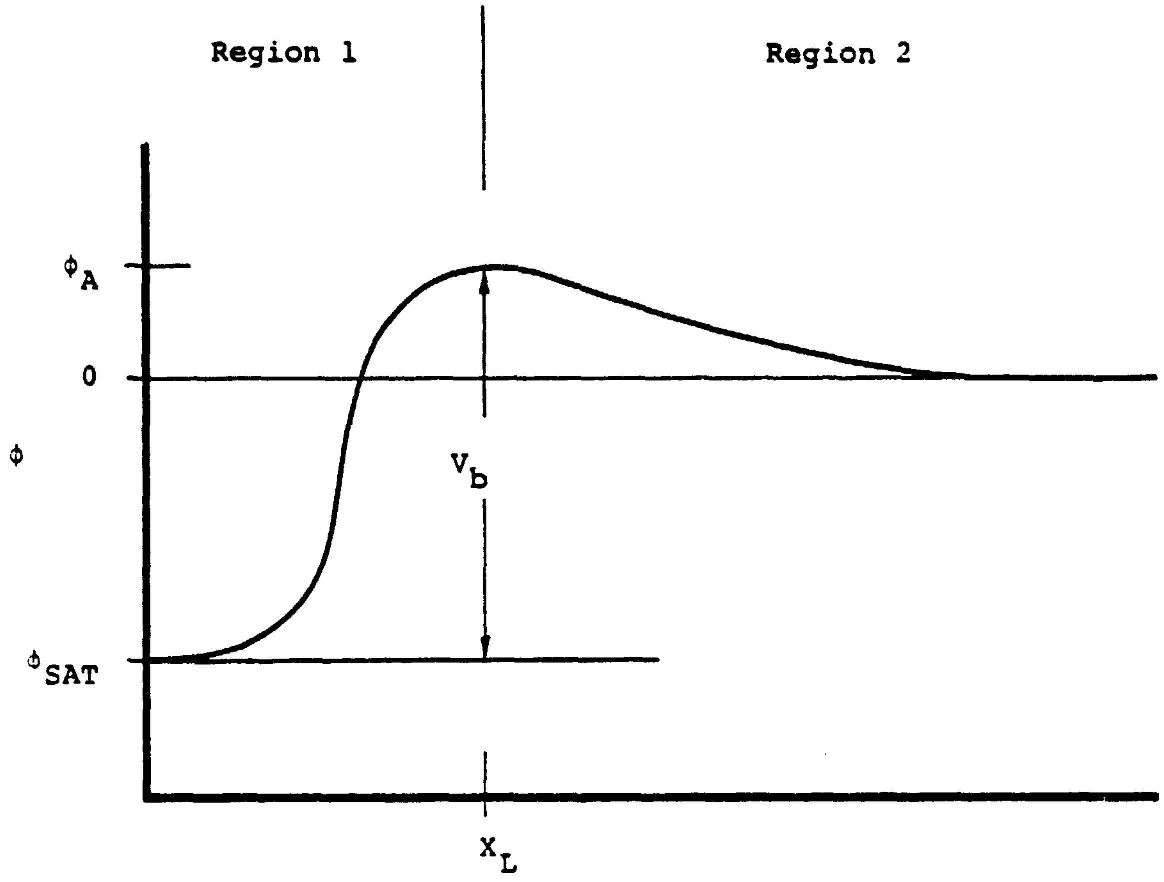

Figure 7.20. Qualitative dependence of the potential along a line normal to the emitting surface. ϕ_{SAT} is the satellite ground potential, ϕ_A is the virtual anode potential, V_b is the energy of emitted ions, and X_L is the distance to the virtual anode.

for all the cases studied here, the satellite current is much less than the beam current, the barrier must be sufficient to limit the beam. Using our assumption of a monoenergetic beam we get

$$V_b = \phi_A - \phi_{SAT}$$

where V_b is the beam voltage, ϕ_A is the virtual anode potential and ϕ_{SAT} is the satellite ground potential. Since the initial beam ion density is many orders of magnitude larger than the ambient electron density (neutralizer off), in the analysis below we will neglect the effects of ambient screening in Region 1.

In Region 2 we have cold ions leaving the barrier and streaming into space. Note that the ion velocities monotonically increase with distance beyond the virtual anode, located at a distance X_L from the emitter. The potential decays at long distances due to the ambient plasma screening. While the screening is essential for any ion current to exist, we will show below that the amount of current is insensitive to both the plasma Debye length and the precise nature of the shielding.

The two regions are coupled by solving for the satellite potential, ϕ_{SAT}, for which the ion current in Region 2, I_∞, balances the net satellite current I_{SAT}.

$$I_\infty(\phi_A) + I_{SAT}(\phi_{SAT}) = 0$$

I_{SAT} is gotten from the I-V characteristic of the satellite as calculated by NASCAP.

REGION 1

The formation of the virtual anode in front of the disk emitter is inherently a two-dimensional problem, since the space charge expands the beam as well as slows it. For the purposes of this study we have developed a simple, albeit ad hoc, model of the beam spreading which allows us to estimate the size and shape of the virtual anode using one-dimensional spherical diode theory. We emphasize that this is probably the weakest part of the theory, but qualitatively it does account for the beam spreading.

In Figure 7.21a we illustrate the virtual anode formation. In Figure 7.21b we show the geometric construction which we use to convert the actual multidimensional case into a solid angle of $2\pi(1-\cos\theta)$ of a concentric spherical emitter. The chord of the virtual anode is set equal to the emitting disk diameter plus twice the limiting distance. From this assumption we get the following geometrical relations:

$$r_0 = r_1 + X_L$$

$$r_1 = a + \frac{a}{2X_L}$$

$$1 - \cos\theta = \frac{X_L}{r_0}$$

where r_0 is the virtual anode radius, r_1 the emitter radius, X_L the limiting distance, a the disk radius, and θ the half cone angle. We complete the equations by relating the beam current I_B to the total Child's law current, I_S, of a concentric spherical diode with ratio of radii r_0/r_1

$$I_S = \frac{2.9 \times 10^{-5}}{\sqrt{\frac{M}{m}}} \frac{V_b^{3/2}}{\alpha^2\left(\frac{r_0}{r_1}\right)}$$

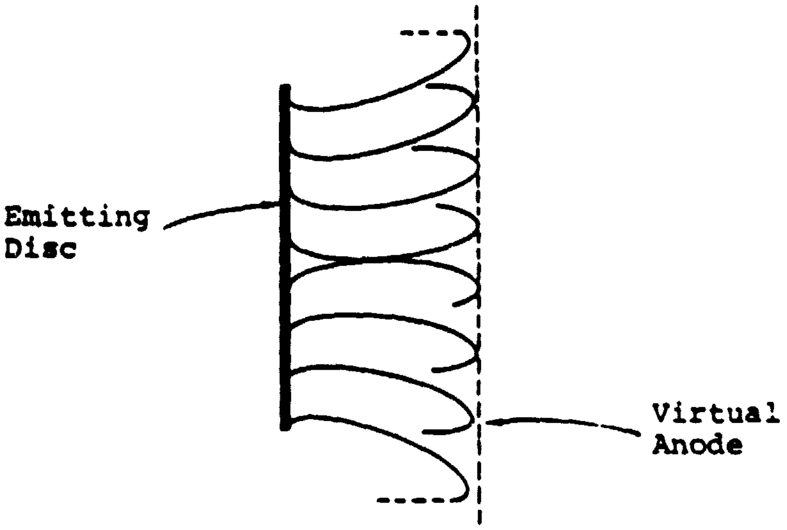

Figure 7.21a. Virtual anode formation in front of an emitting disk.

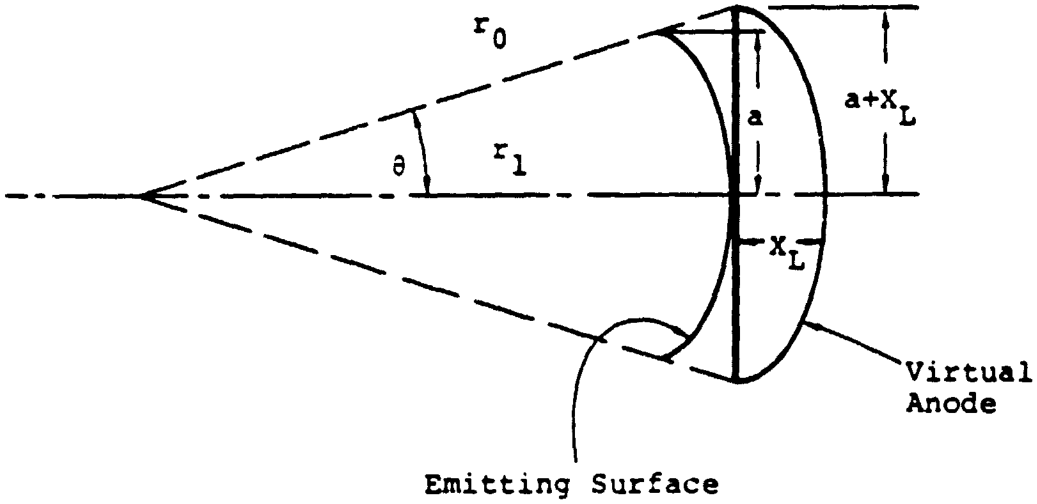

Figure 7.21b. Our model emitter where the disk now represents a solid angle $2\pi(1-\cos\theta)$ of a sphere of radius r_1 emitting and forming a virtual anode at a radius $r_0 = r_1 + X_L$.

$$I_{REG\ 1} = \frac{2\pi(1-\cos\theta)}{4\pi} I_S$$

$$I_{PEG\ 2} = 2\ I_B - I_{SAT}$$

The current in Region 1, $I_{REG\ 1}$, is almost twice the beam current, I_B, because most of the current is reflected from the space charge barrier. This is especially true in the 2 mA case since the beam current, 2 mA, is much greater than the satellite current ∿0.02 mA.

The solution of these equations for V_b = 1100 volts, a = 0.635 cm and M = 131 amu is given in Table 7.4. Notice that only for the high current case is the limiting distance smaller than the disk radius, a. The virtual anode becomes more hemispherical with decreasing beam current. For the 0.08 mA case the half cone angle is almost 80 degrees.

TABLE 7.4. VIRTUAL ANODE PARAMETERS AS A FUNCTION OF BEAM CURRENT FOR V_b = 1100 VOLTS: EMITTER DISK RADIUS a = 0.635 cm

I_B (ma)	X_L (cm)	R_0 (cm)	$(1-\cos\theta)$
2.0	0.30	1.57	0.19
0.3	1.08	1.89	0.57
0.08	2.93	3.62	0.81

REGION 2

In Region 2 we have calculated the current emitted by a sphere into a plasma. In the cases of interest $\lambda_D >> r_o$, the effective radius of the emitter. Poisson's equation including both beam and ambient plasma densities is

$$\nabla^2\phi = \frac{-I_{\text{spherical}}}{r^2 \sqrt{\frac{2e}{M}\left(\phi_A - \phi\right)}} - 4\pi\, \rho_{\text{ambient}}$$

We approximate the ambient charge density using the linear term

$$-4\pi\, \rho_{\text{ambient}} = \frac{\phi}{\lambda_D^2}$$

We have also used the approximation

$$-4\pi\, \rho_{\text{ambient}} = \frac{1}{\lambda_D^2} \frac{\phi}{1 + \phi^{3/2}}$$

to account for electron acceleration in the sheath.

The current for a given ϕ_A that satisfies the boundary conditions at infinity ($\phi_\infty \rightarrow 0$) is remarkably insensitive to the form of ambient plasma screening. Indeed for $\lambda_D/r_o = 200$ the two forms predict the same current to within 1 percent. This is due primarily to the dominance of beam space charge at small radii and the insensitivity of concentric spherical emitters to the radius of the virtual anode. Table 7.5 shows the space charge limited current for both approximations as a function of λ_D/r_o for a spherical emitter at 700 volts. The results scale as $V^{3/2}$ and depend only on λ_D/r_o, the same as a conventional spherical diode. For planar geometries, the relationship between the screening length λ_D, the emitter voltage and the current density can be solved analytically (see Appendix B). Then the analogy between λ_D and the associated diode spacing is exact with the effective gap distance, $d_{effective}$, just a constant times λ_D

$$d_{effective} = \frac{2\sqrt{2}}{3} \lambda_D$$

$$V_{effective} = \phi_A - \phi_o = \frac{2}{3} \phi_A$$

$$J_{planar} = 2.64 \times 10^{-6} \frac{V^{3/2}}{\lambda_D^2}$$

with V in volts and d in cm.

The spherical current is related to the satellite current by the subtended solid angle:

$$I_{SPHERICAL} = I_{SAT}/(1-\cos\theta)$$

Examining Table 7.5 it is apparent that the solid angle of the emitter is more important than the emitter radius in determining the voltage required for a given current emission. This is because the largest space charge effects occur close to the emitter surface.

TABLE 7.5. TOTAL SPHERICAL XENON ION CURRENTS INTO A PLASMA FOR AN EMITTER AT 700 VOLTS.

λ_D/r_o	$I\left(\frac{\phi}{\lambda_D^2}\right)$ (mA)	$I\left(\frac{1}{\lambda_D^2} \frac{\phi}{1+\phi^{3/2}}\right)$ (mA)
1	2.59	1.78
5	0.72	0.64
10	0.52	0.49
200	0.25	0.25
700	0.21	0.21

Note that at large λ_D/r_C the current is insensitive to both the ratio of the Debye length to emitter radius and to the form of the plasma screening.

7.4.2 Results and Discussion

We couple Regions 1 and 2 in order to determine the virtual anode voltage required for emitters with radii and solid angles as described in Table 7.4 to emit prescribed ion currents into a 700 cm Debye length plasma. The satellite voltage is found assuming it is 1100 volts below the virtual anode potential. The results for various satellite currents are shown in Table 7.6. The blank entry for case 1, I_{SAT} = 0.05 mA is because analysis suggests this is a physically unrealizable case. The predicted satellite voltage is positive which would severely reduce the satellite current below 0.05 mA.

The range of ambient currents to the SCATHA satellite in sunlight was determined using the NASCAP code. A mild environment was considered, described by Maxwellian electron and ion distributions with $n_e = n_i = 1\ \mathrm{cm}^{-3}$ and $T_e = T_i = 1$ eV. In such an environment, the ambient current is dominated by photoemission. The maximum current is emitted when the satellite is uniformly negatively charged. The current is +60 μA at -1000 volts, decreasing slowly with voltage to approximately 50 μA at -100 volts. Lower current levels are obtained when the insulating surfaces are discharged so that positive fields develop to limit photoemission. This occurs in several seconds. With the conductors fixed to -1000 volts and the insulating surfaces largely discharged, the net current was reduced to 18 μA.

TABLE 7.6. SATELLITE VOLTAGES FOR THREE BEAM CURRENT LEVELS AS A FUNCTION OF SATELLITE CURRENT

Case 1 $I_B = 2$ mA, $V_B = 1100$ Volts

I_{SAT} (mA)	Φ_A (volts)	Φ_{SAT} (volts)
0.05	1288	-
0.02	696	-402
0.01	440	-660

Case 2 $I_B = 0.3$ mA, $V_B = 1100$ Volts

I_{SAT} (mA)	Φ_A (volts)	Φ_{SAT} (volts)
0.05	570	-530
0.02	309	-791
0.01	195	-905

Case 3 $I_B = 0.08$ mA, $V_B = 1100$ Volts

I_{SAT} (mA)	Φ_A (volts)	Φ_{SAT} (volts)
0.05	440	-660
0.02	240	-860
0.01	150	-950

7.5 DISCUSSION

The analysis presented here is qualitative in nature and was performed for the purpose of identifying the relevant physics of space charge limited ion emission from a satellite. The results agree with experiment to the extent that lower beam currents produce larger negative satellite potentials. Also, the magnitude of the potential variations are similar to those observed. Our analysis indicates that the magnitude of the potential variations is a function of the geometry of space charge barrier, and since we estimate this rather crudely, our results are not to be considered qualitatively accurate.

More accurate results could be obtained in the following manner. First a local two-dimensional particle pushing analysis of the space charge limiting of the emitter would be performed. Since the plasma boundary conditions influence this only very weakly, this part could be easily performed including such phenomena as gun optics. Then given the space charge barrier, multidimensional space charge limited currents in space beyond the barrier could be calculated as a function of satellite potential. This would include the dipolar nature of the space potential in Region 2, which will increase the beam divergence substantially in the high beam current cases.

8. DETECTOR MODELING

The SCATHA spacecraft has on board several particle detector experiments which monitor particle fluxes at geosynchronous orbit. The experiments SC2, SC5, SC6, SC7, and SC9 were designed to measure electron and ion fluxes in the energy range which causes the charging of exposed spacecraft materials, 0 to ∿80 keV. The SC6 experiment never operated in orbit, and the SC7 experiment operated only briefly, so attention will focus on the remaining three experiments. This chapter describes the use of the NASCAP "DETECTOR" mode to simulate the response of the SCATHA particle detectors.

A particle detector with an unobstructed field of view operating on an uncharged, magnetically clean spacecraft can measure particle fluxes which accurately reflect the state of the ambient plasma environment. Differential charging and local geometric effects produce electrostatic fields near a spacecraft which can distort the trajectories of incoming particles. Low energy electrons emitted from highly charged regions of a spacecraft can be observed as high energy electrons incident elsewhere on the vehicle. The NASCAP DETECTOR model was designed to assist in the identification and interpretation of such occurrences. The operation of the DETECTOR routines is described in detail elsewhere.[2] Briefly, numerical reverse trajectory tracking is used to connect particle orbits incident at a specified detector location on the vehicle with a postulated phase space distribution at a large distance. The predicted response can be displayed as a function of view direction or incident particle energy, and plots of the trajectories are produced.

The simulations described in the following sections were performed to illustrate expected detector responses using the charged states of the SCATHA spacecraft generated in the studies described in Chapter 5. Three representative cases were selected:

Case 1: High temperature plasma in sunlight. See Section 5.3, Figures 5.9-5.11. Spacecraft ground at +4 volts.

Case 2: High temperature plasma in eclipse. See Section 5.1, Figures 5.3 and 5.4. Spacecraft ground at -6400 volts.

Case 3: Moderate temperature plasma in eclipse. See Section 5.2, Figures 5.6-5.8. Spacecraft ground at -140 volts.

The first case represents a nearly uncharged state of the vehicle, while the next two cases had significant differential charging, especially along the SC2 and SC6 booms. Depending on the operational state of the satellite (i.e., whether or not the boom mounted experiments were grounded, biased, or allowed to float at the time of interest) the differential charging pattern represented by these cases can be altered significantly. The simulations described in the following sections were chosen to illustrate the most severe type of vehicle perturbations which can be expected. In all three cases, the phase space distribution at infinity was assumed to be isotropic and characterized by the appropriate single Maxwellian representation from Table 4.1. A constant B-field of 10^{-3} gauss along the +y axis was used in all cases as representative of geosynchronous conditions. Since even a 10 volt electron has a Larmor radius of 12 m for this field, the turning of orbits by the magnetic field is negligible. For further discussion of this point, see Section 8.2 below.

8.1 SC2 DETECTOR SIMULATIONS

This section describes simulation of the response of the SC2-3 detector mounted on the SCATHA bellyband, near the base of the SC2-2 boom. Two similar detectors are mounted at the ends of the SC2 booms: the SC2-2 detector has an unobstructed field of view, while the SC2-1 detector looks back towards the vehicle body. As the results below demonstrate, the electrostatic fields from the SC2-2 boom can significantly perturb the trajectories of particles observed by SC2-3.

The predicted response of SC2-3 in the Case 1 environment is illustrated in Figure 8.1, and the associated incoming electron and proton trajectories are shown in Figure 8.2. Since the satellite is almost uncharged, the trajectories are nearly unaffected. Only the lowest energy electrons (a few eV) are significantly perturbed as they travel nearly parallel to the SC2 boom. Figure 8.3 displays expected response for the Case 3 environment. Since the vehicle ground is charged to -6400 V, protons below this energy are not observed. Any incident protons below this energy must have originated elsewhere on the vehicle, as shown in Figure 8.4. Electron trajectories are distorted only slightly in the repelling fields for this case. Displayed in Figures 8.5 and 8.6 are corresponding results for the Case 3 environment. The SC2 boom tips are highly charged in this case, while the ground conductor is at -140 volts. Both electron and ion trajectories are severely distorted in the spacecraft fields, and the expected detector response is accordingly modified. Some low energy protons actually orbit the boom tip before arriving at the detector, completely distorting the information regarding angular dependence of incoming particle trajectories.

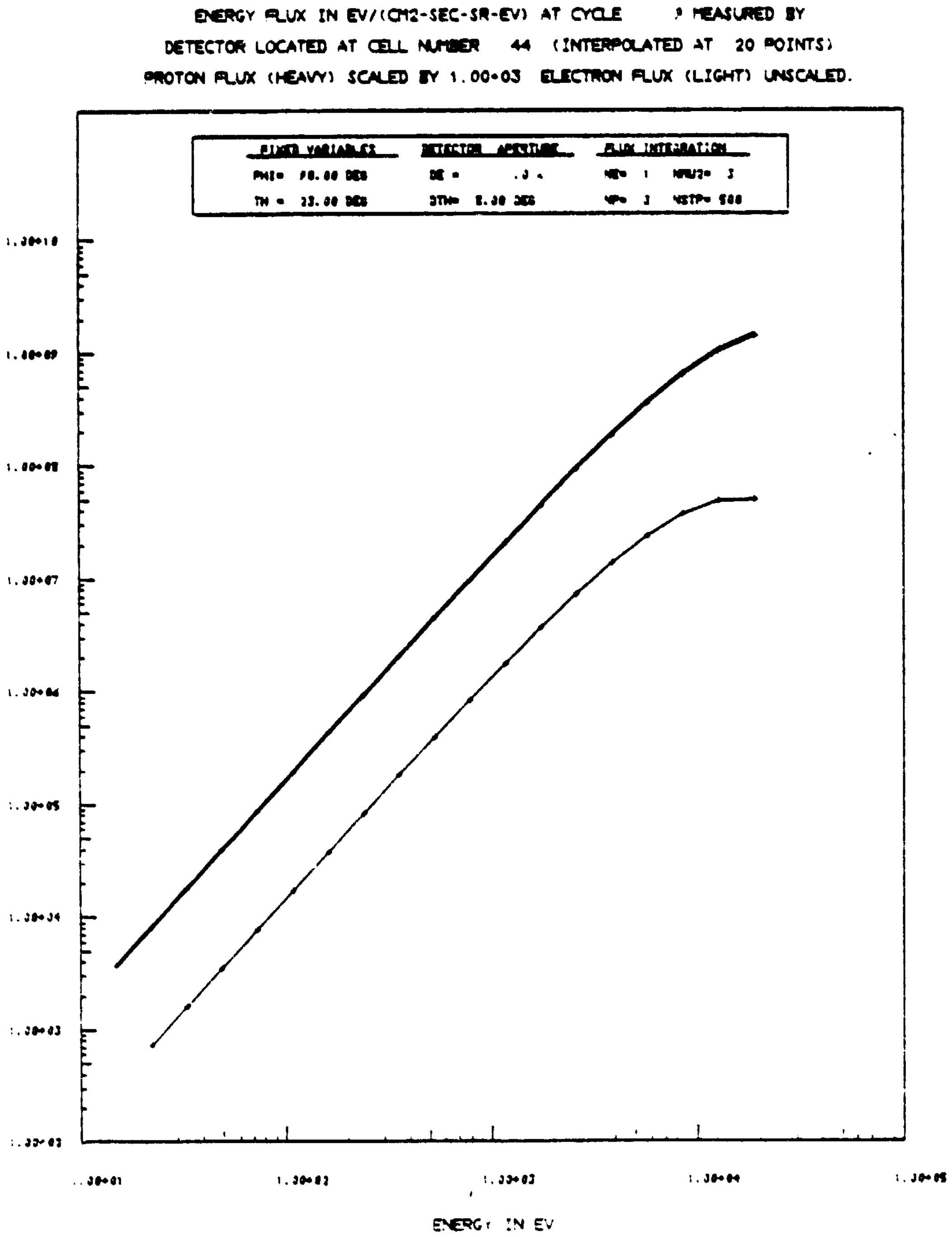

Figure 8.1. Simulated response of SC2-3 to incoming electrons and protons, 10-19,000 eV, in Case 1 environment.

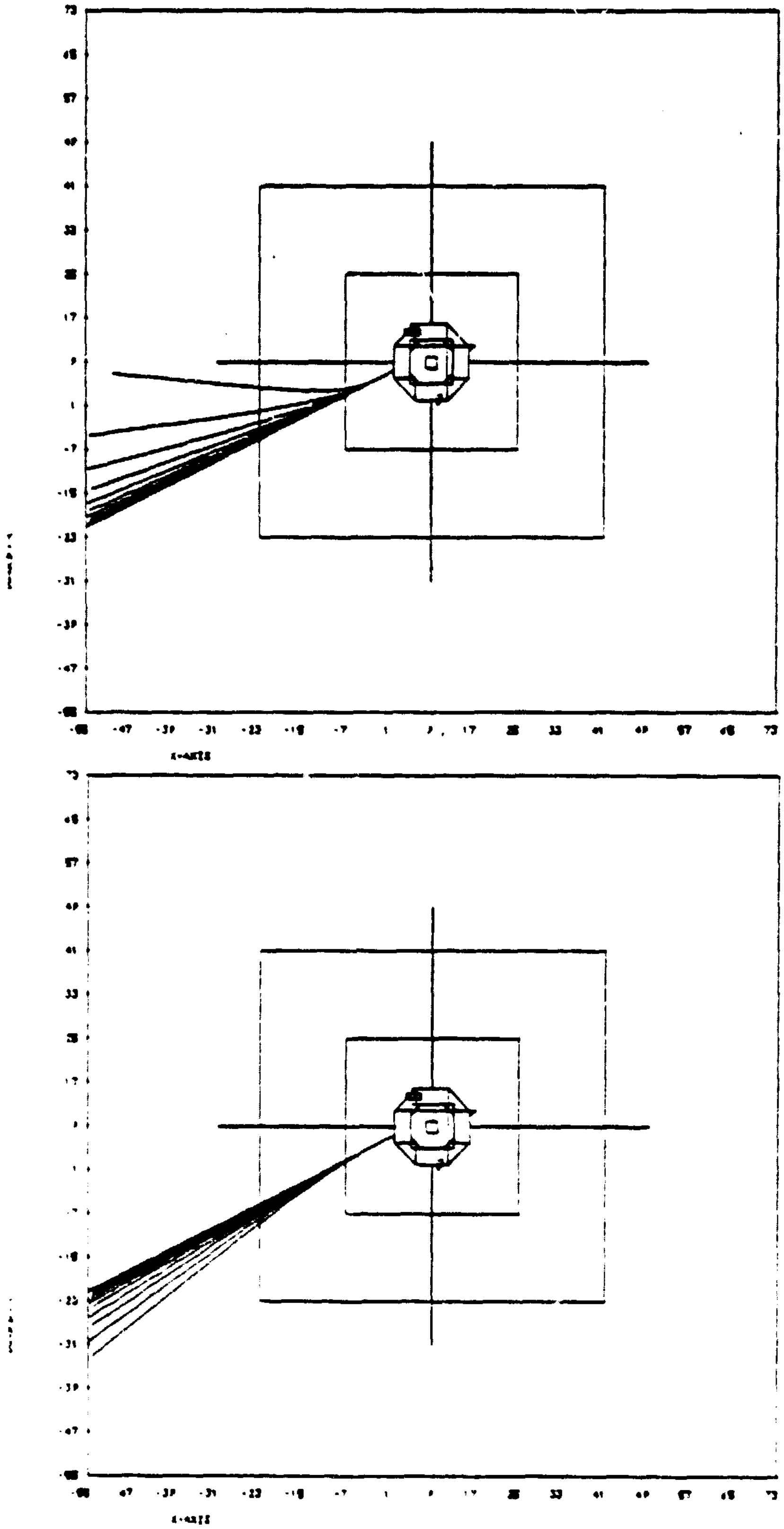

Figure 8.2. Trajectories of electrons (top) and protons (bottom) logarithmically spaced from 10-19,000 eV, observed at SC2-3 location for Case 1 environment. Lowest energy electrons (ions) are deflected towards (away from) positive SC2 boom.

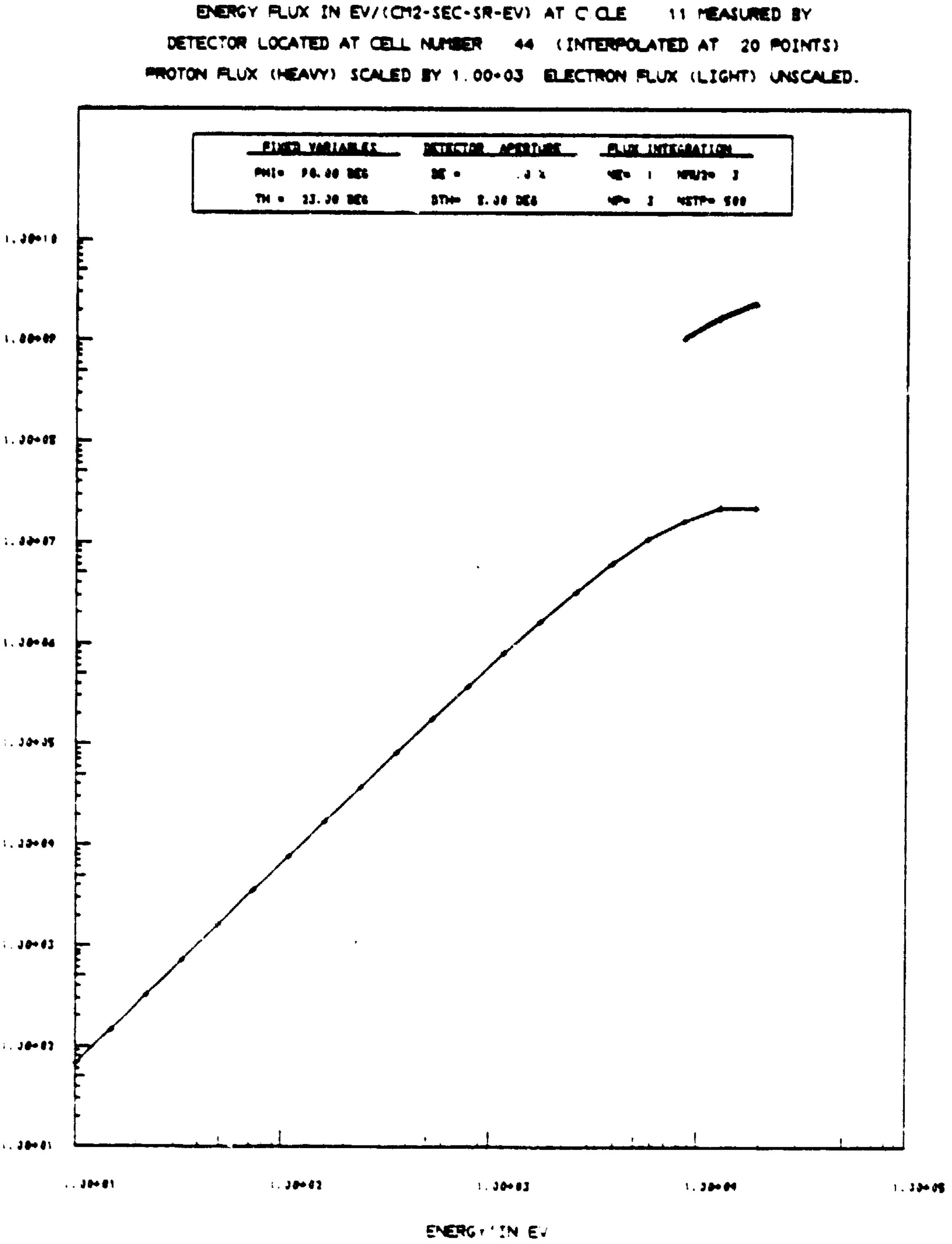

Figure 8.3. Simulated response of SC2-3 to incoming electrons and protons, 10-19,000 eV, in Case 2 environment.

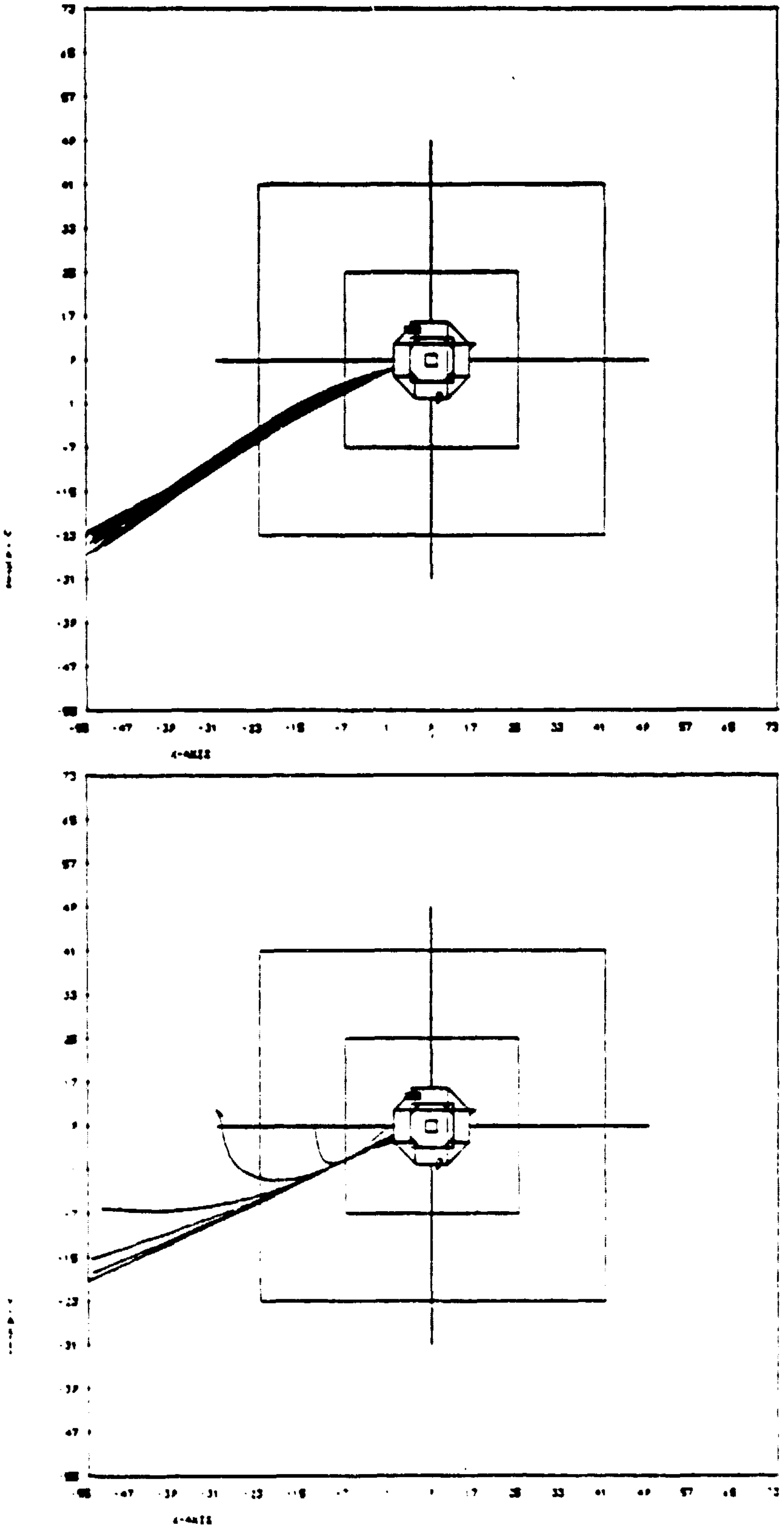

Figure 8.4. Trajectories of electrons (top) and protons (bottom) logarithmically spaced from 10-19,000 eV, observed at SC2-3 location for Case 2 environment. Proton trajectories below 6400 eV originate on the vehicle.

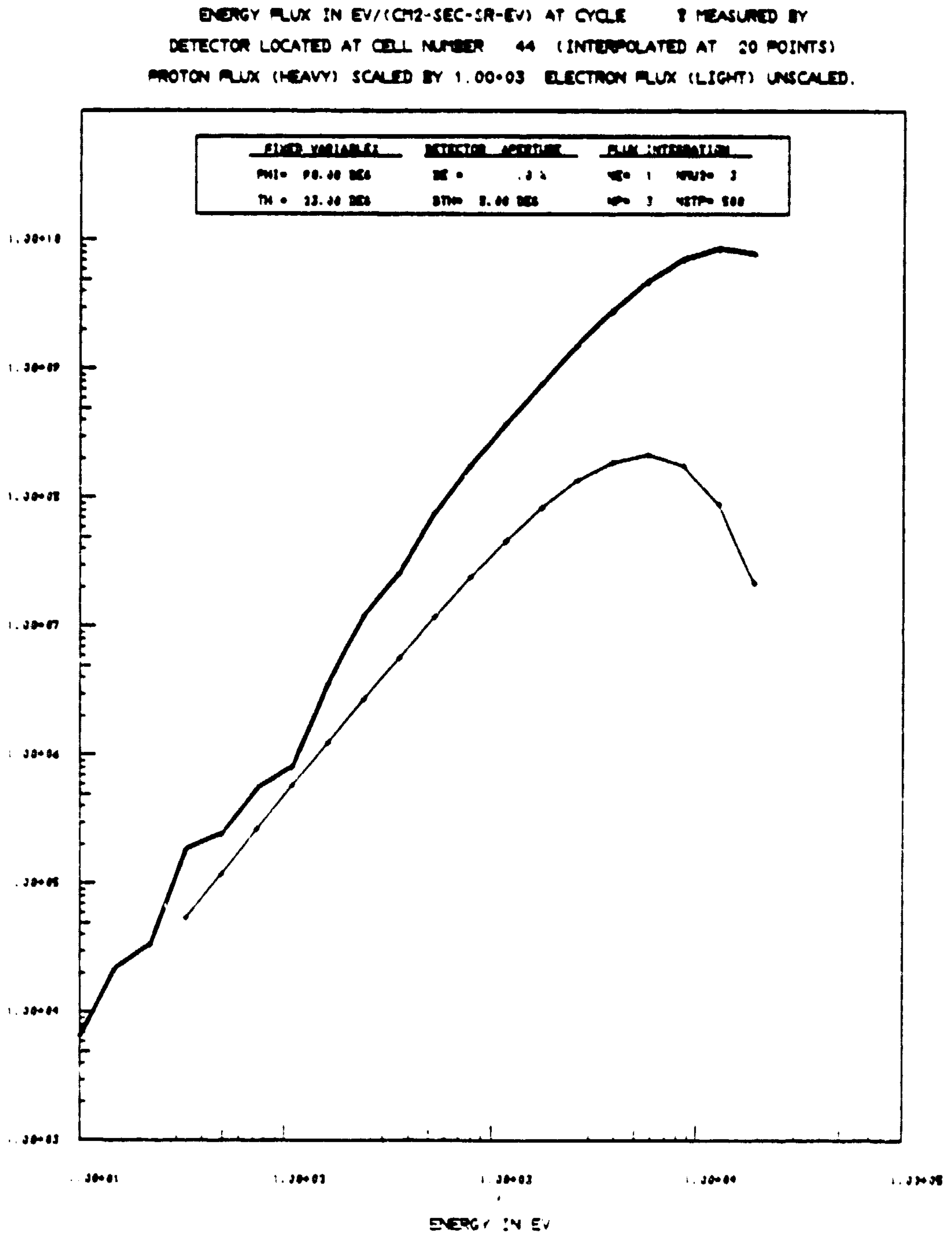

Figure 8.5. Simulated response of SC2-3 to incoming electrons and protons, 10-19,000 eV, in Case 3 environment.

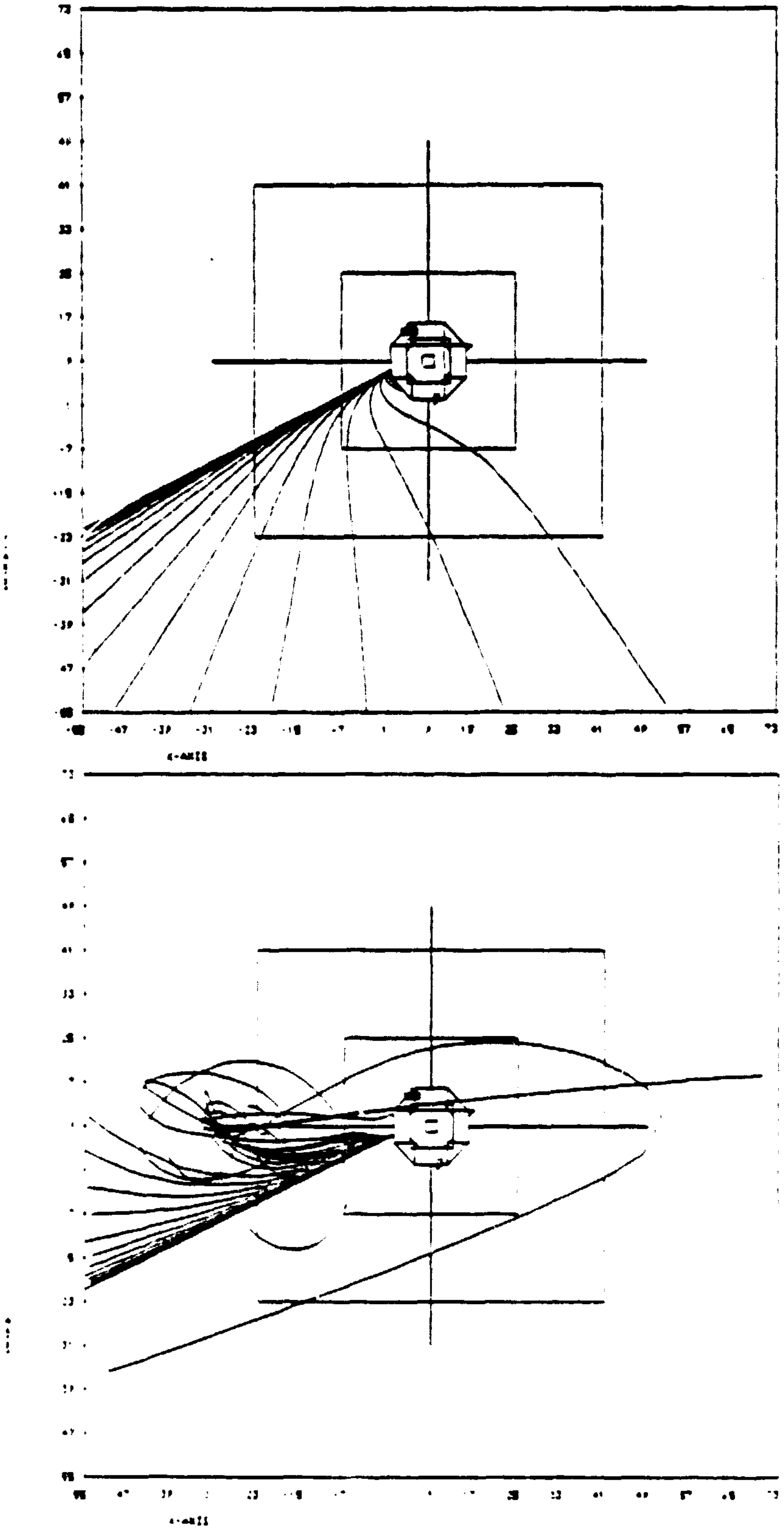

Figure 8.6. Trajectories of electrons (top) and protons (bottom) logarithmically spaced from 10-19,000 eV, observed at SC2-3 location for Case 3 environment. Many proton trajectories orbit the negatively charged SC2 boom tip without actually striking the boom.

8.2 SC5 DETECTOR SIMULATIONS

The SC5 experiment includes two electrostatic analyzers which measure electron and ion fluxes between 50 eV and 60 keV. These detectors view parallel and perpendicular to the satellite spin axis, with the bellyband (perpendicular) detector rotating approximately in the plane of the ambient magnetic field. During magnetic substorms, the response of the SC5 bellyband detectors on SCATHA have exhibited variation depending strongly on the azimuth about the spin axis. The considerations presented below agree that such a feature of the response is characteristic of anisotropy of the particle flux beyond the range of influence R of the satellite and is not induced by complex interaction involving the electric fields of the charged satellite and the ambient magnetic fields. More precisely, the satellite electric fields will not cause an isotropic distribution of particles originating from beyond R to appear as an anisotropic distribution at the detector.

Consider first the relevant length scales of the problem

$$R \approx \lambda_D \approx 743 \sqrt{\frac{\theta \text{ eV}}{n_e}} \text{ cm} \quad \text{Debye length} \qquad (8.1)$$

$$\lambda_p = 1.7 \times 10^2 \sqrt{\frac{E_e}{B}} \text{ cm} \quad \text{proton Larmor radius} \qquad (8.2)$$

$$\lambda_e = \frac{3.7 \sqrt{E_e}}{B} \text{ cm} \quad \text{electron Larmor radius} \qquad (8.3)$$

where θ eV is the plasma temperature, n_e the electron density, B the ambient magnetic field in gauss, and $E_p (E_e)$ the energy in eV of protons (electrons) in the plasma beyond R. For $\theta \sim 10^4$ eV, $B \approx 10^{-3}$ gauss, $E_p \gtrsim 100$ eV, $n \sim 1 \text{ cm}^{-3}$

$$\lambda_D << \lambda_p \quad \left(\frac{\lambda_D}{\lambda_p} \sim 4 \times 10^{-3}\right) \tag{6.4}$$

Even for electrons with sufficient energy to reach the satellite ($E_e \sim \theta \sim |V_{sat}|$)

$$\lambda_D/\lambda_e \sim 0.2 \tag{6.5}$$

Consequently, the trajectories of protons after entering the range of influence of the satellite are negligibly influenced by the ambient magnetic field. We therefore ignore B in subsequent considerations.

Now consider the eclipsed satellite in a substorm environment. Examination of various time scales for differential charging as well as detailed NASCAP calculations indicate that the electric field structure in the space around the spacecraft when viewed in the frame of reference rotating with the satellite, does not change substantially in the course of one rotation. A gain in flux that is isotropic beyond R would appear isotropic at the detector, and any apparent anisotropy must be present in the particle distributions at large distances from the satellite.

A primary effect of the satellite induced electric field is to distort the volume elements in phase space. To determine the region of velocity space beyond R that corresponds to regions sampled at the detector position can be determined by reverse tracking of particles entering the detector. The trajectories presented in Section 8.4 for the SC9 high energy detector are very similar to the corresponding simulation results for the parallel SC5 detector, except that the very low energy range (<50 eV) is not monitored by SC5. Figures 8.7 through 8.10 illustrate simulated response for the SC5 bellyband detector in the Case 2 and Case 3 environments. (The trajectories for the Case 1 environment are essentially undistorted straight line paths.) Figure 8.7 shows the characteristic cutoff of protons below the vehicle potential for Case 2, and the perturbation of the proton trajectories by the charged satellite is visible in Figure 8.8. In Case 3, the charged SC2 boom tip has similar effect on the incident protons and electrons as was observed for the SC2-3 detector. The simulated response and the corresponding trajectories are shown in Figures 8.9 and 8.10.

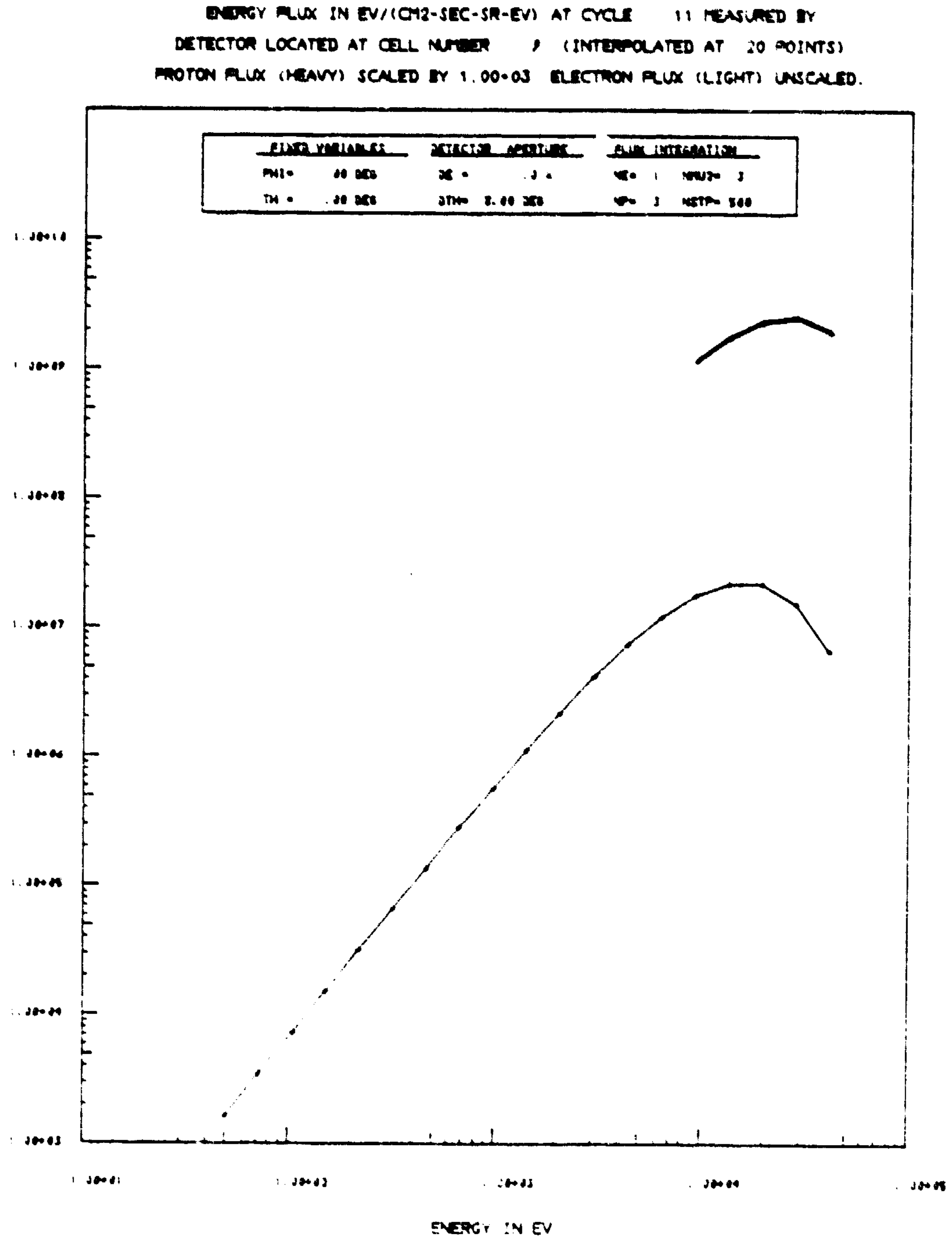

Figure 8.7. Simulated response of SC5 bellyband detector to incoming electrons and protons, 50-60,000 eV, in Case 2 environment.

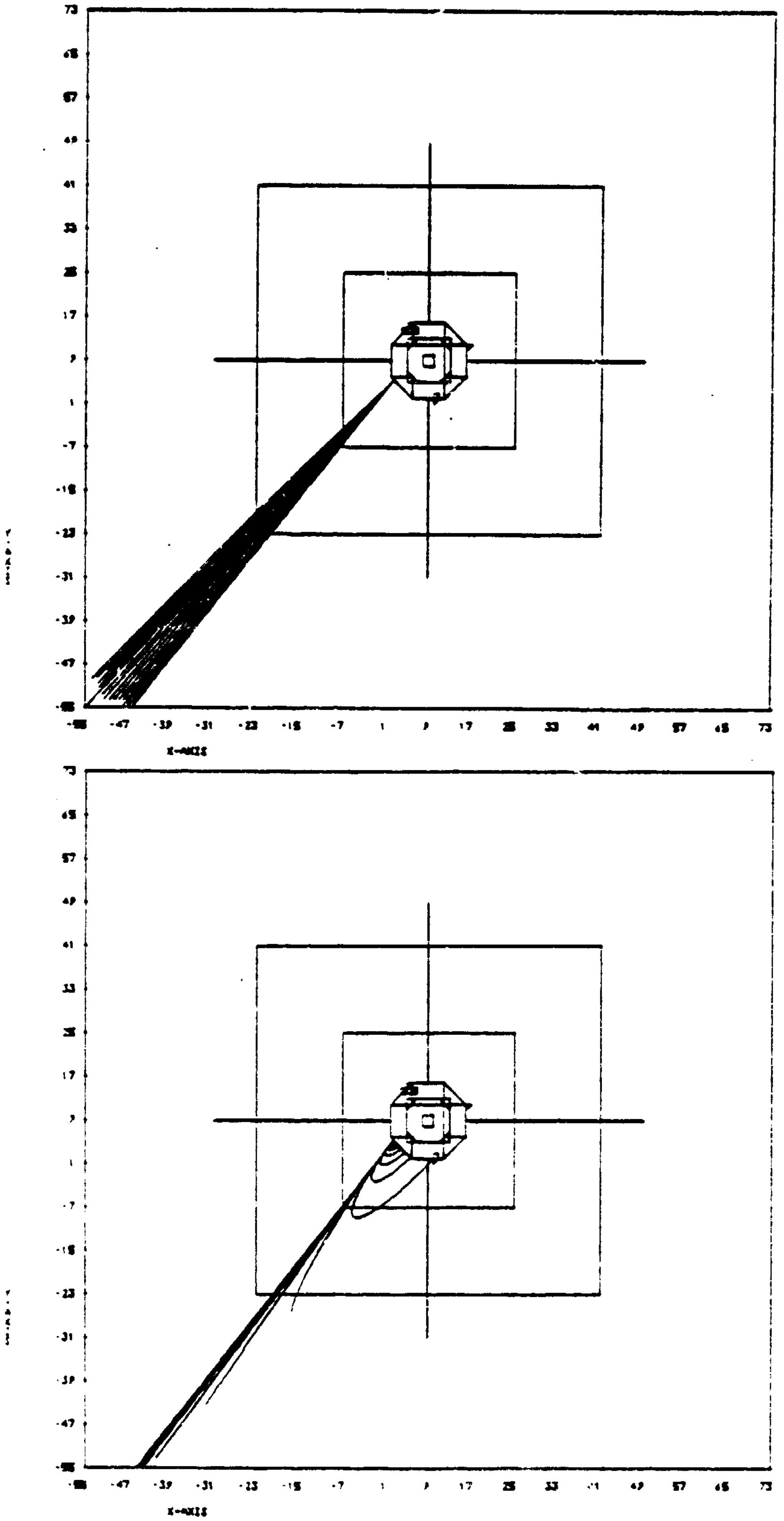

Figure 8.8. Trajectories of electrons (top) and protons (bottom) logarithmically spaced from 50-60,000 eV, observed at SC5 bellyband detector.

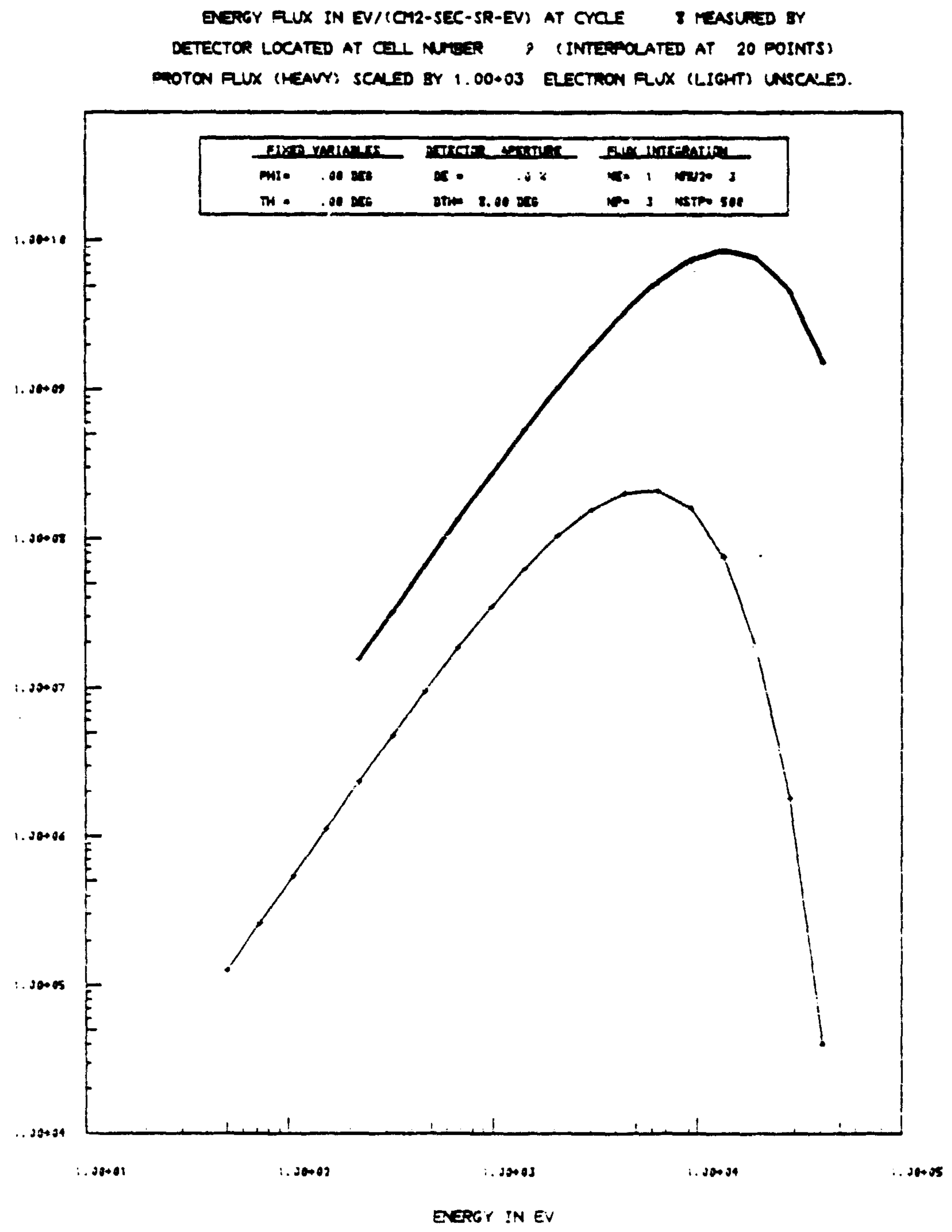

Figure 8.9. Simulated response of SC5 bellyband detector to incoming electrons and protons, 50-60,000 eV, in Case 3 environment.

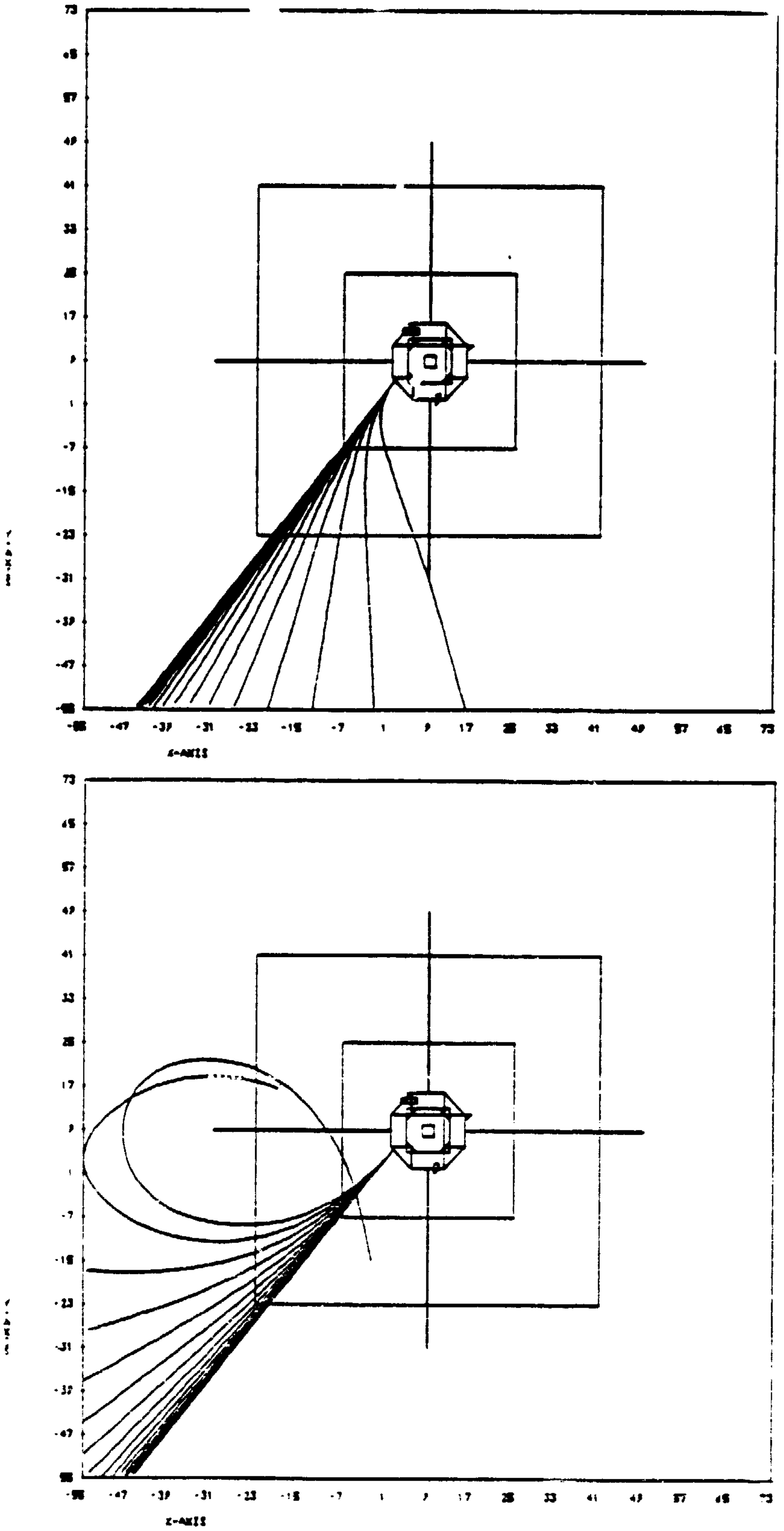

Figure 8.10. Trajectories of electrons (top) and protons (bottom) logarithmically spaced from 50-60,000 eV, observed at SC5 bellyband detector.

8.3 SC7 DETECTOR SIMULATIONS

The SC7 light ion mass spectrometer measures the cold (0 < 100 eV) ionic component of the plasma using three sensors located parallel, antiparallel, and perpendicular to the satellite spin axis. The SC7 detectors have a much larger field of view, 110°, than the other particle spectrometers. Since low energy ions are observed, their trajectories can be perturbed by the electrostatic fields of the satellite even when the vehicle is not highly charged. Two comparison cases have been run to illustrate this effect. These trajectories differ from others presented in this chapter in that the energy is fixed for all trajectories while the azimuthal angle of the incident particles is varied from 0 to 360°. The polar incident angle was fixed at 45°. Figure 8.11 shows trajectories of 50 eV protons entering the SC7-1 bellyband detector for the Case 1 potentials. Little perturbation of the trajectories is observed in these weak fields. Trajectories for the Case 3 moderate temperature plasma are illustrated in Figure 8.12. Here significant distortion of incoming trajectories results from the influence of the highly charged SC2 boom tips. Similar effects can be seen for the SC7-2 and -3 detectors.

8.4 SC9 DETECTOR SIMULATIONS

The SC9 UCSD charged particle experiment consists of three detectors mounted together on the forward surface of the satellite. There are two rotating detectors for electrons and ions, one scanning the range 0.2 eV to 1550 eV and the other scanning the range 1 eV to 81 keV. The third detector scans the low energy range for ions only. This section reports simulations of detector response at fixed detector angles while scanning the lower and higher energy ranges.

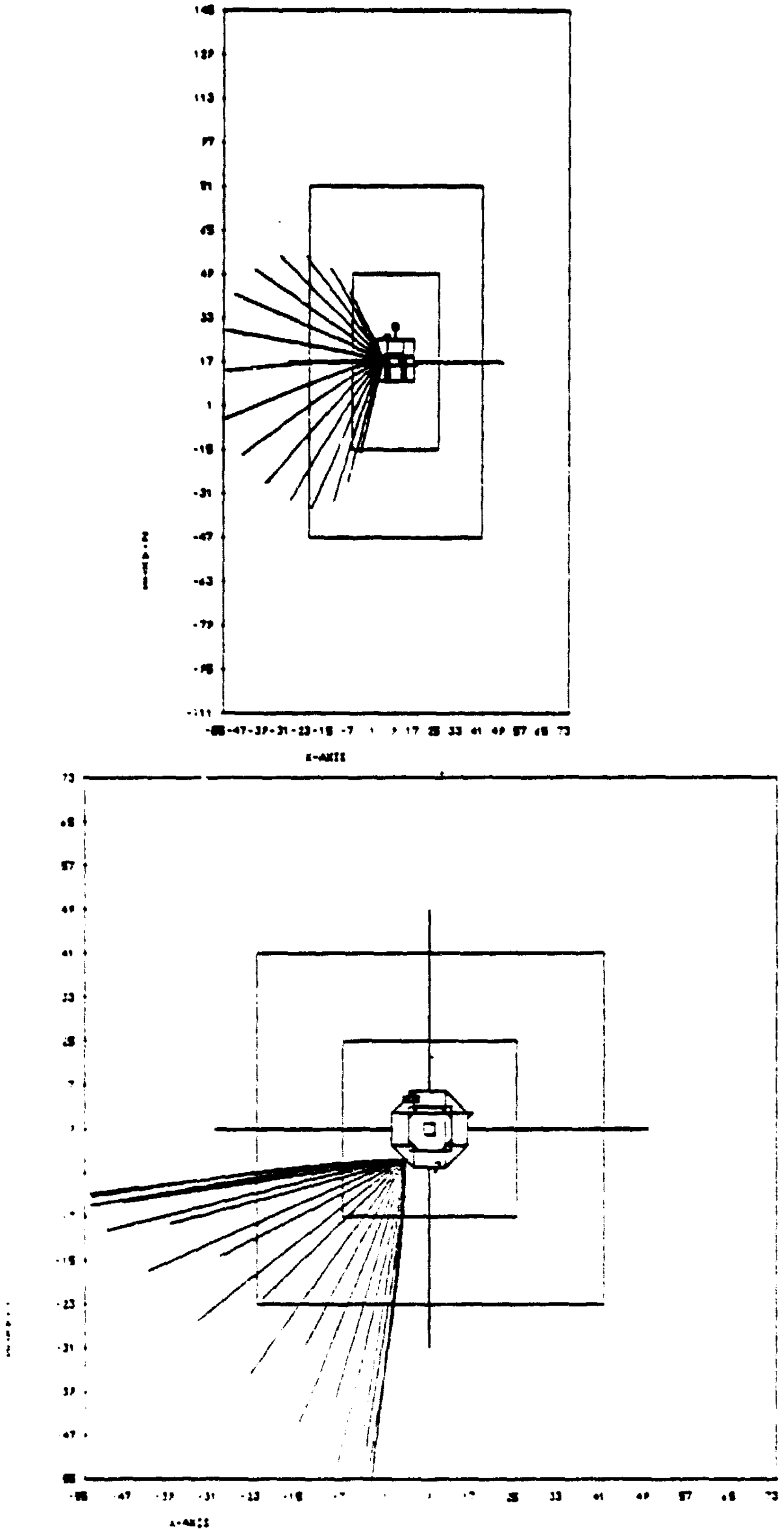

Figure 8.11. Trajectories of protons in X-Z plane (top) and X-Y plane (bottom) observed at SC7-1 detector for Case 2 environment.

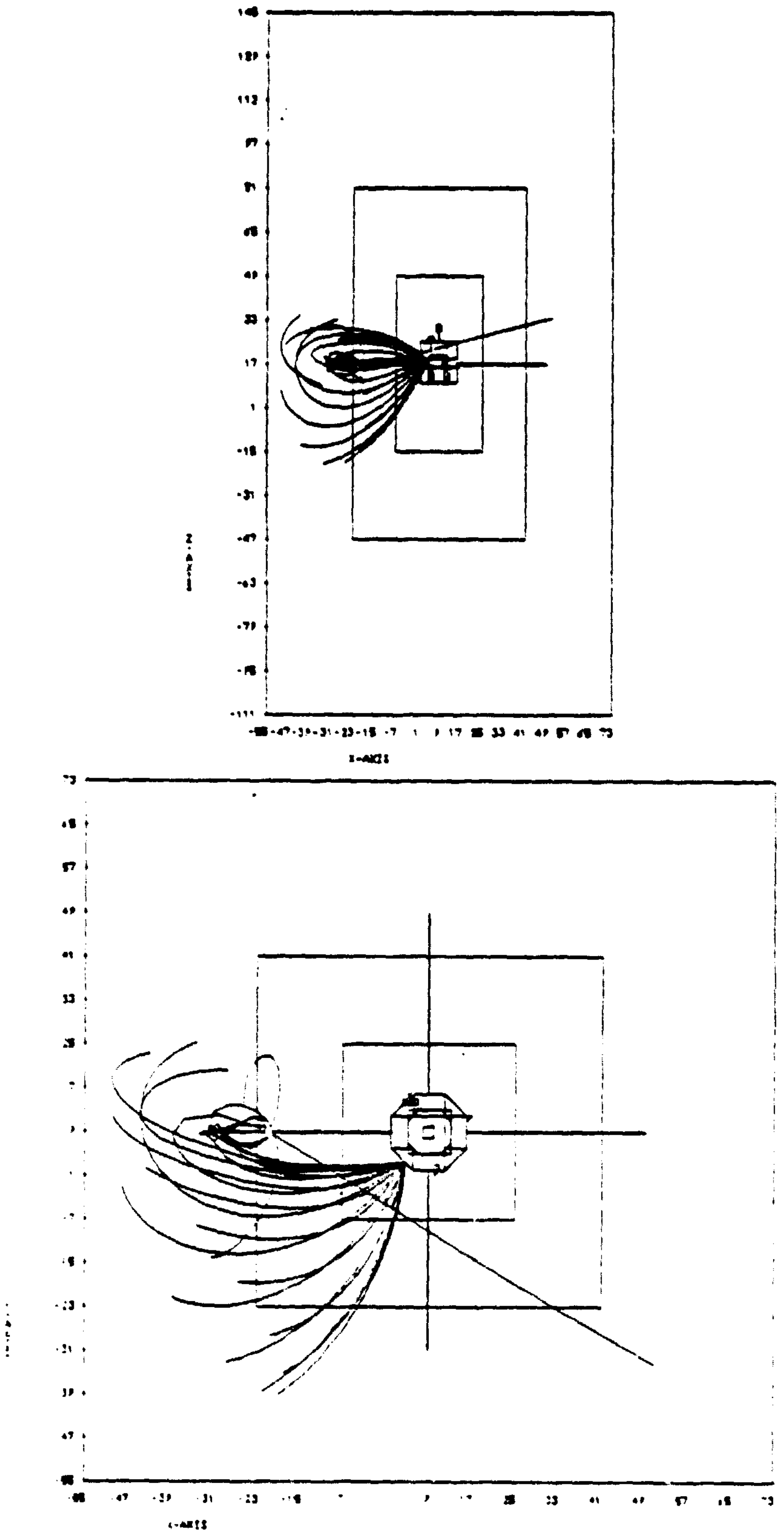

Figure 8.12. Trajectories of protons in X-Z plane (top) and X-Y plane (bottom) observed at SC7-1 detector for Case 3 environment.

Detector response in the two high temperature plasma cases are represented in Figures 8.13 through 8.16. For Case 1, with the vehicle essentially uncharged, the incident spectrum to the high energy detector looking parallel to the spin axis appears as in Figure 8.13. Only the very lowest energy electron trajectories, at a few eV, are perturbed by the weak spacecraft fields, as shown in Figure 8.14. Corresponding results for the highly charged eclipse state, Case 2, are shown in Figures 8.15 and 8.16. Protons below the spacecraft potential, -6400 V, have trajectories terminating elsewhere on the vehicle. Finally, the response to the moderate temperature environment, Case 3, is illustrated in Figures 8.17 and 8.18. The proton spectrum cuts off at the spacecraft potential, -140 volts, and the trajectories are dramatically perturbed by the SC2 boom. The smooth spectrum for incident electrons gives no hint that the low energy trajectories are influenced by stray fields from the OMNI antenna.

The response of the low energy ion fixed angle detector is even more interesting in the Case 3 environment. The predicted incident spectrum has a gap in the middle energy range, shown in Figure 8.19. The corresponding trajectories, Figure 8.20, illustrate the reason for the complex response. High energy protons travel to the detector in nearly straight paths. Middle range protons are accelerated towards the charged SC2 boom, where they impact, leading to the gap in the spectrum. The lowest energy electrons are accelerated so strongly towards the boom tip that they pass below the boom plane and then orbit the boom once without striking, then pass away from the boom region and connect to trajectories at infinity.

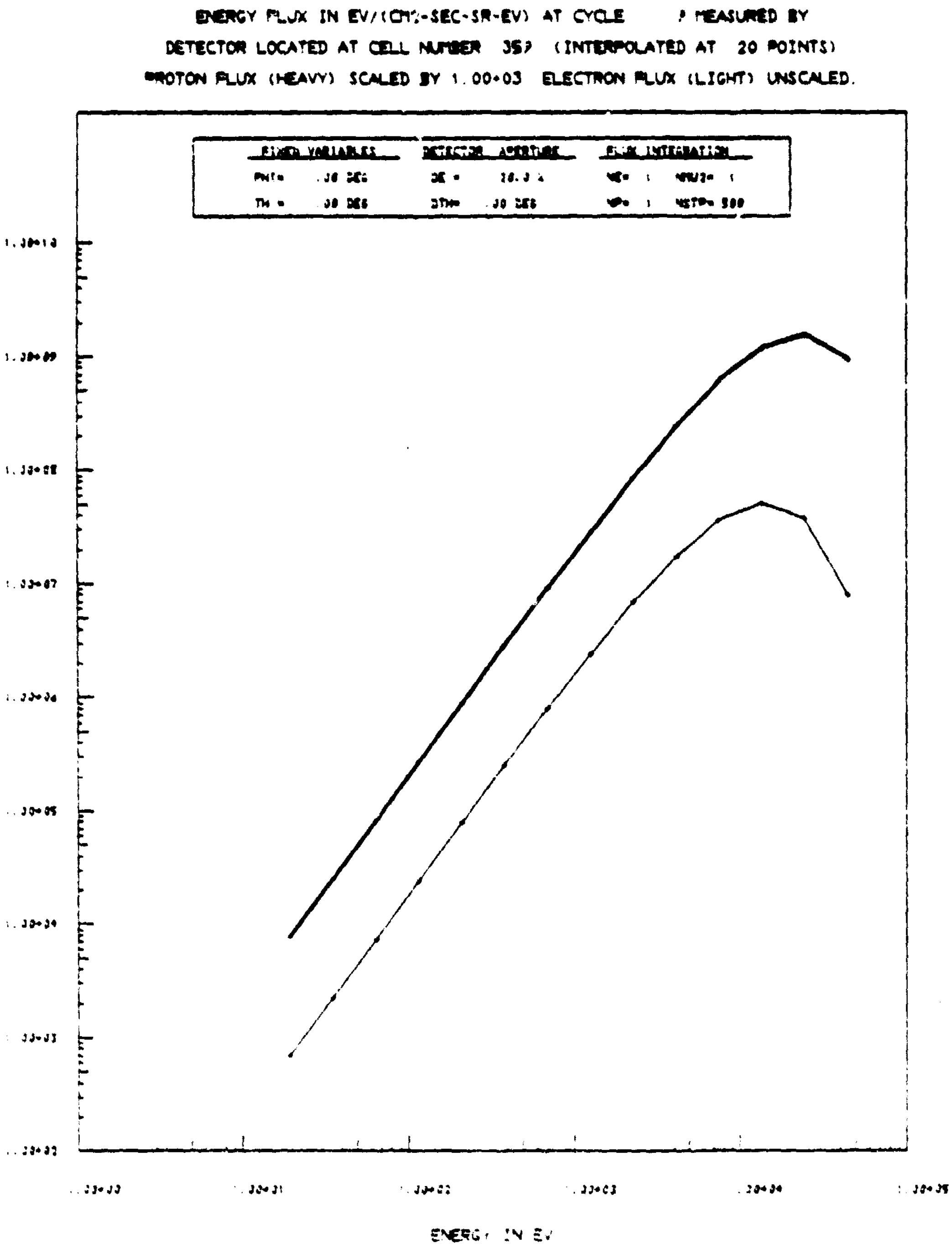

Figure 8.13. Simulated response of SC9 NS detector to incoming electrons and protons, 1-81,000 eV, in Case 1 environment.

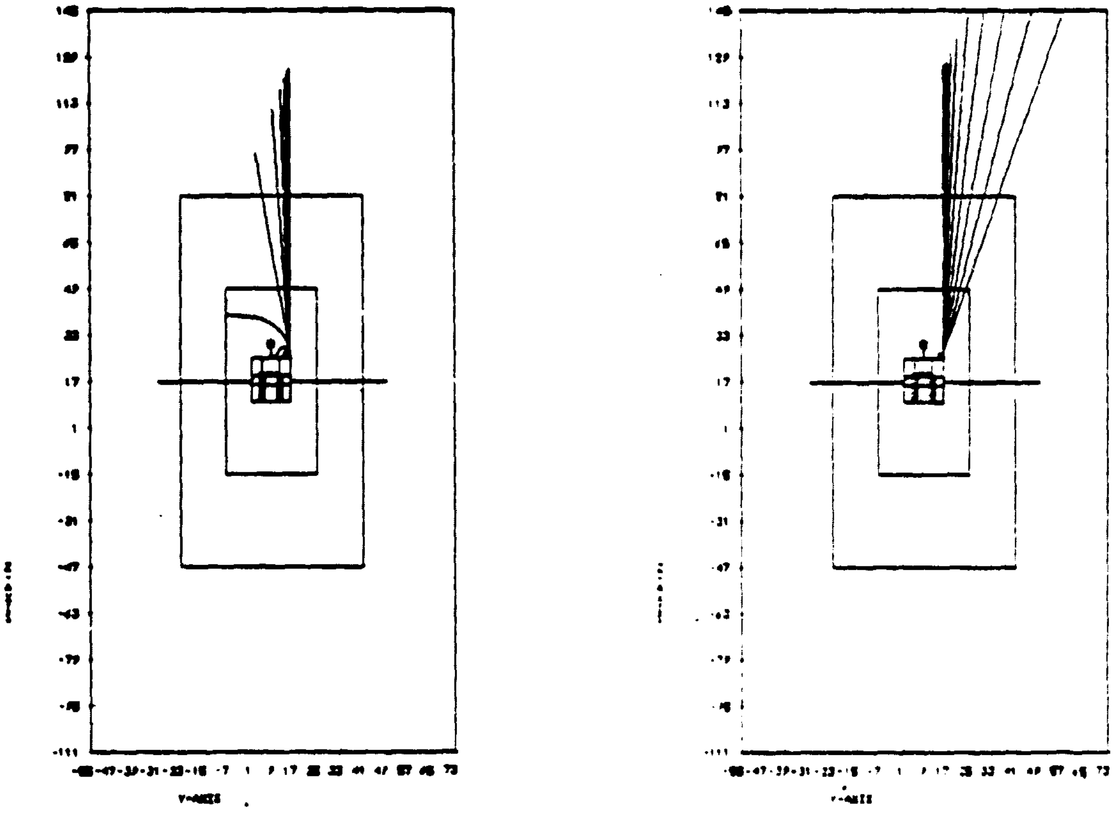

Figure 8.14. Trajectories of electrons (left) and protons (right) logarithmically spaced from 1-81,000 eV, observed at SC9 location for Case 1 environment.

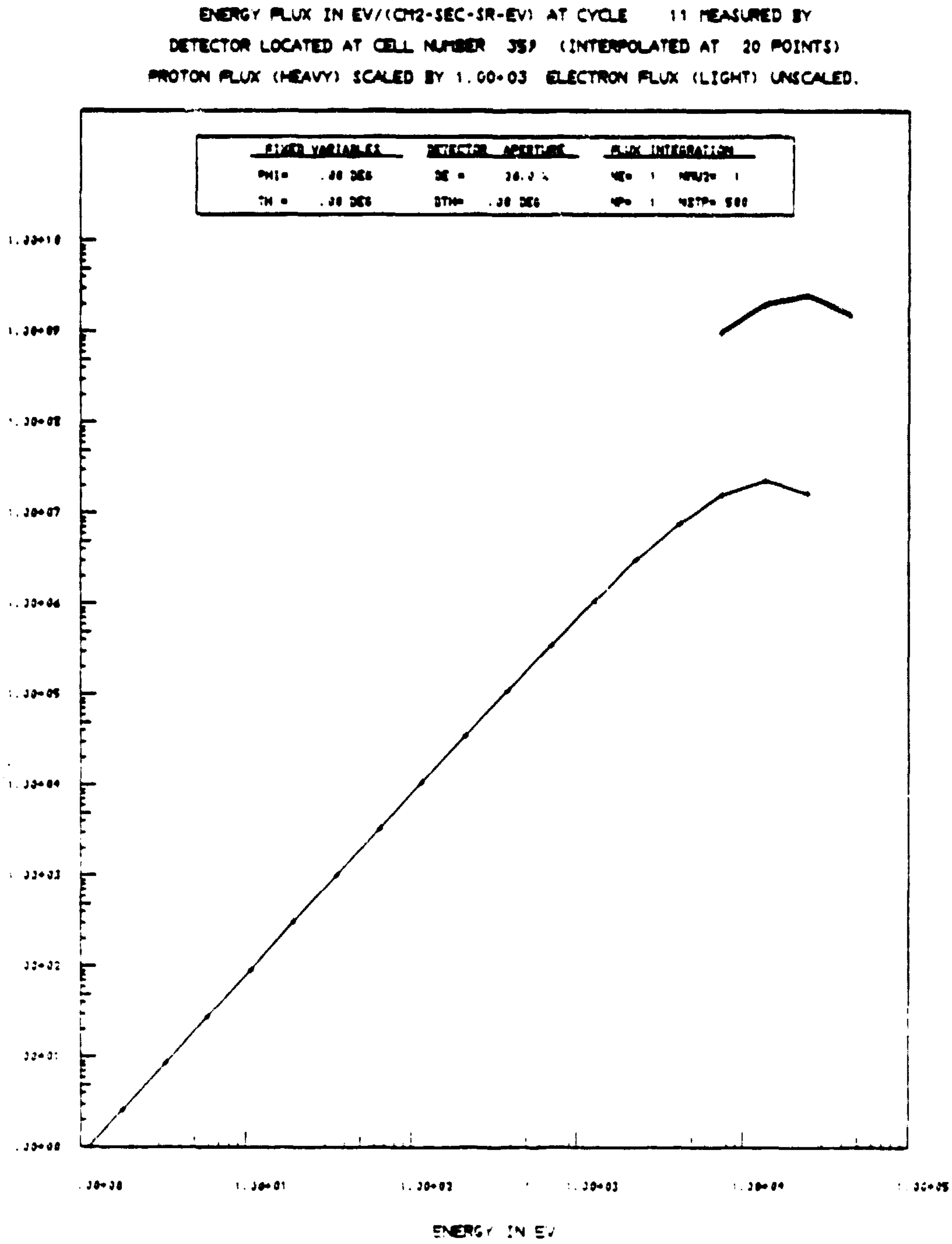

Figure 8.15. Simulated response of SC9 NS detector to incoming electrons and protons, 1-81,000 eV, in Case 2 environment.

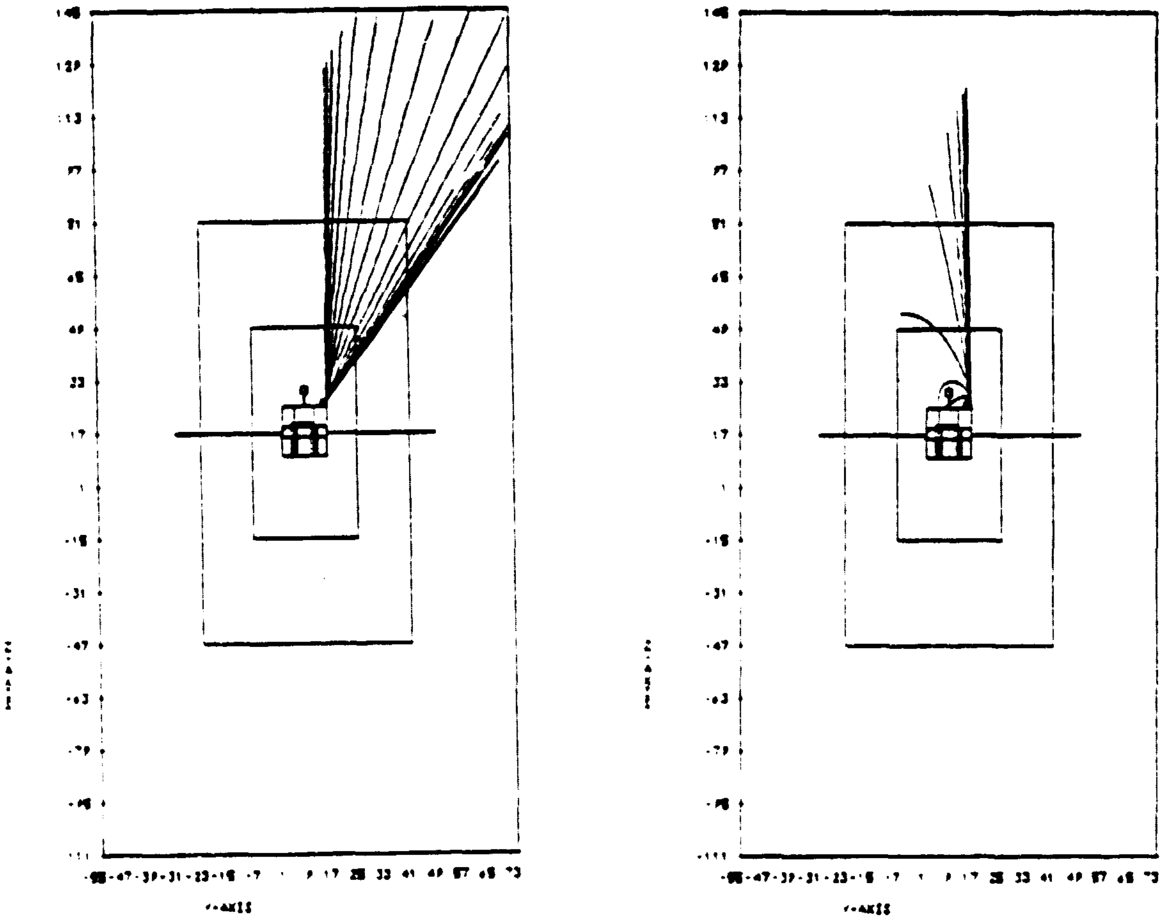

Figure 8.16. Trajectories of electrons (left) and protons (right) logarithmically spaced from 1-81,000 eV, observed at SC9 location for Case 2 environment.

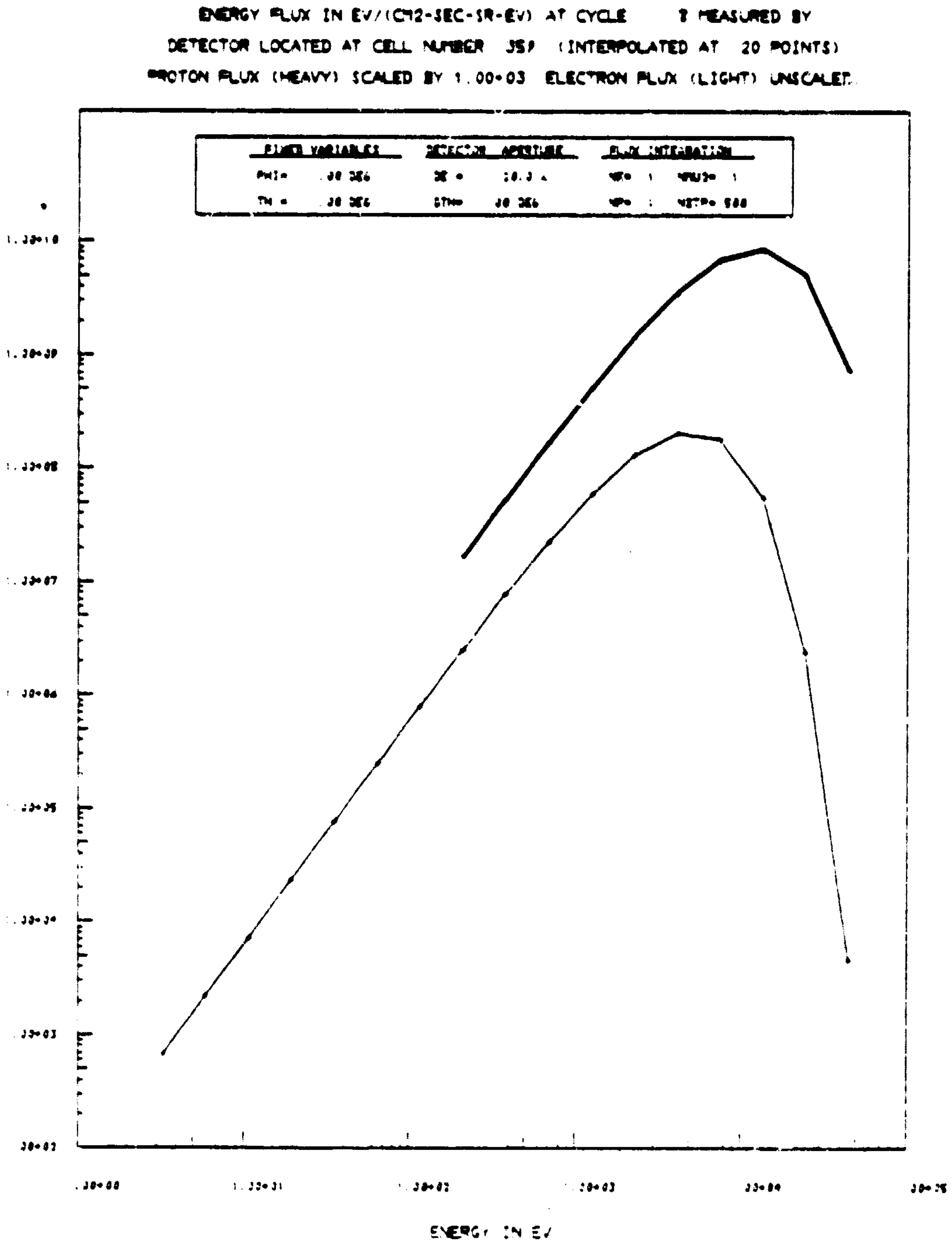

Figure 8.17. Simulated response of SC9 NS detector to incoming electrons and protons, 1-81,000 eV, in Case 3 environment.

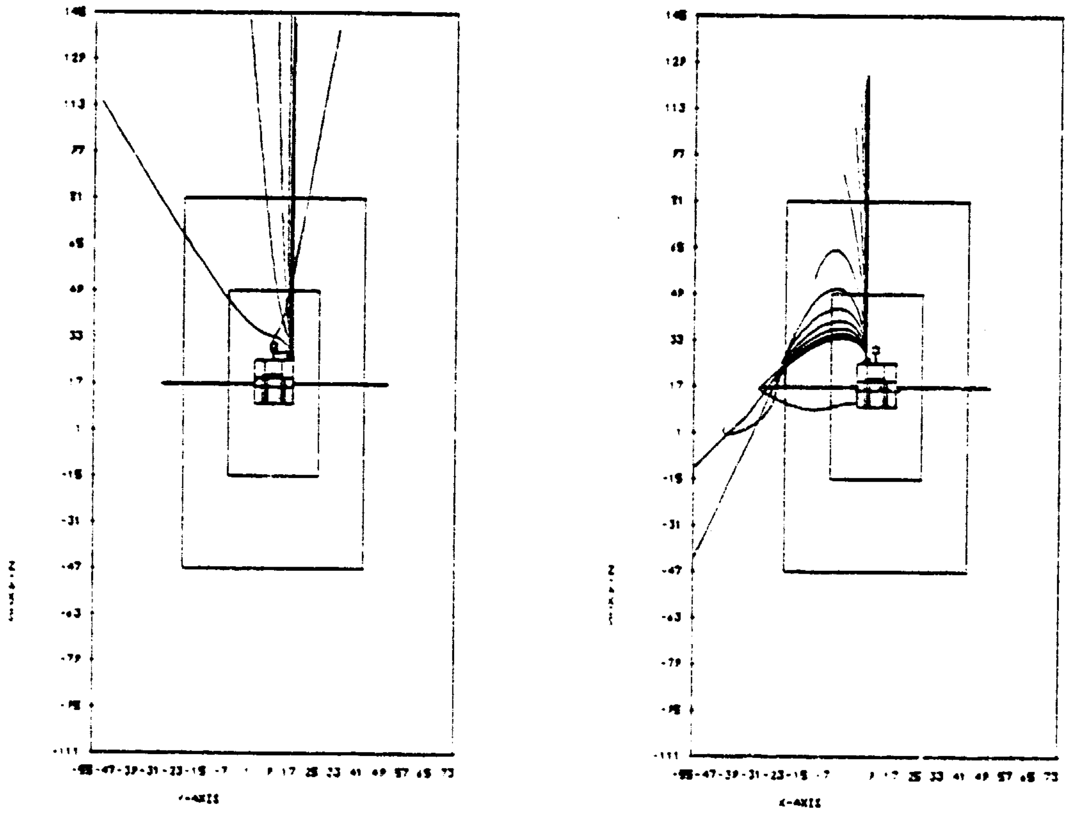

Figure 8.18. Trajectories of electrons (left) and protons (right), logarithmically spaced from 1-81,000 eV, observed at SC9 location for Case 3 environment.

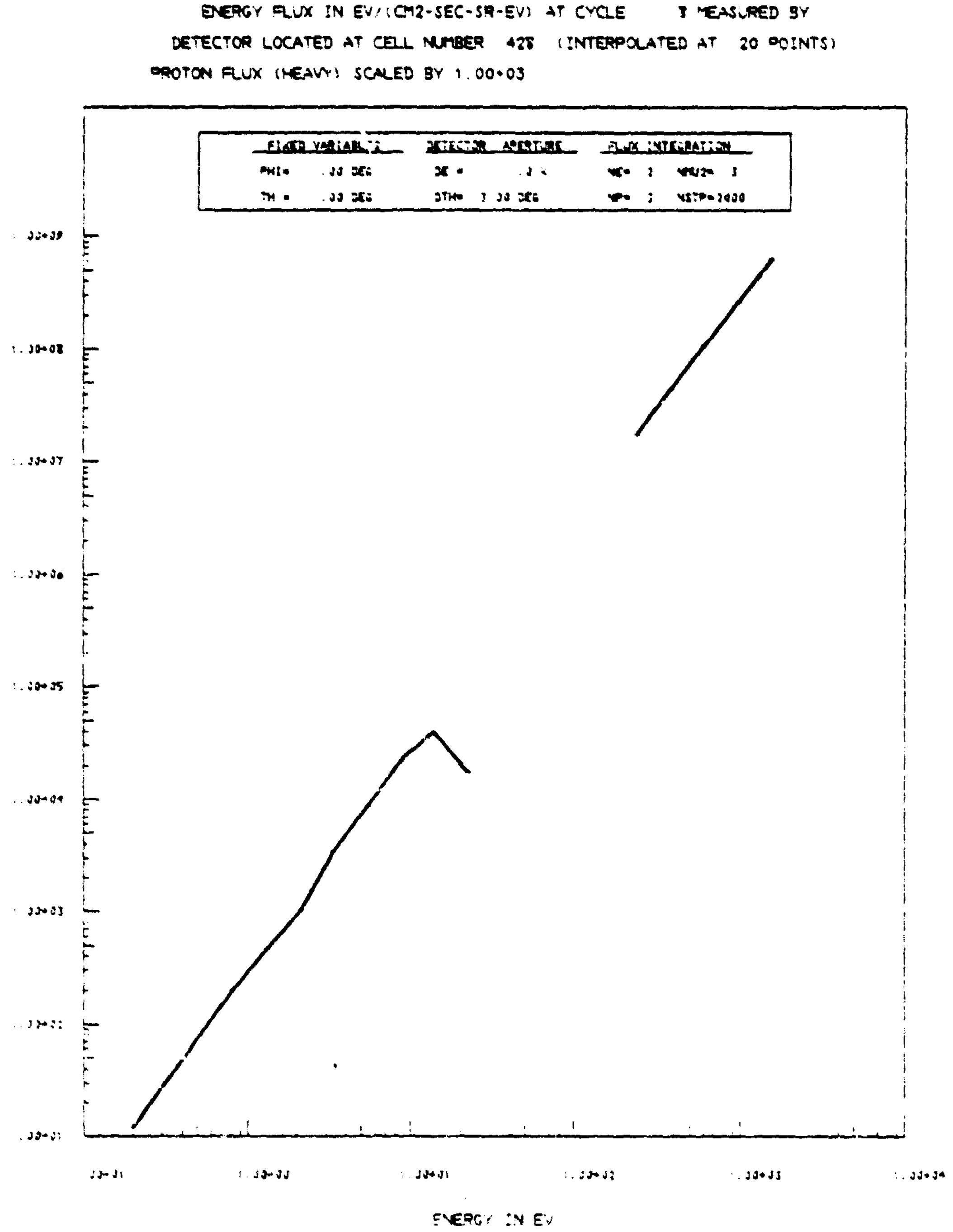

Figure 8.19. Simulated response of SC9 fixed head ion detector to incoming protons, 0.2-1550 eV, in Case 2 environment.

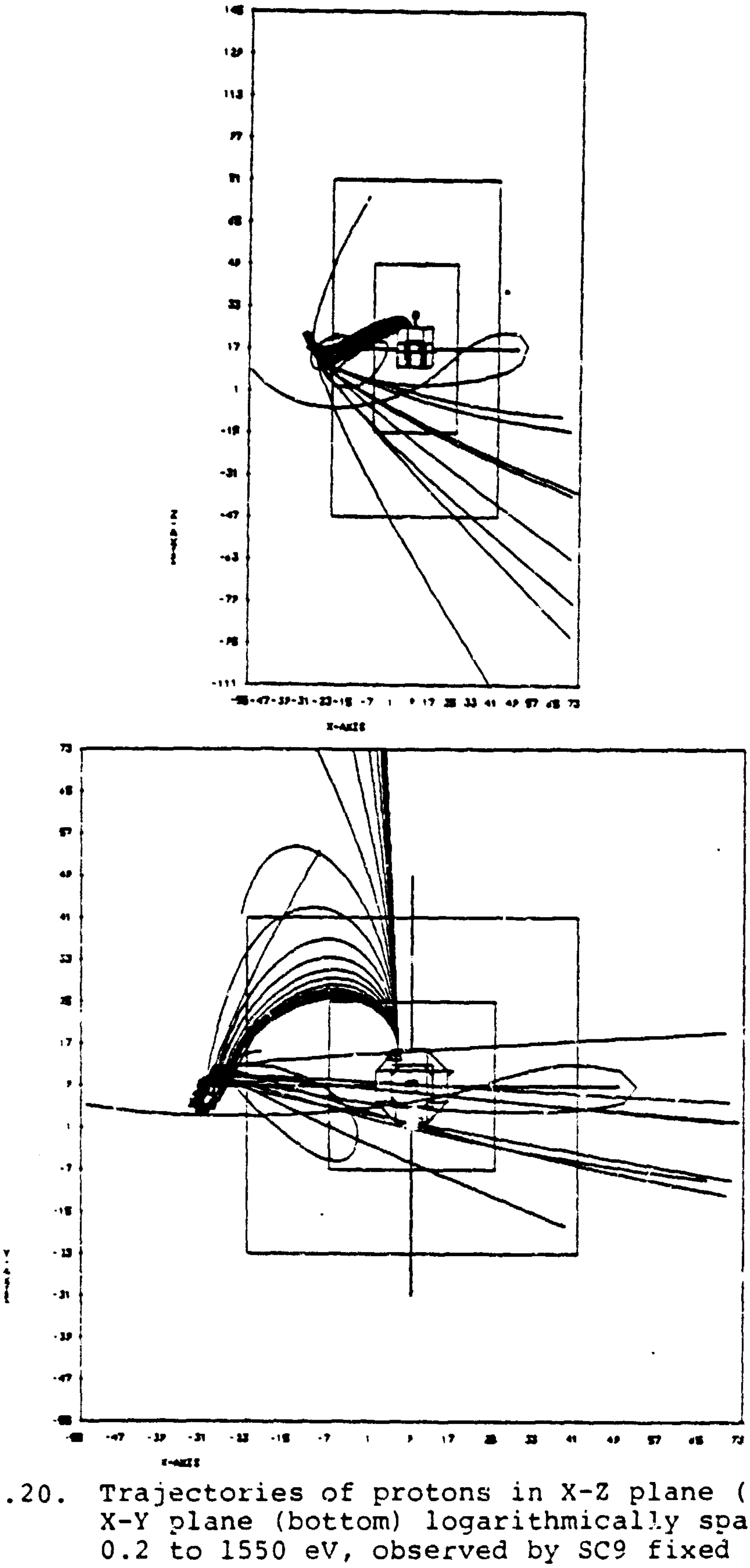

Figure 8.20. Trajectories of protons in X-Z plane (top) and X-Y plane (bottom) logarithmically spaced from 0.2 to 1550 eV, observed by SC9 fixed head detector.

9. HOT SPOT THEORY

The study of dark side potentials in limiting the effectiveness of photoelectrons to discharge sunlit surfaces has raised the question as to the effect of small shaded insulators on nearby photoemission. Some estimates of such effects have been found by numerical calculations, but in order to get a better overall understanding we have also examined the problem analytically. The analysis described below should prove useful in understanding the importance of highly charged hot spots on the SCATHA spacecraft.

We have constructed a model problem of a single circular region on an infinite insulating plane. The circle is uniformly charged to a large negative voltage V, ($\sim$-5 kV) while the remainder of the plane is exposed to intense sunlight and an incident high energy electron flux (e.g., 5 kV Maxwellian). In the absence of the negative region, the photoemission would completely discharge the insulator and the potential would be a few volts positive uniformly on the plane. The "hot spot" sets up a local potential barrier which prevents photo and secondary electrons from leaving the insulator. As a result, charge accumulates and the insulator goes negative. Below we discuss using analytical models of the spatial dependence of the potential caused by the "hot spot" effect.

9.1 HOT SPOT IN THE ABSENCE OF SHEATH CONDUCTION

In the case where sheath conduction is small, the influence of a hot spot is similar to that of the negatively charged dark side in the sunlit sphere case discussed by Katz, et al.[2] The essential feature is that photoemission and secondary emission can support only very small electric fields normal to the emitting surfaces. As a result, equipotential contours from a flat circular hot spot on an infinite insulating plane must be approximately normal to the plane. The net effect is to make the insulator "disappear" (see Figure 9.1). A similar effect with regards to photoemitting booms was observed by Schnuelle, et al. on the NASCAP model of SCATHA.[5]

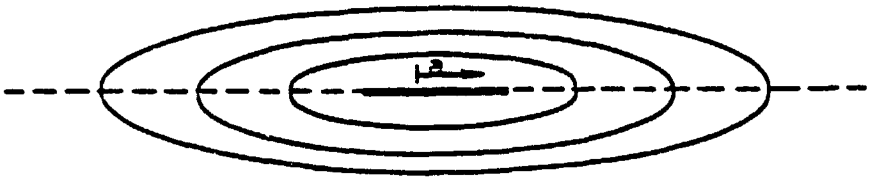

Figure 9.1. Potential contours around an isolated disk. Since the contours are perpendicular to the dashed line, the electric field normal to the line is precisely zero.

The analytical potential in the plane of a disk at potential V_o of radius a falls off in r as

$$V(r) = \frac{2V_o}{\pi} \arcsin (a/r) \quad (r > a) \tag{9.1}$$

In the limit of $r \gg r_o$ (see Table 9.1)

$$V(r) \cong \frac{2V_o}{\pi} \left(\frac{a}{r}\right) \tag{9.2}$$

From previous experience with photosheath behavior we imagine this to be a good representation of the hot spot influence, and a rigorous upper bound of the potential deviation from the same case without a hot spot.

TABLE 9.1. COMPARISON OF ANALYTICAL REPRESENTATIONS OF HOT SPOT POTENTIALS

r	$2/\pi \arcsin 1/r$	$2/\pi r$
1	1	
1.001	0.991	0.637
1.01	0.910	
1.1	0.726	
1.2	0.627	0.531
1.5	0.465	0.424
2.0	0.333	0.318
3.0	0.216	0.212

As a check of the usefulness of this approach we set up a NASCAP model of a charged square on an insulating octagonal surface. Increased secondary electron emission was used instead of sunlight so that both sides of the octagonal object would be the same. This was done to prevent "dark side" effects (such as saddle points), from masking hot spot effects. The "hot spot" consisted of biasing the potentials on nine surface cells to 5000 volts negative with respect to spacecraft ground. Since NASCAP linearly averages surface cell potentials to get nodal potentials, the effective area of the hot spot was $4\Delta X^2$ or 0.04 m^2. The radius of a disk with the same area would be 0.113 meters. Figure 9.2 shows the test object. In Table 9.2 we show the surface cell potentials along line x = 0 when V_o had floated to -5880 and compared to

$$V_{theory} = -\frac{2 \cdot 5880}{\pi} \arcsin\left(\frac{0.1128}{r}\right) \tag{9.3}$$

Not surprisingly, the comparison is quite good, much better than 10 percent. This case was run primarily as a test of usefulness of the particular NASCAP object for representing a circular hot spot, as well as to demonstrate the validity of the simple insulating theory.

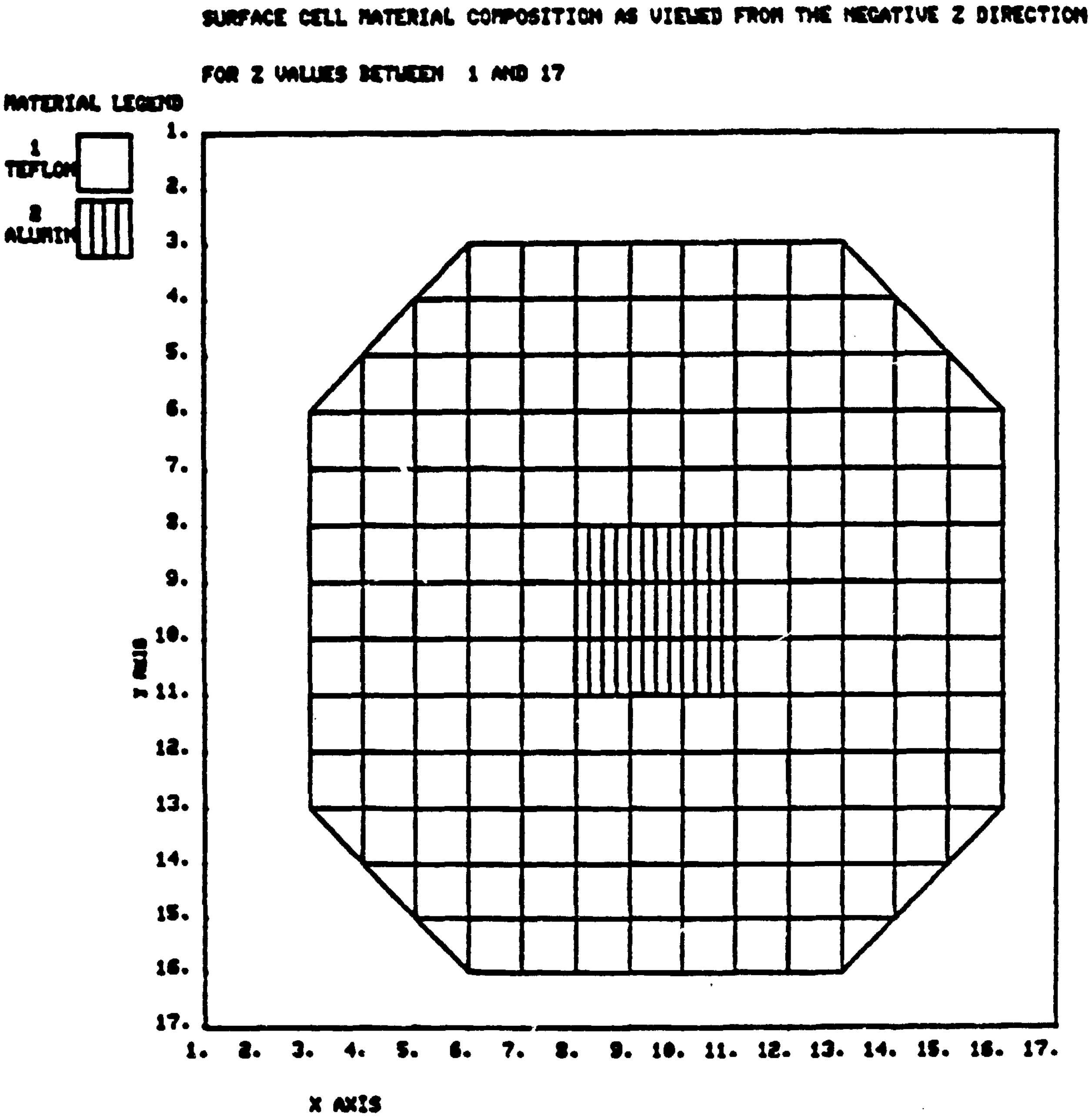

Figure 9.2. NASCAP test object.

TABLE 9.2. PERFECTLY INSULATING HOT SPOT POTENTIALS

$V_o = 5880$ $a = 0.1128$

R	V_{theory}	V_{NASCAP}
.2	-2248	-2110
.3	-1446	-1480
.4	-1072	-1070
.5	-843	-838
.6	-709	-688

9.2 PHOTOCONDUCTIVITY EFFECTS

The low energy electrons reflected by the potential barrier in front of the plate can carry current in the plane. The effect of this is to discharge the plate somewhat from the perfectly insulating case discussed in the previous section. However, from our experience from dark side saddle-points we do not expect a drastic modification of the results. The fundamental assumption is that the potential change, no matter how small, is large enough to prevent <u>all</u> low energy electrons from leaving the surface. As a result <u>all</u> of the incident plasma current must be transported away from the hot spot region as skin current to outside of the disk.

As a model problem we examine the same disk charged to potential V_o on an insulated flat plate. The disk has a radius a. The boundary condition on the plate is $V(\infty) = 0$ and the skin current, K, is zero at $r = a$. Current continuity on the plate is the fundamental equation for this system

$$\nabla \cdot K + J_o = 0 \qquad (9.4)$$

where J_o is the incident plasma current. Photosheath conduction is modeled by an effective conductivity

$$K = \sigma E_{||} \tag{9.5}$$

Using the effective photosheath formulation derived by Mandell, et al.,[7] we retain the inverse square dependence of the conductivity on the surface normal electric field, e.g.,

$$\sigma = A/E_{\perp}^2 \tag{9.6}$$

At a radius r the surface current integrated around the circumference must equal the integral of the incident current J_o over the disk from radius, a, of the hot spot to r.

$$K 2\pi r = \int_0^r J_o(r')\, 2\pi r' dr' \tag{9.7}$$

For simplicity let us assume J_o constant. Since we are assuming photoelectrons do not escape, a similar assumption concerning secondaries is equally valid. This helps justify J_o being a constant.

$$K 2\pi r = J_o \pi (r^2 - a^2) \tag{9.8}$$

Substituting for K

$$2\pi r \sigma E_{||} = J_o \pi (r^2 - a^2) \tag{9.9}$$

$$2\pi r \frac{A\, E_{||}}{E_{\perp}^2} = J_o \pi (r^2 - a^2) \tag{9.10}$$

We will expand around the zero conductivity solution, assuming small perturbations. Since for the zero conducting case

$E_\perp = 0$, we get

$$\left(E_\perp^1\right)^2 = \frac{2Ar}{J_o(r^2 - a^2)} E_{||}^o \tag{9.11}$$

where the superscript zero identifies the zero conductivity case and the one indicates the perturbed solution. To relate $E_\perp^1$ to a $\Delta V(r) \equiv V^1(r) - V^o(r)$ we must estimate the effective capacitance per unit area of the surface as a function of the radius r. To do this we have made the assumption that the capacitance is the same as the mean capacitance per unit area of an isolated disk of radius r. First we calculate the charge per unit area of a disk at potential V. At large radii (d >> r) the potential looks like

$$\phi = \frac{2\ Vr}{\pi d} = \frac{Q_{disk}}{4\pi\varepsilon_o d} \tag{9.12}$$

$$Q_{disk} = 8\varepsilon_o\ Vr \tag{9.13}$$

$$\left\langle E_\perp \right\rangle = \left(\frac{Q}{2\pi r^2}\right) \frac{1}{\varepsilon_o} = \frac{4V}{\pi r} \tag{9.14}$$

The term $2\pi r^2$ is the area of both sides of the disk, which enters in the perfectly insulating case.

Substituting we get a simple algebraic expression for ΔV in terms of $E_{||}^o$

$$(\Delta V)^2 = \frac{\pi^2\ r^3\ A\ E_{||}^o}{8(r^2 - a^2)J_o} \tag{9.15}$$

but

$$E^{o}_{||} = - \frac{d}{dr} \frac{2V_o}{\pi} \sin^{-1} \frac{a}{r} = \frac{2V_o}{\pi} \frac{a}{r^2} \frac{1}{\left(1 - \frac{a^2}{r^2}\right)^{1/2}}$$

$$= \frac{2V_o}{\pi} \frac{a}{r} \frac{1}{(r^2 - a^2)^{1/2}} \qquad (9.16)$$

Substituting for $E^{o}_{||}$

$$(\Delta V)^2 = \frac{V_o \pi}{4J_o} \frac{a\ r^2}{(r^2 - a^2)^{3/2}} \cdot A \qquad (9.17)$$

From Reference 7

$$A \simeq 4 \ \langle \varepsilon \rangle \ J_{sec}$$

$$(\Delta V)^2 = \pi V_o \frac{a\ r^2}{(r^2 - a^2)^{3/2}} \langle \varepsilon \rangle \frac{J_{sec}}{J_o} \qquad (9.18)$$

To examine the usefulness of this expression we ran the identical NASCAP case in the insulating case, but included secondary sheath conductivity as per Reference 7. The relevant values are

$$\langle \varepsilon \rangle = 2 \text{ eV}$$

$$\frac{J_{sec}}{J_o} = 7.6$$

$$V_o = -5880$$

and the effective

$$a = 0.1128$$

was used in the perfectly insulating case. The comparison of theory and experiment is shown in Table 9.3. While the agreement is not as good as in the perfectly insulating case, it is still better than 20 percent.

TABLE 9.3. HOT SPOT WITH PHOTOCONDUCTIVITIES

$V_o = -5890 \qquad a = 0.1128$

R	ΔV_{theory}	ΔV_{NASCAP}	V_{theory}	V_{NASCAP}
.2	531	570	-1717	-1540
.3	250	390	-1196	-1090
.4	169	282	-903	-788
.5	129	174	-714	-664
.6	105	117	-604	-571

9.3 CONCLUSIONS

Both the simple theory and NASCAP predict hot spots to affect insulating surfaces on a scale of the hot spot size. The similarity between hot spot effects and other potential barriers seen in the sunlit sphere and SCATHA calculations is more than coincidental. The dominant physical mechanism is the photo and secondary electron limiting which sets small normal electric field boundary conditions on the Poisson problem. This makes the exposed insulator seem to "disappear". The photosheath conductivity is effective in diminishing hot spot effects, but its inverse square dependence on normal electric field strength minimizes any difference in the solution.

It is worth noting that not only was the conducting sheath in the NASCAP example useful as a test of the simple theory, but it was also a good test of the NASCAP photosheath conduction algorithm. The sensitivity of the conductivity to small field changes led to small (~50 volt) oscillations in the final solution.

10. THE STRUCTURE OF THE LOW ENERGY PHOTOELECTRON SPACE CHARGE SHEATH

One aspect of spacecraft charging that had not been thoroughly investigated using NASCAP has been the structure of the space charge barrier formed by photoelectrons. This barrier, while small in voltage compared to substorm induced charging, is of interest both theoretically and experimentally. Experiments, such as SC-10 and SC-2 can make inferences about the sheath structure. The extent and magnitude of the sheath can be important in unfolding ambient electric field data.

Previous NASCAP calculations did not take the space charge of the photosheath into account because the voltage perturbations of the sheath are extremely small compared to the kilovolt/meter fields set up by differential or spacecraft charging during substorms. However, for the case of the unfolding of SC-10 during quiescent conditions, the space charge sheath is the dominant source of field differentials between the two halves of the dipole. This experiment has provided electric field strength as a function of distance in front of SCATHA.

10.1 CODE MODIFICATIONS

In order to predict the space charge barrier, a slight modification of the NASCAP explicit photosheath treatment was necessary. The "SHEATH" option in NASCAP predicts photocharge densities, but does not use them for potential calculations. The space charge calculations run for SCATHA were made using the calculated space charge, and the potentials and charge densities were iterated on until self-consistency was obtained between the potentials and the charge densities obtained from particle tracking. This procedure converged quite rapidly. Another improvement in the "SHEATH" routine, that is, emission of photoelectrons at several angles rather than just normal to the surface, was made to calculate more accurate charge densities.

These modified SHEATH routines are not designed for general use with NASCAP for several reasons. First, the self-consistent routines are presently implemented only for fixed spacecraft ground potentials, since the net photosheath currents are not available to the LONGTIMESTEP features of the code. Secondly, to track particles and iterate on the potentials would make this procedure prohibitive to use on a production basis because of computer time requirements. However, for those interested in scientific investigations of the low energy sheath structure the keyword in the RDOPT file is "SHEATH SELF CONSISTENT". A number can be included on the card after these keywords to specify the charge density relaxation parameter, α;

$$\rho = \alpha\rho_{new} + (1-\alpha)\rho_{old} \qquad (10.1)$$

A value of unity for α would correspond to explicit iteration. The default value is

$$\alpha_{default} = 0.5 \qquad (10.2)$$

With the default value of the relaxation parameter a typical run converged to within ±5 percent in the charge density after five iterations.

10.2 RESULTS

Tests of the new SHEATH routines were performed using a simplified version of the SCATHA one-grid model. A zone size of 0.23 m was used on a SCATHA model with no booms. The surfaces were all treated as conductors with a photoyield of 2×10^{-5} A/m^2. Calculations were performed at fixed satellite potentials of +0.5, +1.0, and +5.0 volts. Figures 10.1 through 10.6 illustrate the results for the most interesting

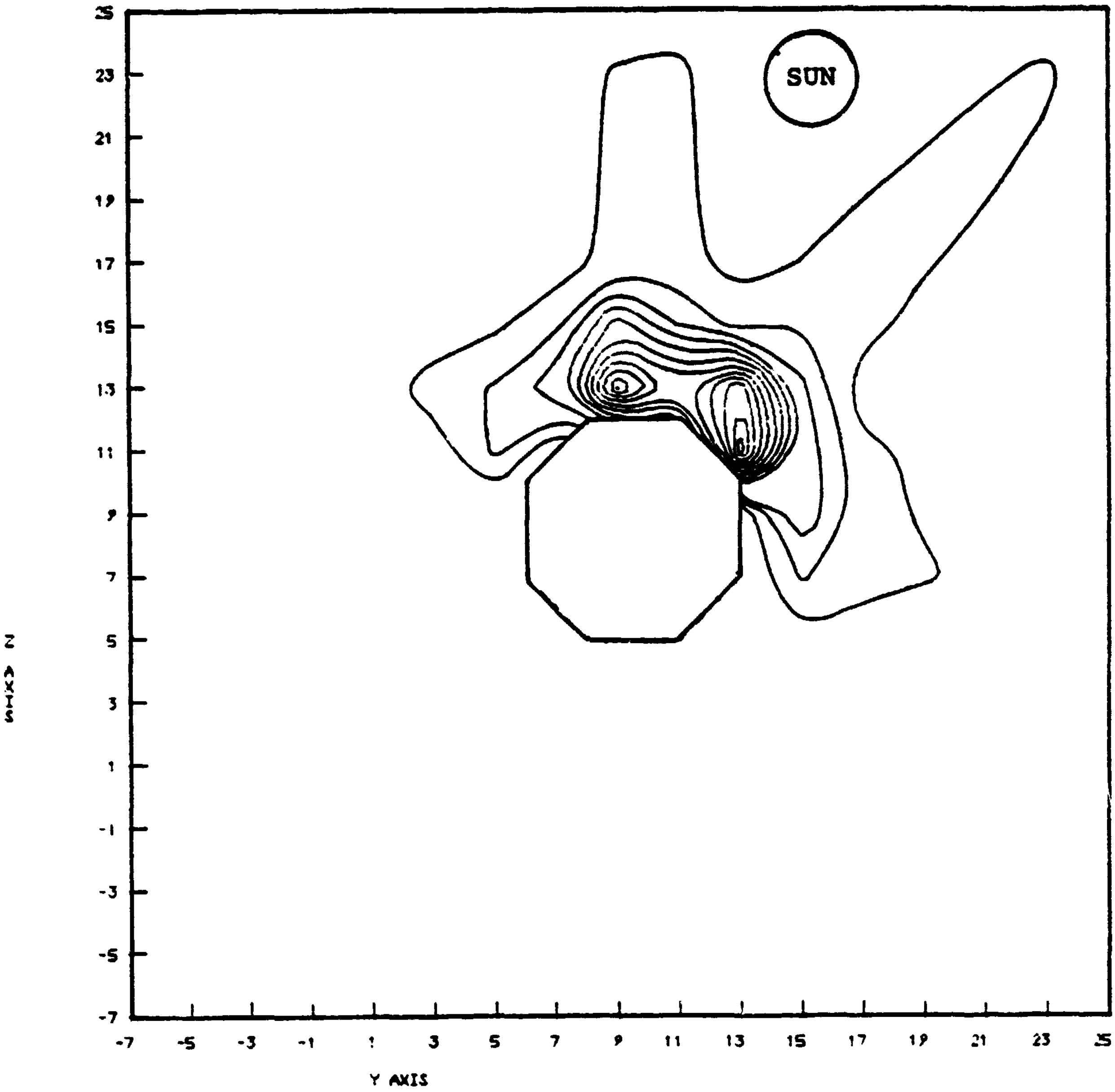

Figure 10.1. Self-consistent sheath contours around a simplified SCATHA model, vehicle potential = +0.5 volts, top view. Contours are in units of code units of charge per cubic mesh unit, from 0. to -0.24 in steps of 0.02. The zone size is 0.23 m; to convert the contour levels to coul/m^3, multiply by $\varepsilon_o/(0.23)^2 = 1.67 \times 10^{-10}$.

C-3

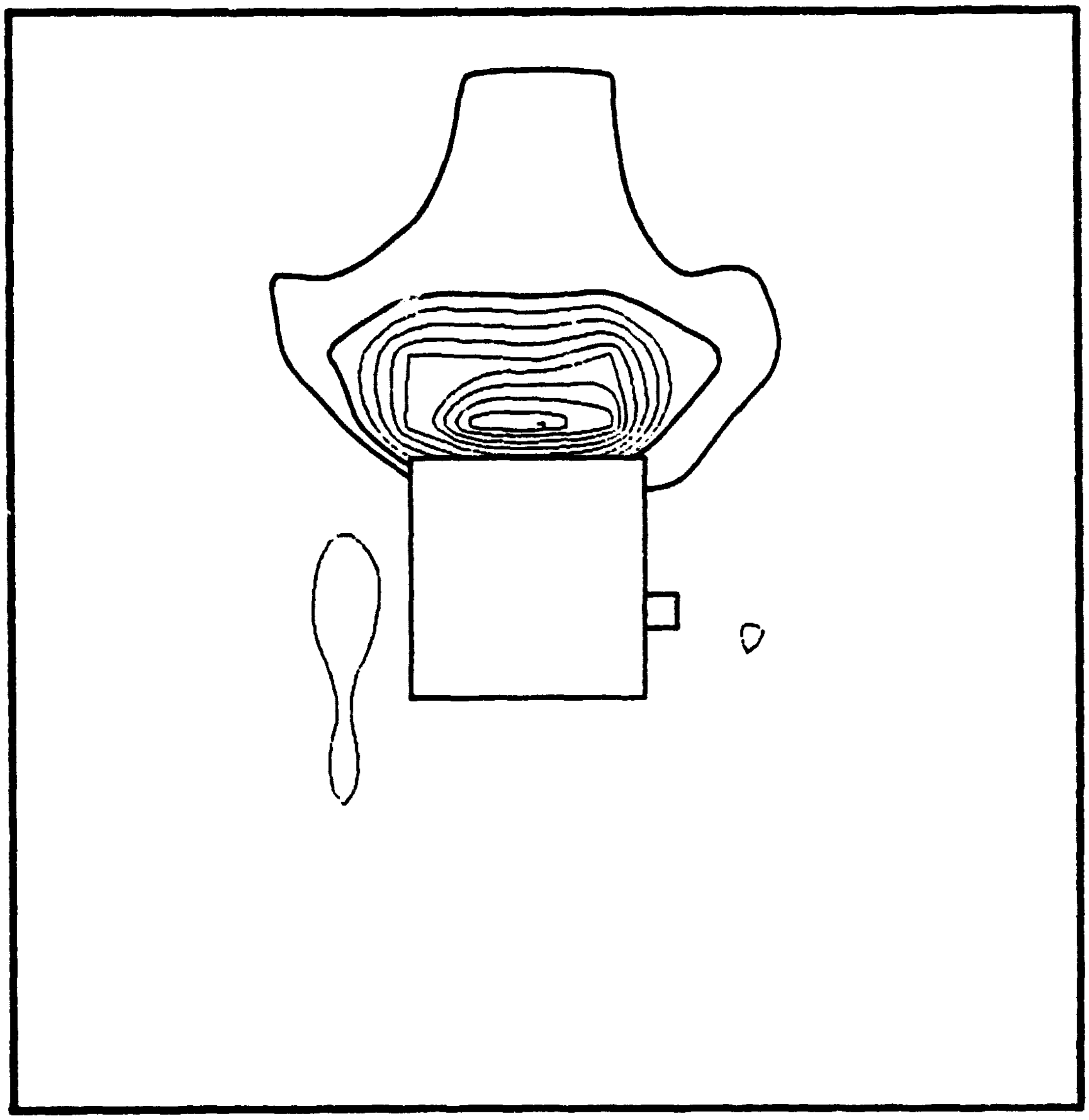

Figure 10.2. Self-consistent sheath contours around a simplified SCATHA model, vehicle potential = +0.5 volts, side view. Contour levels are the same as in Figure 10.1.

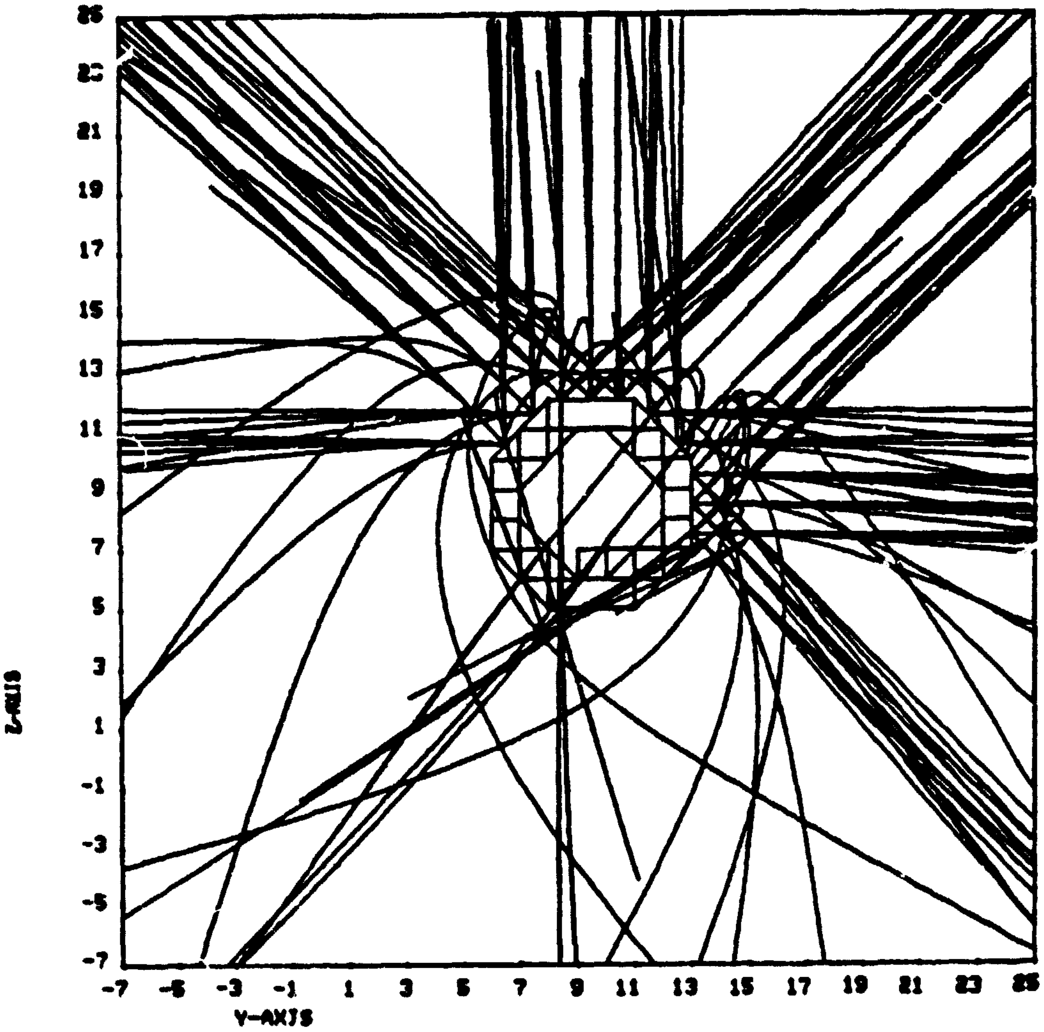

Figure 10.3. Photoelectron trajectories from bellyband cells for simplified SCATHA model, vehicle potential = +0.5 volts. Lower energy electrons are returned to the vehicle by the space charge barrier.

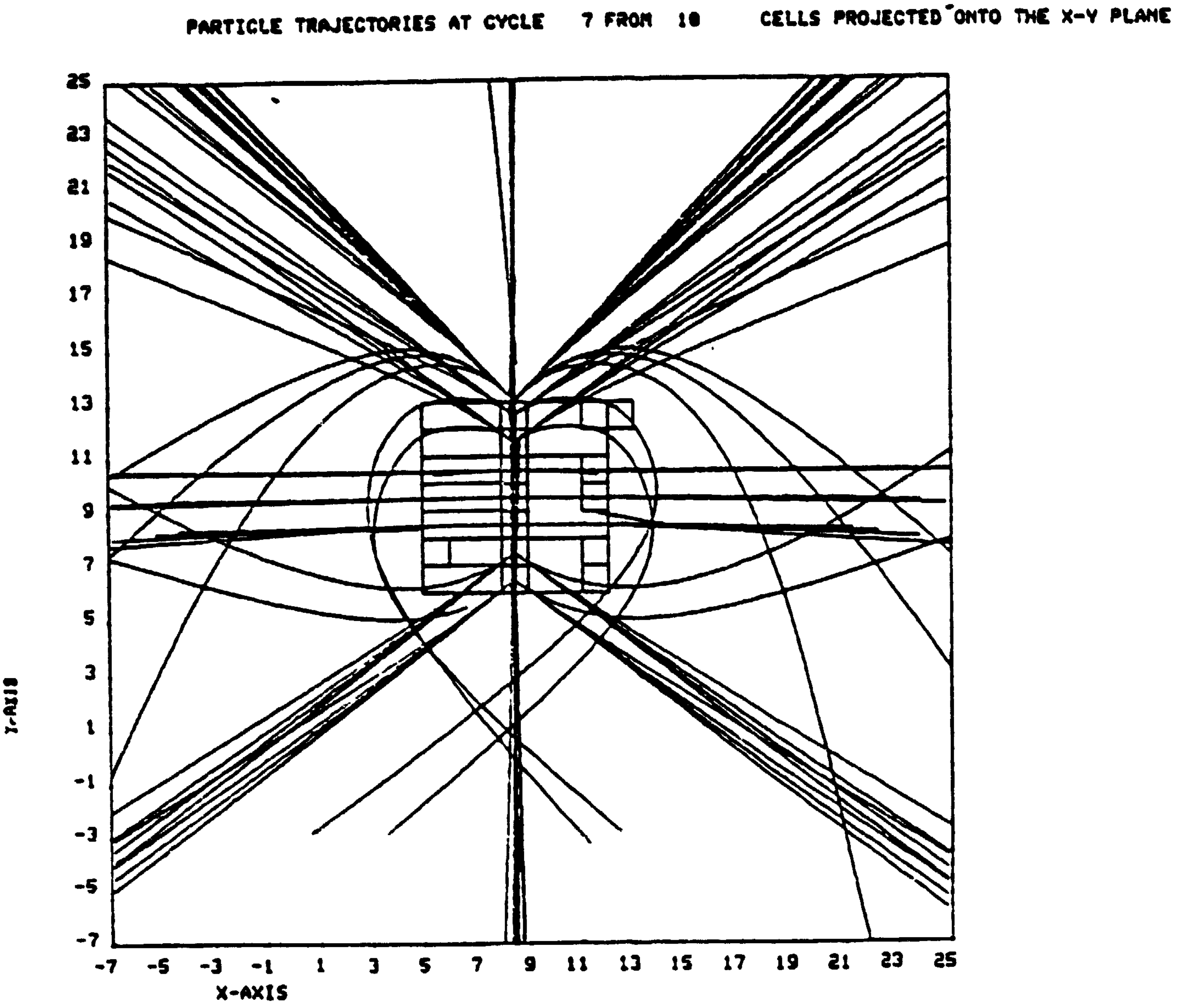

Figure 10.4. Photoelectron trajectories from bellyband cells for simplified SCATHA model, vehicle potential = +0.5 volts. Lower energy electrons are returned to the vehicle by the space charge barrier.

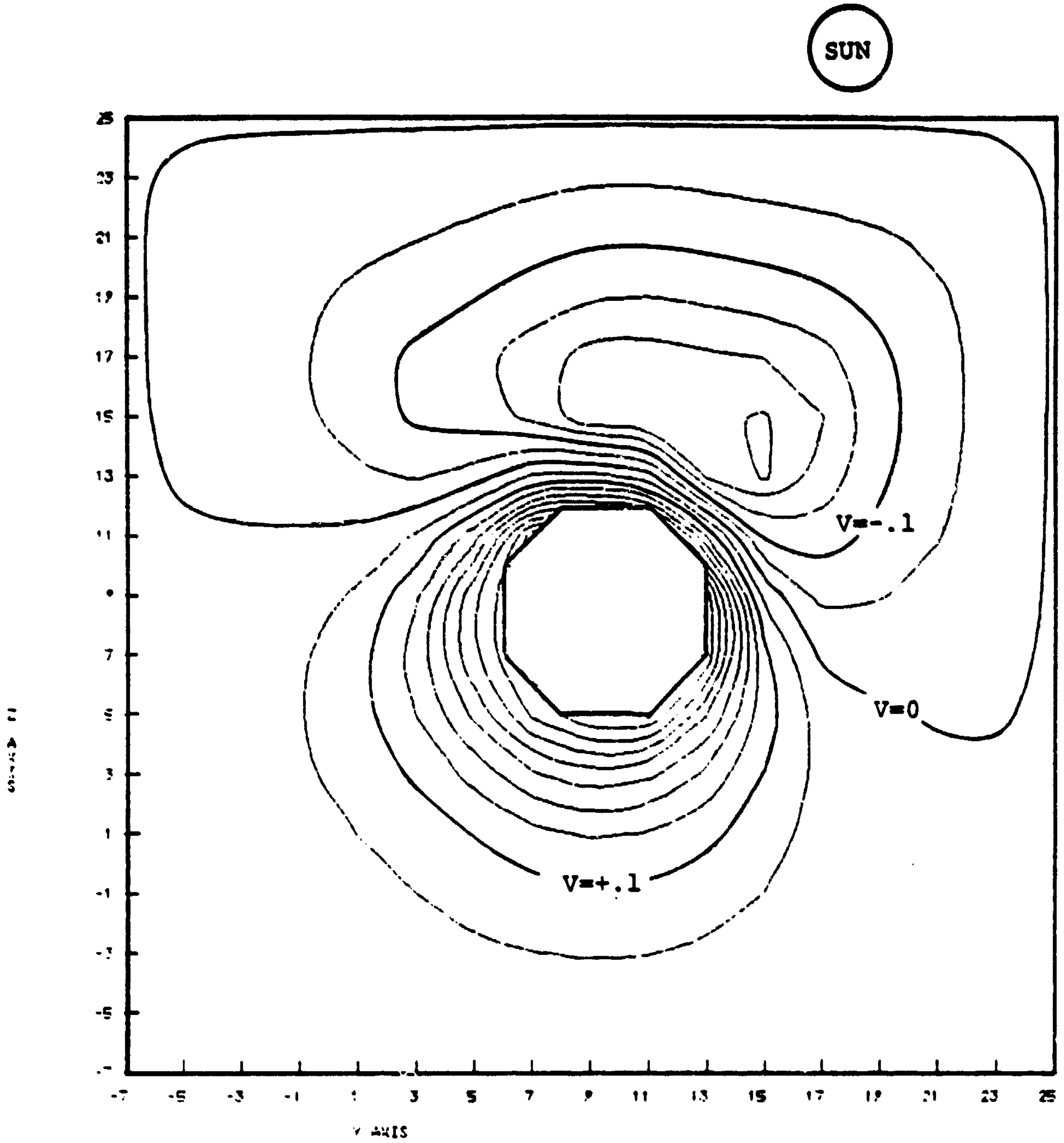

Figure 10.5. Self-consistent potential contours around a simplified SCATHA model, vehicle potential = +0.5 volts, top view. Contour spacing = 0.05 volts.

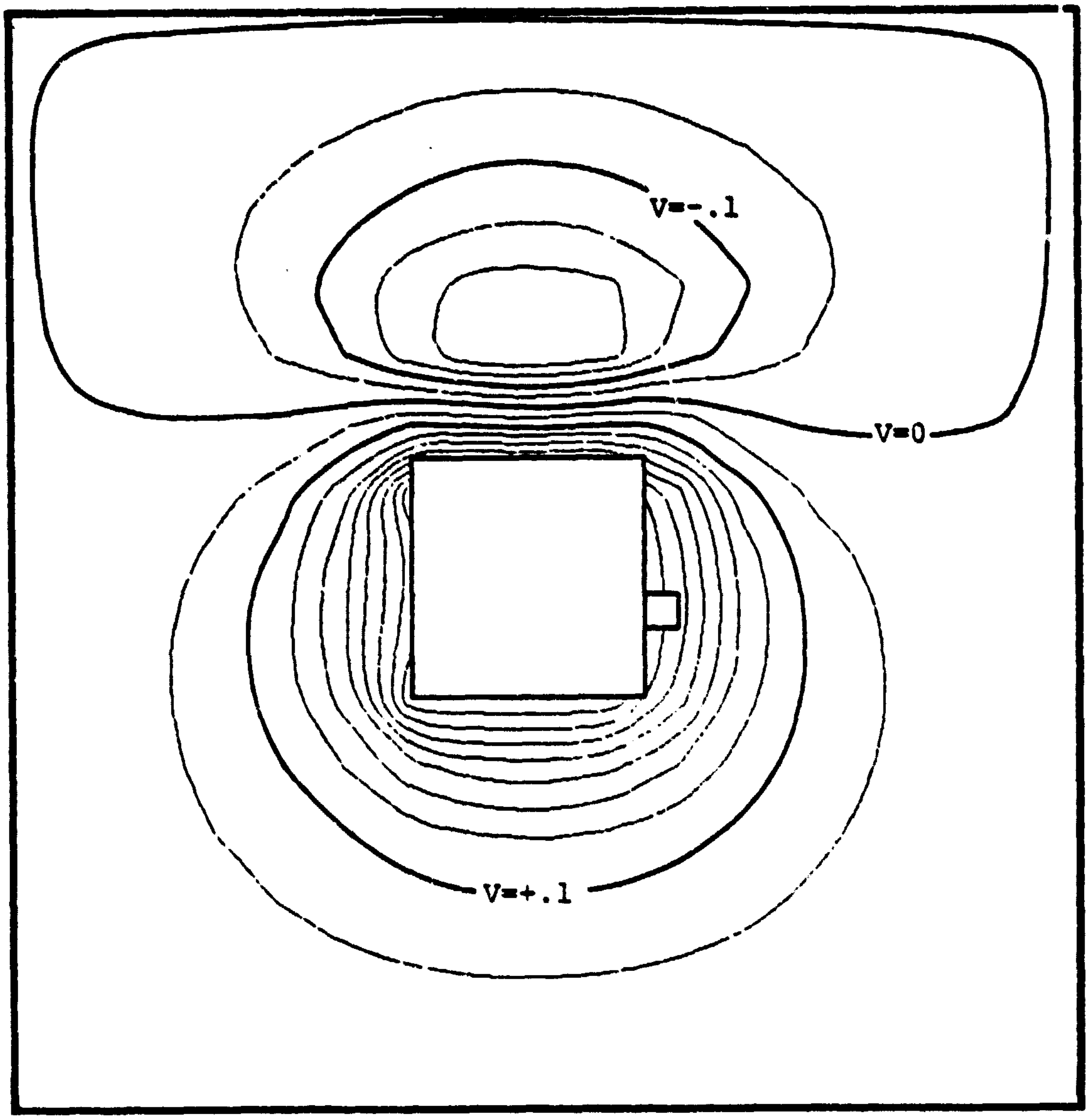

Figure 10.6. Self-consistent potential contours around a simplified SCATHA model, vehicle potential = +0.5 volts, side view. Contour spacing = 0.05 volts.

case, when the vehicle is at +0.5 volts. The space charge density is shown in Figures 10.1 and 10.2. The irregular appearance of the contours is a reflection of the rather small number of particles tracked, five energies at each of five angles for every surface cell. Typical particle trajectories are shown in Figures 10.3 and 10.4; the effect of the space charge barrier is clear for the lower energy particles. A barrier of approximately 0.75 volts forms at a distance of 75 cm above the emitting surfaces, as shown in Figures 10.5 and 10.6, leading to a potential minimum at -0.25 volts.

Similar calculations at +1.0 and +5.0 volts satellite potential are shown in Figures 10.7 through 10.10. The space charge perturbation is smaller in these cases, so that in the +5.0 volt case the space potentials are everywhere positive, the only effect being a slight compression of the contours on the sunlit side.

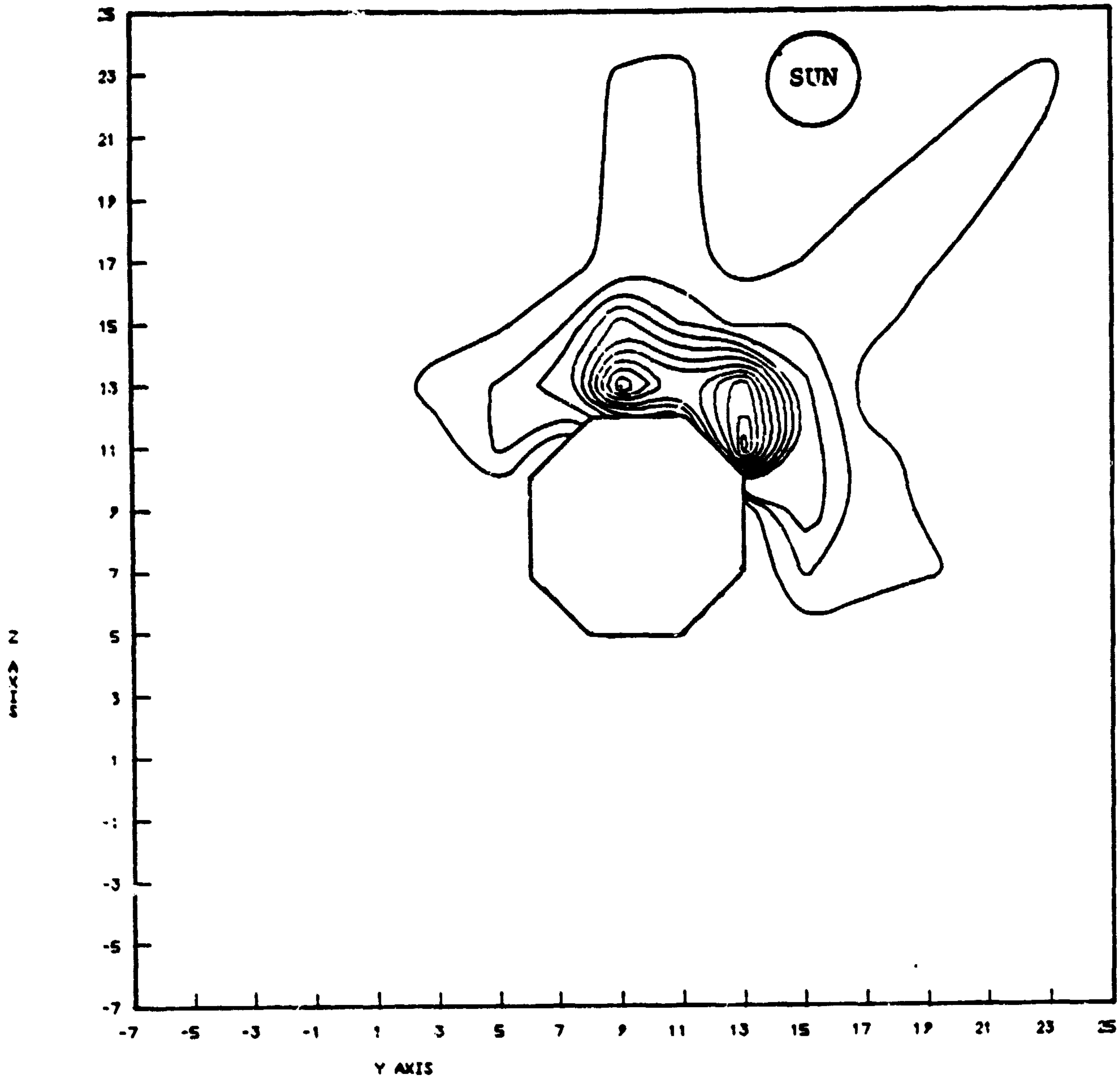

Figure 10.7. Self-consistent sheath contours around a simplified SCATHA model, vehicle potential = +1.0 volt, top view. Contour levels are the same as in Figure 10.1.

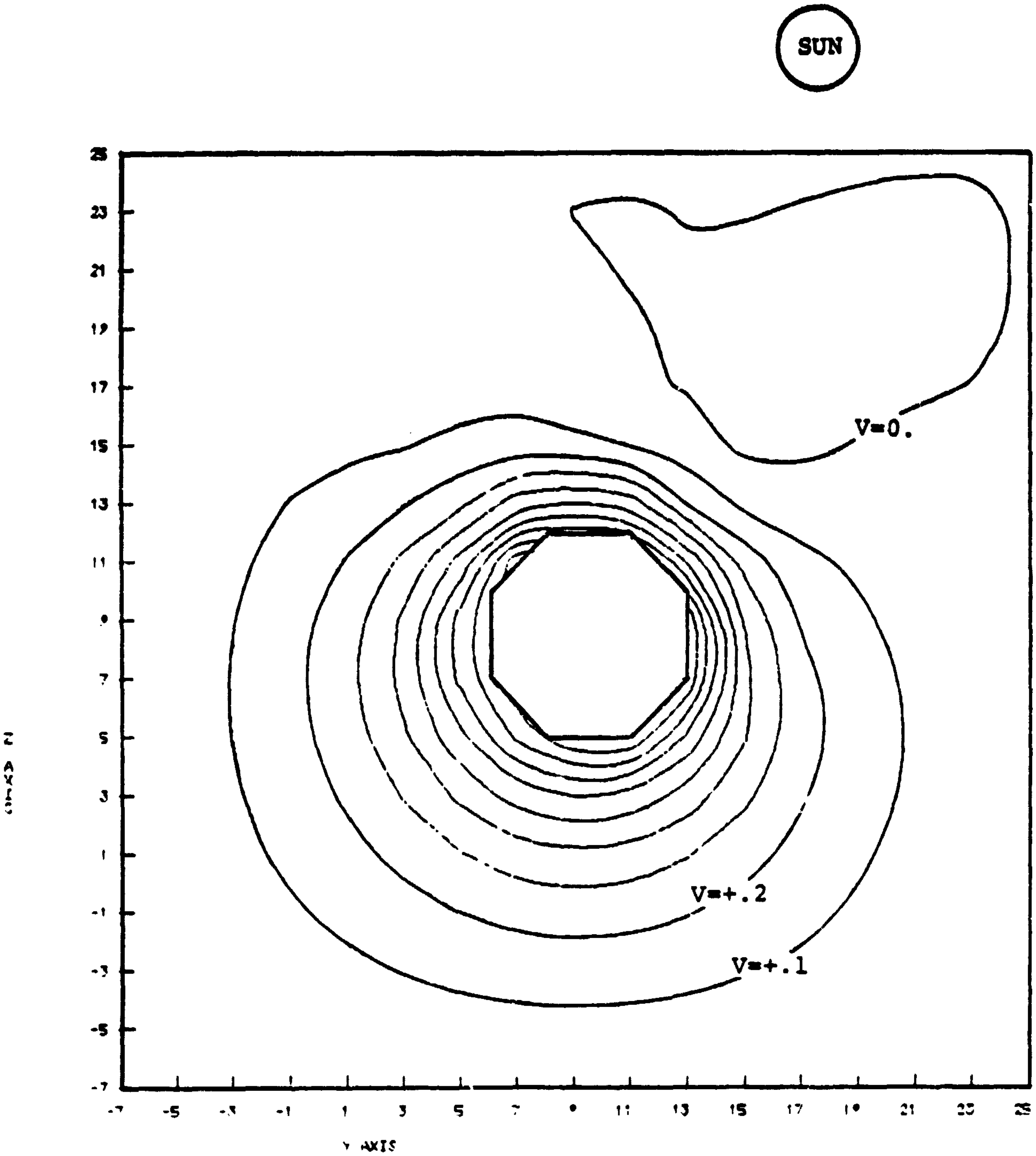

Figure 10.8. Self-consistent potential contours around a simplified SCATHA model, vehicle potential = +1.0 volt, top view. Contour spacing = 0.1 volt.

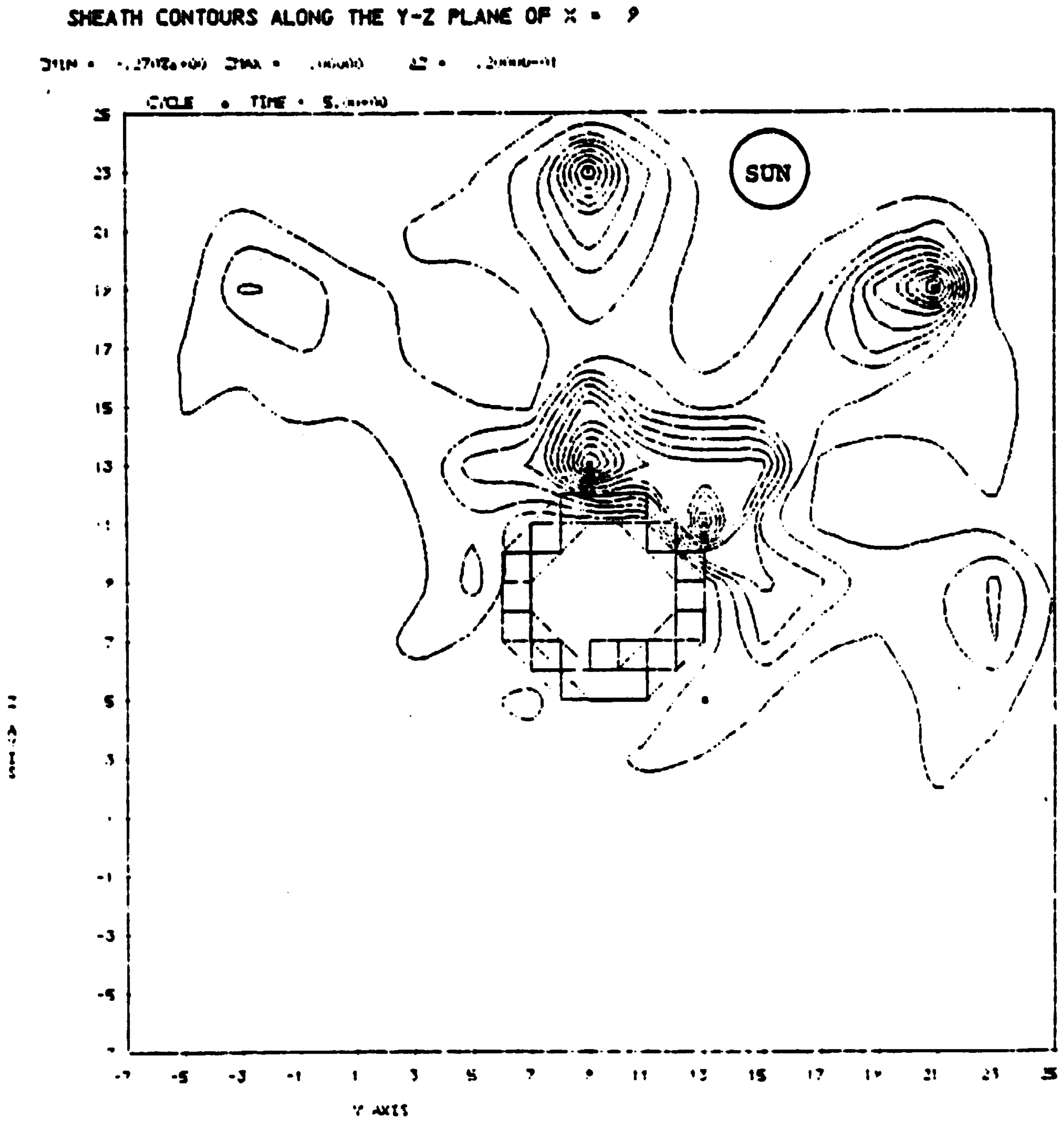

Figure 10.9. Self-consistent sheath contours around a simplified SCATHA model, vehicle potential = +5 volts, top view. Contour levels are the same as in Figure 10.1. Multiple maxima reflect the use of discrete energies to model a Maxwellian energy distribution.

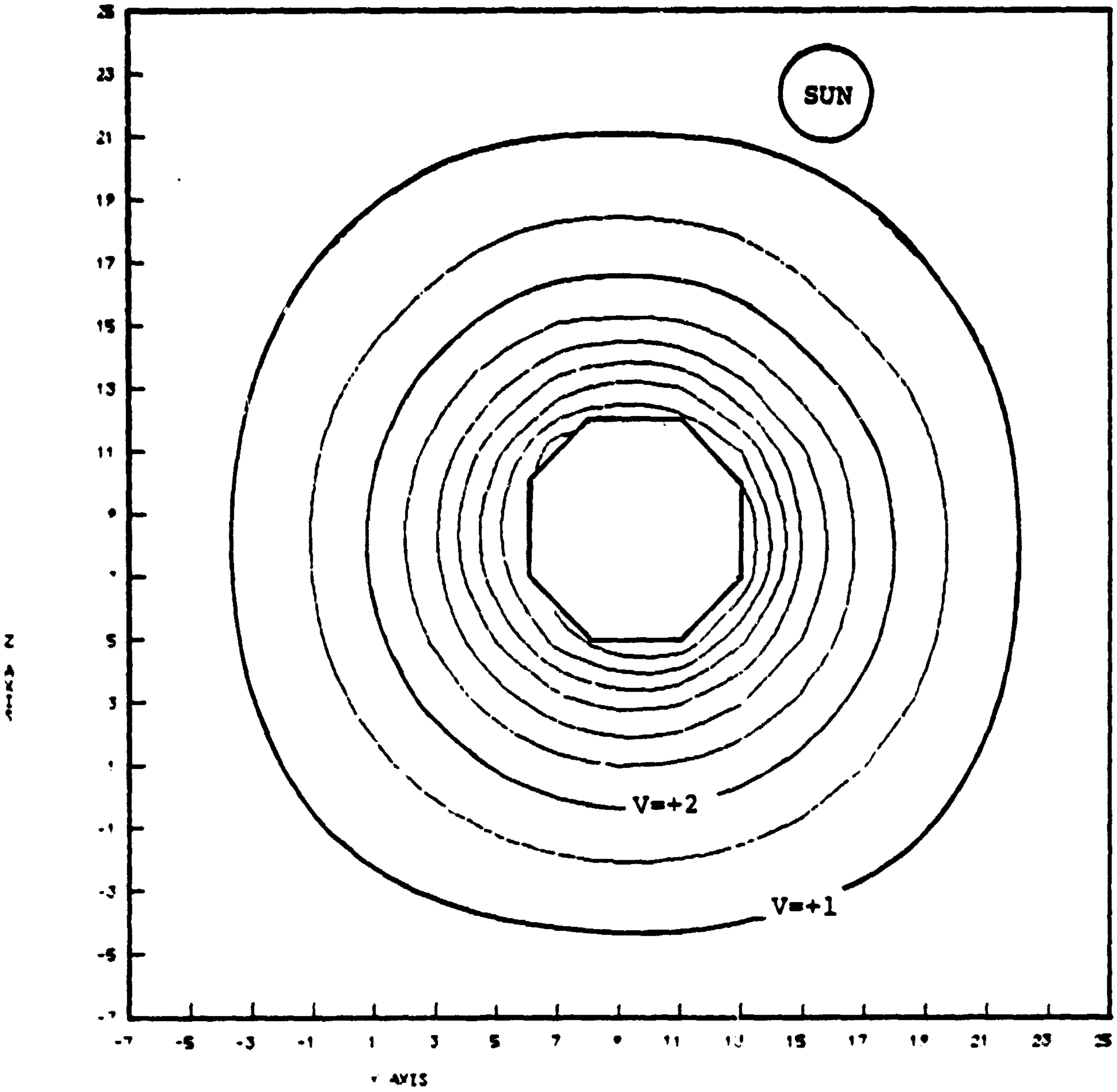

Figure 10.10. Self-consistent potential contours around a simplified SCATHA model, vehicle potential = +5.0 volts, top view. Contour spacing = 0.5 volt.

11. SCATHA BODY SHADOWING

Shadowing tables for individual SCATHA experiments have been described previously.[8] For considerations of the overall response of the spacecraft to the environment, similar tables for the spacecraft body will be useful. This chapter describes a set of tables and formulae which have been developed to provide shadowing information for body elements of the SCATHA satellite. Section 11.1 describes the general features of the body shadowing problem, and Section 11.2 describes the set of tables and formulae which have been developed.

11.1 BODY SHADOWING PROBLEM DEFINITION

The correspondence between the rectangular coordinate system of the SCATHA satellite and the spherical coordinate system used to define the sun direction vector is illustrated in the diagram below.

The Y-Z plane is defined by the delta attach fitting interface (about 5.1 inches below the bottom of the substrate). The SC11 boom lies along the negative Y axis ($\phi = 180°$, $\theta = 90°$). The top of the satellite (where the SC1-3 is located) is at X = 73.82 inches while the bottom is at X = 5.10 inches. In orbital configuration $85° \leq \theta \leq 90°$. (The same coordinate systems were employed in Reference 8.)

Imagine dividing the exposed SCATHA body into distinct elements, as shown in Figure 11.1.

- forward surface
- aft surface
- top solar array
- bottom solar array
- bellyband

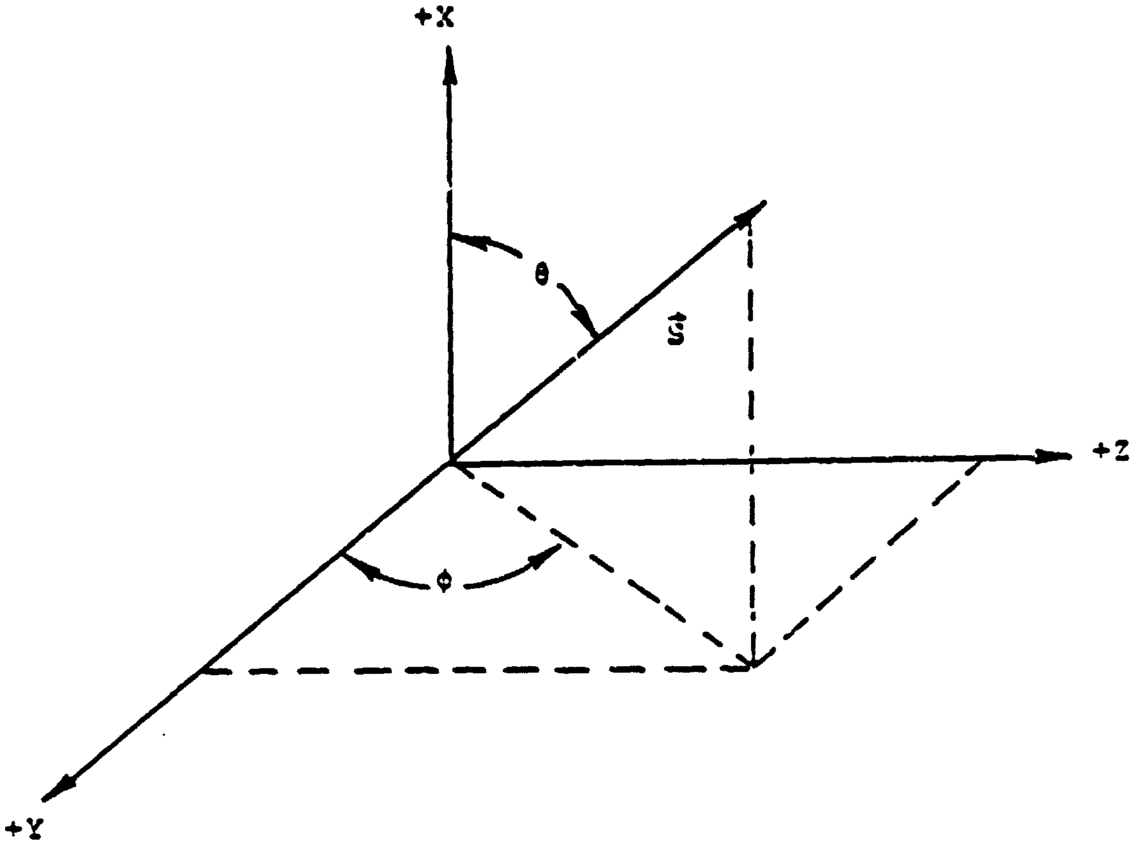

$\vec{S}$ = direction vector to sun

θ = polar angle (angle between +X axis and $\vec{S}$)

ϕ = azimuthal angle (angle between +Y axis and projection of $\vec{S}$ onto Y-Z plane)

+X axis is the cylinder axis of the main satellite body

The problem is to calculate effective illuminated areas, A_i, for each element as a function of solar angles θ and ϕ. The total solar energy incident upon the i^{th} element, E_i, is then given by

$$E_i(\theta,\phi) = A_i(\theta,\phi) \cdot I$$

where I is the solar intensity (energy/area). Note that since the spacecraft body is a cylinder of radius 33.6 inches and height 68.7 inches, the total solar energy incident on the

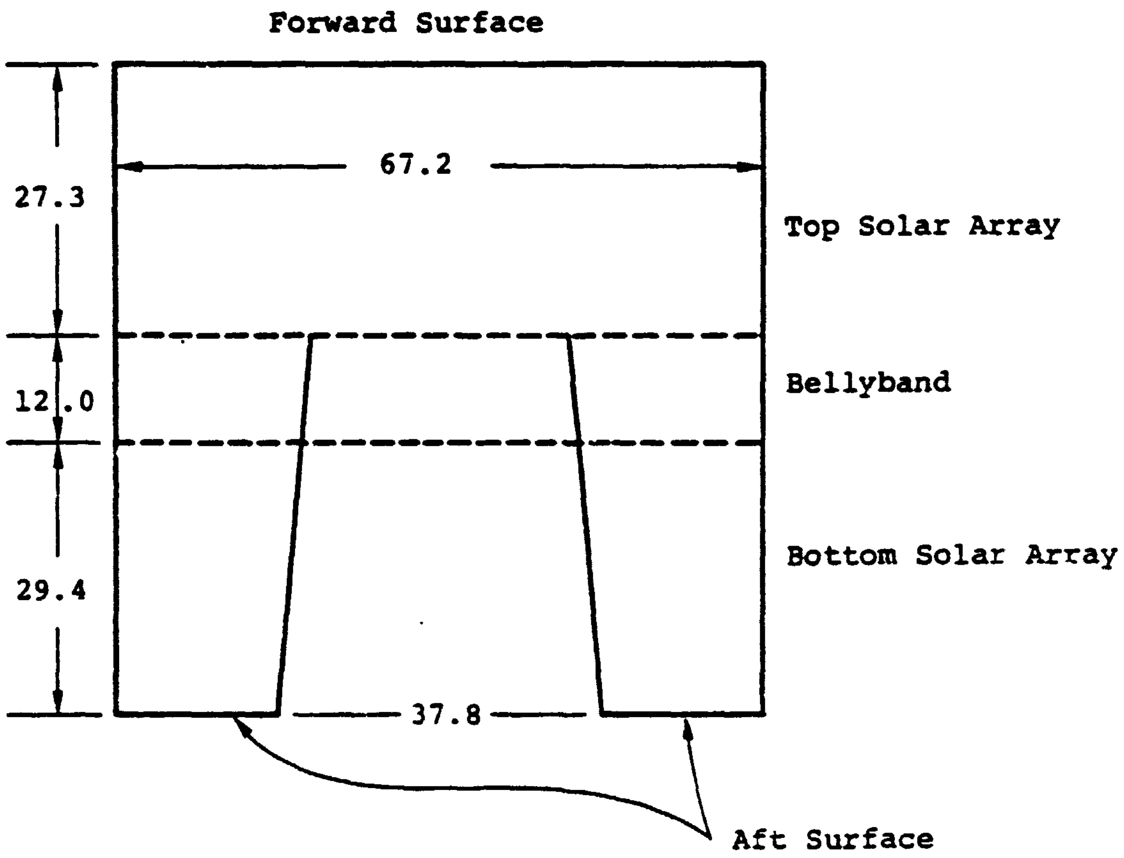

Figure 11.1. Section through SCATHA body center, illustrating exposed surface elements. All dimensions are in inches.

body is approximately E = 4617 I where I is in energy/sq. in. Because of their relatively large lengths, the boom surfaces will collect significant solar energy, although the importance of such collection is minimized due to the weak capacitive coupling of these surfaces to spacecraft ground.

11.2 SHADOWING TABLES FOR BODY ELEMENTS

The shadowing information required for body elements is to be used in analyses of the overall response of the vehicle to the spacecraft environment. The accuracy required for such considerations is much less than that needed for analyses of individual experiments. Accordingly, reasonable approximations have been made to simplify the calculations where appropriate for the various body elements, as discussed below. None of the approximations employed will lead to errors of more than 5 percent in calculated effective illuminated areas.

Bellyband Surface

Shadowing of the bellyband surface involved the most effort since the short booms cast shadows mainly in this region. The five short booms were treated as 1.7 inch radius cylinders. The 3.5 inches radius spheres at the end of the SC2 booms were also distinguished as shadowing elements. Experiments mounted at the ends of the remaining booms were not distinguished, but the lengths of these booms were adjusted slightly to approximate the shadowing effects. The cylindrical shadowing elements used are listed in Table 11.1. With these approximations, the projections of the bellyband and shadowing elements can be analytically projected into two dimensions, and the effective illuminated areas calculated directly. The results are displayed in Table 11.2, in 1° increments for polar angle θ and 5° increments for azimuthal angle ϕ. The effective illuminated area of the bellyband averaged over a full rotation is given in Table 11.2 for values of the polar angle θ.

TABLE 11.1. CYLINDRICAL SHADOWING ELEMENTS FOR BELLYBAND

Boom	Length	Azimuthal Angle
SC1	97 inches	343°
SC2-1	118 inches	303°
SC2-2	118 inches	123°
SC6	124 inches	12°
SC11	164 inches	180°

The SC1, SC6, and SC11 boom elements are slightly longer than the booms themselves to approximate shadowing by the experiments at the boom tips. All cylinders have diameters of 1.7 inches.

Top/Bottom Solar Arrays, Aft Surface

The top and bottom solar arrays and the aft surface are not significantly shadowed. The largest shadowing of these three areas occurs for the bottom solar array, where the SC2 booms can shadow up to 4 percent of the maximum effective illuminated area. Referring to the dimensions in Figure 11.1, the effective areas are then as follows:

Top solar array, $A = 1835 \sin\theta$

Bottom solar array, $A = 1976 \sin\theta$

Aft surface, $A = 2425 \sin\left(\theta - \frac{\pi}{2}\right), \quad \theta > \pi/2$

$A = 0, \quad \theta < \pi/2$

(all in square inches).

Forward Surface

The lower portion of the OMNI antenna and the SC9 experiment shadow the top surface. The NASCAP SCATHA model was used to represent the shadowing of the top surface, and the HIDCEL shadowing features of the code were employed directly. The error introduced by the limited resolution of

TABLE 11.2. EFFECTIVE ILLUMINATED AREAS FOR BELLYBAND

PHI	THETA 85	86	87	88	89	90	91	92	93	94	95
0	765.	760.	751.	733.	714.	722.	714.	712.	710.	712.	717.
5	769.	765.	757.	745.	740.	745.	740.	737.	735.	732.	735.
10	772.	769.	765.	763.	765.	768.	765.	760.	756.	752.	751.
15	773.	770.	768.	767.	767.	769.	767.	763.	760.	756.	756.
20	772.	769.	767.	762.	753.	757.	753.	752.	750.	748.	752.
25	771.	769.	765.	757.	744.	762.	744.	742.	740.	741.	747.
30	771.	769.	764.	754.	757.	767.	757.	751.	750.	749.	747.
35	772.	769.	764.	759.	766.	772.	766.	759.	758.	757.	756.
40	773.	770.	766.	768.	772.	776.	772.	768.	765.	764.	763.
45	774.	772.	771.	774.	777.	779.	777.	774.	771.	770.	769.
50	776.	775.	777.	779.	781.	782.	781.	779.	777.	775.	774.
55	778.	779.	781.	782.	783.	784.	783.	782.	781.	779.	778.
60	781.	782.	783.	784.	785.	786.	785.	784.	783.	782.	781.
65	783.	784.	785.	785.	786.	786.	786.	785.	765.	784.	783.
70	783.	784.	785.	786.	786.	786.	786.	786.	785.	784.	783.
75	782.	784.	784.	785.	785.	786.	785.	785.	784.	784.	782.
80	781.	782.	783.	784.	784.	784.	784.	784.	783.	762.	781.
85	780.	780.	781.	781.	782.	782.	782.	781.	781.	780.	779.
90	781.	778.	778.	779.	779.	779.	779.	779.	778.	777.	776.
95	782.	779.	775.	775.	775.	776.	775.	775.	774.	773.	772.
100	783.	780.	775.	770.	771.	772.	771.	770.	769.	768.	767.
105	785.	782.	777.	768.	765.	767.	765.	764.	763.	762.	761.
110	787.	785.	781.	768.	743.	746.	743.	742.	741.	748.	763.
115	789.	788.	786.	770.	748.	736.	734.	733.	735.	746.	764.
120	790.	790.	790.	778.	762.	751.	749.	747.	746.	755.	768.
125	788.	788.	768.	777.	762.	752.	750.	747.	746.	754.	767.
130	781.	781.	779.	764.	743.	731.	730.	729.	730.	741.	757.
135	774.	773.	769.	754.	724.	711.	709.	708.	714.	730.	750.
140	767.	764.	759.	750.	745.	746.	745.	745.	744.	743.	742.
145	763.	757.	752.	746.	746.	746.	746.	746.	745.	744.	742.

All entries in square inches.

TABLE 11.2. EFFECTIVE ILLUMINATED AREAS FOR BELLYBAND (CONTINUED)

PHI	THETA 85	86	87	88	89	90	91	92	93	94	95
150	761.	754.	747.	746.	746.	747.	746.	746.	745.	744.	743.
155	761.	755.	748.	746.	746.	747.	746.	746.	745.	744.	743.
160	764.	760.	755.	746.	746.	746.	746.	745.	745.	743.	742.
165	770.	767.	763.	754.	745.	745.	745.	744.	743.	742.	744.
170	777.	776.	773.	766.	746.	744.	743.	742.	743.	752.	756.
175	784.	784.	783.	780.	769.	770.	769.	768.	765.	768.	770.
180	789.	790.	791.	792.	792.	797.	792.	787.	781.	780.	779.
185	790.	790.	785.	786.	775.	775.	775.	773.	770.	774.	775.
190	788.	787.	784.	777.	757.	759.	754.	753.	754.	762.	767.
195	786.	784.	779.	770.	761.	764.	761.	760.	759.	758.	761.
200	734.	781.	776.	767.	767.	769.	767.	767.	766.	765.	763.
205	782.	779.	775.	772.	773.	773.	773.	772.	772.	771.	769.
210	782.	779.	777.	777.	778.	778.	778.	777.	777.	776.	774.
215	792.	780.	781.	781.	782.	782.	762.	781.	761.	780.	779.
220	783.	784.	784.	785.	785.	786.	785.	785.	784.	784.	792.
225	785.	786.	787.	788.	788.	788.	788.	788.	787.	786.	785.
230	787.	789.	789.	790.	790.	791.	790.	790.	789.	789.	787.
235	789.	790.	791.	791.	792.	792.	792.	791.	791.	790.	789.
240	789.	791.	791.	792.	792.	793.	792.	792.	791.	791.	789.
245	789.	790.	791.	792.	792.	792.	792.	792.	791.	790.	789.
250	788.	789.	790.	791.	791.	791.	791.	791.	790.	789.	788.
255	787.	788.	789.	789.	790.	790.	790.	789.	789.	788.	787.
260	794.	785.	786.	787.	787.	787.	787.	787.	786.	785.	784.
265	781.	781.	782.	783.	784.	784.	784.	783.	782.	781.	780.
270	779.	777.	777.	778.	779.	780.	779.	778.	777.	776.	775.
275	778.	775.	771.	771.	774.	776.	774.	771.	771.	770.	768.
280	778.	775.	770.	765.	768.	772.	768.	765.	764.	763.	762.
285	778.	775.	770.	761.	760.	767.	760.	758.	757.	755.	754.
290	778.	776.	773.	759.	735.	746.	735.	734.	732.	739.	754.
295	778.	777.	776.	760.	738.	727.	725.	723.	725.	736.	753.

All entries in square inches.

TABLE 11.2. EFFECTIVE ILLUMINATED AREAS FOR BELLYBAND (CONTINUED)

PHI	THETA 85	86	87	88	89	90	91	92	93	94	95
300	776.	777.	777.	766.	751.	740.	738.	735.	734.	742.	755.
305	773.	772.	773.	763.	750.	740.	737.	733.	730.	738.	750.
310	766.	763.	760.	747.	728.	719.	715.	712.	711.	721.	737.
315	760.	755.	747.	733.	707.	697.	692.	688.	691.	707.	726.
320	756.	749.	738.	724.	725.	731.	725.	719.	717.	716.	714.
325	752.	746.	735.	718.	721.	731.	721.	715.	714.	712.	711.
330	750.	744.	735.	726.	721.	731.	721.	718.	717.	715.	716.
335	751.	746.	741.	736.	734.	734.	734.	733.	731.	729.	726.
340	755.	750.	748.	747.	748.	748.	748.	746.	743.	740.	737.
345	758.	755.	750.	749.	750.	751.	750.	748.	745.	741.	737.
350	760.	756.	748.	737.	735.	735.	735.	734.	732.	730.	727.
355	763.	757.	748.	730.	719.	721.	719.	718.	717.	715.	714.
360	765.	760.	751.	733.	714.	722.	714.	712.	710.	712.	717.
AVG	776.	774.	771.	766.	761.	761.	759.	757.	756.	757.	759.

All entries in square inches.

the model is no more than a few percent. Table 9.3 gives the results, which were renormalized to the correct total area presented by the cylindrical spacecraft forward surface. Entries for the regions $\phi < 120$ and $\phi > 300$ are omitted, since the SC9 cluster does not shadow the top surface in this region, and the OMNI shadowing is essentially constant. Therefore the missing entries are identical to the $\phi = 120$ values.

TABLE 11.3. EFFECTIVE ILLUMINATED AREAS FOR TOP SURFACE

PHI	THETA				
	85	86	87	88	89
120	286.	229.	172.	114.	57.
130	280.	224.	168.	112.	56.
140	273.	218.	164.	109.	55.
150	262.	210.	157.	105.	52.
160	250.	200.	150.	100.	50.
170	242.	194.	145.	97.	48.
180	238.	191.	143.	95.	48.
190	231.	185.	139.	93.	46.
200	232.	185.	139.	93.	46.
210	234.	186.	140.	93.	47.
220	238.	190.	142.	95.	47.
230	232.	184.	138.	92.	46.
240	240.	192.	144.	96.	48.
250	248.	199.	149.	100.	50.
260	260.	208.	156.	104.	52.
270	275.	220.	165.	110.	55.
260	282.	226.	169.	113.	56.
290	287.	229.	172.	115.	57.
300	289.	231.	173.	116.	58.
AVG	270.	216.	162.	108.	54.

All entries in square inches. Averages include the values for $\phi > 300$ and $\phi < 120$, which are identical to the $\phi = 120$ values.

12. CHARGING OF LARGE SPACE STRUCTURES

With the advent of the shuttle era, there is increased interest in the charging characteristics of larger space structures, particularly in polar earth orbit. We have investigated the charging of a large sphere subject to the environment by the shuttle orbiter as it passes through the auroral regions in its low polar earth orbit.

The shuttle orbiter, passing through the ionosphere at altitudes of a few hundred kilometers, develops electrical potentials through accretion of charge from the natural environment. Under normal ambient conditions the particle energies viewed from the satellite range from a few tenths of an electron volt to a few volts. Thus, the magnitude of vehicle potentials are at most a few volts. However, while passing through polar latitudes the vehicle may be subjected to a substantial flux of energetic electrons moving through the auroral zone following their injection in the magnetosphere. This may cause charging to high potentials.

Most experimental studies of spacecraft charging in low earth orbit have concerned small objects ($\sim$1 m) moving through the ionosphere. In the absence of energetic precipitating electrons, the magnitude of the observed electric potentials on the INJUN 5 satellite were less than a few volts, in accordance with theoretical expectations.[17] Even during impulsive precipitation events, observed potentials did not exceed -40 volts negative.

More recently, theoretical studies have focused on charging of large objects. Parker has presented a method for computing sheath structures of large spherical bodies with high-voltage surfaces and with photoelectric/secondary emission.[18] McCoy _et al._ have considered problems associated with the operation of large, high-voltage solar arrays in the ionosphere.[19] Liemohn has considered the electrical charging of the shuttle orbiter in the absence of fluxes of energetic precipitating electrons.[20] Inouye et al.[20] investigated the charging of a space based radar system having an antenna with a diameter of about 70 meters.[21] Their calculation of electrical potentials in the presence of energetic particles are based on the application of orbit limited theory of Langmuir and Mott-Smith to determine the currents of attracted species.[22]

The investigations of charging presented below are for the regime where body dimensions are large compared to the relevant Debye length. In this regime the currents of attracted species are estimated by adapting the large spherical probe theories of Langmuir and Blodgett[23] and Al'pert et al.[24] We examine the charging of a conducting sphere subjected to intense fluxes of energetic electrons. Factors relevant to a more thorough analysis of complex objects with dielectric surfaces are summarized. Conclusions are given in the final section of this chapter.

12.1 ANALYSIS

The purpose of the following analysis is to estimate the magnitudes of potential that develop on objects in low earth orbit (200 to 400 km) when subjected to high fluxes ($\sim 200\ \mu A/m^2$) of hot (5 to 10 keV) precipitating magnetospheric electrons. Nominal values of the satellite and environmental parameters relevant to the analysis are summarized in Table 12.1.

We are concerned primarily with the possibly large negative potentials that may be produced by the currents of hot electrons incident from the magnetosphere. Questions related to the satellite wake and its structure are not considered; we consider the ram ion current density $NeV_o \sim 10^{-8}$ amp/cm^2 apparent to a co-moving observer as the only relevant

TABLE 12.1. NOMINAL VALUES OF PARAMETERS WHICH INFLUENCE ELECTRICAL CHARGING IN LOW EARTH ORBIT

Sphere Diameter	1000 cm
Satellite Velocity V_o	8×10^5 cm/sec
Ambient Ion Temperature θ_i	.1 - .5 eV
Ambient Electron Temperature θ_e	.1 - .5 eV
Precipitating (Hot) Electron Temperature θ_p	5 - 10 keV
Neutral Atom Density (0)	10^{10} cm^{-3}
Ion Density (0^+)	$10^4 - 10^6$ cm^{-3}
Ambient Debye Length	≤ 1 cm
Thermal Electron Larmor Radius	2 cm
Hot Electron Larmor Radius	400 cm
Ion Larmor Radius	300 cm
Current Density (amp/cm^2)	
Thermal Electron j_e	10^{-7}
Thermal Ion (0^+) j_i	10^{-10}
Photoelectron j_ν	10^{-9}
Precipitating (Hot) Electron j_p	2×10^{-8}
Ram Ion j_r	10^{-8}

attribute of the satellite motion. Thus, for example, it is anticipated that the $V_o \times B$ inductive electric fields are small relative to the electrostatic fields produced by charging.

To proceed further, let us first neglect the magnetic field. The effects of a magnetic field will be discussed later. The flux of hot electrons to the satellite is assumed unidirectional. Since the ram ion energy ($E_o \simeq 5$ eV) is much larger than the ion temperature, the ram ion flux will also be considered unidirectional. In the absence of electric potential the precipitating electron and ram ion currents to the satellite will be $j_p \pi R_o^2$ and $j_r \pi R_o^2$, respectively.

For negative potentials electrons are repelled and the current of precipitating electrons at the satellite is approximately $j_p \pi R_o^2 \exp\{e\phi/\theta_p\}$. This is an accurate approximation if the effective collection radius R_c is not much greater than R_o, that is, if the thickness $R_c - R_o$ of the non-neutral space charge region around the object is less than the satellite radius. For all practical purposes in the cases of interest, $-e\phi >> \theta_e$. Thus the cold plasma electrons do not enter the sheath region.

The effect of space charge upon current collection in low earth orbit by large high voltage objects is well-known, having been studied both theoretically and with laboratory experiments. Space charge effects dramatically reduce the current collected per unit area compared to those predicted by orbit limited theory. The I-V characteristics of a spherical probe with a ratio of radius to Debye length of 10 is shown in Figure 12.1. The current collected per unit area at large voltages is substantially less than the very large Debye length orbit limited theory would predict. However, the auroral electron fluxes in polar earth orbit are incident currents which may be substantially larger than

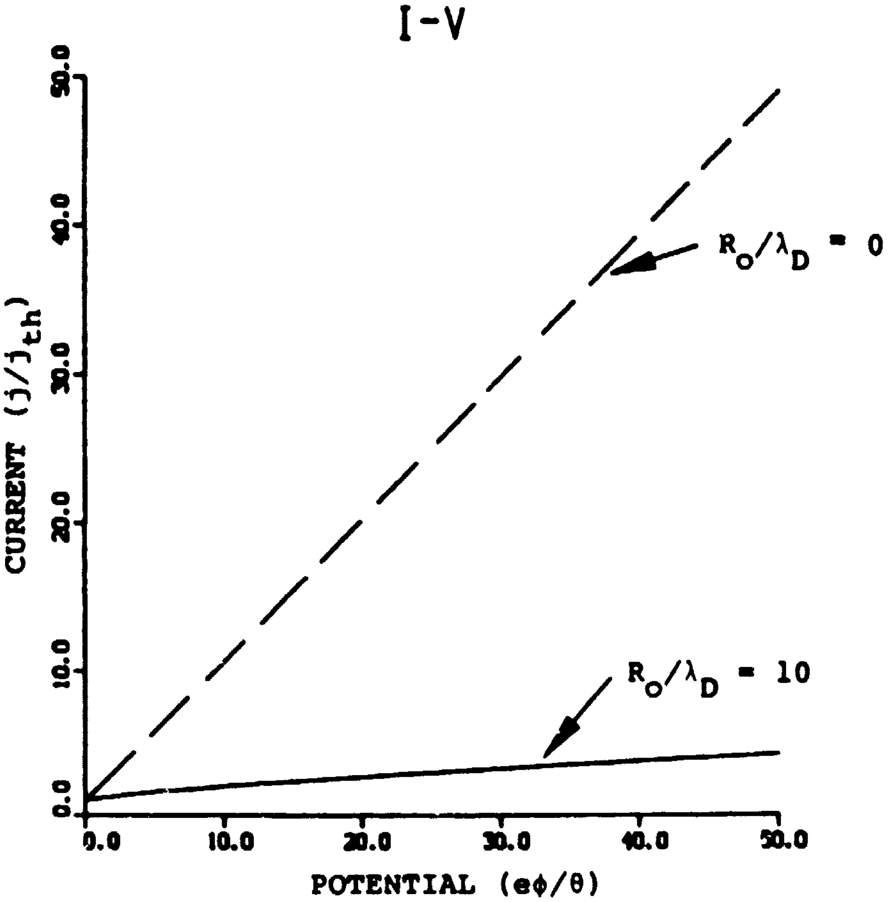

Figure 12.1. The I-V characteristic for a spherical probe in a small Debye length plasma. Note how even at large potentials the probe collects just a few times the plasma thermal current. The dashed line is for long Debye length orbit limited collection. It is not applicable to large objects in low earth orbit.

the ram ion currents. We are then interested in the inverse function, that is, the V-I characteristic (Figure 12.2). Note how dramatically the probe voltage must rise to increase the current collected per unit area. It is this steep V-I characteristic which forms the basis of the following analysis.

The theory of the sheath surrounding a large spherical probe with radius $R_o >> \lambda_D$ at high potential $|e\phi| >> \theta_e$, θ_i in an isotropic plasma is given in Langmuir and Blodgett[23] and Al'pert et al.[24] The effective collection radius R_c for the case of ion attraction can be expressed as

$$\frac{R_c}{R_o} = F\left(\frac{e\phi}{\theta} \left(\frac{\lambda}{R_o}\right)^{4/3} \right) \qquad (12.1)$$

where θ is the temperature of the attracted species and λ the Debye length. F is an increasing function of its argument and hence of the satellite potential.

In order to adapt the Langmuir-Blodgett theory as an approximation to the case of streaming ions, we relate the temperature θ to the kinetic energy E_o of ions relative to the satellite by requiring that current entering the sheath in the isotropic and streaming cases be the same,

$$NV_o \pi R_c^2 = 4\pi R_c^2 \, N(8\theta/\pi M)^{1/2} \qquad (12.2)$$

giving

$$\theta = \frac{\pi M V_o^2}{8} = \frac{\pi E_o}{4} \qquad (12.3)$$

where M is the ionic mass. The equivalent Debye length is

$$\lambda \approx 743 \; (N/\theta)^{1/2} \text{ cm} \qquad (12.4)$$

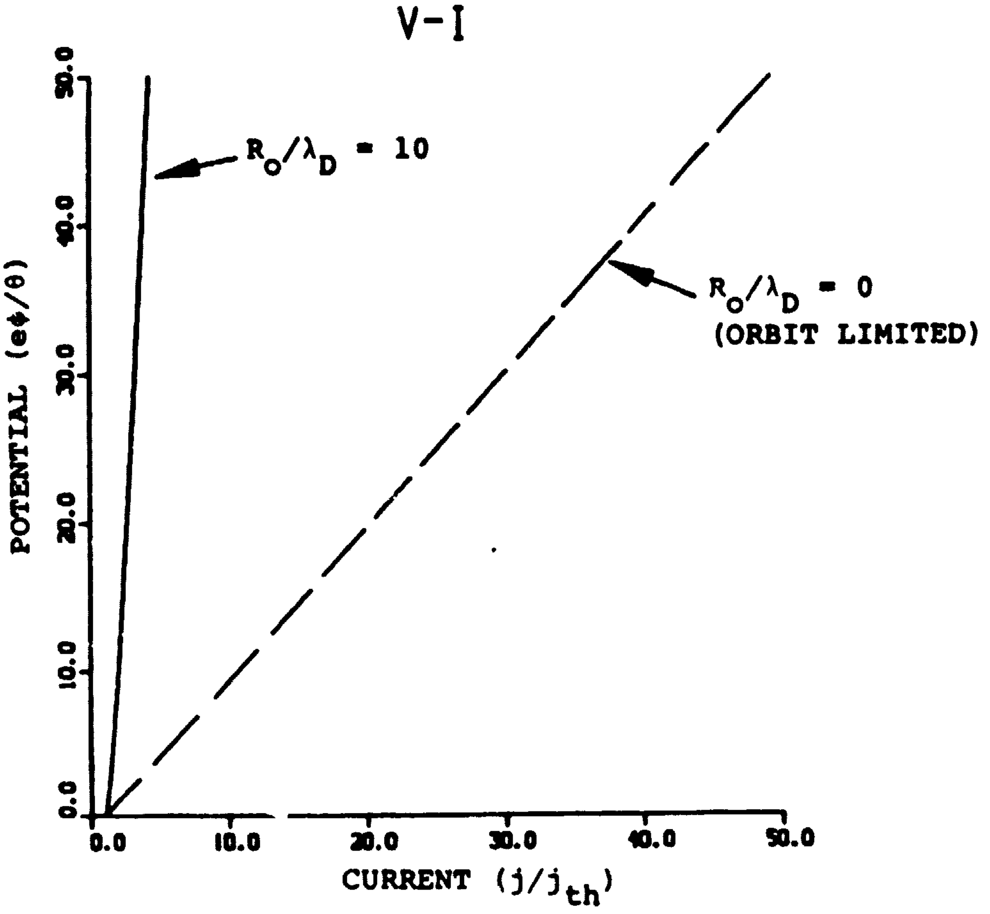

Figure 12.2. The V-I characteristic for a spherical probe in a small Debye length plasma. Note how even a small increase in probe current causes a very large change in the potential of the sphere. The dashed line is for long Debye length, orbit limited collection.

Table 12.2 gives values of R_c/R_o as a function of $z \equiv (e\phi/\theta)(\lambda/R_o)^{4/3}$. For values of $R_c/R_o \leq 1.05$, the collection radius and potential are related by the plane electrode Child-Langmuir law

$$\frac{R_c}{R} = 1 + \frac{2\sqrt{2}}{3} z^{3/4} \tag{12.5}$$

with an accuracy better than 3 percent.

The potential on the sphere is determined by balance of currents.

$$\pi R_o^2 \, j_p(1-s_p) e^{e\phi/\theta_p} = \pi R_c^2 \, j_r(1+s_i) + I_\nu \tag{12.6}$$

where $s_p(s_i)$ is the total secondary yield from electron (ion) impact and I_ν is the total photoemission current.

Defining

$$\bar{j}_p = j_p(1-s_p)$$

$$\bar{j}_r = j_r(1+s_i)$$

as effective electron and ion current densities corrected for secondary emission, Eq. (12.6) becomes

$$\kappa = \bar{j}_p/\bar{j}_r = \left(\frac{R_c}{R_o}\right)^2 \exp|e\phi/\theta_p| + \frac{I_\nu}{\bar{j}_r \, \pi r_o^2} \tag{12.7}$$

Figure 12.3 shows the dark potential on spheres of 0.5 and 5 m radius as a function of ratio of precipitating electron to ram ion current densities in a plasma with ambient density 10^5 cm^{-3}. For a given current ratio the potential on the sphere scales roughly as the radius. More precisely, the potential scales with radius as $(R_o/\lambda)^{4/3}$ for $|e\phi| << \theta_p$,

TABLE 12.2. EFFECTIVE COLLECTION RADIUS AS FUNCTION OF $z \equiv e\phi/\theta(\lambda/R_o)^{4/3}$

R_c/R_o	z
1.005	.001
1.018	.005
1.030	.010
1.050	.019
1.100	.052
1.150	.094
1.200	.143
1.250	.199
1.300	.264
1.340	.337
1.400	.421
1.450	.510
1.500	.610
1.600	.833
1.700	1.092
1.800	1.384
1.900	1.711
2.000	2.074
2.100	2.479
2.200	2.919
2.300	3.400
2.400	3.920
2.500	4.479
2.600	5.113
2.700	5.752
2.800	6.472
2.900	7.196

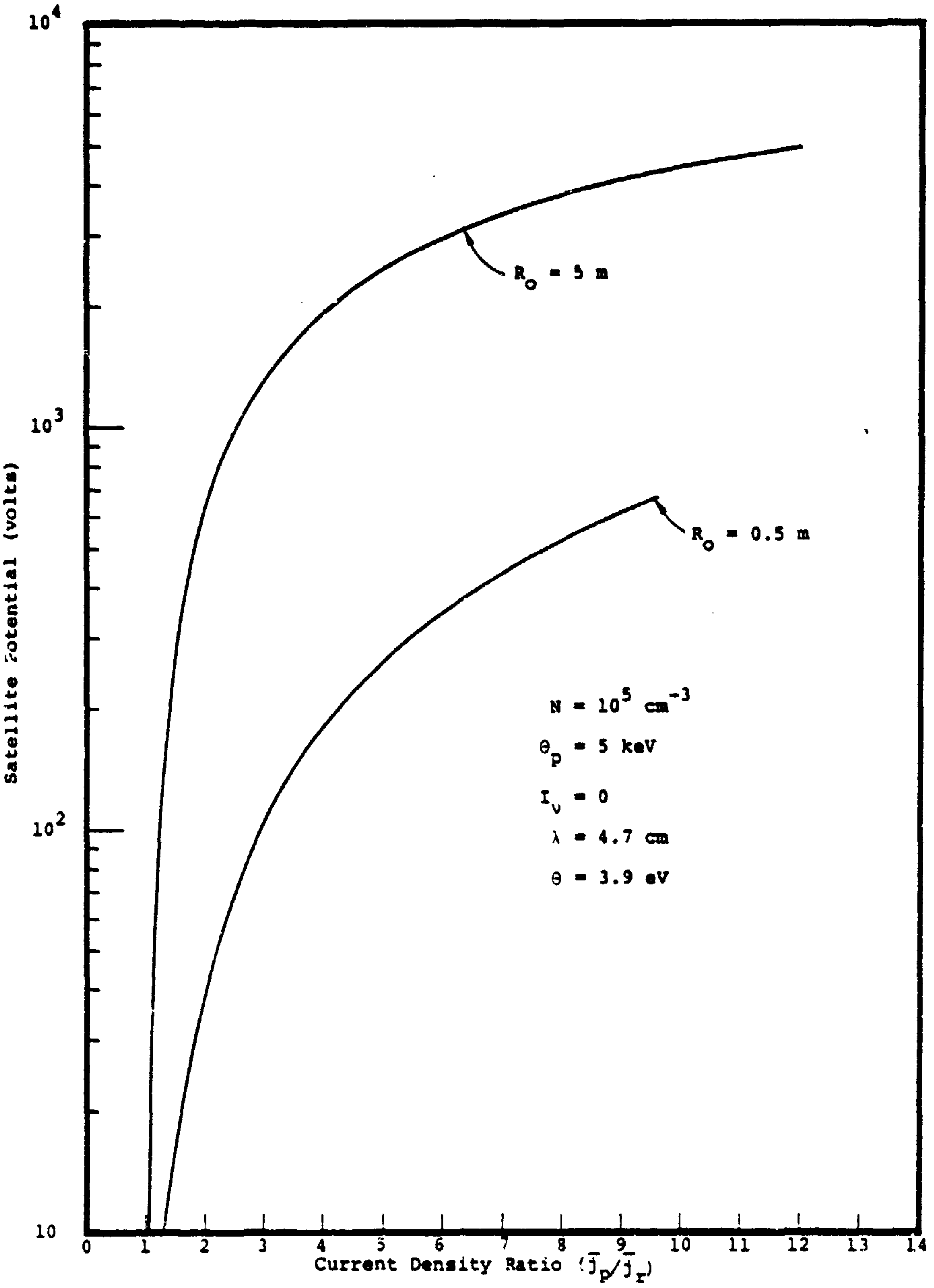

Figure 12.3. Satellite potential as function of current density ratio.

but somewhat more slowly with R_o/λ as $|e\phi|$ increases. Observe that the potential is an extremely sensitive function of $\bar{j}_p/\bar{j}_r$ for values of this ratio near unity, especially for the larger sphere.

The theory predicts that the 5 m sphere will charge to about the 1 kilovolt level for electron to ram ion current density ratios of only about two. This is to be contrasted with the result predicted by orbit limited ion collection. The approximate dark current balance

$$\frac{j_p}{j_r} \approx \left(1 + \frac{|e\phi|}{\theta}\right) e^{|e\phi|/\theta_p}$$

for orbit limited collection predicts, for example, that $j_p/j_r \approx 300$ would be required to sustain a 1 kilovolt potential on the sphere.

12.2 DISCUSSION

Several effects have been neglected in determining that hot electrons precipitating from the magnetosphere can charge a large object to kilovolt potentials. We shall now argue that accounting for these effects will not alter the conclusion that such high potentials should be expected for the assumed charging environment.

Consider first the effect of a magnetic field on the ram ions entering the sheath surrounding the satellite. A component of magnetic field perpendicular to the satellite velocity will tend to insulate the surface from the ram ion currents, leading to larger negative potential of the satellite. For cases of interest however, the effect is negligible. A measure of the size of this effect is given by

$$\alpha = \frac{\frac{1}{2} M \omega_{ci}^2 d^2}{|e\phi|} \simeq \omega_{ci}^2 \tau^2$$

where M is the ion mass, ω_{ci} its gyrofrequency, d the thickness of the sheath, and τ the flight time of an ion across the sheath. For the cases represented in Figure 12.1, $d \lesssim R$, so that

$$\alpha \lesssim 0.2/|e\phi \text{ (volts)}|$$

which is negligibly small except at very low levels of satellite potential.

The hot electrons responsible for charging the satellite were considered to approach the space charge sheath unidirectionally, as pertains in the limit of strong magnetic fields where the Larmor radius is small compared with the radius of the satellite. More probably, the electrons, because of their pitch angle distribution, would enter the repulsive sheath with a more nearly isotropic distribution of directions. Assuming that the one sided thermal plasma current densities are the same in the unidirectional and isotropic limits, the effective electron current toward one hemisphere of the satellite in the isotropic limit is twice that which pertains in the unidirectional case. In the absence of no other effect associated with the magnetic field, the result would be greater charging.

The charging current given by Eq. (12.6) for the case of repelled electrons incident unidirectionally from infinity applies in the limit of zero gyroradius. In the opposite limit of vanishing magnetic fields, again assuming that electrons enter the sheath unidirectionally, fewer electrons reach the satellite because of the deflection by the repulsive electric field. The reduction in current is small however, and the charging current accurately represented by Eq. (12.6) provided that the repulsive potential on the satellite satisfies $(e\phi/\theta_p)^2 << 1$. This requirement, which is satisfied in the case of Figure 1 for potentials less than about 2 kV, follows from the conservation laws of energy and angular momentum which permit one to express the current to the satellite as

$$I = N_o(m/2\pi\Theta_p)^{1/2} \; \pi R_c^2 \int_{\left(\frac{2e\phi}{m}\right)^{1/2}}^{\infty} dv \; v e^{-mv^2/2\Theta_p} \left\{1 - \frac{2e\phi}{mv^2}\right\}$$

Essentially, the electron current crossing the sheath is not substantially modified by the magnetic field, a circumstance we expect to pertain is long as

$$(\omega_{ce}\tau)^2 \, \frac{1}{2} \, m \, \omega_{ce}^2 \, d^2/\Theta_p << 1$$

This condition is well satisfied for potentials in Figure 12.3 at the kilovolt level.

In applying the Langmuir-Blodgett probe theory, we have neglected the contribution of electrons to the space charge in the sheath. This is a valid approximation because the velocity of electrons in the sheath is large compared with ion velocities, except perhaps for the contribution of secondary and photoelectrons near the surface. Near the surface, however, the electric fields are dominated by surface charge and little affected by space charge.

Secondary and photoelectrons move through the sheath with smaller energies than the precipitating magnetospheric electrons and are therefore more strongly affected by the magnetic field. The potential developed by the satellite is affected however only if the emitted electrons return to the surface, leading to higher potentials than if the electrons escape.

In all previous considerations, we have supposed that the satellite is a conducting sphere. The shuttle orbiter is actually a geometrically complex object whose surface is coated with dielectric materials, and both ion and electron fluxes are apt to be strongly heterogeneous functions over the satellite's surface. The degree of heterogeneity will be affected by the geometry of the satellite, its motion through the ionosphere, the variation of surface properties, such as secondary yield, and by the magnetic field. Undoubtedly the sheath surrounding the orbiter will have a complicated geometrical structure not easily represented by simple spherical probe models. Multidimensional computer models will be required to determine the strong differential voltages which are expected to develop on the vehicle.

12.3 CONCLUSIONS

Ambient currents of hot electrons (5-10 keV) of 200 $\mu A/m^2$ will charge a 5 meter sphere in low polar earth orbit to kilovolt potentials in eclipse. Such potentials are about 1 order of magnitude larger than occur for smaller satellites ($\sim R_o \sim 0.5$ m) in a similar orbit. On this basis, one should expect negative potentials of around 1 kilovolt to develop on the shuttle orbiter. Because of the dielectric coating on the orbiter, and the non-uniform character of the charged particle fluxes expected at the vehicle's surface, differential surface potentials of the order of one kilovolt should also occur.

13. CONCLUSIONS AND RECOMMENDATIONS

The simulations of the charging response of the SCATHA spacecraft described in the above chapters were based on the actual observed plasma environments as well as prototypical representations of the geosynchronous ambient plasma. This chapter provides a brief summary of the major simulation results, and gives an assessment of the validity and implications of these results when possible. The studies to date, together with preliminary reports of data from the SCATHA spacecraft, suggest several avenues for extension of the simulations, and these avenues are briefly described as well.

Perhaps the most important result of the simulations was a prediction originally made before the launch of the vehicle,[5] and emphasized by the simulations described in Chapter 5: the SCATHA booms were isolated as the most likely sites for discharges to occur. In fact, the only charging related malfunction observed, the SC2 experiment failure and the associated telemetry upset on day 89, seems to have been caused by just such a discharge. Continuing analysis of this event is in progress, but the observed effects are consistent with a scenario based on a surface flashover along the SC2 booms. Thus the NASCAP/SCATHA model served one of its major purposes: likely discharge sites on an operational spacecraft were correctly identified in advance of their occurrence.

Simulation of the "passive" charging event that occurred during eclipse on day 87, 1979, described in Chapter 6, represents the first unambiguous test of the NASCAP code. It is a test that was passed most convincingly. These results, coupled with the realistic potentials predicted by the test environment simulations reported in Chapter 5, allows us to conclude that NASCAP is a predictive code, and that we can calculate the potentials of spacecraft under realistic conditions with added confidence.

Simulations of charging in sunlight have revealed two interesting features. The first effect, which was also observed during the eclipse charging in the moderate temperature plasma, was the importance of field limiting of low energy fluxes (secondaries and photoelectrons) in decreasing predicted equilibrium potentials. Such field limiting is the likely mechanism which led to the observed sunlight charging of SCATHA to a few hundred volts negative on several occasions.[9] This same mechanism can also prevent the SSPM reference band from tracking plasma ground in sunlight. The second effect of interest was the persistence of differential potentials in the simulation of the exit from eclipse, which led to some spacecraft surfaces being driven to positive potentials for brief periods. Since the vehicle upset on day 89 was associated with high positive vehicle potentials, the transient response during eclipse exit bears further investigation.

Three specific design suggestions for passive mitigation of spacecraft charging effects emerge from the studies described above:

1. Eliminate exposed surfaces weakly capacitively coupled to spacecraft ground, as typically represented by the SCATHA booms.
2. Include material charging response as a design consideration. Use of high atomic number materials having high backscattering yields and coatings having very high secondary yields (MgF_2 on solar cell covers) along with materials having more typical charging characteristics guarantees the development of differential charging.
3. Avoid large insulating areas which are shadowed for long periods, such as the white paint coating on the SCATHA aft surface, in order to reduce field limiting of low energy emission.

Perhaps the most serious question concerning spacecraft charging that still remains unanswered is the mechanism of natural discharge. Even though the potential for damage arising from such discharges is a major motivation behind the effort to understand charging, a successful model explaining how and when discharges occur has yet to be developed. Included among the many suggestions that have been made is the correlation between discharge and the radiation-induced bulk conductivity, pointed out in Chapter 4. Future analysis of SCATHA charging should focus on those days when discharges were either unusually frequent or unexpectedly absent, and include the entire plasma spectrum up to MeV energies.

APPENDIX A

SCATHA MODEL MATERIAL PLOTS GENERATED BY NASCAP CODE

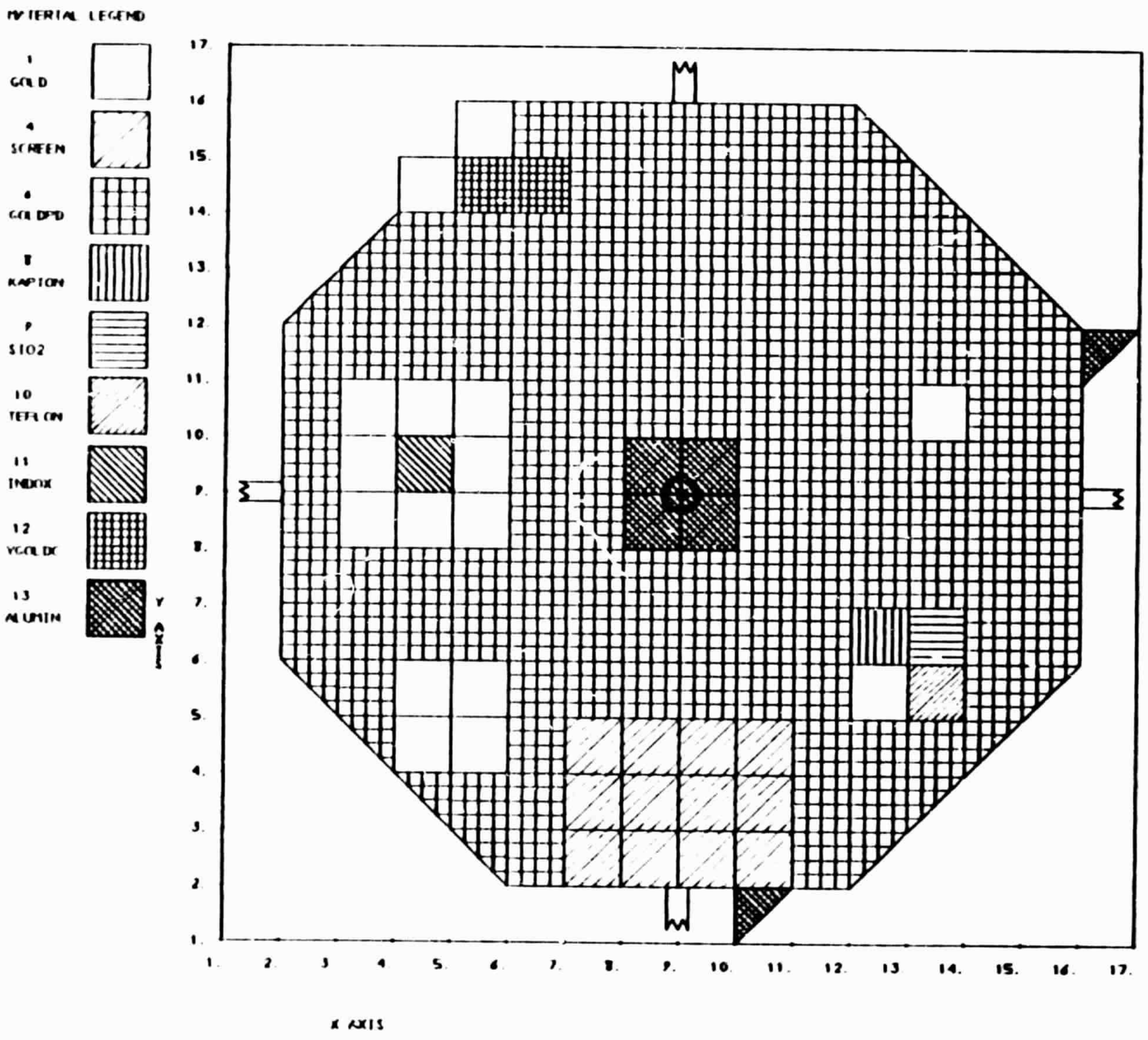

Figure A.1. Surface cell material composition as viewed from the positive Z direction for Z values between 1 and 33.

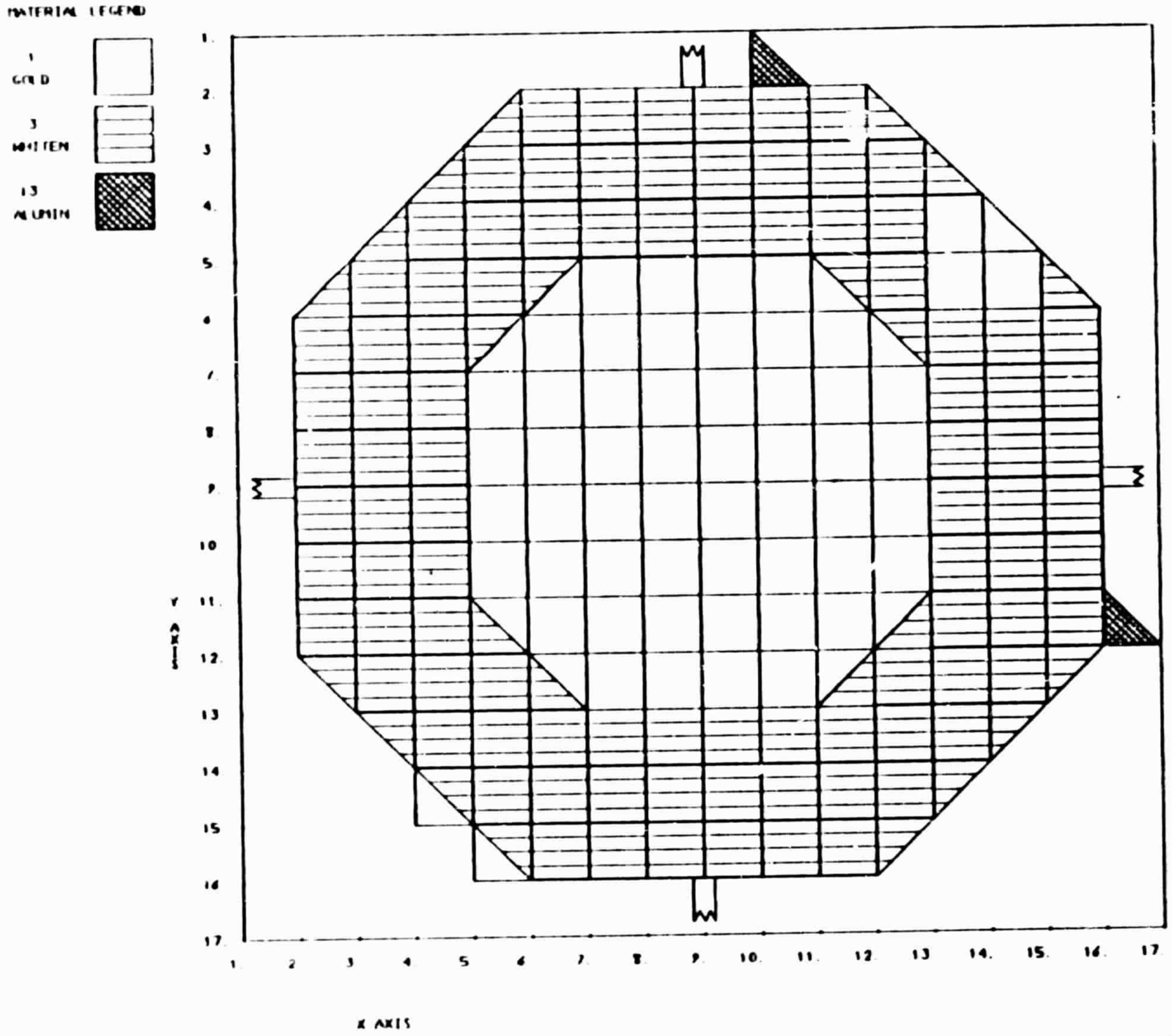

Figure A.2. Surface cell material composition as viewed from the negative Z direction for Z values between 1 and 33.

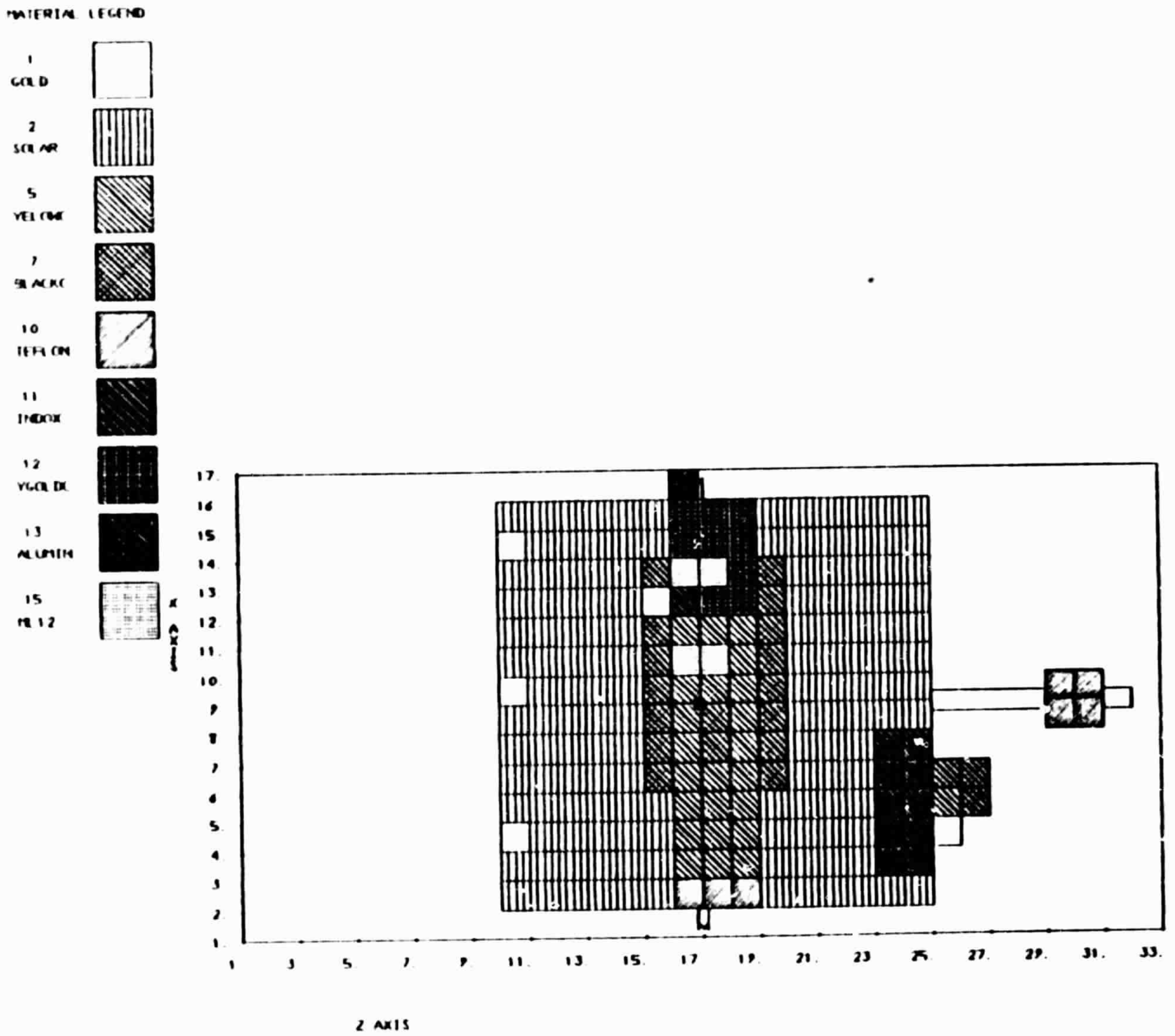

Figure A.3. Surface cell material composition as viewed from the positive Y direction for Y values between 1 and 17.

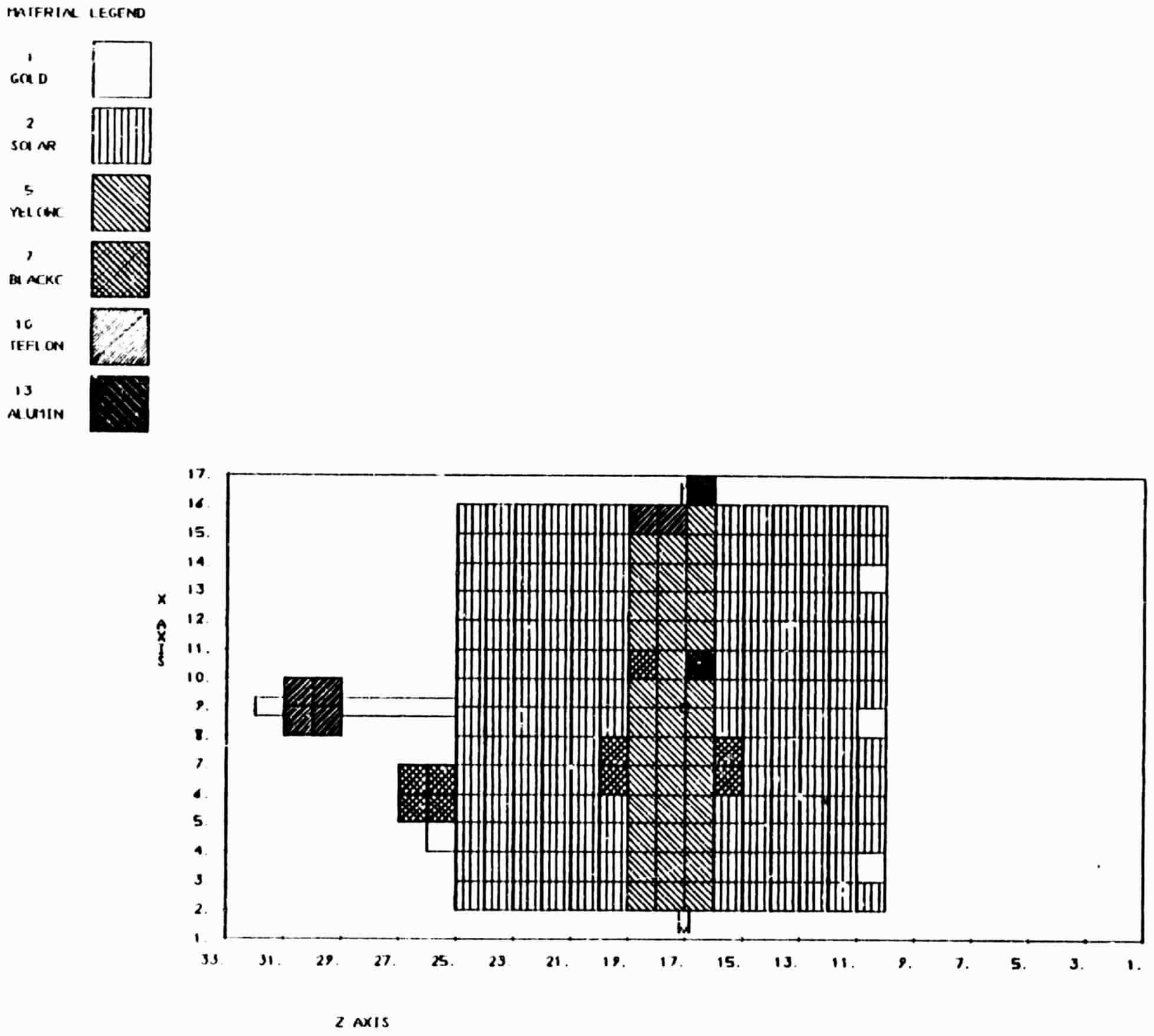

Figure A.4. Surface cell material composition as viewed from the negative Y direction for Y values between 1 and 17.

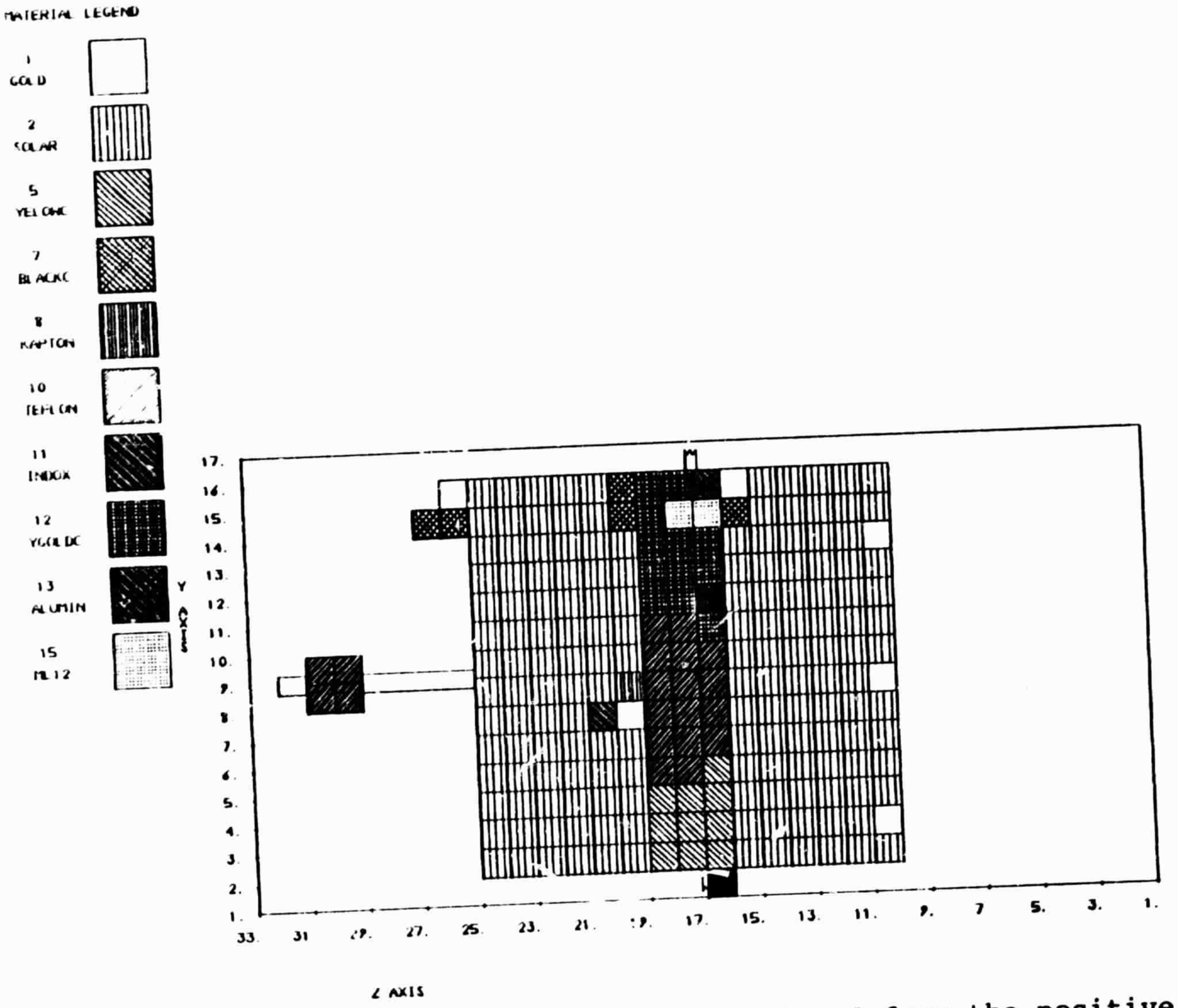

Figure A.5. Surface cell material composition as viewed from the positive X direction for X values between 1 and 17.

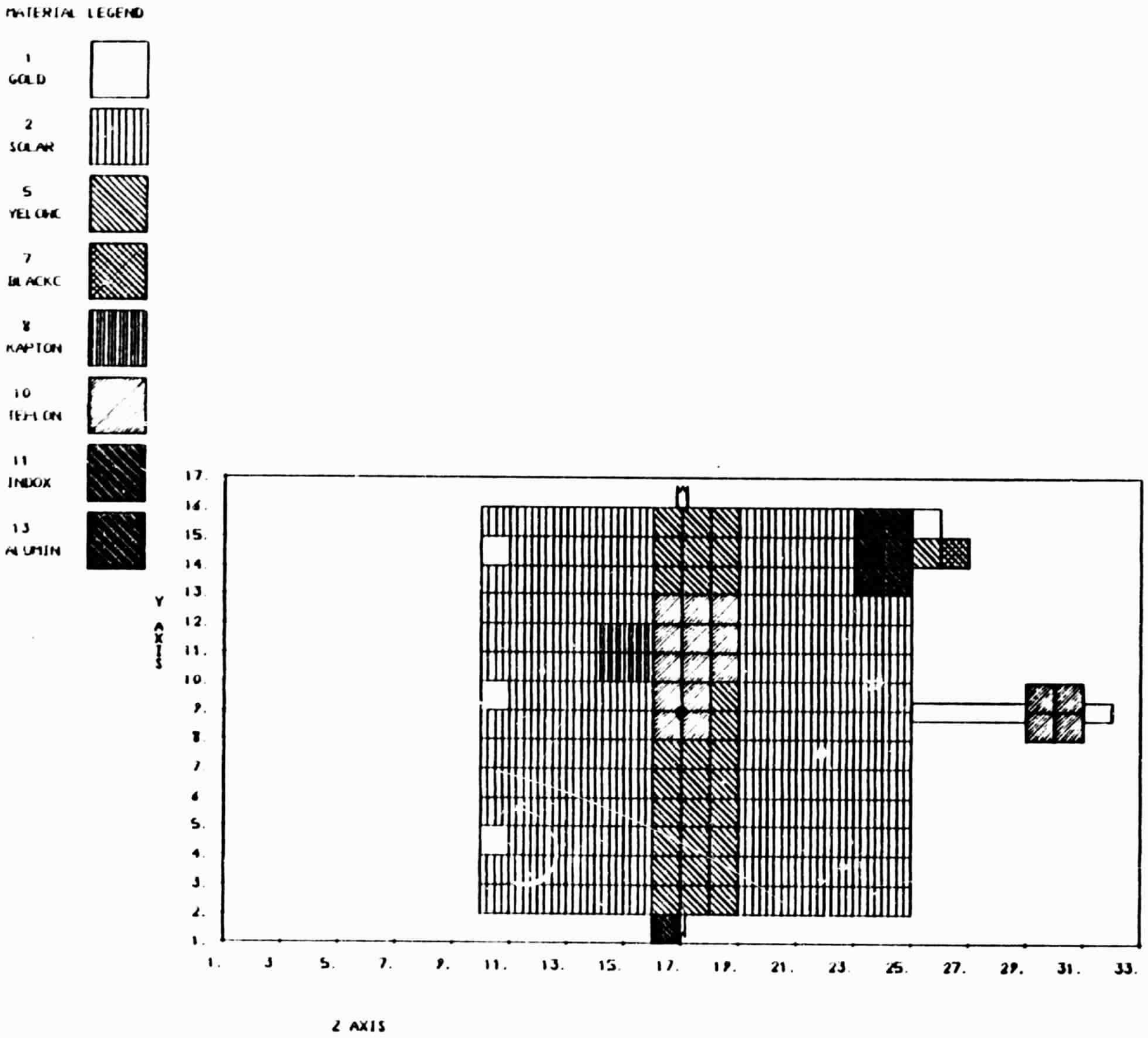

Figure A.6. Surface cell material composition as viewed from the negative X direction for X values between 1 and 17.

APPENDIX B

ANALYTICAL SOLUTION OF 1-D POISSON EQUATION FOR SC4 ION GUN MODEL

For the planar case, the Poisson equation for space charge limited emission of cold ions into an ambient plasma whose shielding effect is assumed to be proportional to the potential is given by (esu)

$$\frac{\partial^2\phi}{\partial x^2} = \frac{-4\pi j}{\left(\frac{2e}{m}\right)^{1/2}\left(\phi_A-\phi\right)^{1/2}} + \frac{\phi}{\lambda_D^2} \qquad (B.1)$$

where ϕ_A is the potential of the virtual anode at $x = 0$ and j is the current density. We seek solutions of Eq. (B.1) which satisfy the boundary condition $(\partial\phi/dx) = 0$ at $x = 0$ and decrease monotonically as x increases for zero to ∞.

The first integral of Eq. (B.1) gives

$$\frac{1}{2}\left(\frac{\partial\phi}{\partial x}\right) = 8\pi j\left(\frac{2e}{m}\right)^{-1/2}(\phi_A-\phi)^{1/2} + \frac{1}{2\lambda_D^2}\left(\phi^2-\phi_A^2\right) = G(\phi,\phi_A)$$

The electric field vanishes for ϕ_o given by

$$G(\phi_o,\phi_A) = 0 \qquad (B.2)$$

and the position of this zero occurs at $x = \infty$ if

$$\left(\frac{\partial G}{\partial\phi}\right)_{\phi=\phi_o} = 0 \qquad (B.3)$$

This last condition is just equivalent to the vanishing of the right hand side of (B.1) for $\phi = \phi_o$.

Equations (B.2) and (B.3) give

$$\frac{\phi_o}{\lambda_D^2} = 4\pi j\left(\frac{2e}{m}\right)^{-1/2} (\phi_A-\phi_o)^{-1/2}$$

$$\frac{\phi_o^2 - \phi_A^2}{\lambda_D^2} = -16\pi j\left(\frac{2e}{m}\right)^{-1/2} (\phi_A-\phi_o)^{1/2}$$

It follows that

$$\phi_o = \phi_A/3$$

and

$$j = \frac{1}{8\pi}\left(\frac{2e}{m}\right)^{1/2} \frac{(\phi_A-\phi_o)^{3/2}}{\lambda_D^2}$$

APPENDIX C

FORMAT FOR TABULATED SPECTRAL DATA

For NASCAP operating in the DIRECT mode to be able to read on the tabulated data, it must be prepared according to the following specifications and format.

1. Magnetic Tape Characteristics

Spectra can be provided on a coded 9-track magnetic tape with the following characteristics:

unlabelled
1600 bpi
EBCDIC or ASCII coded
fixed length record: 80 characters per record
fixed block size: 20 records per block

2. Data Format

Each data tape will consist of header records followed by repeated series of data records. The data will be read by a FORTRAN program using the FORMAT statements indicated below.

HEADER RECORD 1. DETECTOR FORMAT (80A1)

Identifies the detector(s) used to obtain the data.

HEADER RECORD 2. SOURCE FORMAT (80A1)

Identifies the individual(s) responsible for preparing the data.

HEADER RECORDS 3 through 10. COMMENTS FORMAT (80A1)

Any relevant information regarding the data can be included here, such as date data tape was generated, detector mode of operation, and what corrections have been applied to the raw data.

HEADER RECORD 11. $YEAR_0$, DAY_0, SEC_0,
$YEAR_1$, DAY_1, SEC_1 FORMAT (10F8.0)

$YEAR_0$, DAY_0, SEC_0 = time of earliest spectrum on tape

$YEAR_1$, DAY_1, SEC_1 = time of latest spectrum on tape

Each series of data records will represent a complete energy scan by the detector.

DATA RECORD 1. YEAR, DAY, SEC, NBINS, DELTA, VSAT,
$|\vec{S}|$, SX, SY, SZ FORMAT (10F8.0)

YEAR, DAY, SEC = time energy scan was begun

NBINS = number of distinct energy bins in the scan

DELTA = time (seconds) between each data point in the scan of the spectrum

VSAT = satellite potential during scan (volts)

$|\vec{S}|$ = sun intensity (1.0 = full sun)

SX, SY, SZ = normalized sun direction vector components at start of scan

DATA RECORDS 2 through (NBINS+1). ENERGY, $\log_{10}(F_i)$,
$\log_{10}(F_e)$, Ω, α, BX, BY, BZ FORMAT (10F8.0)

Each of these records represents a data point on the scan of the energy range

ENERGY = energy (eV)

F_i = ion distribution function (sec^3/m^6)

F_e = electron distribution function (sec^3/m^6)

Ω = detector view angle (degrees)

α = pitch angle (degrees)

BX, BY, BZ = magnetic field vector components ($nT \simeq 10^{-9}$ W/m^2)

(The α value is redundant since it can be calculated from Ω and the magnetic field vector.)

DATA RECORD NBINS+2. (END OF DATA MARKER) FORMAT (10F8.0)

This record will contain any negative real number to indicate the end of the spectral scan. (This record is redundant since NBINS is known.)

The data records 1 through (NBINS+2) are then repeated for each spectrum. Some of the information above may not be available for each spectrum or each data point. The following conventions can be used to indicate that the data is to be ignored:

VSAT: any value greater than +10000
$|\vec{S}|$: any negative value
SX, SY, SZ: blank or zero
F_i, F_e: blank or zero
Ω, α: any value greater than 360
BX, BY, BZ: blank or zero

```
(nP!
    1:DETECTOR >NORTH/SOUTH ON SC-9
    2:SOURCE   >J. DAVID NICHOLS/ UCSD
    3:COMMENTS>BACKGROUND COUNT SET AT 100
    4:COMMENTS>POTENTIAL ESTIMATED FROM DISTRABUTION FUN
    5:COMMENTS>NO SUN VECTOR OR ABSOLUTE ATTITUDE INFORM
    6:COMMENTS>I TRIED TO GIVE MORE CLOSELY SPACED DATA WHEN
    7:COMMENTS>THE POTENTIAL IS CHANGING MOST RAPIDLY
    9:COMMENTS>WE COME OUT OF ECLIPSE ABOUT 17:15
    9:COMMENTS>FOR ABOUT 10 MINUTES AFTER THIS POTENTIALS ARE
   10.COMMENTSONLY ROUGH ESTIMATES - HIGHLY UNCERTAIN
   11:     1979        87     59400      1979        87     63053
   12:     1979        87     59473        64      0.25        0.    -1.00      0.00      0.00      0.00
   13:    -3.90      0.00      0.00      0.00     86.20    -12.09  -173.27     90.26
   14:    -1.60      0.00      0.00      0.00     86.50    -11.80  -162.32    108.95
   15:     1.00      0.00    -11.18      0.00     86.50    -11.80  -162.32    108.95
   16:     4.00      0.00    -12.91      0.00     86.50    -11.80  -162.32    108.95
   17:     7.40      0.00    -14.34      0.00     86.50    -11.80  -162.32    108.95
   18:    11.40      0.00    -14.86      0.00     86.80    -11.80  -149.58    126.12
   19:    16.00      0.00    -15.20      0.00     86.80    -11.80  -149.58    126.12
   20:    21.20      0.00    -15.64      0.00     86.80    -11.80  -149.58    126.12
   21:    27.20      0.00    -15.82      0.00     86.80    -11.80  -149.58    126.12
   22:    34.00      0.00    -15.92      0.00     87.00    -12.09  -134.77    141.54
   23:    41.90      0.00    -16.03      0.00     87.00    -12.09  -134.77    141.54
   24:    50.90      0.00    -16.00      0.00     87.00    -12.09  -134.77    141.54
   25:    61.30    -12.22    -16.08      0.00     87.00    -12.09  -134.77    141.54
   26:    73.10      0.00    -16.14      0.00     87.20    -12.09  -118.75    155.79
   27:    86.60    -12.52    -16.16      0.00     87.20    -12.09  -118.75    155.79
   28:   102.20      0.00    -16.20      0.00     87.20    -12.09  -118.75    155.79
   29:   119.90      0.00    -16.27      0.00     87.20    -12.09  -118.75    155.79
   30:   140.30    -12.94    -16.31      0.00     87.50    -12.09  -100.98    167.95
   31:   163.60    -12.77    -16.36      0.00     87.50    -12.09  -100.98    167.95
   32:   190.30    -12.48    -16.32      0.00     87.50    -12.09  -100.98    167.95
   33:   220.90    -13.33    -16.35      0.00     87.50    -12.09  -100.98    167.95
   34:   255.90    -12.83    -16.37      0.00     87.70    -12.09   -82.02    178.04
   35:   295.90    -12.96    -16.43      0.00     87.70    -12.09   -82.02    178.04
   36:   341.80    -13.41    -16.47      0.00     87.70    -12.09   -82.02    178.04
   37:   394.40    -12.97    -16.55      0.00     87.70    -12.09   -82.02    178.04
   38:   454.60    -13.65    -16.59      0.00     87.90    -12.09   -62.18    185.80
   39:   523.50    -13.28    -16.70      0.00     87.90    -12.09   -62.18    185.80
   40:   602.40    -13.39    -16.85      0.00     87.90    -12.09   -62.18    185.80
   41:   692.70    -13.19    -16.94      0.00     87.90    -12.09   -62.18    185.80
   42:   796.20    -13.48    -17.03      0.00     88.10    -12.09   -41.71    191.44
   43:   914.60    -13.71    -17.14      0.00     88.10    -12.09   -41.71    191.44
   44:  1050.20    -13.59    -17.26      0.00     88.10    -12.09   -41.71    191.44
   45:  1205.50    -13.63    -17.38      0.00     88.10    -12.09   -41.71    191.44
   46:  1383.30    -13.52    -17.50      0.00     88.30    -12.09   -20.39    195.00
   47:  1586.90    -13.83    -17.70      0.00     88.30    -12.09   -20.39    195.00
   48:  1820.00    -13.62    -17.89      0.00     88.30    -12.09   -20.39    195.00
   49:  2087.00    -13.51    -18.06      0.00     88.30    -12.09   -20.39    195.00
   50:  2392.60    -13.63    -18.20      0.00     88.40    -12.39     1.05    196.19
   51:  2742.50    -13.95    -18.33      0.00     88.40    -12.39     1.05    196.19
   52:  3143.20    -14.07    -18.58      0.00     88.40    -12.39     1.05    196.19
   53:  3602.00    -14.11    -18.80      0.00     88.40    -12.39     1.05    196.19
   54:  4127.30    -14.01    -19.07      0.00     88.40    -12.69    22.37    195.00
   55:  4728.70    -14.37    -19.32      0.00     88.40    -12.69    22.37    195.00
   56:  5417.40    -14.33    -19.74      0.00     88.40    -12.69    22.37    195.00
   57:  6206.00    -14.46    -19.85      0.00     88.40    -12.69    22.37    195.00
   58:  7108.80    -14.46    -20.28      0.00     88.50    -12.98    43.40    191.44
   59:  8142.70    -14.55    -20.72      0.00     88.50    -12.98    43.40    191.44
   60:  9326.40    -14.59    -20.97      0.00     88.50    -12.98    43.40    191.44
   61: 10681.70    -14.67    -20.96      0.00     88.50    -12.98    43.40    191.44
   62: 12233.60    -14.79    -21.22      0.00     88.50    -13.28    63.87    185.51
   63: 14010.50    -14.89    -21.24      0.00     88.50    -13.28    63.87    185.51
   64: 16045.00    -15.05    -21.48      0.00     88.50    -13.28    63.87    185.51
   65: 18374.60    -15.37    -22.22      0.00     88.50    -13.29    63.87    185.51
   66: 21041.90    -15.34    -21.91      0.00     88.40    -13.58    83.71    177.44
   67: 24096.00    -15.49    -21.76      0.00     88.40    -13.58    83.71    177.44
   68: 27592.90    -15.70    -21.78      0.00     88.40    -13.58    83.71    177.44
   69: 31595.90    -15.80    -22.17      0.00     88.40    -13.58    83.71    177.44
   70: 36181.50    -16.08      0.00      0.00     88.50    -13.58   102.96    167.06
   71: 41430.90    -16.10    -22.38      0.00     88.50    -13.58   102.96    167.06
   72: 47441.40    -16.02    -23.30      0.00     88.50    -13.58   102.96    167.06
   73: 54323.40    -16.47    -22.69      0.00     88.50    -13.58   102.96    167.06
   74: 62203.30    -16.65    -23.23      0.00     88.40    -13.87   120.48    154.90
   75: 71225.80    -17.08      0.00      0.00     88.40    -13.87   120.48    154.90
   76: 81556.60    -17.51    -23.28      0.00     88.40    -13.87   120.48    154.90
   77:      -1.
   78:     1979        87     59673        64      0.25        0.    -1.00      0.00      0.00      0.00
   79:    -3.90      0.00      0.00      0.00     90.40      0.36   174.39    -87.55
   80:    -1.70      0.00      0.00      0.00     90.20      0.95   163.43   -106.57
   81:     1.00      0.00    -11.15      0.00     90.30      0.95   163.43   -106.57
   82:     4.00      0.00    -12.96      0.00     90.30      0.95   163.43   -106.57
   83:     7.40      0.00    -13.68      0.00     90.30      0.95   163.43   -106.57
   84:    11.40      0.00    -14.24      0.00     90.20      1.25   150.40   -123.70
   85:    16.00      0.00    -14.70      0.00     90.20      1.25   150.40   -123.70
   86:    21.20      0.00    -15.05      0.00     90.20      1.25   150.40   -123.70
   87:    27.20      0.00    -15.27      0.00     90.30      1.25   150.40   -123.70
   88:    34.00      0.00    -15.55      0.00     89.80      0.95   135.98   -139.72
   89:    41.90    -11.89    -15.72      0.00     89.80      0.75   135.98   -139.72
   90:    50.90      0.00    -15.90      0.00     89.80      0.75   135.98   -139.72
   91:    61.20      0.00    -16.01      0.00     89.80      0.75   135.98   -139.72
```

etc.

TABLE C1.

Example of a DIRECT data file.

ORIGINAL PAGE IS
OF POOR QUALITY

```
(nP)
 1:DETECTOR)NORTH/SOUTH ON SC-9
 2:SOURCE   )J. DAVID NICHOLS/ UCSD
 3:COMMENTS)BACKGROUND COUNT SET AT 100
 4:COMMENTS)POTENTIAL ESTIMATED FROM DISTRABUTION FUN
 5:COMMENTS)NO SUN VECTOR OR ABSOLUTE ATTITUDE INFORM
 6:COMMENTS)I TRIED TO GIVE MORE CLOSELY SPACED DATA WHEN
 7:COMMENTS)THE POTENTIAL IS CHANGING MOST RAPIDLY
 9:COMMENTS)WE COME OUT OF ECLIPSE ABOUT 17:15
 9:COMMENTS)FOR ABOUT 10 MINUTES AFTER THIS POTENTIALS ARE
10.COMMENTSONLY ROUGH ESTIMATES - HIGHLY UNCERTAIN
11:      1979        87    59400      1979        87    63053
12:      1979        87    59473        64      0.25       0.    -1.00      0.00       0.00       0.00
13:     -3.90      0.00     0.00      0.00     86.20   -12.09 -173.27     90.26
14:     -1.60      0.00     0.00      0.00     86.50   -11.80 -162.32    108.95
15:      1.00      0.00   -11.18      0.00     96.50   -11.80 -162.32    108.95
16:      4.00      0.00   -12.91      0.00     86.50   -11.80 -162.32    108.95
17:      7.40      0.00   -14.34      0.00     96.50   -11.80 -162.32    108.95
18:     11.40      0.00   -14.86      0.00     86.80   -11.80 -149.58    126.12
19:     16.00      0.00   -15.20      0.00     86.80   -11.80 -149.58    126.12
20:     21.20      0.00   -15.64      0.00     86.80   -11.80 -149.58    126.12
21:     27.20      0.00   -15.82      0.00     96.80   -11.80 -149.58    126.12
22:     34.00      0.00   -15.92      0.00     87.00   -12.09 -134.77    141.54
23:     41.90      0.00   -16.03      0.00     87.00   -12.09 -134.77    141.54
24:     50.90      0.00   -16.00      0.00     87.00   -12.09 -134.77    141.54
25:     61.30    -12.22   -16.08      0.00     87.00   -12.09 -134.77    141.54
26:     73.10      0.00   -16.14      0.00     87.20   -12.09 -118.75    155.79
27:     86.60    -12.52   -16.16      0.00     87.20   -12.09 -118.75    155.79
28:    102.20      0.00   -16.20      0.00     87.20   -12.09 -118.75    155.79
29:    119.90      0.00   -16.27      0.00     97.20   -12.09 -118.75    155.79
30:    140.30    -12.94   -16.31      0.00     87.50   -12.09 -100.98    167.95
31:    163.60    -12.77   -16.36      0.00     87.50   -12.09 -100.98    167.95
32:    190.30    -12.48   -16.32      0.00     87.50   -12.09 -100.99    167.95
33:    220.90    -13.33   -16.35      0.00     97.50   -12.09 -100.98    167.95
34:    255.90    -12.83   -16.37      0.00     87.70   -12.09   -82.02    179.04
35:    295.90    -12.96   -16.43      0.00     97.70   -12.09   -92.02    173.04
36:    341.80    -13.41   -16.47      0.00     87.70   -12.09   -82.02    179.04
37:    394.40    -12.97   -16.55      0.00     87.70   -12.09   -82.02    179.04
38:    454.60    -13.65   -16.59      0.00     87.90   -12.09   -62.18    185.80
39:    523.50    -13.28   -16.70      0.00     97.90   -12.09   -62.18    195.90
40:    602.40    -13.39   -16.85      0.00     87.90   -12.09   -62.18    185.80
41:    692.70    -13.19   -16.94      0.00     97.90   -12.09   -62.18    195.90
42:    796.20    -13.48   -17.03      0.00     88.10   -12.09   -41.71    191.44
43:    914.60    -13.71   -17.14      0.00     88.10   -12.09   -41.71    191.44
44:   1050.20    -13.59   -17.26      0.00     88.10   -12.09   -41.71    191.44
45:   1205.50    -13.63   -17.38      0.00     88.10   -12.09   -41.71    191.44
46:   1383.30    -13.32   -17.50      0.00     88.30   -12.09   -20.39    195.00
47:   1586.90    -13.83   -17.70      0.00     99.30   -12.09   -20.39    195.00
48:   1820.00    -13.62   -17.89      0.00     88.30   -12.09   -20.39    195.00
49:   2087.00    -13.51   -18.06      0.00     88.30   -12.09   -20.39    195.00
50:   2392.60    -13.63   -18.20      0.00     88.40   -12.39     1.05    196.19
51:   2742.50    -13.95   -18.23      0.00     88.40   -12.39     1.05    196.19
52:   3143.20    -14.07   -18.58      0.00     88.40   -12.39     1.05    196.19
53:   3602.00    -14.11   -18.80      0.00     88.40   -12.39     1.05    196.10
54:   4127.30    -14.31   -19.07      0.00     88.40   -12.69    22.37    195.00
55:   4728.70    -14.37   -19.32      0.00     88.40   -12.69    22.37    195.00
56:   5417.40    -14.33   -19.74      0.00     88.40   -12.69    22.37    195.00
57:   6206.00    -14.40   -19.85      0.00     88.40   -12.69    22.37    195.00
58:   7108.30    -14.46   -20.28      0.00     88.50   -12.99    43.40    191.44
59:   8142.70    -14.55   -20.72      0.00     99.50   -12.99    43.40    191.44
60:   9326.40    -14.59   -20.97      0.00     86.50   -12.99    43.40    191.4
61:  10681.70    -14.67   -20.96      0.00     88.50   -12.98    43.40    191.44
62:  12233.60    -14.79   -21.22      0.00     88.50   -13.29    63.87    185.51
63: [illegible]   -14.39   -21.24      0.00     88.50   -13.29    63.87    185.51
64:  16045.20    -15.75   -21.43      0.00     88.50   -13.28    63.87    185.5
65:  18374.60    -15.37   -22.22      0.00     88.50   -13.29    63.37    185.51
66:  21041.90    -15.34   -21.91      0.00     88.40   -13.58    83.71    177.44
67:  24095.00    -15.49   -21.76      0.00     88.40   -13.58    83.71    177.44
68:  27592.90    -15.70   -21.78      0.00     88.40   -13.58    83.71    177.44
69:  31595.90    -15.80   -22.17      0.00     88.40   -13.58    83.71    177.44
70:  36181.50    -16.08     0.00      0.00     88.50   -13.58   102.94 [illegible]
71:  41430.90    -16.10   -22.39      0.00     88.50   -13.58   102.96 [illegible]
72:  47441.40    -16.02   -23.30      0.00     88.50   -13.58   102.96 [illegible]
73:  54323.40    -16.47   -22.67      0.00     88.50   -13.58 [illegible] [illegible]
74:  62203.30    -16.65   -23.23      0.00     88.40   -13.87 [illegible] [illegible]
75: [illegible]   -17.06     0.00      0.00     88.40   -13.87 [illegible] [illegible]
76: [illegible]   -17.51   -23.26      0.00     88.40   -13.87 [illegible] [illegible]
77:     -1.
78:      1979        87    59473        64      0.25       0.    -1.00      0.00       0.00       0.00
79:     -3.90      0.00     0.00      0.00 [illegible] [illegible] [illegible] [illegible]
80: [illegible]    0.00     0.00      0.00 [illegible] [illegible] [illegible] [illegible]
81: [illegible]    0.00   -11.15      0.00 [illegible] [illegible] [illegible] [illegible]
82: [illegible]
83: [illegible]
84: [illegible]
85: [illegible]
86: [illegible]
87: [illegible]
88: [illegible]
89: [illegible]
90: [illegible]
91: [illegible]
```

etc.

TABLE C1.

Example of a DIRECT data file.

ORIGINAL PAGE IS
OF POOR QUALITY

APPENDIX D

FITTING THE TABULATED DATA TO FUNCTIONAL FORMS

1. Single Maxwellian Fits

The data was fit to a form

$$f(E) = N \cdot \left(\frac{m}{2\pi T}\right)^{3/2} e^{-E/T}$$

where m is the particle mass and T is the temperature of the Maxwellian. The density N is given by the zeroth moment MO

$$MO = \frac{4\pi}{m}\left(\frac{2}{m}\right)^{1/2} \int_0^{\infty} E^{1/2} f(E)\, dE = N \qquad (D.1)$$

Equation (A.1) applies when the spacecraft is not charged. For a potential of ϕ on the spacecraft the expression is modified.

$$MO = \frac{4\pi}{m}\left(\frac{2}{m}\right)^{1/2} \int_C^{\infty} E^{1/2} f(E + q\phi)\, dE$$

where C is the energy of the lowest energy data points included in the fit (i.e., the cutoff) and q is the charge on the particle at hand.

$$f(E + q\phi) = e^{-q\phi/T} f(E)$$

$$\therefore \quad MO = \left(\frac{4\pi}{m}\right)\left(\frac{2}{m}\right)^{1/2} N \cdot \left(\frac{m}{2\pi T}\right)^{3/2} e^{-q\phi/T} \int_C^{\infty} E^{1/2} e^{-E/T}\, dE$$

$$MO = \left(\frac{4\pi}{m}\right)\left(\frac{2}{m}\right)^{1/2} N \cdot \left(\frac{m}{2\pi T}\right)^{3/2} e^{-q\phi/T}\, \Gamma(3/2, y)$$

It is easy to show that

$$\frac{MO}{N} = e^{-q\phi/T}\,\frac{\Gamma(3/2,y)}{\Gamma(3/2)} = e^{-q\phi/T}\left[\mathrm{erfc}(y^{1/2}) + \frac{2}{\sqrt{\pi}}\,y^{1/2}\,e^{-y}\right]$$

where $y = C/T$.

$$\therefore \qquad N = MO\;e^{q\phi/T}\left[\mathrm{erfc}(y^{1/2}) + 2\left(\frac{y}{\pi}\right)^{1/2} e^{-y}\right]^{-1} \qquad \text{(D.2)}$$

Hence we can estimate the density N by measuring the moment MO:

$$MO = \sum_{E=C}^{10^6} E^{1/2}\,f(E)\,\Delta E \qquad \text{(D.3)}$$

The second moment, M2, has the form

$$M2 = \frac{2}{3}\cdot\left(\frac{4\pi}{m}\right)\left(\frac{2}{m}\right)^{1/2}\int_0^\infty E^{3/2}\,f(E)\,dE = N\cdot T$$

for an uncharged spacecraft. Introducing a cutoff C and potential ϕ leads to a result similar to that for MO:

$$T = \frac{\frac{M2}{MO}\left[\mathrm{erfc}(y^{1/2}) + e^{-y}\,2\cdot\left(\frac{y}{\pi}\right)^{1/2}\right]}{\left[\mathrm{erfc}(y^{1/2}) + e^{-y}\left(2\left(\frac{y}{\pi}\right)^{1/2} + \frac{4}{3}\,\frac{y^{3/2}}{\pi^{1/2}}\right)\right]} \qquad \text{(D.4)}$$

Equations (D.2) and (D.4) form two nonlinear simultaneous equations for T and N. Solution by iteration leads to values for N and T that make up the single Maxwellian fit.

2. Double Maxwellian Fits

The double Maxwellian fits were made by minimizing the relative error (least squares). The desired function has the form:

$$f(E) = N_1 \left(\frac{m}{2\pi T_1}\right)^{3/2} e^{-E/T_1} + N_2 \left(\frac{m}{2\pi T_2}\right)^{3/2} e^{-E/T_2} \qquad (D.5)$$

An initial choice of values for T_1 and T_2 were made. The fit was made to agree exactly with the measured data at two points, one from the low and the other from the high energy regime. This determined the values of N_1 and N_2. and had the effect of weighting the fit around the fixed points and ensuring a good compromise fit over the whole energy range. All possible combinations of choices for T_1 and T_2, between realistic limits, were tried and the values that gave the minimum error were used as the double Maxwellian fit parameters.

3. Discussion

In all of the fits a cutoff of 1000 eV was used for the repelled species (electrons); i.e., only data above 1000 eV was included in the fits. Using data below this value lead to erratic and often rather unphysical values for the fitting parameters. For the attracted species (ions) the cutoff was taken as 1000 eV or the spacecraft potential, which ever was the greater. In the double Maxwellian fitting procedure the lower limit for the choice of temperature was forced to be one-half of the spacecraft potential for the repelled species. This ensured the absence of low temperature, high density components which were not observable at the surface due to the spacecraft potential.

REFERENCES

1. Katz, I., D. E. Parks, M. J. Mandell, J. M. Harvey, D. H. Brownell, Jr., S. S. Wang and M. Rotenberg, "A Three-Dimensional Dynamic Study of Electrostatic Charging in Materials," NASA CR-135256, August 1977.

2. Katz, I., J. J. Cassidy, M. J. Mandell, G. W. Schnuelle, P. G. Steen, D. E. Parks, M. Rotenberg and J. H. Alexander, "Extension, Validation, and Application of the NASCAP Code," NASA CR-159595, January 1979.

3. Cassidy, J. J., "NASCAP User's Manual – 1978," NASA CR-159417, August 1978.

4. Katz, I., J. J. Cassidy, M. J. Mandell, G. W. Schnuelle, P. G. Steen and J. C. Roche, "The Capabilities of the NASA Charging Analyzer Program," Proceedings of the Spacecraft Charging Technology Conference, 1978, NASA Conference Publication 2071, AFGL-TR-79-0082.

5. Schnuelle, G. W., D. E. Parks, I. Katz, M. J. Mandell, P. G. Steen, J. J. Cassidy and A. Rubin, "Charging Analysis of the SCATHA Satellite," Proceedings of the Spacecraft Charging Technology Conference, 1978, NASA Conference Publication 2071, AFGL-TR-79-0082.

6. Schnuelle, G. W., I. Katz, M. J. Mandell and A. G. Rubin, "Simulation of the Charging of the SCATHA (P78-2) Satellite," presented at the AGU Fall Meeting, San Francisco, December 1979.

7. Mandell, M. J., I. Katz and G. W. Schnuelle, "Photoelectron Charge Density and Transport Near Differentially Charged Spacecraft," IEEE Trans. Nuc. Sci., NS-26, 1979.

8. Steen, P. G., "SCATHA Experiment Shadowing Study," Systems, Science and Software Topical Report, SSS-R-78-3658, May 1978.

9. Whipple, E. C., personal communication.

10. Mizera, P. F., "Natural-Artificial Charging: Results From the Satellite Surface Potential Monitor Flown on P78-2," presented at AIAA Aerospace Sciences Meeting, January 1980.

11. Ashley, J. C., C. J. Tung, V. E. Anderson and R. H. Ritchie, (i) AFCRL-TR-75-0583; (ii) RADC-TR-76-220; (iii) RADC-TR-76-125; (iv) IEEE Trans. Nucl. Sci., NS-25/6, 1566, 1978.

12. Kaye, S., *et al.*, SC8 data.

13. Frederickson, A. R., NASA Conference Publication 2071, AFGL-TR-79-0082, 559, 1978.

14. Treadaway, M., presented at SCATHA meeting, Aerospace Corporation, September 1980.

15. Frederickson, A. R., IEEE Nuc. Sci., NS-24, 2532, 1975.

16. Nightingale, R. W., *et al.*, SC3 data, Lockheed Research Publication, LMSC/D766804.

17. Sagalyn, R. C. and W. J. Burke, "INJUN 5 Observations of Vehicle POtential Fluctuations at 2500 km," Proceedings of the Spacecraft Charging Technology Conference, AFGL-TR-77-0051, NASA TMX-73537, February 1977.

18. Parker, L. W., "Plasmasheath-Photosheath Theory for Large High-Voltage Space Structures," *Space Systems and Their Interaction with Earth's Space Environment*, Progress in Astronautics and Aeronautics, *71*, 477, 1980.

19. McCoy, J. E., A. Konradi and O. K. Garriott, ibid, p. 523.

20. Liemohn, H. B., "Electrical Charging of Shuttle Orbiter," Battelle, Pacific Northwest Laboratories Report BN 5A 518, June 1976.

21. Inouye, G. T., R. L. Wax, A. Rosen and N. L. Sanders, "Study of Space Environment Physical Processes and Coupling Mechanisms," AFGL-TR-79-0206, September 1979.

22. Mott-Smith, H. M. and I. Langmuir, Phys. Rev., *28*, 727, 1926.

23. Langmuir, I. and K. Blodgett, Phys. Rev., *22*, 347, 1923; *24*, 99, 1924.

24. Al'pert, Ya. L., A. V. Gurevich and L. P. Pitaevskii, "Space Physics With Artificial Satellites," Consultants Bureau, New York, pp. 186-210, 1965.